

Assessment of bolted connections for supporting structures of offshore wind turbine towers

Mechanical performance and structural health monitoring

Cheng, L.

DOI

[10.4233/uuid:fb1e3e10-0495-43e8-a53c-299062dbe58f](https://doi.org/10.4233/uuid:fb1e3e10-0495-43e8-a53c-299062dbe58f)

Publication date

2023

Document Version

Final published version

Citation (APA)

Cheng, L. (2023). *Assessment of bolted connections for supporting structures of offshore wind turbine towers: Mechanical performance and structural health monitoring*. [Dissertation (TU Delft), Delft University of Technology]. <https://doi.org/10.4233/uuid:fb1e3e10-0495-43e8-a53c-299062dbe58f>

Important note

To cite this publication, please use the final published version (if applicable). Please check the document version above.

Copyright

Other than for strictly personal use, it is not permitted to download, forward or distribute the text or part of it, without the consent of the author(s) and/or copyright holder(s), unless the work is under an open content license such as Creative Commons.

Takedown policy

Please contact us and provide details if you believe this document breaches copyrights. We will remove access to the work immediately and investigate your claim.

Assessment of bolted connections for supporting structures of offshore wind turbine towers

Mechanical performance and structural health monitoring

Propositions

Accompanying the dissertation

Assessment of bolted connections for supporting structures of offshore wind turbine towers

Mechanical performance and structural health monitoring

By

Lu Cheng

- 1 A finite element model that mostly accurately simulates the real situation is not the best one. [This proposition pertains to this dissertation]
- 2 Small-scale tests are sufficient to deliver convincing results for bolted connections. [This proposition pertains to this dissertation]
- 3 Conference discussion is the most efficient method to understand a technology's pros and cons. [This proposition pertains to this dissertation]
- 4 The majority of researchers view artificial intelligence techniques as tools rather than algorithms. [This proposition pertains to this dissertation]
- 5 PhD researchers benefit from participating in as much related research as possible.
- 6 Perseverance and resilience are more valuable qualities for pursuing a PhD than intelligence.
- 7 Negative feedback during a PhD should be appreciated.
- 8 A basic understanding of fatigue assists PhD students in preventing overstress during their studies.
- 9 Ranking oneself to peers is not significant during PhD journey.
- 10 Deciding what to prepare for dinner is more difficult than making a research plan.

These propositions are regarded as opposable and defensible, and have been approved as such by the promotor Prof.dr. M. Veljkovic and promotor Dr. R. M. Groves.

Assessment of bolted connections for supporting structures of offshore wind turbine towers

Mechanical performance and structural health monitoring

Dissertation

for the purpose of obtaining the degree of doctor

at Delft University of Technology

by the authority of the Rector Magnificus, Prof.dr.ir. T.H.J.J. van der Hagen

chair of the Board for Doctorates

to be defended publicly on

Monday 3 July 2023 at 17:30 o'clock

by

Lu CHENG

Master of Engineering in Structural Engineering,

Dalian University of Technology, China,

Born in Shanxi, China

This dissertation has been approved by the promotors

Composition of the doctoral committee

Rector Magnificus	chairperson
Prof.dr. M. Veljkovic	Delft University of Technology, promotor
Dr. R. M. Groves	Delft University of Technology, promotor

Independent members:

Prof.dr.ir. L.J. Sluys	Delft University of Technology
Prof.dr. C. Rebelo	University of Coimbra, Portugal
Prof.dr. R. Pullin	Cardiff University, United Kingdom
Prof.dr. H. Xin	Xi'an Jiaotong University, China
Dr.ir. Y. Yang	Delft University of Technology
Prof.dr. Z. Li	Delft University of Technology, reserve member



This research was financially supported by China Scholarship Council.

Keywords: C1 wedge connection, ring flange connection, tensile behavior, fatigue performance, finite element modelling, Acoustic emission, thin PZT sensors

Printed by: Ipskamp Printing, The Netherlands

Cover design: Lu Cheng, Ze Chang, and Yu Chen

Copy right @ 2023 by Lu Cheng

ISBN: 978-94-6366-707-4

To my family

CONTENTS

CONTENTS	7
1. GENERAL INTRODUCTION	11
1.1 RESEARCH BACKGROUND	12
1.2 RESEARCH SIGNIFICANCE	21
1.3 RESEARCH QUESTIONS	22
1.4 RESEARCH METHOD	23
1.5 THESIS OUTLINE	25
REFERENCES	27
2. THE C1 WEDGE CONNECTION, TENSILE BEHAVIOUR OF A SEGMENT TEST	33
2.1 INTRODUCTION	34
2.2 EXPERIMENTAL PROGRAM	35
2.3 FE SIMULATION	39
2.4 EXPERIMENTAL AND FE RESULTS	47
2.5 PARAMETRIC ANALYSIS	57
2.6 CONCLUSION	60
REFERENCES	62
3. COMPARATIVE STUDY ON MECHANICAL BEHAVIOUR OF CONNECTIONS	65
3.1 INTRODUCTION	66
3.2 INVESTIGATED CONNECTIONS	66
3.3 EXPERIMENTAL WORK	69
3.4 FE MODELLING OF CONNECTIONS	71
3.5 PARAMETRIC STUDIES ON TENSILE BEHAVIOUR	80
3.6 PARAMETRIC STUDIES ON FATIGUE PERFORMANCE	89
3.7 COMPARISON BETWEEN CONNECTIONS	95
3.8 CONCLUSION	97
REFERENCES	99

4. IDENTIFYING DEFORMATION STAGE BY ACOUSTIC EMISSION	103
4.1 INTRODUCTION	104
4.2 PROPOSED DENOISING METHODOLOGY	105
4.3 EVALUATION OF SSA-VMD METHOD	108
4.4 EXPERIMENTAL STUDIES	113
4.5 APPLICATION OF ANN FOR CLASSIFICATION	116
4.6 CONCLUSION	122
REFERENCES	124
5. DATA LEVEL FUSION OF ACOUSTIC EMISSION SENSORS	129
5.1 INTRODUCTION	130
5.2 OVERVIEW OF THEORETICAL BACKGROUND	133
5.3 EXPERIMENTAL SET-UP	138
5.4 EXPERIMENTAL RESULTS DISCUSSION	142
5.5 DATA FUSION OF MULTIPLE THIN PZT SENSORS	148
5.6 CONCLUSION	156
REFERENCES	158
6. EARLY FATIGUE DAMAGE DETECTION BY ACOUSTIC EMISSION	163
6.1 INTRODUCTION	164
6.2 THE PROPOSED DAMAGE DETECTION METHOD	166
6.3 EXPERIMENTAL SET-UP	168
6.4 DAMAGE MONITORING OF CT SPECIMENS	173
6.5 EARLY WARNING FOR C1-WC	178
6.6 CONCLUSION	181
REFERENCES	183
7. CONCLUSIONS AND RECOMMENDATIONS	187
7.1 CONCLUSIONS	188
7.2 RECOMMENDATION FOR FUTURE WORK	190
SUMMARY	193
SAMENVATTING	195
ACKNOWLEDGMENTS	199

LIST OF PUBLICATIONS	203
CURRICULUM VITAE	205

1. GENERAL INTRODUCTION

This chapter presents the background of bolted connections used in offshore wind turbine towers. The research significance, objectives and methods are introduced afterwards. In the end, the thesis outline is given.

1.1 RESEARCH BACKGROUND

1.1.1 Society relevance

Wind power has been one of the most affordable resources in terms of renewable electric energy supply and carbon emissions reduction [1–3]. A wind farm is primarily made up of a group of wind turbines, which are placed in certain locations on land or in sea to harvest the onshore and offshore wind energy, respectively. Onshore wind farms are known for their fast installation time, but they are typically less efficient than offshore wind farms due to the lower average wind speeds and the absence of physical obstructions provided by the surrounding landscape and built environment. In contrast, by exploiting powerful and more consistent offshore wind power, offshore wind farms (OWFs) ensure the generation of electrical energy with fewer negative environmental impacts [4,5]. This reinforces the demand for larger capacity and more efficient offshore wind turbines (OWTs).

Over the past decade, the offshore wind industry in Europe has grown rapidly, with noticeable benefits to both the environment and the economy. Europe now has 28.4 GW of installed offshore capacity, which has risen by almost 56% annually from 2011 to 2022 [6,7]. Fig. 1-1 shows the growth of OWFs in Europe since 2011 with aspects of installed capacity, size, and locations. The average rated capacity of turbines and OWF size in 2021 are 2.4 and 2.2 times of those in 2011, respectively. Before 2013, no OWF was located further away than 50 km off the shore. In the last 10 years, the average water depth shows an increasing trend, as well as the average OWF size. The average distance in recent years has fallen because fewer projects are built at a greater distance.

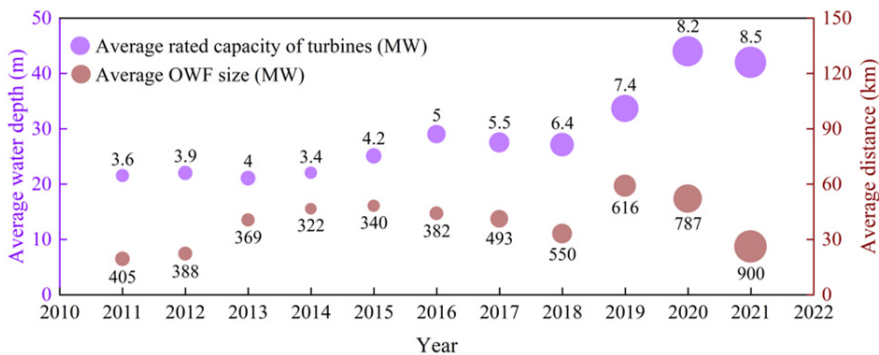


Fig. 1-1 Development of OWFs in terms of average water depth and rated capacity of turbines (violet), and average distance to coast and OWF size (brown) in Europe

According to the size of the turbine, the depth of the water, and the geotechnical conditions, five types of foundations are frequently utilized in OWF projects (see Fig. 1-2). Among them, the monopile (MP) foundation, which reaches 4914 units, continues to be the most popular foundation type (82%) [8]. Its predominance can be attributed to the simplicity of its design, fabrication, and execution.

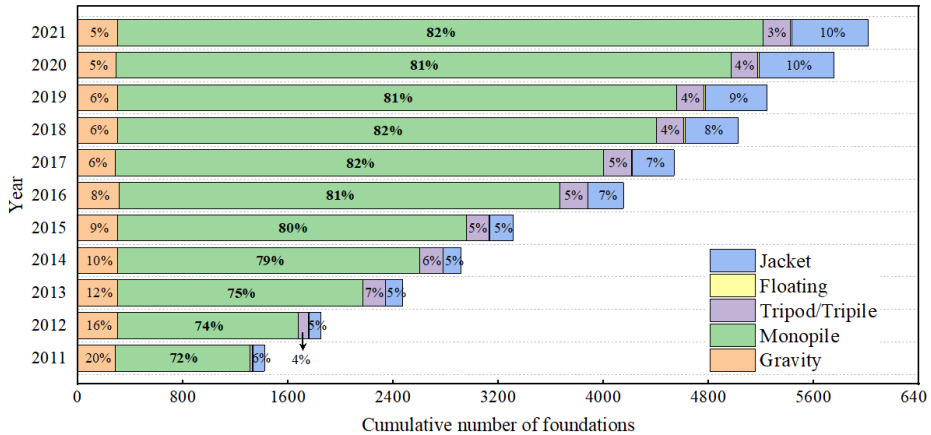


Fig. 1-2 Share of foundation types of OWF projects in Europe [5,7,8]

Currently, OWFs with rather large wind turbines positioned at depths of more than 30 m also adopt monopole substructures [9], where large-diameter monopiles are required to guarantee structural stiffness. Given that wind speed tends to increase as height increases, turbine towers are likewise getting taller to harvest more energy. The requirement for increasing the size of the supporting structures has been observed for the new generation of OWTs [5,10,11]. For example, monopiles for the recently commissioned project HE DREIHT OFFSHORE WIND [12] will be installed in a water depth of 40 m with a hub height of 140 m above sea level and a rotor diameter of 236 m. Such supporting structures belong to XXL monopiles reaching lengths of 120 m, 10 m in diameter and weight of 2400 tonnes [13,14].

Such huge diameters and heights result in exponentially rising costs. The connections between the MP, driven into the seabed, and the transition piece (TP) connected to the top of the MP are consequently subjected to much larger forces and moments. Therefore, to ensure the satisfactory structural performance of OWFs, the TP-MP connections must be both easy to maintain and safe to install, while also being technologically feasible. Several options are attracting attention to study, such as bolted ring-flange (RF) connections [15–18], ring-flange connections with defined contacts (RFD) [15,19], and C1 wedge connections (C1-WCs) [20,21].

1.1.2 Development of MP-TP connections

The bolted ring-flange connection (RF) is considered the most promising and common solution for OWT [22–28]. By utilizing the conventional segment approach, analytical models and design principles have been proposed for this connection [15,16]. The Schmidt/Neuper model [29] is most widely used for fatigue limit states (FLS) assessment and the Petersen/Seidel model [16,30] for ultimate limit states (ULS). Standard design procedures are provided by guidelines and codes, including (a) DNVGL-ST-0126 [31]; (b) DIN 18088-3 [32]; (c) VDI 2230 Part I [33]; (d) IEC 61400-6 [34]; (e) RP-C203 [35]. The ULS and FLS conditions are two essentials for RF connection

design. The overall resistance of RF connections is strongly linked to the used high-strength bolt behaviour [25,36,37]. Design standards and recommendations provide bolt fatigue detail category 50 (if the bending stresses are included) [37,38]. A reduction factor should be considered for the fatigue resistance of bolts with a diameter larger than 30 mm [39,40].

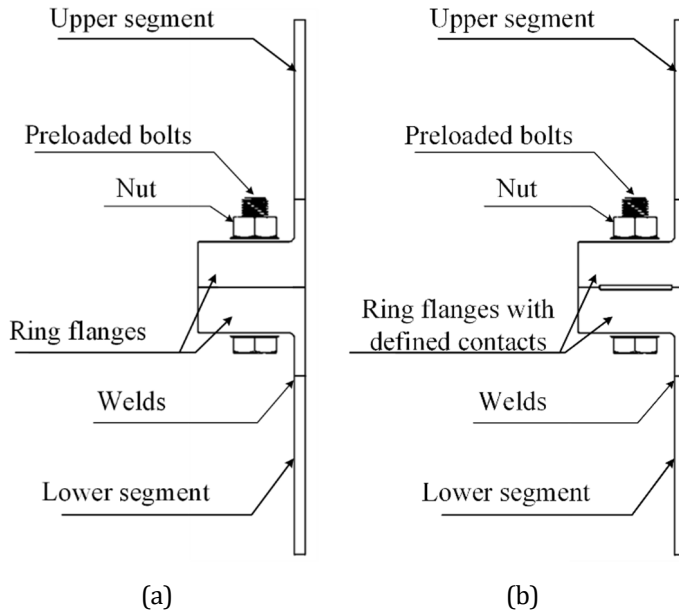


Fig. 1-3 (a) Ring flange connection (RF); (b) Ring flange connection with defined contacts (RFD)

Apart from the RF connection [16], the RFD connection is a concept which shows favourable fatigue performance. It is not used in practice to the best of the author's knowledge. Nonetheless, this connection presents notable advantages worth exploring. The pretension bolts action is transferred through two clearly defined contact surfaces in RFD connections, instead of the continuous contact surfaces in RF connections (see Fig. 1-3). RFD connection was proposed in a Master thesis project and studied by Krutschinna [19]. He provided an analytical model to evaluate the bolt force evolution in RFD connections by FE analyses. A comparison of the mechanical behaviour between RF and RFD connections with different bolt types was highlighted in [41].

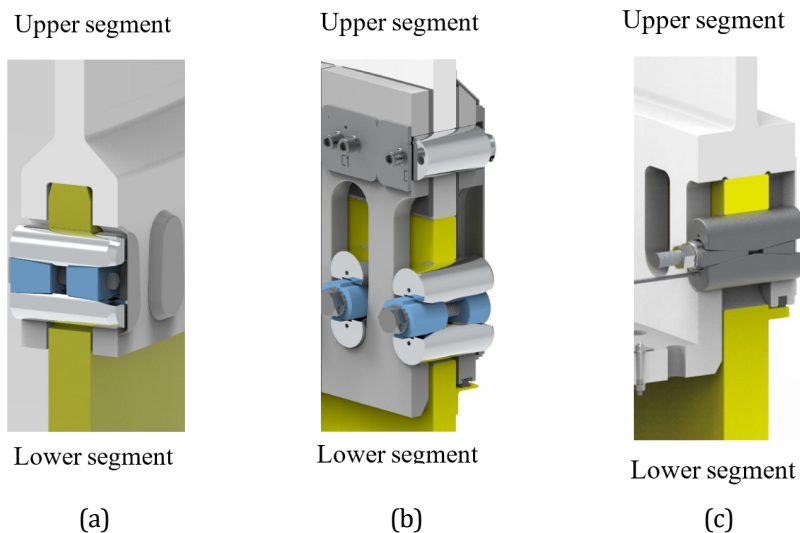


Fig. 1-4 Development of C1 Wedge connection. (a) First generation with forged upper segment; (b) Second generation with pinned-assembly upper segment; (c) Third generation with welded upper segment

The C1-WC was designed by the company C1 Connections B.V. [20,21] in early 2017. As illustrated in Fig. 1-4, three generations of the C1 wedge connection have been developed so far to improve fatigue resistance. A detailed analysis of the first generation of the C1 wedge connection was conducted experimentally and numerically under monotonic and fatigue conditions [42,43]. The fracture occurred at the hole of the lower segment. Detail category 92 [39] was obtained for the innovative C1 wedge connection, which demonstrates a noticeable improvement in the fatigue resistance compared to the detail category 50 of bolts in the ring flange connections [37,38]. To guarantee the resistance of the cylindrical tower (monopile), a set of analytical calculations was carried out e.g., the net section resistance in the smallest cross sections. It was found that the ultimate limit state (ULS) of this connection is primarily controlled by the tensile resistance of the main plates. A full-scale finite element (FE) model was built to investigate the global structural behaviour of the tower using C1 wedge connections [43]. The considered tower segments were 15 m long on both sides of the connection with an outer diameter of 7 m. The design procedure and related analytical model were proposed and validated. After that, the forged upper segment in the first-generation design was modified to a pinned assembly in the upper segment, see Fig. 1-4 (b). As seen in Fig. 1-4 (c), additional improvements in the third generation of C1 wedge connections are related to the integration of the upper segment with webs by using butt welds.

1.1.3 Material degradation in MP-TP connections

The degradation of macroscopic mechanical properties of a steel structure appears while in service, originating from void nucleation together with inelastic deformation

[44]. Steel structures then collapse when significant deformation has accumulated. Especially, OWTs operate in harsh environments characterized by the constant presence of wind, wave, and current forces, as well as variable amplitude cyclic loads. The fatigue performance of the MP-TP connection is the primary consideration in wind turbine tower design [25]. To ensure the longevity of the connection, it is preferable to design the MP-TP connection to make the fatigue failure occur at an extremely high number of load cycles, namely high cyclic fatigue (HCF) [45]. HCF refers to the loads within the elastic region of the material. The transition between HCF and LCF is determined by whether the plastic deformation happens, which is detrimental to the remaining service life of the entire steel structure. A method to infer whether plastic deformation has occurred is therefore needed.

Additionally, dynamic loads from winds and waves can cause iterative deterioration and crack initiation, eventually leading to fracture. Cracks usually originate at the material surface where peak stress occurs [46]. Fatigue failures can occur quickly from crack initiation to total failure without significant prior deformations. Catastrophic failure of OWTs can result from fatigue damage to the MP-TP connection, underscoring the need for early detection of fatigue damage in the MP-TP connection to prevent complete collapse.

A substantial amount of study into the mechanical behaviour description and damage propagation of steel material has contributed to their safe application [47–52]. In addition to destructive testing methods, recent advancements in non-destructive testing (NDT) techniques offer new opportunities for ensuring the integrity of structures, enabling non-invasive and continuous structural health monitoring (SHM) [53].

1.1.4 NDT Methods for Structural Health Monitoring

Each NDT method has its own set of advantages and disadvantages and, therefore, some are better suited than others for a particular application. Fig. 1-5 illustrates the most used NDT techniques. All the major NDT techniques can be categorized into two types: active techniques and passive techniques based on the principles. For active techniques, a test medium is applied to the test specimen and a response is expected if a flaw or defect is present; the response is then detected and recorded by some means. Passive techniques are those that monitor the item during either a typical load environment or a proof cycle and attempt to determine the presence of the defect. Specifically, infrared thermography and acoustic emission actually can be active or passive depending on the certain application.

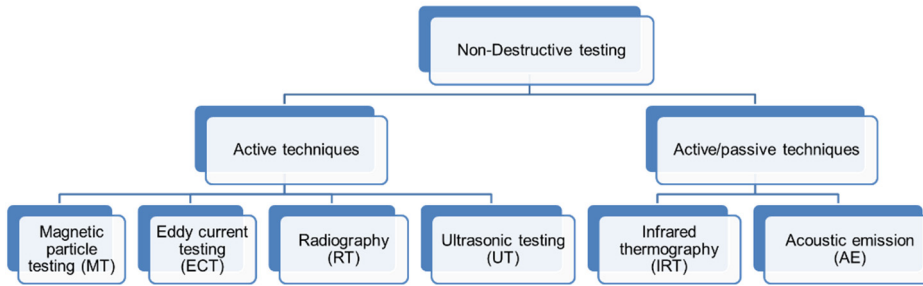


Fig. 1-5 Illustration of Non-destructive testing (NDT) techniques

Several factors need to be taken into account when selecting NDT techniques [54,55]:

- Stages in the lifetime of the structures that the NDT method is applied: (a) Design, (b) processing, (c) manufacturing or (d) in-service monitoring;
- Objectives of using the NDT method: (a) damage identification, (b) damage localization, (c) damage size and severity assessment or (d) remaining life prediction;
- Feasibility of the NDT method available
- Economic criteria;

Table 1-1 and Table 1-2 present the characteristics and differences of these techniques, further details can be found in [56]. It can be found that there are two major differences between Acoustic emission (AE) and other NDT techniques:

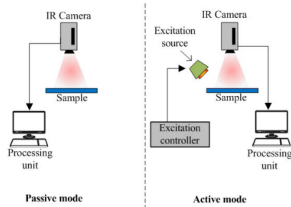
- AE is suitable for real-time monitoring to detect the growth or movement of defects, while other NDT techniques can only detect the presence of defects [57];
- AE is best suited for monitoring an entire structure, namely global monitoring, as long as the structure is acoustically coupled, whereas most other techniques are local scans [58].

In the realm of real-time monitoring for offshore wind turbine towers, conducting a comprehensive assessment of both internal and surface defects holds paramount importance. However, NDT methods such as Magnetic Testing (MT) and Eddy Current Testing (ECT) prove impractical for effectively monitoring internal defects. Additionally, the high cost associated with Radiographic Testing (RT) restricts its feasibility for offshore wind turbine towers. Although Ultrasonic Testing (UT) can be applied for defect detection, it falls short in its ability to identify the growth or movement of defects. Therefore, the Acoustic Emission (AE) method stands out as the optimal solution for real-time monitoring of offshore wind turbine towers.

Table 1-1 Common NDT methods

Methods	Illustration	Principle	Application	Pros	Cons
MT [59]		<p>Magnetize the inspected material first and the discontinuity of the inspected specimen generates leakage of magnetic flux</p>	<ul style="list-style-type: none"> - Inspect the surface break, defects and discontinuity 	<ul style="list-style-type: none"> - Low cost - Portable - Subsurface defects 	<ul style="list-style-type: none"> - Only applicable for Ferromagnetic materials - Pre/post cleaning necessary - Demagnetization required after the test
ECT [60]		<p>The presence of discontinuity weakens the secondary magnetic field generated by Eddy currents</p>	<ul style="list-style-type: none"> - Surface defects, cracks, and corrosion - Waviness detection 	<ul style="list-style-type: none"> - High speed - Low cost - No probe contact required 	<ul style="list-style-type: none"> - Only applicable to a conductive material - Surface roughness may affect test quality
RT [61]		<p>Radiation passes through the inspected specimen and the backscatter data contain information about the changes in material properties or internal delaminations</p>	<ul style="list-style-type: none"> - Ascertain material thickness or density variation - Access to internal non-homogeneities within the depth of material 	<ul style="list-style-type: none"> - Permanent records - Geometry variation does not affect the direction of the radiation beam 	<ul style="list-style-type: none"> - Radiation hazard - Expensive - Linear defects may be missed - Depth of defect not indicated
UT [56]		<p>Employs a transducer to generate high-frequency sound waves toward a specimen under test and capture the reflected wave</p>	<ul style="list-style-type: none"> - Flaw detection - Dimension, bond integrity, erosion & corrosion thickness measurement - Estimation of grain size in metals 	<ul style="list-style-type: none"> - Immediate results - Permanent record capability - Portable - High penetration capability 	<ul style="list-style-type: none"> - Defects may be missed if not in the path of the ultrasonic signal - Not applicable to an irregular surface - Cannot provide real-time detection

IRT [56]



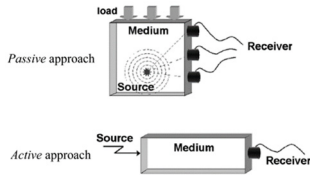
The defective area will generate a different temperature distribution from its neighbours which forms the shape of the defect.

- Structure internal damage
- material strength detection

- Permanent record
- Remote sensing
- Portable

- Expensive
- Reference standards required
- Poor resolution on thick sections

AE [62]



AE is based on the phenomenon of radiation of elastic waves in solids that occurs when a material undergoes irreversible changes in its internal structure.

AE can detect anything that produces a sound which allows for many obscure applications

- Best suited for global monitoring of a structure

- Ability to detect a range of damage mechanisms
- Assesses the structure under real operational conditions

- Cannot detect defects that do not grow
- Noise sensitivity
- High sampling rates generate large volumes of data
- Limited repeatability

Table 1-2 Comparison between common NDT methods [53,56,63]

Techniques	MT	ECT	RT	UT	IRT	AE
Test Obejct	Surface and sub-surface defects	Surface and sub-surface defects	Internal defects	Surface and internal defects	Surface and internal defects	Surface and internal defects
Output	The presence of defects: size, shape, and location				The growth/movement of defects	
Local/global	Local	Local	Local	Local	Local	Local/global
Detection period for large area	Slow	Slow	Slow	Slow	High-speed	High-speed
Cost	Low	Low	Expensive	Low	Expensive	Low
Conatct requirement	One-sided accessible	One-sided accessible	Two-sided accessible	One-sided accessible	No contact	One-sided accessible
Response	Depends on size, shape & orientation of flaw					Depends on source intensity/energy release

Acoustic Emission (AE) technology uses elastic waves generated by a rapid release of energy within a material [64]. In the context of metal materials in engineering applications, the primary AE sources are yielding, crack initiation, crack propagation, and crack opening and closure. Unlike ultrasonic waves that typically operate in the high frequency range up to 50 MHz, the dominant frequency range of AE elastic waves is between 1 kHz to 1000 kHz. An AE system is normally made up of sensors, preamplifiers, and data acquisition devices. AE waves can be recorded by sensors and then analysed to extract information on a number of damage factors, such as material types, plasticity level, loading conditions and microdefects.

A majority of studies for structural health monitoring using the AE technique have been conducted in many fields, such as aerospace [65]. In comparison with these fields, investigations into materials including concrete and steel that constitute the civil infrastructure took place later. In 1972, Pollock and Smith [66] carried out AE monitoring on a portable military bridge for the first time. After that, comprehensive surveys have been carried out for damage identification and classification in concrete structures [67–70]. An extensive review of both lab and field tests performed on concrete, steel and fibre-reinforced polymer (FRP) bridges or bridge parts has been described by Nair and Cai [57]. Whereas, although the successful demonstration of using AE in civil infrastructures, it is surprising to find that the focus of the vast majority of existing work is on simple geometry structures.

In summary, the increasing demand for better utilization of offshore wind resources has led to a significant rise in the use of offshore wind turbines (OWTs). The MP-TP connections between adjacent segments are critical components that ensure the integrity and stability of OWT structures. Various types of connections have been proposed by designers [10] and developed continuously. However, due to the harsh environments and extremely dynamic loads, material degradation of the connection is inevitable, which affects the safety and service life of OWTs. Among the available non-destructive methods (NDT) for structural health monitoring, the Acoustic Emission (AE) technique outperforms others due to its real-time and global monitoring capabilities.

1.2 RESEARCH SIGNIFICANCE

Among these connections, the bolted ring-flange (RF) connection is utilized extensively in the most recent OWT projects in Europe, such as Nobel wind Offshore Wind Farm [28]. A new generation of OWTs requires RF connections with much thicker ring flanges and larger bolts/studs with a diameter up to 80 mm (M80). However, a more comprehensive investigation is required due to these two reasons [10,71,72]: (1) current design processes, manufacturing tolerances, and construction are insufficient to apply larger ring flanges and bolts/studs optimally; (2) The fatigue performance of the RF connection with larger bolts (studs)/flanges needs to be quantitatively evaluated with an improved analytical model. As a competitive MP-TP connection, the utilization of C1 wedge connection is not limited by the above issues. A systematic

understanding of the mechanical performance of C1 wedge connection could contribute to the development and application of the new generation of OWTs.

In addition, connections for support structures are exposed to the harsh environment during the service life of the OWTs. Material degradation and local cracks of the C1 wedge connection are inevitable to affect the serviceability of OWTs. A need for a reliable and rigorous monitoring system is evident. Taking the requirements of cost-effectiveness, global, and real-time monitoring into account, AE is the best-suited method for monitoring the connections in OWTs. AE has been extensively used in early damage detection and real-time assessment of steel structures [57,73–75]. Despite these advantages, challenges still exist in using AE technique for monitoring applications, especially in the area of monitoring steel structures with complex and large geometries. The effectiveness of the AE monitoring technique heavily depends on the quality of the measured AE signals, whereas, the collected AE signals are always accompanied by complex noise in practical cases. Moreover, fatigue damage typically occurs from the inside of the connections, where commercial bulky AE sensors cannot be used. Thin and miniature PZT (Lead Zirconate Titanate) sensors with a thickness smaller than 1 mm could be chosen as substitutes. Compared to commercial AE sensors, they are more sensitive to noise and less effective to detect damage in structures with thick plates [76]. These observations lead to the necessity to verify the efficiency of AE in monitoring the C1 wedge connection by thin PZT sensors.

Therefore, the primary objective of this research is to investigate the mechanical behavior of the C1 wedge connection and its potential application, while also assessing its health status by using AE monitoring.

1.3 RESEARCH QUESTIONS

The main research questions are: *How can the performance of the C1 wedge connection be effectively characterized and its material degradation detected by the AE technique?*

Upon reviewing the development of existing MP-TP connections, it becomes apparent that a comprehensive understanding of the mechanical behavior of the C1 wedge connection is currently lacking. This connection comprises multiple components that interact under the applied loading, and thus understanding the interaction between contacts and stress response is crucial to explore its practical application and further improvement. The first sub-question of this study pertains to the investigation of the mechanical and functional performance of the C1 wedge connection, which will be addressed in Chapter 2.

Q1: How can the mechanical performance of the C1 wedge connection be investigated under static and cyclic tensile loading conditions?

The appropriate selection of an MP-TP connection is crucial for ensuring the overall competitiveness and structural integrity of OWTs. While individual connections have been investigated in various aspects, there is a lack of research that quantitatively

compares alternative connections. Specifically, there is a need for a study that highlights the novelty and features of the C1 wedge connection (C1-WC) in comparison to the conventional bolted ring flange (RF) connection and the ring flange connection with defined contact surfaces (RFD). This quantitative comparison will address the second sub-question of this study. Chapter 3 will present the findings of this investigation.

Q2: How can the performance between various types of MP-TP connections be compared?

Currently, comprehensive analyses of the AE signals produced by the tensile deformation of metal materials have been carried out [77–81]. Although the regular pattern of AE activities for metal material deformation has been identified, the related quantitative description is not transferable between studies. Additionally, it has been observed that signals generated during plastic deformation exhibit an overlapped distribution of AE features with signals produced during final fracture [82]. This makes it challenging to distinguish between signals generated during plastic deformation and fracture based solely on certain or synthetic analyses of AE features. Moreover, the collected AE signals are often accompanied by complex noise in practical cases, such as friction noise between components and equipment or background noise from the environment. This leads to the third sub-question of this study. The proposed method for addressing this issue will be presented in Chapter 4.

Q3: How can the performance of the AE technique for identifying the deformation stage of metal be improved in a noisy environment?

The sensitivity of the AE sensors is critical for AE monitoring. Over the past decade, numerous studies have demonstrated the feasibility of monitoring acoustic emissions with thin PZT sensors in thin plate-like materials [83–86]. However, there has been a lack of prior selection studies for thin PZT sensors in passive sensing applications [83,87]. Moreover, the efficiency of thin PZT sensors is affected by noise due to a lower signal-to-noise ratio (SNR), and they are less effective for monitoring thick steel plates. Hence, new signal processing methods are required to enhance the accuracy of passive AE applications with thin PZT sensors, especially for structures with complex geometry and thick plates. This leads to the final sub-question, which will be addressed in Chapters 5 and 6.

Q4: How can the efficiency of AE monitoring by thin PZT sensors be improved to detect structures with complex geometry and thick plates?

1.4 RESEARCH METHOD

The primary objective of this thesis is to investigate the mechanical behavior and assess the health status of the C1 wedge connection. This involves gaining a deeper understanding of the behavior of the C1 wedge connection, as well as developing new signal processing methods to explore the potential of AE for monitoring material

degradation in this connection. To achieve these objectives, specific research methodologies have been developed for each research sub-question.

Q1: How can the mechanical performance of the C1 wedge connection be investigated under static and cyclic tensile loading conditions?

To address Q1, a combination of experimental and numerical analyses were conducted. Destructive testing methods, including static and cyclic tensile tests, were performed to determine the mechanical properties of the C1 wedge connection. Laboratory experiments were conducted using down-scaled segment specimens, which is a standard approach to evaluate the performance of MP-TP connections. Additionally, numerical simulations were employed to provide more detailed information for practical applications and further optimization of these connections. A finite element model with similar geometry to the experiments was created using the software ABQSU. Tensile coupon tests were performed to formulate an accurate stress-strain material model for the main components of the connection. Once validated, the FE model was used for parametric analysis to quantify the influence of the preloading force P_c , the bolt grade, and the friction coefficient between contacts. In summary, Chapter 2 describes the ultimate resistance and failure mechanism of the down-scaled segment using the C1 wedge connection under axial tensile and low cycle loads.

Q2: How can the performance between various types of MP-TP connections be compared?

Tower connections need to be checked for both the ultimate tensile limit state (ULS) and fatigue limit state (FLS) [88]. To make a valid comparison between different connections, the geometry of connections and associated segments were designed to have identical ultimate tensile strength. Preparing ring flange specimens with thick ring flanges and high-diameter bolts can be costly and time-consuming. Numerical simulation using advanced FE models is an affordable and effective method to gain a deeper understanding of the connections than physical tests. With validated FE models for each connection, I performed a parametric analysis to assess the influence of important parameters on the behaviour of connections. The parameters include the lateral boundary condition on the sides of the segment/flange (BC1/BC2), preload coefficient ρ (0.70, 0.55, 0.40, and 0.25), and the steel strength (S355, S460, and S690). Generally, Chapter 3 compares the tensile behaviour and fatigue performance of various connections.

Q3: How can improve the performance of identifying the performance stage of metal by AE technique in a noisy environment?

Metal deformation can be categorized into four stages: elastic, yield, uniform plastic, and necking. Each stage corresponds to a different degree of material damage. To address Q3, tensile tests on coupon scales were performed to collect AEs signals at different deformation stages. AE signals generated by metal deformation are typically nonlinear and non-stationary [89]. Signal decomposition methods are presented to decompose the nonstationary signals into several regular clear sub-signals, which can

be effectively used to remove the noises of nonstationary signals. Hence, a decomposition-based method is proposed to filter the noise embedded in the real AE signals from material deformation. In addition, to distinguish the AE features from different deformation stages, the artificial neural network (ANN) is used to identify the deformation stage of steel materials with the input of features extracted from the filtered AE signals. In conclusion, Chapter 4 proposes a hybrid method that combines these techniques to improve the application of AE for deformation stage identification.

Q4: How can the efficiency of AE monitoring by thin PZT sensors be improved to detect damage in structures with complex geometry and thick plates?

To enhance the functionality of thin PZT sensors in AE applications, the first perspective proposed is to employ multiple thin PZT sensors and to fuse their responses. A criterion for selecting the optimal thin PZT sensors as receivers is proposed and a configuration is designed for multiple sensors. Data fusion enables information extraction from the combination of different datasets instead of analyzing each dataset separately. Thus, Chapter 5 proposes a novel data-level fusion-based method to improve the completeness of the signal information captured by thin PZT sensors.

The second perspective proposed is to improve the detection efficiency of thin PZT sensors. While numerous studies have linked changes in cumulative AE features and crack growth behaviour [90–94] with the use of commercial AE sensors, this method is not applicable and efficient with thin PZT sensors. Therefore, Chapter 6 introduces a baseline-based method for damage detection in structural health monitoring (SHM).

1.5 THESIS OUTLINE

As shown in Fig. 1-6, the thesis contains seven chapters. The outline of each chapter is as follows:

Chapter 1 serves as an introduction to the research background, research objectives and thesis outline.

Chapter 2 presents the conducted experimental and numerical study on the C1 wedge connection. Advanced quasi-static FE analysis results are compared to the experimental results. Based on the validated FE model, a parametric study is carried out to analyze the influence of the bolt grade, friction coefficient between contact surfaces, and preloading force level on the mechanical behaviour of the C1 wedge connection.

Chapter 3 contains a quantitative comparison between three types of connections: a conventional bolted ring flange (RF) connection, a ring flange connection with defined contact surfaces (RFD), and a C1 wedge connection (C1-WC). This chapter compares the tensile behaviour and fatigue performance of these connections by validated finite element (FE) simulation and analysis.

Chapter 4 presents a hybrid model for deformation stage identification, which combines a self-adaptive denoising technique and an Artificial neural network (ANN). In pursuit of model generality, AE signals were collected from tensile coupon tests with various steel materials and loading speeds.

Chapter 5 proposes a method to enhance the functionality of thin PZT sensors in AE applications by employing multiple thin PZT sensors and performing a data-level fusion of their outputs.

Chapter 6 introduces a new baseline-based method that utilizes thin PZT sensors for early detection of fatigue damage in the restricted-access area. Other monitoring techniques such as digital image correlation (DIC), crack propagation gauges, and distributed optical fiber sensors (DOFS) are also employed to supplement the detection results of AE.

Chapter 7 provides the main findings of this thesis and gives recommendations for future studies.

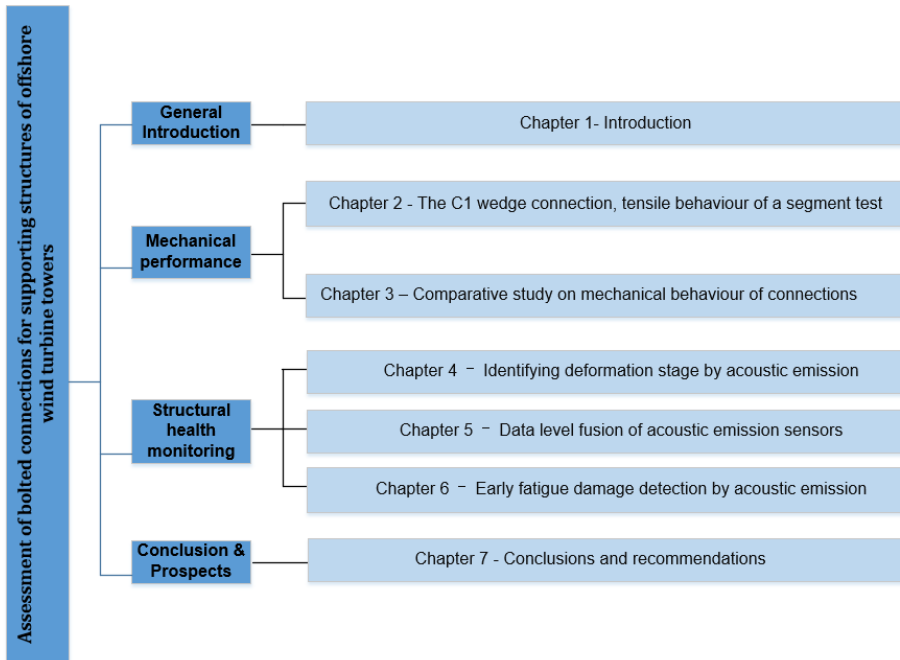


Fig. 1-6 Thesis outline

REFERENCES

- [1] R. Wiser, J. Rand, J. Seel, P. Beiter, E. Baker, E. Lantz, P. Gilman, Expert elicitation survey predicts 37% to 49% declines in wind energy costs by 2050, *Nat. Energy*. 6 (2021) 555–565. <https://doi.org/10.1038/s41560-021-00810-z>.
- [2] H. Díaz, C. Guedes Soares, Review of the current status, technology and future trends of offshore wind farms, *Ocean Eng.* 209 (2020) 107381. <https://doi.org/10.1016/j.OCEANENG.2020.107381>.
- [3] D. Liao, S.P. Zhu, J.A.F.O. Correia, A.M.P. De Jesus, M. Veljkovic, F. Berto, Fatigue reliability of wind turbines: historical perspectives, recent developments and future prospects, *Renew. Energy*. 200 (2022) 724–742. <https://doi.org/10.1016/j.RENENE.2022.09.093>.
- [4] E.P.P. Soares-Ramos, L. de Oliveira-Assis, R. Sarrias-Mena, L.M. Fernández-Ramírez, Current status and future trends of offshore wind power in Europe, *Energy*. 202 (2020) 117787. <https://doi.org/10.1016/j.ENERGY.2020.117787>.
- [5] V. Igwemezie, A. Mehmanparast, A. Kolios, Current trend in offshore wind energy sector and material requirements for fatigue resistance improvement in large wind turbine support structures – A review, *Renew. Sustain. Energy Rev.* 101 (2019) 181–196. <https://doi.org/10.1016/j.RSER.2018.11.002>.
- [6] WindEurope, Offshore wind energy 2022 mid-year statistics, (2022). <https://windeurope.org/intelligence-platform/product/offshore-wind-energy-2022-mid-year-statistics/>.
- [7] WindEurope, Offshore wind in Europe - key trends and statistics 2020, (2021). <https://windeurope.org/intelligence-platform/product/offshore-wind-in-europe-key-trends-and-statistics-2020/>.
- [8] WindEurope, Offshore wind in Europe - key trends and statistics 2021, (2021). <https://windeurope.org/intelligence-platform/product/offshore-wind-in-europe-key-trends-and-statistics-2021/>.
- [9] S. Bhattacharya, Challenges in design of foundations for offshore wind turbines, *Eng. Technol. Ref.* 1 (2014) 922. <https://doi.org/10.1049/ETR.2014.0041>.
- [10] A. Mehmanparast, S. Lotfian, S.P. Vipin, A review of challenges and opportunities associated with bolted flange connections in the offshore wind industry, *Metals (Basel)*. 10 (2020) 732. <https://doi.org/10.3390/MET10060732>.
- [11] R. Matos, M.R. Shah Mohammadi, C. Rebelo, A year-long monitoring of preloaded free-maintenance bolts – Estimation of preload loss on BobTail bolts, *Renew. Energy*. 116 (2018) 123–135. <https://doi.org/10.1016/j.RENENE.2017.05.092>.
- [12] HE DREIHT OFFSHORE WIND, (n.d.). <https://www.eib.org/en/projects/pipelines/all/20220473> (accessed April 18, 2023).
- [13] Germany: EIB co-finances large offshore wind farm in the North Sea with EnBW, (n.d.). <https://www.eib.org/en/press/all/2023-148-germany-eib-co-finances-large-offshore-wind-farm-in-the-north-sea-with-enbw> (accessed April 18, 2023).
- [14] BOSLAN | Monopile Foundations, (n.d.). <https://www.boslan.com/offshore-wind-farms/monopile-foundations/> (accessed April 18, 2023).
- [15] C. Petersen, *Stahlbau: Grundlagen der Berechnung und baulichen Ausbildung von Stahlbauten [Steel construction: Basics of calculation and structural design of steel structures]*, Vieweg, 1993.

- [16] H. Schmidt, M. Neuper, Zum elastostatischen Tragverhalten exzentrisch gezogener L- Stöße mit vorgespannten Schrauben [On the elastostatic load-bearing behaviour of eccentrically drawn L-joints with preloaded bolts], *Stahlbau*. 66 (1997) 163–168.
- [17] M. Seidel, A. Stang, F. Wegener, C. Schierl, P. Schaumann, Full-scale validation of FE models for geometrically imperfect flange connections, *J. Constr. Steel Res.* 187 (2021) 106955. <https://doi.org/10.1016/j.jcsr.2021.106955>.
- [18] W. Weijtjens, A. Stang, C. Devriendt, P. Schaumann, Bolted ring flanges in offshore-wind support structures - in-situ validation of load-transfer behaviour, *J. Constr. Steel Res.* 176 (2021) 106361. <https://doi.org/10.1016/j.jcsr.2020.106361>.
- [19] Lutz Kruttschinna, Untersuchungen zum Tragverhalten von Ringflanschsegmenten mit definierten Kontaktflächen [Investigations on the load-bearing behaviour of annular flange segments with defined contact surfaces], Universität Hannover, 1999.
- [20] The C1 wedge connections, (n.d.). <https://c1connections.com/> (accessed March 9, 2022).
- [21] K.E.Y. Creusen, G. Misios, J.S. Winkes, M. Veljkovic, Introducing the C1 Wedge Connection, *Steel Constr.* 15 (2022) 13–25. <https://doi.org/10.1002/STCO.202100039>.
- [22] P. Schaumann, M. Seidel, P. Schaumann, M. Seidel, Failure analysis of bolted steel flanges, in: *Proc. Seventh Int. Symp. Struct. Fail. Plast.*, 2000. <https://doi.org/10.1016/B978-008043875-7/50211-2>.
- [23] C.A. Madsen, J.-C. Kragh-Poulsen, K.J. Thage, M.J. Andreassen, Analytical and numerical investigation of bolted steel ring flange connection for offshore wind monopile foundations, in: *IOP Conf. Ser. Mater. Sci. Eng.*, IOP Publishing, 2017. <https://doi.org/10.1088/1757-899X/276/1/012034>.
- [24] P. Schaumann, R. Eichstädt, Experimental and analytical fatigue assessment of high-strength bolts for wind turbine structures, in: 2018. <https://www.researchgate.net/publication/335703565> (accessed October 19, 2019).
- [25] P. Schaumann, R. Eichstädt, A. Stang, Advanced performance assessment methods for high-strength bolts in ring-flange connections, *Stahlbau*. 87 (2018) 446–455. <https://doi.org/10.1002/stab.201810601>.
- [26] Amrumbank West, (n.d.). <https://www.rwe.com/en/our-portfolio/our-sites/wind-farm-amrumbank> (accessed March 9, 2022).
- [27] Humber Gateway offshore wind farm, (n.d.). <https://uk-ireland.rwe.com/locations/humber-gateway-offshore-wind-farm> (accessed March 9, 2022).
- [28] Nobelwind Offshore Wind Farm, North Sea, Belgium, (n.d.). <https://www.power-technology.com/projects/nobelwind-offshore-wind-farm/> (accessed March 9, 2022).
- [29] C. Petersen, Nachweis der Betriebsfestigkeit exzentrisch beanspruchter Ringflanschverbindungen [Verification of the fatigue strength of eccentrically loaded annular flange connections], *Stahlbau*. 67 (1998) 191–203. <https://doi.org/10.1002/STAB.199800690>.
- [30] M. Seidel, Zur Bemessung geschraubter Ringflanschverbindungen von Windenergieanlagen [For dimensioning bolted annular flange connections of wind turbines], Leibniz Universität Hannover, 2001. <https://doi.org/10.13140/RG.2.2.14685.36328>.
- [31] DNVGL-ST-0126, Support structures for wind turbines, 2018.
- [32] DIN 18088-3, Design standard - structures for wind turbines and platforms – part 3: steel structures, 2019.
- [33] VDI 2230 Part I: Systematic calculation of highly stressed bolted joints Joints with one cylindrical bolt, 2003.

- [34] IEC 61400-6, Wind turbines – part 6: Tower and foundation design requirements, 2016.
- [35] DNVGL, RP-C203: Fatigue design of offshore steel structures, 2014.
- [36] P. Schaumann, D.-I. Frithjof Marten, Fatigue resistance of high strength bolts with large diameters, in: Proc. Int. Symp. Steel Struct. ISSS, Seoul, Korea, 2009: pp. 12–14.
- [37] J. Maljaars, M. Euler, Fatigue S-N curves of bolts and bolted connections for application in civil engineering structures, Int. J. Fatigue. 151 (2021) 106355. <https://doi.org/10.1016/j.ijfatigue.2021.106355>.
- [38] P. Schaumann, R. Eichstädt, Ermüdung sehr großer HV-Schraubengarnituren [Fatigue of very large HV-bolt assemblies], Stahlbau. 85 (2016) 604–611. <https://doi.org/10.1002/STAB.201610410>.
- [39] EN 1993-1-9: Eurocode 3: Design of steel structures – Part 1-9: Fatigue., 2005.
- [40] BS 7608:2014. Guide to fatigue design and assessment of steel products. BSI, 2014.
- [41] L. Cheng, H. Xin, M. Veljkovic, Numerical analysis of ring flange connection with defined surface area, Ce/Papers. 4 (2021) 182–188. <https://doi.org/10.1002/CEPA.1279>.
- [42] BLUE Wedge Connection, Fatigue test - TU Delft scaled 2 - Test Report, RND-01-STGR0202, 2019.
- [43] G. Misios, Effect on flange waviness on the C1 Wedge Connection, Delft University of Technology, 2019. <https://repository.tudelft.nl/islandora/object/uuid%3A434a42ff-9b52-45bb-b906-d15a213f5aef> (accessed January 5, 2021).
- [44] F. Sun, B. Xiao, Y. Zhang, Quantitative damage evaluation of LY225 steel under monotonic tensile loading based on acoustic emission entropy, J. Constr. Steel Res. 185 (2021) 106860. <https://doi.org/10.1016/j.jcsr.2021.106860>.
- [45] B. Yeter, Y. Garbatov, Structural integrity assessment of fixed support structures for offshore wind turbines: A review, Ocean Eng. 244 (2022) 110271. <https://doi.org/10.1016/j.oceaneng.2021.110271>.
- [46] M. Veljkovic, C. Heistermann, M. Pavlovic, M. Feldmann, D. Pak, C. Richter, C. Rebelo, P. Pinto, R. Matos, C. Baniotopoulos, M. Gkantou, V. Dehan, G. Nüsse, High-Strength Steel Tower for Wind Turbines (HISTWIN_Plus) Background Document, 17 (2015). http://www.winercost.com/cost_files/HISTWIN_Plus_Report.pdf.
- [47] A.M.P. De Jesus, R. Matos, B.F.C. Fontoura, C. Rebelo, L. Simões Da Silva, M. Veljkovic, A comparison of the fatigue behavior between S355 and S690 steel grades, J. Constr. Steel Res. 79 (2012) 140–150. <https://doi.org/10.1016/j.jcsr.2012.07.021>.
- [48] F. Yang, M. Veljkovic, Y. Liu, Ductile damage model calibration for high-strength structural steels, Constr. Build. Mater. 263 (2020) 120632. <https://doi.org/10.1016/j.conbuildmat.2020.120632>.
- [49] L.J. Jia, H. Kuwamura, Ductile fracture simulation of structural steels under monotonic tension, J. Struct. Eng. (United States). 140 (2014). [https://doi.org/10.1061/\(ASCE\)ST.1943-541X.0000944](https://doi.org/10.1061/(ASCE)ST.1943-541X.0000944).
- [50] H.C. Ho, K.F. Chung, X. Liu, M. Xiao, D.A. Nethercot, Modelling tensile tests on high strength S690 steel materials undergoing large deformations, Eng. Struct. 192 (2019) 305–322. <https://doi.org/10.1016/j.engstruct.2019.04.057>.
- [51] R. Yan, H. Xin, F. Yang, H. El Bamby, M. Veljkovic, K. Mela, A method for determining the constitutive model of the heat-affected zone using digital image correlation, Constr. Build. Mater. 342 (2022) 127981. <https://doi.org/10.1016/j.conbuildmat.2022.127981>.

- [52] R. Yan, H. Xin, K. Mela, H. El Bamby, M. Veljkovic, Fracture simulation of welded RHS X-joints using GTN damage model, *Adv. Struct. Eng.* 2022 (2022) 1–20. https://doi.org/10.1177/13694332221137175/ASSET/IMAGES/LARGE/10.1177_1369433221137175-FIG21.JPEG.
- [53] K. Schabowicz, *Non-Destructive Testing of Materials in Civil Engineering*, Materials (Basel). 12 (2019) 3237. <https://doi.org/10.3390/ma12193237>.
- [54] G. Rihar, Selection of NDT method and the extent of testing, in: 4th Int. Conf. Slov. Soc. Nondestruct. Test. "Application Contemp. Nondestruct. Test. Eng., 1997: pp. 295–305.
- [55] P. Kot, M. Muradov, M. Gkantou, G.S. Kamaris, K. Hashim, D. Yeboah, Recent Advancements in Non-Destructive Testing Techniques for Structural Health Monitoring, *Appl. Sci.* 2021, Vol. 11, Page 2750. 11 (2021) 2750. <https://doi.org/10.3390/APP11062750>.
- [56] N.H.M.M. Shrifan, M.F. Akbar, N.A.M. Isa, Prospect of using artificial intelligence for microwave nondestructive testing technique: A review, *IEEE Access.* 7 (2019) 110628–110650. <https://doi.org/10.1109/ACCESS.2019.2934143>.
- [57] A. Nair, C.S. Cai, Acoustic emission monitoring of bridges: Review and case studies, *Eng. Struct.* 32 (2010) 1704–1714. <https://doi.org/10.1016/j.engstruct.2010.02.020>.
- [58] S. Kashif Ur Rehman, Z. Ibrahim, S.A. Memon, M. Jameel, Nondestructive test methods for concrete bridges: A review, *Constr. Build. Mater.* 107 (2016) 58–86.
- [59] A. Zolfaghari, A. Zolfaghari, F. Kolahan, Reliability and sensitivity of magnetic particle nondestructive testing in detecting the surface cracks of welded components, *Nondestruct. Test. Eval.* 33 (2018) 290–300. <https://doi.org/10.1080/10589759.2018.1428322>.
- [60] P.D. Toasa Caiza, R. Schwendemann, P. Calero, T. Ummenhofer, Portable Generator to Detect Cracks on Large Steel Structures: An Application of Inductive Thermography, *J. Nondestruct. Eval.* 40 (2021). <https://doi.org/10.1007/S10921-021-00795-5>.
- [61] S. Saber, G.I. Selim, Higher-Order Statistics for Automatic Weld Defect Detection, *J. Softw. Eng. Appl.* 06 (2013) 251–258. <https://doi.org/10.4236/JSEA.2013.65031>.
- [62] Z. Fatematuz, Evaluation of material crack using acoustic emission technique, Queensland University of Technology, 206AD.
- [63] M. Kaphle, M. Sc, Analysis of acoustic emission data for accurate damage assessment for structural health monitoring applications, 2012.
- [64] A.T. Green, C.S. Lockman, R.K. Steele, Acoustic verification of structural integrity of polaris chambers, *Mod. Plast.* 41 (1964) 137–139.
- [65] M.A. Haile, N.E. Bordick, J.C. Riddick, Distributed acoustic emission sensing for large complex air structures, *Struct. Heal. Monit.* 17 (2018) 624–634. <https://doi.org/10.1177/1475921717714614>.
- [66] A.A. Pollock, B. Smith, Acoustic emission monitoring of a military bridge, *Nondestruct. Test.* 5 (1972) 164–186.
- [67] K. Ohno, M. Ohtsu, Crack classification in concrete based on acoustic emission, *Constr. Build. Mater.* 24 (2010) 2339–2346. <https://doi.org/10.1016/j.conbuildmat.2010.05.004>.
- [68] N.M. Bunnori, R.J. Lark, K.M. Holford, The use of acoustic emission for the early detection of cracking in concrete structures, *Mag. Concr. Res.* 63 (2011) 683–688.
- [69] M.A.A. Aldahdooh, N.M. Bunnori, M.A. Megat Johari, Damage evaluation of reinforced concrete beams with varying thickness using the acoustic emission technique, *Constr. Build. Mater.* 44 (2013) 812–821. <https://doi.org/10.1016/j.conbuildmat.2012.11.099>.

- [70] R. Worley, M.M. Dewoolkar, T. Xia, R. Farrell, D. Orfeo, D. Burns, D.R. Huston, Acoustic Emission Sensing for Crack Monitoring in Prefabricated and Prestressed Reinforced Concrete Bridge Girders, *J. Bridg. Eng.* 24 (2019) 04019018. [https://doi.org/10.1061/\(ASCE\)BE.1943-5592.0001377](https://doi.org/10.1061/(ASCE)BE.1943-5592.0001377).
- [71] Bolt & Beautiful, (n.d.). <https://grow-offshorewind.nl/project/bolt-beautiful>.
- [72] M. Veljkovic, Emerging technologies for future steel structures, in: *Civ. Eng. 2021 Achiev. Visions*, University of Belgrade - Faculty of civil engineering, Belgrade, Serbia, 2021: pp. 121–131. https://www.grf.bg.ac.rs/p/docs/ostalo/zbornik_gra_evinarstvo_2021_1635763208136.pdf.
- [73] H. Xin, L. Cheng, R. Diender, M. Veljkovic, Fracture acoustic emission signals identification of stay cables in bridge engineering application using deep transfer learning and wavelet analysis, *Adv. Bridg. Eng.* 1 (2020) 1–16. <https://doi.org/10.1186/s43251-020-00006-7>.
- [74] K.M. Holford, A.W. Davies, R. Pullin, D.C. Carter, Damage location in steel bridges by acoustic emission, *J. Intell. Mater. Syst. Struct.* 12 (2001) 567–576. <https://doi.org/10.1106/KDNY-AJOU-KP2B-P52R>.
- [75] L. Cheng, H. Xin, R.M. Groves, M. Veljkovic, Acoustic emission source location using Lamb wave propagation simulation and artificial neural network for I-shaped steel girder, *Constr. Build. Mater.* 273 (2021) 121706. <https://doi.org/10.1016/j.conbuildmat.2020.121706>.
- [76] L. Yu, S. Momeni, V. Godinez, V. Giurgiutiu, Adaptation of PWAS Transducers to Acoustic Emission Sensors, (2011). <https://doi.org/10.1117/12.880157>.
- [77] H.N.G. Wadley, C.B. Scruby, Cooling rate effects on acoustic emission-microstructure relationships in ferritic steels, *J. Mater. Sci.* 1991 2621. 26 (1991) 5777–5792. <https://doi.org/10.1007/BF01130115>.
- [78] H.N.G. Wadley, C.B. Scruby, Spheroidal inclusion effects on acoustic emission-microstructural relations in ferritic steels, *J. Mater. Sci.* 1993 289. 28 (1993) 2517–2530. <https://doi.org/10.1007/BF01151687>.
- [79] C.B. Scruby, H.N.G. Wadley, Tempering effects on acoustic emission-microstructural relationships in ferritic steels, *J. Mater. Sci.* 1993 289. 28 (1993) 2501–2516. <https://doi.org/10.1007/BF01151686>.
- [80] C.K. Mukhopadhyay, K.K. Ray, T. Jayakumar, B. Raj, Acoustic emission from tensile deformation of unnotched and notched specimens of AISI type 304 stainless steels, *Mater. Sci. Eng. A.* 255 (1998) 98–106. [https://doi.org/10.1016/s0921-5093\(98\)00771-0](https://doi.org/10.1016/s0921-5093(98)00771-0).
- [81] S. Hao, S. Ramalingam, B.E. Klamecki, Acoustic emission monitoring of sheet metal forming: Characterization of the transducer, the work material and the process, *J. Mater. Process. Technol.* 101 (2000) 124–136. [https://doi.org/10.1016/S0924-0136\(00\)00441-6](https://doi.org/10.1016/S0924-0136(00)00441-6).
- [82] L. Cheng, H. Xin, R.M. Groves, M. Veljkovic, Plasticity and damage characteristic of acoustic emission signals for S460 steel exposed to tensile load, in: *Virtual Conf. Mech. Fatigue*, University of Porto, Portugal, 2020. https://www.researchgate.net/publication/344235805_Plasticity_and_damage_characteristic_of_acoustic_emission_signals_for_S460_steel_exposed_to_tensile_load.
- [83] L. Yu, S. Momeni, V. Godinez, V. Giurgiutiu, P. Ziehl, J. Yu, Dual mode sensing with low-profile piezoelectric thin wafer sensors for steel bridge crack detection and diagnosis, *Adv. Civ. Eng.* 2012 (2012). <https://doi.org/10.1155/2012/402179>.
- [84] Y. Bhuiyan, B. Lin, V. Giurgiutiu, Acoustic emission sensor effect and waveform evolution during fatigue crack growth in thin metallic plate, *Orig. Artic. J. Intell. Mater. Syst. Struct.* 29 (2018) 1275–1284. <https://doi.org/10.1177/1045389X17730930>.

- [85] T. Jiang, Y. Zhang, L. Wang, L. Zhang, G. Song, Monitoring fatigue damage of modular bridge expansion joints using piezoceramic transducers, *Sensors*. 18 (2018) 3973. <https://doi.org/10.3390/s18113973>.
- [86] X. Zhang, L. Zhang, L. Liu, L. Huo, Tension monitoring of wedge connection using piezoceramic transducers and wavelet packet analysis method, *Sensors*. 20 (2020) 364. <https://doi.org/10.3390/s20020364>.
- [87] B. Trujillo, A. Zagrai, D. Meisner, S. Momeni, Monitoring of Acoustic Emission Activity using Thin Wafer Piezoelectric Sensors, in: 21th Annu. Int. Symp. Smart Struct. Mater. + NDE Heal. Monit. Diagnostics, n.d.
- [88] M. Veljkovic, M. Feldmann, J. Naumes, D. Pak, L. Simões da Silva, C. Rebelo, Wind turbine tower design, erection and maintenance, in: *Wind Energy Syst. Optimising Des. Constr. Safe Reliab. Oper.*, Woodhead P, 2010: pp. 274–300. <https://doi.org/10.1533/9780857090638.2.274>.
- [89] X. Li, A brief review: acoustic emission method for tool wear monitoring during turning, *Int. J. Mach. Tools Manuf.* 42 (2002) 157–165. [https://doi.org/10.1016/S0890-6955\(01\)00108-0](https://doi.org/10.1016/S0890-6955(01)00108-0).
- [90] A. Keshtgar, C.M. Sauerbrunn, M. Modarres, Structural reliability prediction using acoustic emission-based modeling of fatigue crack growth, *Appl. Sci.* 8 (2018). <https://doi.org/10.3390/app8081225>.
- [91] P.A. Vanniamparambil, I. Bartoli, K. Hazeli, J. Cuadra, E. Schwartz, R. Saralaya, A. Kontsos, An integrated structural health monitoring approach for crack growth monitoring, *J. Intell. Mater. Syst. Struct.* 23 (2012) 1563–1573. https://doi.org/10.1177/1045389X12447987/ASSET/IMAGES/LARGE/10.1177_1045389X12447987-FIG2.JPEG.
- [92] T. Shiraiwa, H. Takahashi, M. Enoki, Acoustic emission analysis during fatigue crack propagation by Bayesian statistical modeling, *Mater. Sci. Eng. A.* 778 (2020) 139087. <https://doi.org/10.1016/j.msea.2020.139087>.
- [93] M. Rabiei, M. Modarres, Quantitative methods for structural health management using in situ acoustic emission monitoring, *Int. J. Fatigue.* 49 (2013) 81–89. <https://doi.org/10.1016/j.ijfatigue.2012.12.001>.
- [94] A. Krampikowska, R. Pała, I. Dzioba, G. Šwit, The use of the acoustic emission method to identify crack growth in 40CrMo steel, *Materials (Basel)*. 12 (2019) 1–14. <https://doi.org/10.3390/ma12132140>.

2. THE C1 WEDGE CONNECTION, TENSILE BEHAVIOUR OF A SEGMENT TEST

This chapter aims to investigate the tensile behaviour of the second generation of the C1 wedge connection by combining the findings of experiments and finite element (FE) analysis. Advanced quasi-static FE analysis results, considering the most detailed geometry and using an explicit dynamic solver, are compared to the experimental results. Based on the FE model, a parametric study has been carried out to analyze the influence of the bolt grade, friction coefficient between contact surfaces, and preloading force level on mechanical behaviour. The FE simulation provides practical guidance for designing this connection without bolt failure.

This chapter addresses the first research question Q1) and is organized as follows: Section 2.1 introduces the development of the C1 wedge connection. The performed experiments are described in Section 2.2. Section 2.3 presents the FE modelling information. The experimental and numerical results are shown and discussed in Section 2.4. A parametric analysis is conducted in Section 2.5. After that, the conclusions are drawn in Section 2.6.

2.1 INTRODUCTION

Recently finished research projects, OFWEC1 and OFWEC2 (Offshore Wedge Connection), introduced a novel connection called “C1 wedge connection” [1] as an alternative option for the new generation of OWTs. Compared to the conventional RF connections, the C1 wedge connection reduces the construction, installation and maintenance costs by eliminating the thick ring flange and using smaller diameter bolts [2]. Full-scale tests were performed on a 4.5 m-diameter tower within the OFWEC3 project (Fig. 2-1). Additionally, in-situ tower installation was carried out as part of the Arcadis Ost project (Fig. 2-2) [1]. As shown in Fig. 2-1, the personal-free tower alignment was successfully performed [2]. Bolts were then fastened from the inside of the tower during the execution of the C1 wedge connection. Both ultimate limit state (ULS) and fatigue limit state (FLS) resistance was tested in the full-scale tests. These tests demonstrated quick and easy execution of the C1 wedge connection. The C1 wedge connection has been successfully certified by DNV in 2021 [3], and it is anticipated to be continually developed to minimize the costs of the welding while keeping the main concept unchanged.

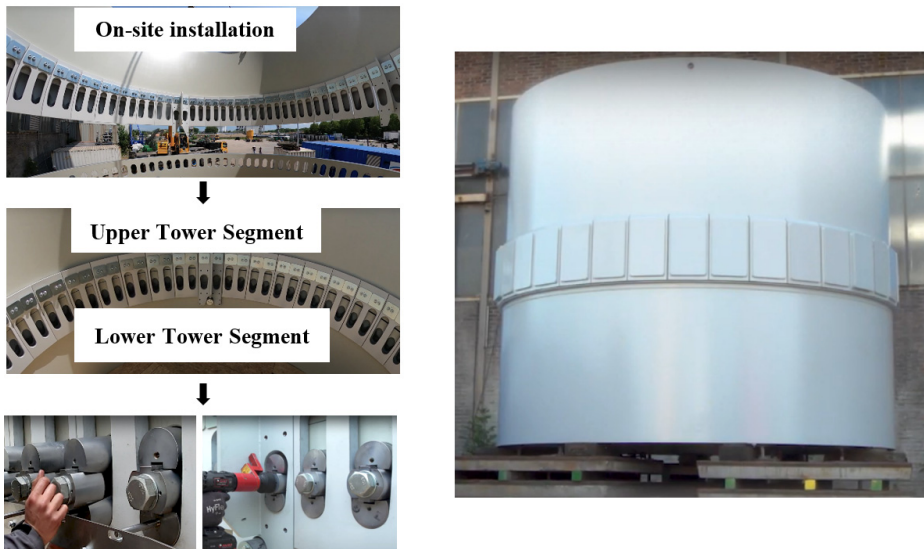


Fig. 2-1 Performed full-scale tests in OFWEC3 project [1]



Fig. 2-2 In-situ installation of the tower with C1 wedge connection [1]

This chapter aims to provide a detailed investigation of the mechanical and functional performance of the second generation of the C1 wedge connection. The ultimate resistance and failure mechanism of the down-scale segment using this type of C1 wedge connection under axial tensile load and low cycle load are described. In addition, detailed finite element (FE) models are established and non-linear analysis is carried out using ABAQUS with the damage material model. FE models are verified by experimental results. The verified FE model will be used to explain the load transfer mechanism of the second generation of the C1 wedge connection. Finally, parametric analysis is performed to build confidence in using the C1 wedge connection in engineering practice.

2.2 EXPERIMENTAL PROGRAM

2.2.1 Geometry of the C1 wedge connection

Fig. 2-3 shows a schematic layout of the investigated connection. In the second generation of the C1 wedge connection, the upper segment and the lower segment are assembled to the webs by two kinds of connections: pinned connections and wedge connections. Elongated holes are machined in the lower segment and webs. The specific wedge connection comprises the horizontal bolt, wedges and blocks with an inclined plane. The slope of the wedge is consistent with the blocks. Horizontal bolt pretension is applied before resisting the external force. The imposed tensile load is transferred through the pinned connection to the webs, followed by the movement of the fastener assembly connection and then to the lower segment.

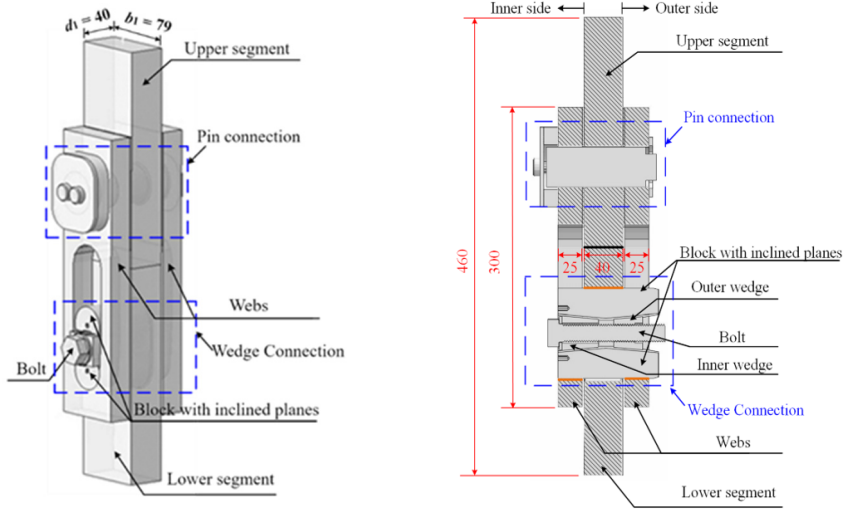


Fig. 2-3. Illustration of a segment specimen (unit: mm)

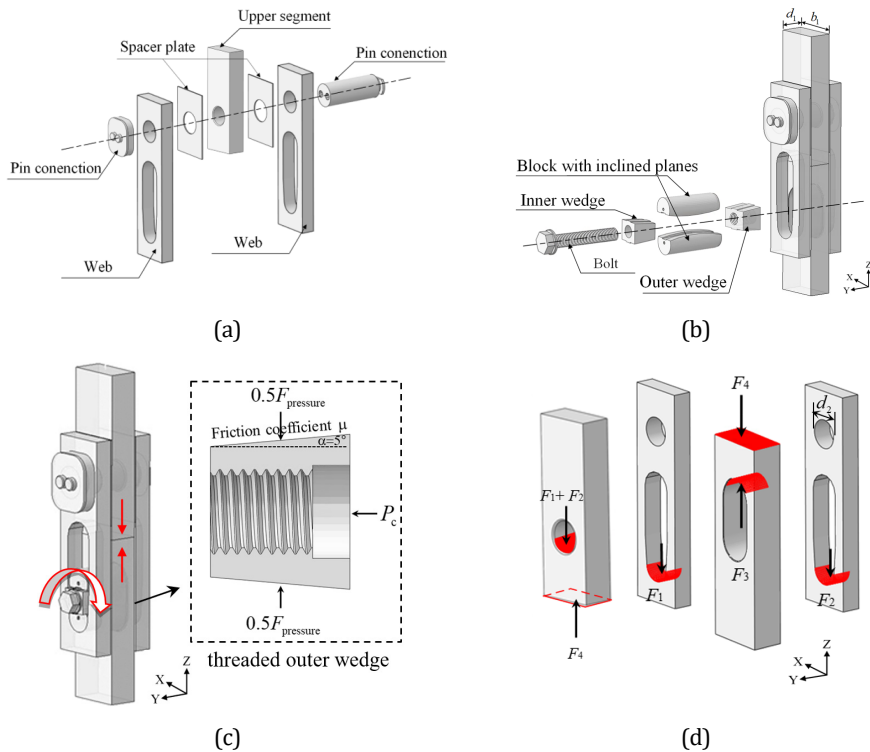


Fig. 2-4. Schematic views of tower segment with the C1 wedge connection in the study. (a) Pre-assembly of the pinned connection; (b) Assembly of the upper part and lower flange fastener; (c) Preloading of the bolt; (d) Contact forces/surfaces after bolt-pretension

In terms of the assembly procedure, a fork-shaped upper segment is obtained by pre-installing the pinned connection at first, see Fig. 2-4 (a). Then, the fastener assembly of the wedge connection is placed in the holes (Fig. 2-4 (b)). Due to the specific design of the holes, the fastener is only in contact with the top of the hole in the lower segment and the bottom of the holes in the webs, as shown in the origin line in Fig. 2-3. The pretension of the horizontal bolt causes the movement of two blocks corresponding to the increment of forces F_1 , F_2 and F_3 ($F_1+F_2=F_3$), which in turn generates the contact pressure F_{pressure} (F_4) between the segments Fig. 2-4 (c) and (d). As presented in Fig. 2-4 (c), the relationship between the bolt pretension force P_c and the generated contact pressure F_{pressure} is:

$$F_{\text{pressure}} = F_4 = P_c / (\tan(\alpha) + \mu) \quad \text{Eq. 2-1}$$

where α is the angle that the wedge makes with the horizontal plane and μ is the friction coefficient between the blocks and the wedges, as shown in Fig. 2-4 (c).

2.2.2 Description of the specimen

Two specimens of the tower segment under tensile force were tested to understand the response of this type of C1 wedge connection (WC) in the segment specimen. The tests were performed in the Structures Laboratory at the Faculty of Civil Engineering and Geosciences, TU Delft. The specimens were scaled down to 1:4 of the prototype with the exact geometric dimensions. The main parameters of these specimens are shown in Fig. 2-3 and Table 2-1. The specimens were denoted as WC1 and WC2. As expressed in Eq. 2-1, the lower friction coefficient μ between the zinc-nickel coated wedge and block inclined plane generates the higher contact pressure. The determination of μ is described in Section 2.3.2. To perform a comparative study, different lubrication states about this contact pair are set for WC1 and WC2, respectively (see Table 2-1). The plate components were made of S460 steel grade for all specimens while the machined parts were made of 34CrNiMo6 steel with a minimum yield strength of 600 MPa. Grade 8.8 high-strength M18 bolts were used in the connection. All bolt threads are lubricated as it is helpful to prevent bolt loosening and thread damage [4]. The lubrication used in experiments was applied with MoS₂ grease.

Table 2-1 Main parameters of the specimens

Specimen	P_c (kN)	Lubricated		Experimental results (kN)			FE analysis results (kN)			Comparison		
		Bolt threads	Wedge/block inclined plane	$N_{c,E}$	$N_{y,E}$	$N_{u,E}$	$N_{c,F}$	$N_{y,F}$	$N_{u,F}$	$N_{c,F}/N_{c,E}$	$N_{y,F}/N_{y,E}$	$N_{u,F}/N_{u,E}$
WC1	95	Yes	No	376	607	861	387	626	813	1.03	1.03	0.94
WC2	80	Yes	Yes	436	625	873	465	629	814	1.07	1.01	0.93

Note: The first subscript c means critical load at the end of the elastic stage, y and u mean the overall yield and ultimate resistance of the specimens. The second subscript E and F stand for results from experiments and FE analysis, respectively.

2.2.3 Experimental set-up and instrumentation

A dedicated test setup was developed to perform the static tension test (see Fig. 2-5) because the capacity of the fatigue test set-up (see in [2]) is insufficient to test this connection to static tensile failure. The lower segment of the wedge connection was welded to a bottom plate. The upper segment was welded to an adaptor which was connected to a top plate with an M56 threaded bolt. The top and bottom plates were bolted to two rigid columns with eight bolts to ensure the rigidity of the entire loading system. Quasi-static loadings were applied through a hollow plunger cylinder with a capacity of 1000 kN.

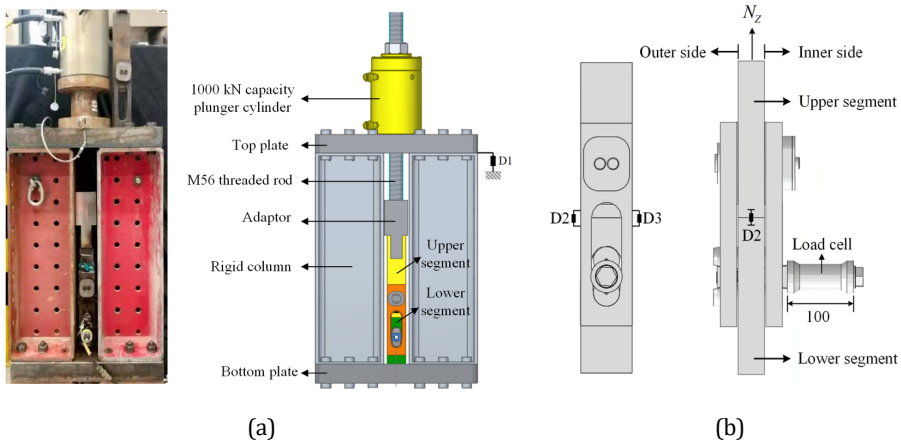


Fig. 2-5. Experimental system. (a) Set-up (b) Displacement measurement (unit: mm)

The applied load N_z , bolt forces and displacements in the Z direction in the connection were measured during the experiments (Fig. 2-5). A digital manometer was used to record the pressure in the cylinder connected to the applied load. D1-D3 are linear variable differential transformers (LVDTs). In detail, D1 measured the displacement of the cylinder to determine the axial deformation of the specimens. D2-D3 were used to measure the gap opening between the connecting segments. The bolt was instrumented with a load cell to calibrate and control the tensile force in the bolt. The total length of the load cell is 100 mm.

The loading procedures of both specimens were divided into two steps: (1) Applied preloading force to the bolts P_c , and (2) imposed tensile forces N_z on the specimen. Two levels of bolt preloading force P_c have been applied on these two specimens, as listed in Table 2-1. Pertaining to imposing tensile load N_z , to explore the mechanical behaviour of the connections under various load levels, two loading protocols with a multi-stage loading method were designed for two specimens, as shown in Fig. 2-6. The yield and ultimate load of the connection N_y and N_u was estimated according to $N_y = f_y \cdot A_s$ and $N_u = f_u \cdot A_s$, respectively. f_y and f_u denotes the measured yield and ultimate strength of S460 material ($f_y = 485$ MPa, $f_u = 620$ MPa). The net cross-section area of the lower segment A_s is calculated by $A_s = d_1 \times (b_1 - d_2) = 1296$ mm². During the tension loading stage, force

and displacement control were used to monitor the load applied to the specimen before and after the ultimate strength of the specimens. The test results will be discussed in conjunction with the numerical results in Section 2.4.

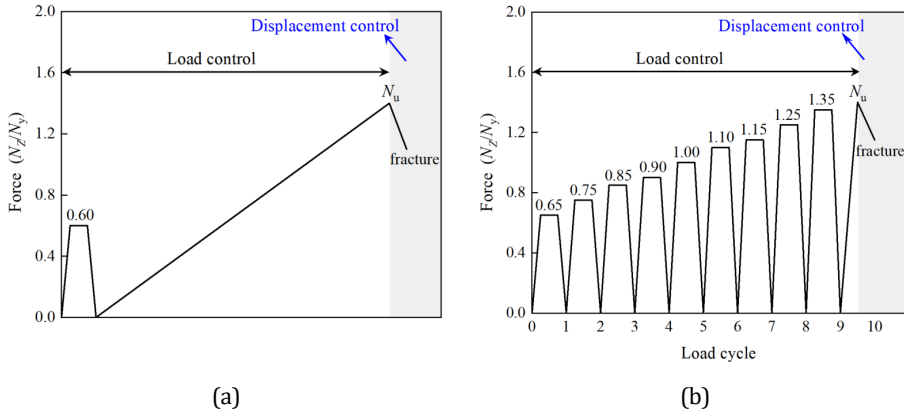


Fig. 2-6. Loading protocols for specimens. (a) WC1 and (b) WC2.

2.3 FE SIMULATION

2.3.1 Basic modelling consideration

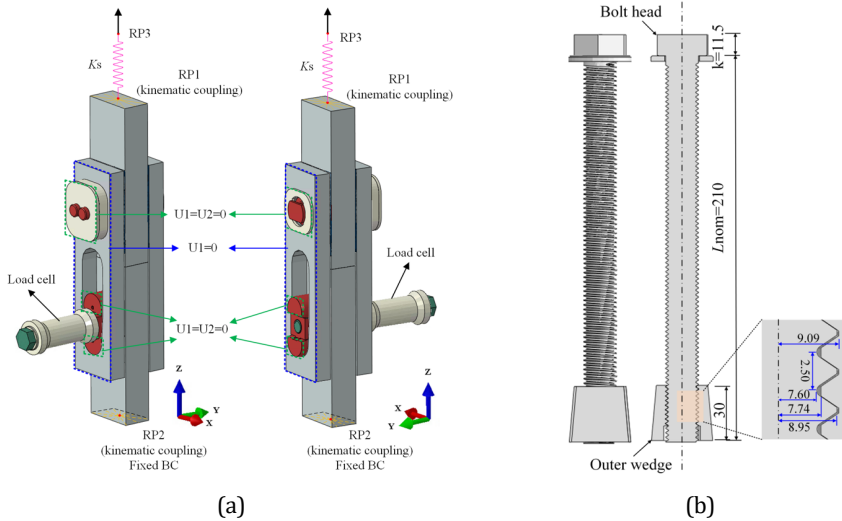


Fig. 2-7. Illustration of FE models. (a) Geometry and boundary conditions (b) Geometrical details of the threaded bolt and outer wedge (unit: mm)

The finite element (FE) model of the specimen was established using ABAQUS/Explicit for analysing its tensile behaviour. The geometry and boundary conditions of the segment models of the C1 wedge connection used in FE analysis are shown in Fig. 2-7 (a). The model comprises all tested specimen components: rolled plate components and machined components. The connectors were modelled with the actual geometry,

and all components (i.e. bolt, washer, inner wedge, outer wedge, blocks) were modelled as separate parts. The threaded bolt and outer wedge were modelled with actual dimensions, see Fig. 2-7 (b), to model as realistically as possible the complex interactions of the connector's components. It should be noted that, due to the complexity of the wedge connection and the high computer consumption of the explicit calculation, the upper segment welded to the test set-up was excluded in the model.

As presented in Fig. 2-7, appropriate boundary conditions were set for the reference points. The upper and lower cross-section surfaces were kinetically coupled to the reference points at the middle of the related surfaces RP1 and RP2, respectively. Fixed support boundary conditions were applied to RP2. Since a part of the deformation of the test set-up is included in the measured displacement, an elastic spring connected to the RP1 was added to account for the elastic deformation of the test set-up and the non-modelled welded part. The equivalent deformation of the entire specimen Δ can be obtained by Eq. 2-2 and Eq. 2-3:

$$\Delta = N_z / K_t = N_z / K_s + N_z / K_{wc} \quad \text{Eq. 2-2}$$

$$K_s = K_t K_{wc} / K_{wc} - K_t \quad \text{Eq. 2-3}$$

where N_z is the tensile force; K_t , K_{wc} , and K_s represent the stiffness of the experimental set-up, specimen, and spring, respectively. K_t is calculated as 219 kN/mm based on the test results. After several trials, K_s was estimated as 275 kN/mm for the analysis and contributes to around 80% of Δ .

2.3.2 Elements types and contact properties

Solid elements were used to model all components of the C1 wedge connections. The mesh details of the FE model are illustrated in Fig. 2-8. The plate components were meshed using eight-node hexahedron linear solid elements with reduced integration (C3D8R). The machined components, namely the bolt, threaded outer wedge, blocks and pin-bar with more complex geometry, were meshed with ten-node modified quadratic tetrahedron elements (C3D10M) to realize the free mesh. A global element size of 3 mm was applied to the bolts, inner wedge and outer wedge, while 1 mm was used for the thread areas. A gradient grid with a maximum size of 10 mm was employed for the upper segment, lower segment and two webs. In the area of plate components close to the fastener assembly, the mesh size was refined to 2 mm.

According to the VDI 2230 standard for bolted joints, the friction coefficient value of 0.04-0.1 is suggested for MoS₂-lubricated surfaces and 0.14-0.24 for zinc-nickel coated surfaces, respectively [5]. To reduce the computational cost and avoid convergence problems, general contact with a "penalty" tangential behaviour and a "hard" normal behaviour were selected to simulate all contact interactions in the specimen. As discussed before, the contact pressure between segments is sensitive to the friction coefficient μ of the inclined planes in the assembly of the wedge connection. Hence, the friction coefficient defined in the general contact was determined by the lubricant states between the wedge and block inclined plane. A friction coefficient μ of 0.18 was assumed for the WC1 without wedge-block lubrication, while a conservative friction

coefficient value of 0.1 was set for pre-lubricated WC2. The selection of these two values can also be calibrated based on the critical load N_c from test results. This is because the imposed load N_z reaches N_c when the contact pressure F_{pressure} (i.e., F_4) degrades to zero. Hence, the contact force F_4 is roughly identical to the N_c measured from the test. The friction coefficient μ can then be derived from the known preload force P_c and the contact force F_4 .

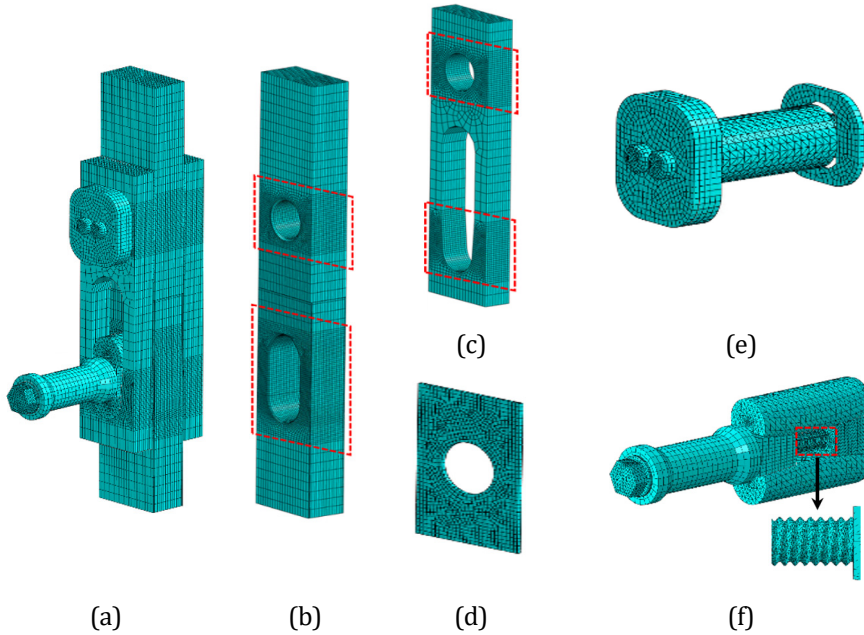


Fig. 2-8. Details of the FE mesh of all components. (a) Overview of the model; (b) Upper and lower segment; (c) Web; (d) Spacer plate; (e) Pinned connection; (f) Wedge connection

2.3.3 Material models

The mechanical properties of the materials used in the FE model are listed in Table 2-2. Five materials were used in the specimen specified by the company, C1 Connections B.V.: (1) S460 structural steel for the plate components, shown in grey in Fig. 2-7; (2) Grade 8.8 /10.9 high strength steel for the M18 bolt, shown in green in Fig. 2-7; (3) 34CrNiMo6 steel for the machined components in the fastener assembly, shown in red in Fig. 2-7; (4) Nylon material for the inserted nylon layer as spacer plate; (5) Considering no plastic deformation appeared in the load cell and pin connection, elastic material for the load cell and pin connection, shown in white in Fig. 2-7. Poisson ratio $\nu = 0.3$ is used for all the components in the FE model. The material property of S460 steel was obtained by performing coupon tensile tests, while the material properties of other parts were selected according to the literature [6–9].

The conventional bilinear isotropic hardening model is not applicable to post-peak behaviour. Hence, the full-range stress-strain constitutive model is used for S460 steel

and the bolt, which is explained in section 2.3.3.1. The damage is expected to occur in the low segment with the smallest cross-section area. Therefore, only the fracture mechanisms of S460 steel are considered in this chapter.

Table 2-2 Material properties.

Component	Density $\frac{den}{(kg/m^3)}$	Young modulus E_0 (MPa)	Steel grade	Yield strength f_y (MPa)	Ultimate strength f_u (MPa)	Peak strain ϵ_u	Ultimate elongation A (%)
Plate	7850	2.1×10^5	S460	485	620	0.125	23
Fastener assembly [6]	7850	2.1×10^5	34CrNiMo6	620	800	-	15
Nylon layer [7]	1350	2.76×10^5	-	-	-	-	-
Load cell/pin connection	7850	2.1×10^5	-	-	-	-	-
M18 bolt [8,9]	7850	2.1×10^5	8.8	776	970	0.05	10
			10.9	945	1050	0.05	10

2.3.3.1 Full-range true stress-strain constitutive material model

It is assumed that the specimen volume remains constant in a uniaxial stress state up to the necking point. The prior-necking true stress-strain relations can be converted from the engineering stress-strain curve, as expressed in Eq. 2-5 and Eq. 2-4.

$$\sigma_t = \sigma_e (1 + \epsilon_e) \quad \text{Eq. 2-4}$$

$$\epsilon_t = \ln(1 + \epsilon_e) \quad \text{Eq. 2-5}$$

where σ_e and ϵ_e mean the engineering stress and strain, measured from the coupon tensile test. σ_t and ϵ_t denote the true stress and strain, respectively.

The post-necking material behaviour could not be obtained simply through extensometer measurements on the coupon specimen due to the variation in the cross-sectional area and the plastic instability [10]. Ling [11] proposed a combined linear and power stress-strain law to describe the post-necking stress-strain relations. This method assumes the empirical low and upper bounds for the post-necking material behaviour with $0 \leq W \leq 1$, and is expressed as:

$$\sigma_t = (W)(a\epsilon_t + b) + (1 - W)(K\epsilon_t^n) \quad \text{Eq. 2-6}$$

where $a = \sigma_{t,u}$, $n = \epsilon_{t,u}$, $b = a(1 - n)$; $K = a/n^n$. $\sigma_{t,u}$ and $\epsilon_{t,u}$ represent the true stress and true strain at the onset of necking, which can be calculated according to Eq. 2-5 and Eq. 2-4. Yang et al. [12,13] proposed that the weighting factor W could be calibrated with values even less than zero or larger than 1. In this chapter, W is calibrated for the investigated steel in the range of -0.5 to 1.5. Fig. 2-9 shows the employed full-range stress-strain relationship for S460 steel in this chapter.

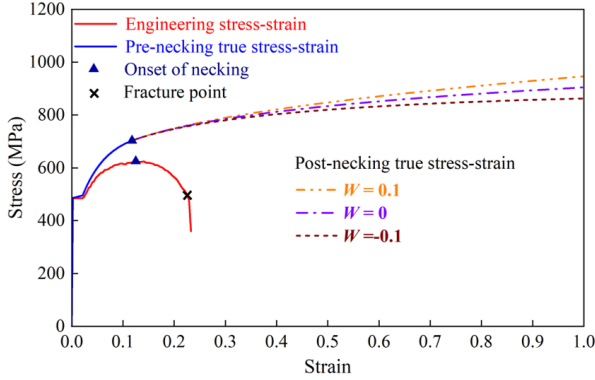


Fig. 2-9. Full-range stress-strain relationship of S460 steel.

2.3.3.2 Rice-Tracy fracture criterion

To simulate the fracture of the material under tensile loading, the Void Growth Model [14,15] (VGM) based on the Rice-Tracey (RT) function is employed in this chapter:

$$\bar{\varepsilon}_D^{\text{pl}} = \alpha \cdot \exp(-\beta \cdot \eta) \quad \text{Eq. 2-7}$$

The model has been coded into ABAQUS as “ductile damage” [16], dependent on the stress triaxiality η . It is assumed that the ductility decreases exponentially with the increased stress triaxiality. Then, the material fracture is predicted to occur when the critical void growth index ($\text{VGI}_{\text{critical}}$) is reached. α and β are two material-dependent parameters, where β is generally taken as 1.5 and α is similar to $\text{VGI}_{\text{critical}}$ which can be calibrated from the test results [17]. The damage initiation criterion is reached when Eq. 2-8 is satisfied, in which $\bar{\varepsilon}^{\text{pl}}$ is the equivalent plastic strain (PEEQ) and the damage index W_D is the damage initiation variable.

$$W_D = \int d\bar{\varepsilon}^{\text{pl}} / \bar{\varepsilon}_D^{\text{pl}} = 1 \quad \text{Eq. 2-8}$$

The mentioned RT criterion is taken as the damage initiation criterion. The damage evolution law is defined by the displacement type with a very small displacement, such as 0.001, at the failure to simulate a sudden load capacity loss after the damage initiation. Element deletion is triggered when $W_D = 1$ in the FE model.

2.3.3.3 Material model calibration

Tensile coupon tests were performed on S460 steel to formulate a full-range true stress-strain constitutive material model. Quasi-static analyses were performed using the explicit dynamic solver in ABAQUS. The coupons were cut from the same batch of S460 steel material used for the C1 wedge connection. The most appropriate W can be calibrated by comparing the engineering stress-strain curves from the FE results and the experimental results.

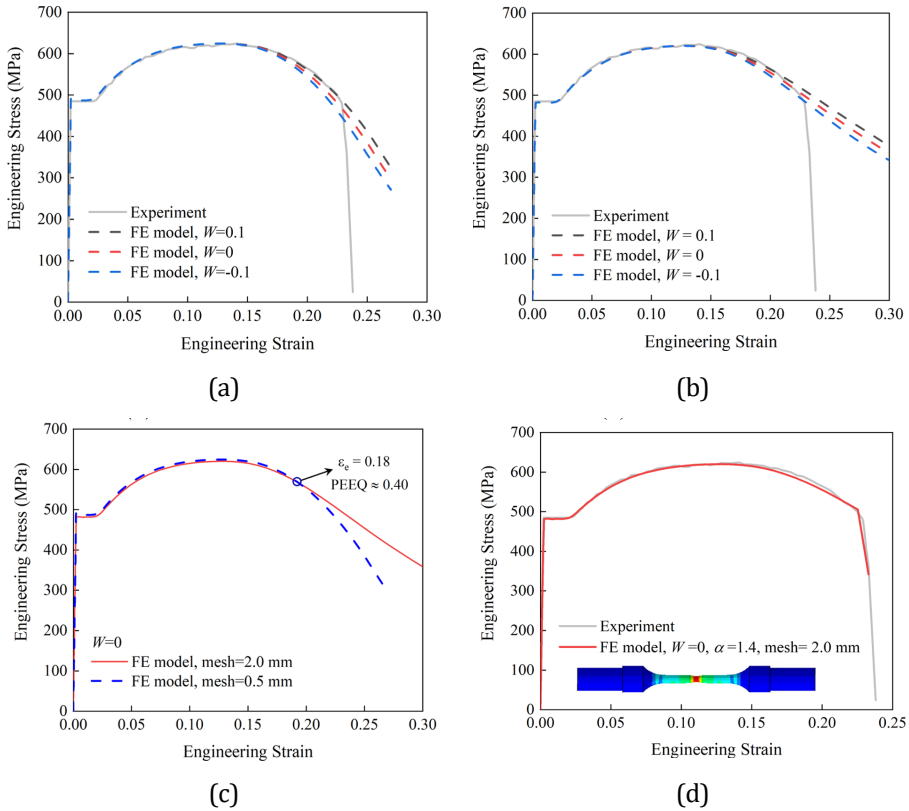


Fig. 2-10. Weighting factor calibration for S460 steel. (a) Mesh size of 0.5 mm; (b) Mesh size of 2.0 mm; (c) $W=0$ with various mesh sizes; (d) Engineering stress-strain comparison between experimental and FE results

A mesh sensitivity analysis was carried out with two mesh sizes of 0.5 mm and 2.0 mm in the gauge parts with a length of 60 mm. Fig. 2-10 (a) and (b) show a comparison between the numerical and experimental engineering stress-strain curves for S460 steel using three weighting factors with an interval of 0.1. A larger weighting factor in the combined linear and power stress-strain law causes a higher engineering stress in the descending stage. Meanwhile, a noticeable effect of the mesh size can be found in Fig. 2-10 (c) when the engineering strain is much larger than the fracture strain. The 0.5 mm mesh results in a sudden drop of load strength at a smaller fracture strain than the comparable one of the 2.0 mm mesh. This indicates that the strain localization effect of the S460 steel is not sensitive to the mesh size before the PEEQ of 0.4 under uniaxial loading. In conclusion, the weighting factor $W=0$ and mesh size 2.0 mm were selected to describe the post-necking behaviour of S460 steel. A good agreement is obtained between the engineering strain-stress curve of S460 material from experimental and FE results, see Fig. 2-10 (d).

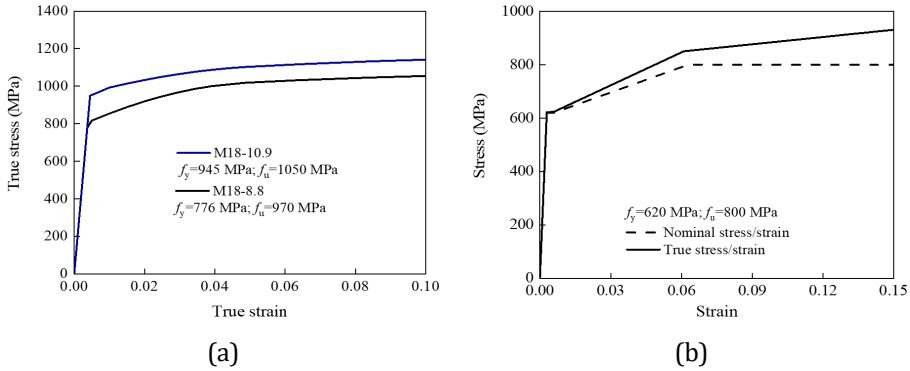


Fig. 2-11. Stress-strain curves for materials used in the bolt and machined components. (a) M18 bolt; (b) 34CrNiMo6 steel

The yield strength of grade 8.8 and 10.9 bolts was determined using the nominal ratio f_y/f_u equal to 0.8 and 0.9, respectively. Following Eq. 2-4 and Eq. 2-5, the pre-necking true stress-strain curve can be obtained. A recent investigation indicates that the post-necking true stress-strain diagram for high-strength bolts under tensile loading can be described as a power strain-stress with a weight factor of 0 [12]. According to the experimental results for the bolt material reported in [8,9], the full-range true stress vs. true strain curves for the bolt can be obtained as shown in Fig. 2-11 (a).

For the sake of simplicity, idealised elastic-plastic-hardening properties were employed for the engineering stress-strain curve of 34CrNiMo6 steel, as shown in Fig. 2-11 (b). This is because no damage is expected in the machined parts of the wedge connection, as the maximum stress level in the FE analysis is about 400 MPa. Engineering stress-strain curves were converted into the true stress-strain curves for input in the ABAQUS plasticity model.

2.3.4 Loading procedure

Two calculation steps were carried out in the model to coincide with the physical test conditions. The bolt was preloaded first by the turn-of-bolt head method and then the model was loaded to failure by applying an axial displacement to the tower segment. In the first step, as illustrated in Fig. 2-12, the edges of the bolt head were coupling constrained to the reference point RP-bolt located in the centre of the bolt head. A rotation was exerted on the RP-bolt around the centreline of the bolt. To reach the design preloading force P_c listed in Table 2-1, trial simulations were performed to determine the rotation angle. The preloading forces in the bolts were obtained by extracting the contact pressure force at the inner washer surface.

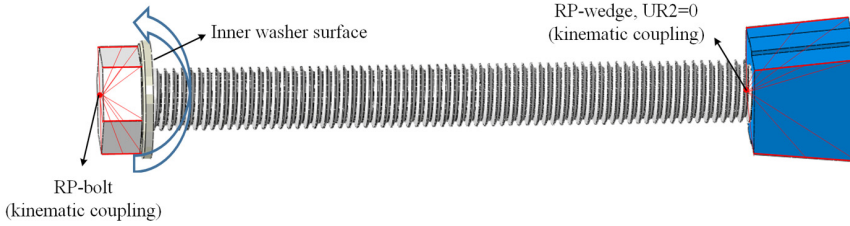


Fig. 2-12. Preloading of the bolts in the FE model

To perform a quasi-static analysis, the explicit solver requires a conditional stability limit which can be approximated in terms of the material density ρ , the characteristic length of the smallest element L_e , and the Lamé parameters λ and μ :

$$\Delta t \approx \min \left(L_e \cdot \sqrt{\rho / (\lambda + 2\mu)} \right) \quad \text{Eq. 2-9}$$

The mesh verification analysis revealed that the smallest stable time increment in the FE model is 1.9×10^{-9} , leading to a large computational cost. The elements limiting the time increment are mainly from the bolt and outer wedge due to the threads, while the average stable time increment for other components was 2.0×10^{-7} . Considering the bolt and outer wedge are not critical components, a semi-automatic mass scaling option was used to shorten the computation time. As a generally accepted indication of the quasi-static analysis, the energy ratio between the kinetic energy to the internal energy should not be noticed throughout most of the simulation, and should not exceed a small fraction (5%-10%). To achieve a trade-off between the computation time and accuracy of the FE model, the target time increment was set to be 1.0×10^{-6} s after several trial computations. The time periods adopted for preloading and loading to failure steps were 2.5 s and 0.25 s, respectively.

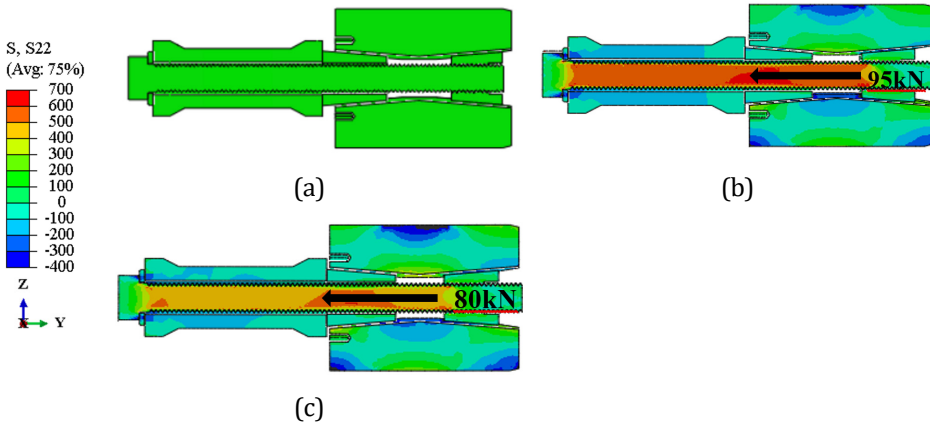


Fig. 2-13. Stress distribution and deformation of the fastener assembly of wedge connection. (a) Initial status; (b) WC1; (c) WC2

The contour plots along the meridional direction in the bolt and wedge connection for each specimen after preloading are shown in Fig. 2-13. Compared to the initial status, the inner and outer wedges approach at different distances due to the various bolt preload levels. Meanwhile, the bolt pretension causes the contact pressure F_4 between segments, as shown in Fig. 2-14. In the second step, an axial load was imposed by setting an upward displacement of the reference point RP3 (Fig. 2-7).

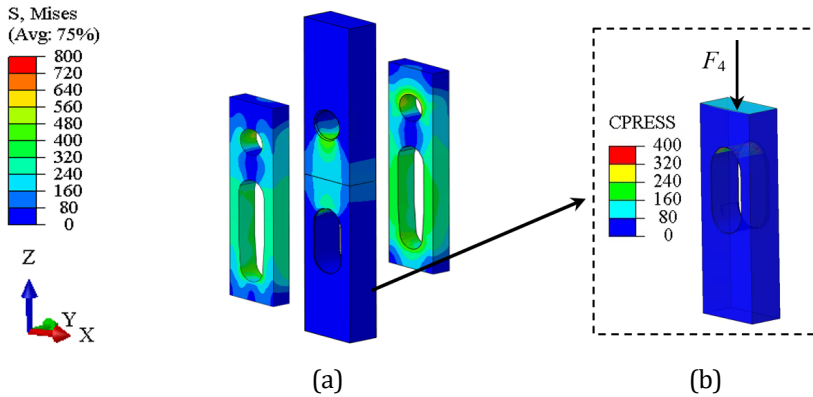


Fig. 2-14. Stress distribution of plate components after bolt preloading. (a) Von Mises stress; (b) Contact force

2.4 EXPERIMENTAL AND FE RESULTS

A corresponding comparison was made between the experimental and FE results shown below, separately for WC1 and WC2. The validated FE model was then used to conduct a parametric study to expand the experiments.

2.4.1 Behaviour of WC1

2.4.1.1 Failure mode

By observing the deformation of WC1 during the loading process with two cycles (Fig. 2-15 (a)), it can be found that the specimen maintains elasticity at the initial stage of the loading. The influence of the first loading-unloading cycle can be neglected within the elastic stage, representing a uniaxial tensile behaviour of the C1 wedge connection. The load-displacement curve in Fig. 2-15 (a) can be separated into three stages. The axial stiffness remains linear in the first stage. The imposed loading at the end of the elastic stage is defined as critical force $N_{c,E}$. After exceeding $N_{c,E}$, the axial stiffness decreases slightly with an increase of displacement. At the end of the second stage, the yield strength $N_{y,E}$ is achieved with a short yield plateau. After that, the specimen behaves nonlinearly, and the axial stiffness degrades gradually until the fracture of the specimen. The peak point of the curve is regarded as the overall axial ultimate resistance.

The relationships of applied load (Nz) versus the displacement from the experiments at the second cycle and FEA results of WC1 are presented in Fig. 2-15 (b). A good

agreement between the experimental results and FE analysis results is achieved. The numerical values accompanied by the corresponding test results are presented in Table 2-1, with a maximum deviation of 7%. A small difference of 11 kN between $N_{c,F}$ and the $N_{c,E}$ verifies the selected friction coefficient μ of 0.18 for generating contact pressure.

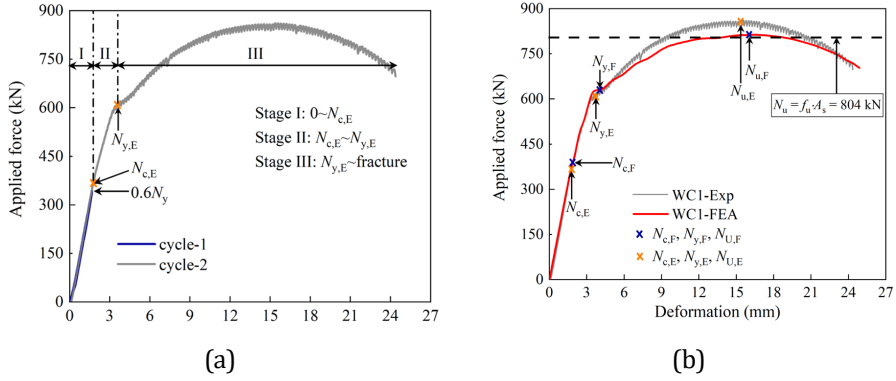


Fig. 2-15. Load-displacement curves of WC1. (a) Experimental results; (b) FEA vs. Exp

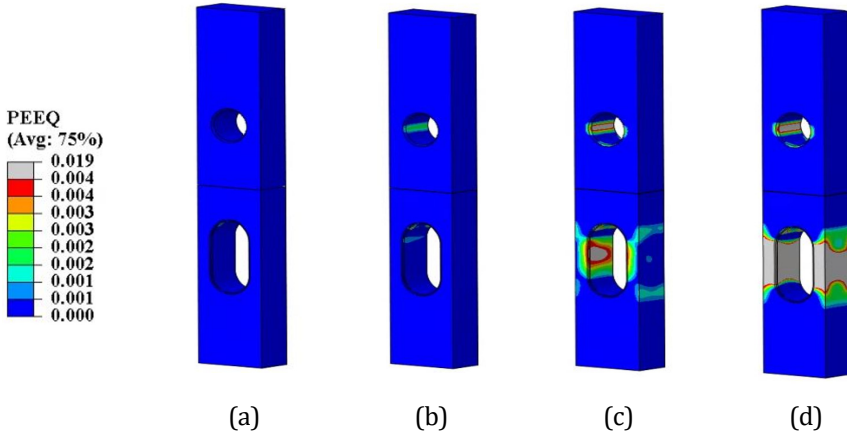


Fig. 2-16. PEEQ distribution in the lower and upper segment at four external loads N_z . (a) $N_z=310$ kN; (b) $N_z=470$ kN; (c) $N_z=620$ kN; (d) $N_z=630$ kN;

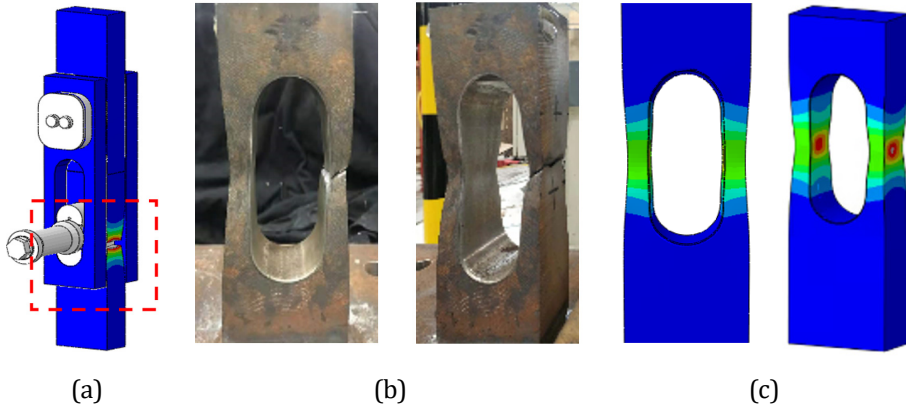


Fig. 2-17. Experimental and FE failure mode of WC1. (a) FE analysis failure; (b) Failure mode of lower segment from the test; (c) Failure mode of lower segment from the FE analysis

Considering the tensile loading is dominantly transferred through the lower and upper segments, the distribution of PEEQ in the segments at four load levels is illustrated in Fig. 2-16. It can be found that local plastification occurs after exceeding the critical load of 387 kN. The lower segment experiences large plastic deformation successively when increasing the load.

Fig. 2-17 shows the failure modes with residual deformation. Apparent necking failure of the lower segment is observed due to the smallest cross-section area A_s compared to the one in the upper segment. At the same time, the upper segment nearly remained undeformed. Hence, the bearing resistance of the specimen can be theoretically determined as $N_u = f_u \cdot A_s = 804 \text{ kN}$ (see Fig. 2-15), where f_u is the ultimate strength of S460 steel. The comparison indicates that the failure mode depicted by the FE analysis reflects the failure process of the experimental specimens very accurately, as shown in Fig. 2-17.

2.4.1.2 Evolution of bolt force

Force in the bolt obtained from the load cell is shown in Fig. 2-18 (a). A slight decline during the first loading-unloading cycle is observed from the experimental results. The bolt force loss can be attributed to many reasons, among others the embedding loss as the contact interfaces in the connections which are usually not perfect with numerous protrusions. However, this fact can be neglected when considering the elastic behaviour of the specimen at the initial stage of the loading. Similarly, the development of bolt force in WC1 includes three characteristic stages. Almost no change in the bolt force is observed in the first stage. In the second and third stages, the bolt force starts to increase nonlinearly with various gradients. Fig. 2-18 (b) shows the results of the bolt force versus the applied load curves from the experimental and FE simulation. An increasing scattering is observed between the test and FE results in the latest stage of loading.

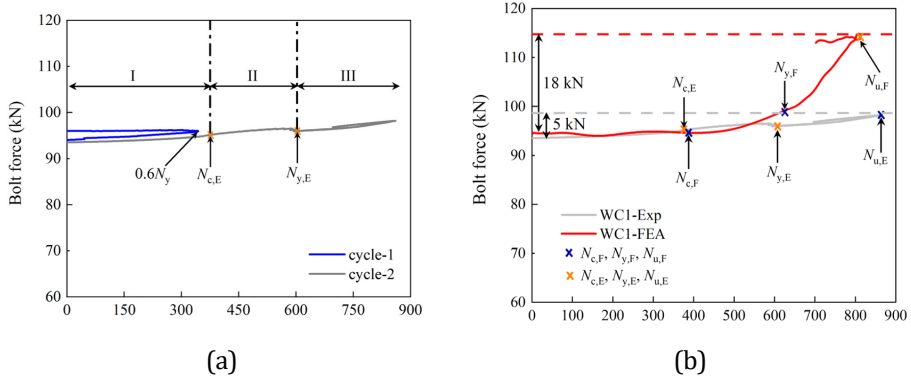


Fig. 2-18. Evolution of bolt force of WC1. (a) Experimental results; (b) FEA vs. Exp

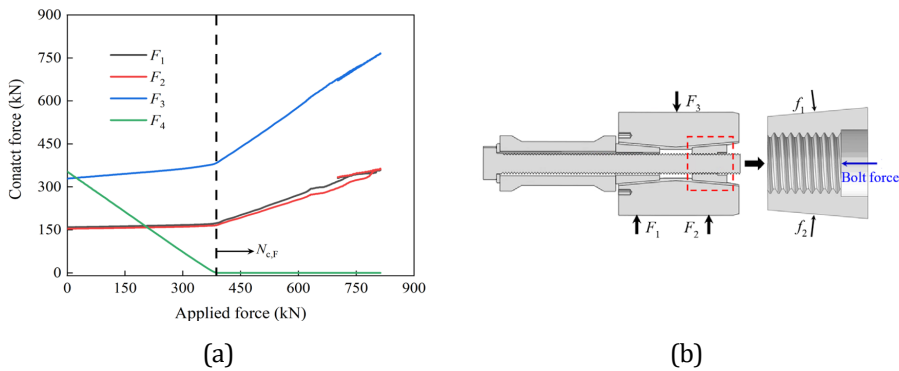


Fig. 2-19. Development of contact force of WC1 from FE analysis. (a) Contact force response of WC1; (b) Illustration of contact force

The contact force responses are extracted from the FE analysis and shown in Fig. 2-19 to identify a point beyond which the increasing gradient of the bolt force appears. The contact pressure F_4 between the upper and lower segment decreases linearly at first, while the contact forces F_1 , F_2 and F_3 maintain the shape approximately with constant bolt force until the critical load $N_{c,F}$. Then, the low segment starts to support the imposed load, leading to an open connection and linearly increasing contact forces F_1 , F_2 and F_3 . It is obvious that the lower block in the C1-WC is subjected to bending as it spans two webs and the lower segment [2]. As F_1 and F_2 are increasing, the bolt receives the load transferred from the blocks with the increasing contact force at the wedge f_1 and f_2 , (as shown in Fig. 2-20). The extraordinarily high contact pressure in Fig. 2-20 is attributed to a mathematical stress singularity that occurred in the steep corner. This stress singularity can be ignored after considering these sharp corners are not critical areas for the mechanical behaviour of the specimen.

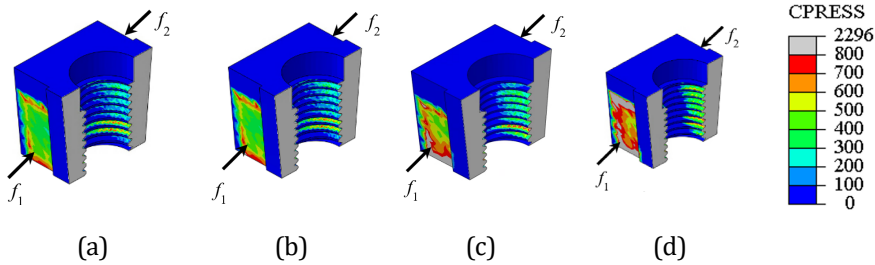


Fig. 2-20. Development of contact force of the outer wedge. (a) $N=0$; (b) at $N_{c,F}$; (c) at $N_{y,F}$; (d) at $N_{u,F}$

It is concluded that the bolt in the C1 wedge connection operates in two ways: (1) it introduces the contact pressure at the preloading stage; and (2) it participates in the load transfer when reaching the critical load N_c . The calculation of WC1, shown in Fig. 2-18 was performed with a uniform friction coefficient of 0.18 for all contacts. However, the friction coefficient for lubricated bolt threads is much close to 0.1, which cannot be simulated via the general contact used in the analysis. Consequently, the high friction coefficient leads to a larger bolt force than obtained in the test results which is beyond the critical load N_c , as shown in Fig. 2-18 (b). The results from the parametric analysis in section 2.5.1 demonstrate the maximum bolt force variation with a friction coefficient of 0.18 is 11 kN larger than with a smaller friction coefficient of 0.1, see Fig. 2-32. A similar influence of friction coefficient on bolted joints was also obtained in [18–21]. Additionally, the deviation observed after N_c can also be attributed to the assumed stress-strain curve of the M18 bolt (Fig. 2-11 (b)).

In terms of the tensile ultimate limit states (ULS), the final failure occurs in the lower segment instead of the bolt. It is observed that the maximum tensile stress of the bolt is below the yield strength. For fatigue limit states (FLS) resistance, the yield strength N_y was considered to be the maximum applied fatigue load. The deviation of bolt force between FE and test results below N_y is neglectable, see Fig. 2-18 (b). The resulting bolt stress variation is 23 MPa and 14 MPa from FE and test results, respectively. These bolt stress ranges are lower than the constant fatigue limit $\Delta\sigma_D$ of 37 MPa for the M18 bolt with the detail category of 50 [22]. Hence, the bolt behaviour is not critical both for ULS and FLS resistance for WC1.

2.4.1.3 Evolution of gap opening

The opening between two segments has been measured for each specimen during the loading of the connection, see Fig. 2-5. The evolution of the gap opening of WC1 is depicted in Fig. 2-21, where the gap opening from LVDT Δ_1 is the mean value of the measurements $(D2+D3)/2$. Similarly, the gap opening behaviour of the connection under uniaxial tensile loading can be separated into three stages with similar boundaries. The gap opening linearly increase to 0.12 mm in the first stage from Fig. 2-21 (a), followed by an increase until 1.7 mm when the final fracture occurs. It should be noted that a difference between the experimental and FE results at the third stage is

apparent, which can be attributed to the fact that the ultimate deformation capacity of the LVDT was reached.

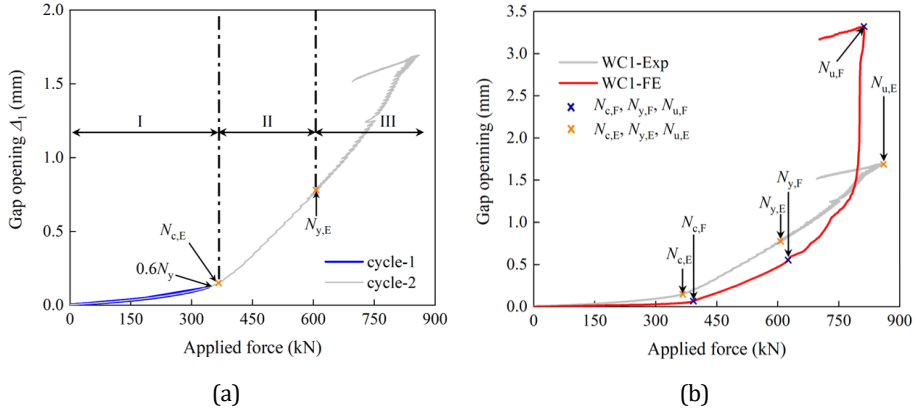


Fig. 2-21. Comparison of gap opening behaviour between experimental and FE results for WC1. (a) Experimental results; (b) FEA vs. Exp

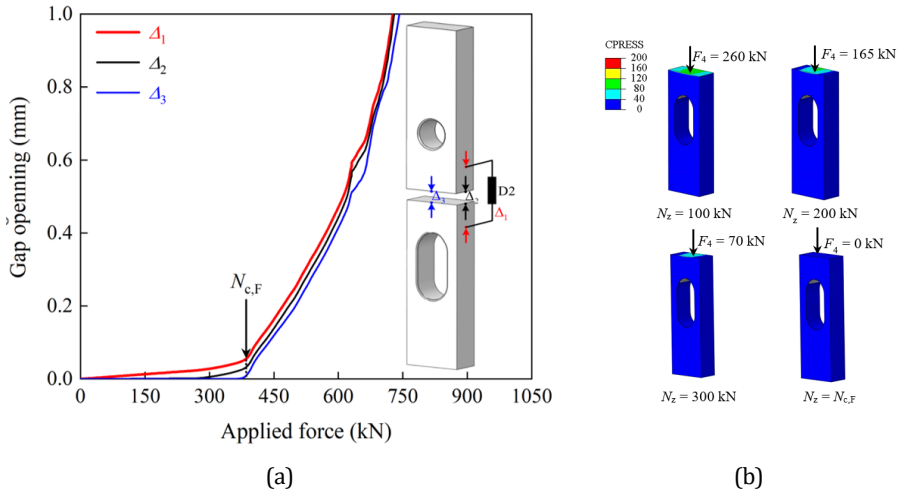


Fig. 2-22. Gap opening behaviour and related contact force. (a) Gap opening behaviour; (b) Contact force in lower segment

Fig. 2-22 compares the gap opening measured from LVDT Δ_1 and the interface of segments Δ_2 / Δ_3 from FE results. Fig. 2-4 shows that the force equilibriums of the upper segment and lower segment under external load N_z are:

$$\Delta N_{upper} = N_z + F_4 - (F_1 + F_2) \tag{Eq. 2-10}$$

$$\Delta N_{lower} = F_3 - F_4 \tag{Eq. 2-11}$$

According to Fig. 2-19, ΔN_{upper} and ΔN_{lower} increase at the beginning with a significant decrease in F_4 and a slight increment in F_3 . Under the applied force of 100 kN, the

resultant forces ΔN_{upper} and ΔN_{lower} are 42 kN and 82 kN in tension. The segments have tiny elastic deformation even with low N_z . Therefore, Δ_1 increases at the beginning due to the elastic deformation that occurred in the steel within the range of the LVDT. It can be observed from Fig. 2-22 (b) that the existing contact force F_4 is dominantly distributed in the middle of the segment. However, there is no contact force at the edge of the segment. That is why the gap opening Δ_2 opens at $N_z = 280$ kN, while Δ_3 opens at the complete degradation of F_4 at $N_{c,F}$.

2.4.2 Behaviour of WC2

2.4.2.1 Failure mode

The load-displacement curves of specimen WC2 are presented in Fig. 2-23. The curves of the FE results agree well with the experimental results. According to Eq. 2-12 the critical load N_c is different from the one at WC1 with a lower friction coefficient μ of 0.10 and bolt preload P_c of 80 kN. The stiffness degradation ratio ξ is defined as k_i/k_1 to reflect the change of the stiffness during the loading-unloading of the segment specimen, where k_1 is the initial stiffness. The stiffness of the i^{th} cycle k_i is calculated by:

$$k_i = (k_{\text{unl},i-1} + k_{\text{rel},i}) / 2 \quad (i=2:10) \quad \text{Eq. 2-12}$$

where $k_{\text{unl},i-1}$ is the tangent stiffness of the unloading path of $i-1^{\text{th}}$ cycle, and $k_{\text{rel},i}$ is the tangent stiffness of the reloading path of i^{th} cycle, as shown in Fig. 2-24 (a).

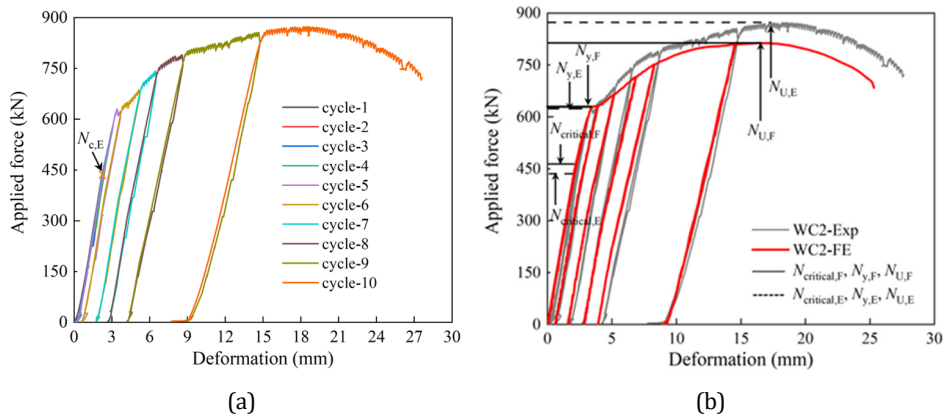


Fig. 2-23. Load-displacement curves of WC2. (a) Experimental results; (b) FEA vs. Exp

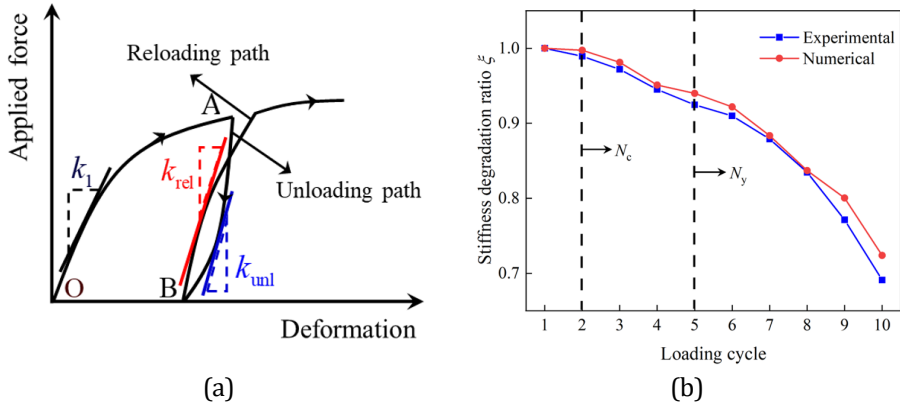


Fig. 2-24. Evolution of stiffness degradation with the number of cycles. (a) Definitions of stiffness; (b) Stiffness degradation curves

Fig. 2-24 (b) shows the stiffness degradation trend with increasing cycles. A drop of 8% of the ξ is observed between the specimen between the 1st and 5th cycles. In terms of the axial load level between the critical load N_c and the yield force N_y , the stiffness reduces gradually at a linear rate from the 2nd to 5th cycle. This can be attributed to the propagation of local plastic deformation in the segments, as shown in Fig. 2-25. Beyond the critical load (after the 2nd cycle), the permanent deformation is introduced into the segment successively. The degradation rate increases after the 5th cycle, corresponding to the larger plastic deformation at the lower segment. Despite the cyclic loading, the failure mode of WC2 is similar to WC1 in the middle section at the elongated hole of the lower segment.

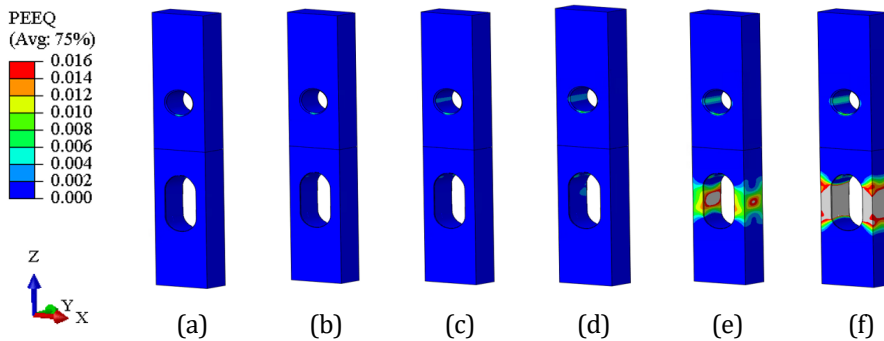


Fig. 2-25. PEEQ distribution in lower and upper segment at the end of unloading of 1st to 6th cycle. (a) 1st cycle; (b) 2nd cycle; (c) 3rd cycle; (d) 4th cycle; (e) 5th cycle

2.4.2.2 Evolution of bolt force

Fig. 2-26 shows the bolt force change during the cyclic loading. A general trend of bolt force evolution at each loading-unloading cycle is shown in Fig. 2-26 (b). The bolt force increases to some extent during the load path OA, followed by a decreasing trend during the unloading path AB.

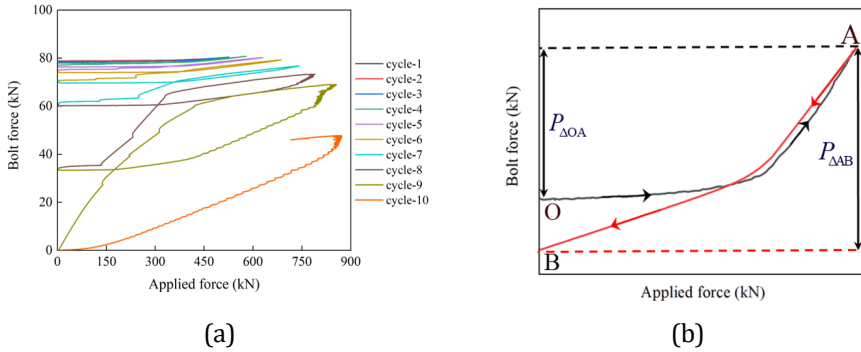


Fig. 2-26. Evolution of bolt force of WC2 from the test. (a) Experimental results; (b) general trend of bolt force variation

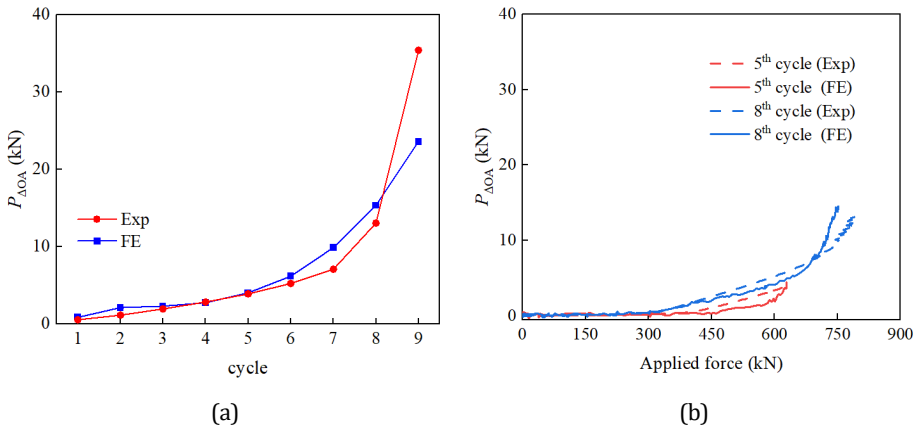


Fig. 2-27. Bolt force variation. (a) during loading-unloading of WC2; (b) at 5th and 8th cycles

A comparison of the bolt force variation $P_{\Delta OA}$ from the test and the FE results is shown in Fig. 2-27 (a), where FE results are basically consistent with the experimental results. In detail, the bolt force keeps constant in the first two cycles. After exceeding the critical load at the 2nd cycle, $P_{\Delta OA}$ increases gradually with the increasing cycles and load levels. $P_{\Delta OA}$ is less than 5 kN when the maximum force of the cyclic loading is below the yield strength of the specimen at the 5th cycle. After that, $P_{\Delta OA}$ increases at a nonlinear and faster rate. The bolt force drops to 0 kN during the unloading path of the 9th cycle. WC2 reached its ultimate strength at the 10th cycle. The results demonstrate that the load capacity of the specimen is not influenced by the loss of the bolt pretension. The maximum bolt stress during the whole cyclic loading is calculated as 420 MPa within the elastic states. Fig. 2-27 (b) shows the FE model for WC2 is capable of simulating the bolt behaviour accurately until the 8th cycle (under an applied force of $1.25 N_y$). This can be attributed to that the applied friction coefficient of 0.1 reasonably mimics the contacts of the pre-lubricated threads. The lubricated states of the practical application of the C1 wedge connection are identical to WC2. Hence, this simulation method is

reasonable to reflect the bolt behaviour in the practical application of the C1 wedge connection.

2.4.2.3 Evolution of gap opening

The evolution of gap opening from LVDT Δ_1 during the cyclic loading from the test is depicted in Fig. 2-28 (a). The corresponding zoomed-in curves during the loading path of each cycle are shown in Fig. 2-28 (b). The gap opening behaviour after reaching the applied force of 808 kN is eliminated as the ultimate deformation capacity of the LVDT was reached. The envelope of gap opening curves from the test and the FE result are compared in Fig. 2-29 to validate the FE model.

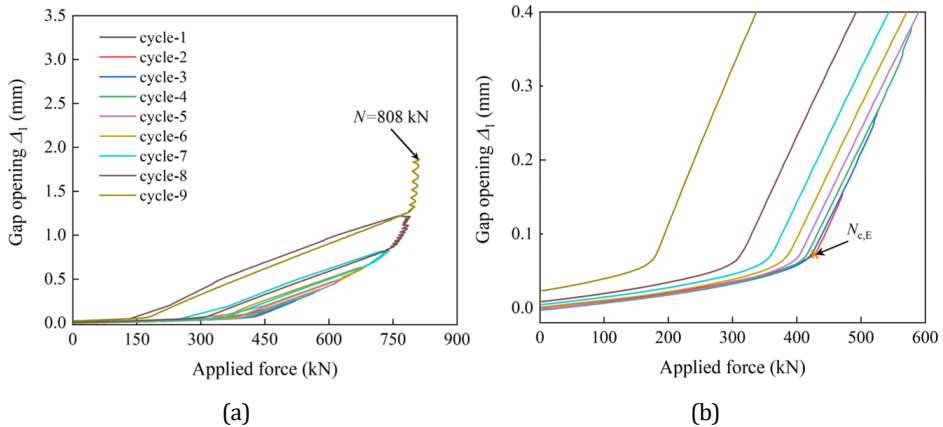


Fig. 2-28. Evolution of gap opening Δ_1 of WC2 from the test.

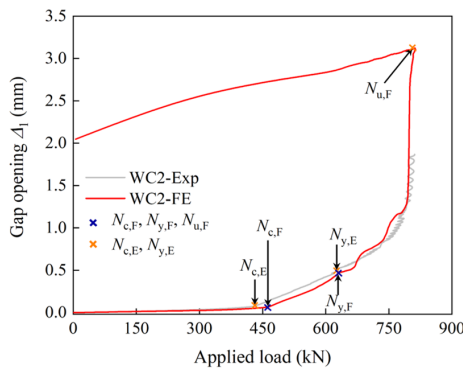


Fig. 2-29. Comparison of gap opening curves from test and FE results.

A critical load change ratio ζ was calculated based on the initial critical load after bolt pretension. As shown in Fig. 2-30, the critical load N_c corresponding to each cycle decreases slightly after the 2nd cycle. A 10% drop is observed at the 5th cycle with the load level N_y . The FE results and experimental results match well, verifying the reliability of the FE model to analyse the cyclic behaviour analysis of the specimen.

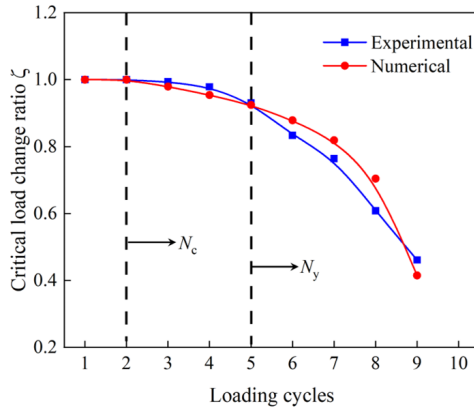


Fig. 2-30. Change of critical load with the number of cycles

2.5 PARAMETRIC ANALYSIS

Considering that the load cell is not included in practice, the FE model has been updated to remove the load cell to conduct the parametric analysis shown in Fig. 2-31. Table 2-3 lists the FE models and corresponding parameters. The nominal length of the bolt L_{nom} is reduced from 220 mm to 120 mm in the updated model due to the eliminated load cell. An upward displacement is imposed on the reference point RP1 at the top of the segment.

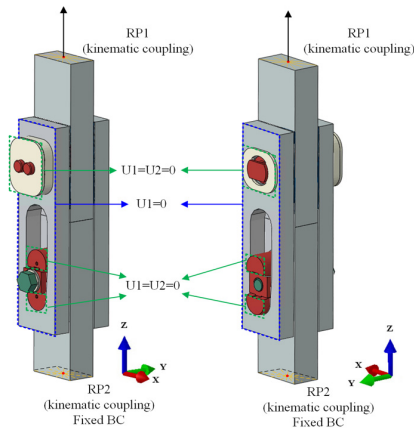


Fig. 2-31. Updated FE model for parametric analysis.

This parametric study aims to quantify the influence of the preloading force P_c , the bolt grade, and the friction coefficient between contacts. It should be noted that the influence of the yield strength f_y of the material and the smallest cross-section area A_s of the lower segment on the mechanical performance are not included. This is because their influence can be determined in a straightforward way from the equation $N_u = f_u A_s$. The

displacement at RP1 and gap opening Δ_2 was extracted from the FE results to evaluate the global and local deformation behaviour of the specimens. Based on the discussion in Sections 2.4.1.2 and 2.4.2.2, it is observed that the efficiency of the FE model for simulating bolt behaviour is not influenced by the friction coefficient within the yield strength N_y . The novelty of the C1 wedge connection is that the bolt is not the critical component under ULS and FLS. It is necessary to check the bolt stress range $\Delta\sigma_b$ under the applied force range ΔN_z equal to N_y , as listed in Table 2-3.

Table 2-3 Main parameters of the FE model

Specimen	L_{nom} (mm)	P_c (kN)	Bolt rotation (rad)	Bolt grade	Friction coefficient μ	$N_{c,F}$ (kN)	Bolt stress range $\Delta\sigma_b$ (MPa)
WC-F1	120	95	27.11	8.8	0.18	387	46
WC-F2	120	95	26.11	10.9	0.18	387	46
WC-F3	120	95	34.40	8.8	0.1	546	5
WC-F4	120	80	29.83	8.8	0.1	470	31
WC-F5	120	65	25.76	8.8	0.1	369	67
WC-F6	120	50	21.53	8.8	0.1	285	93

2.5.1 Influence of the bolt grade/friction coefficient

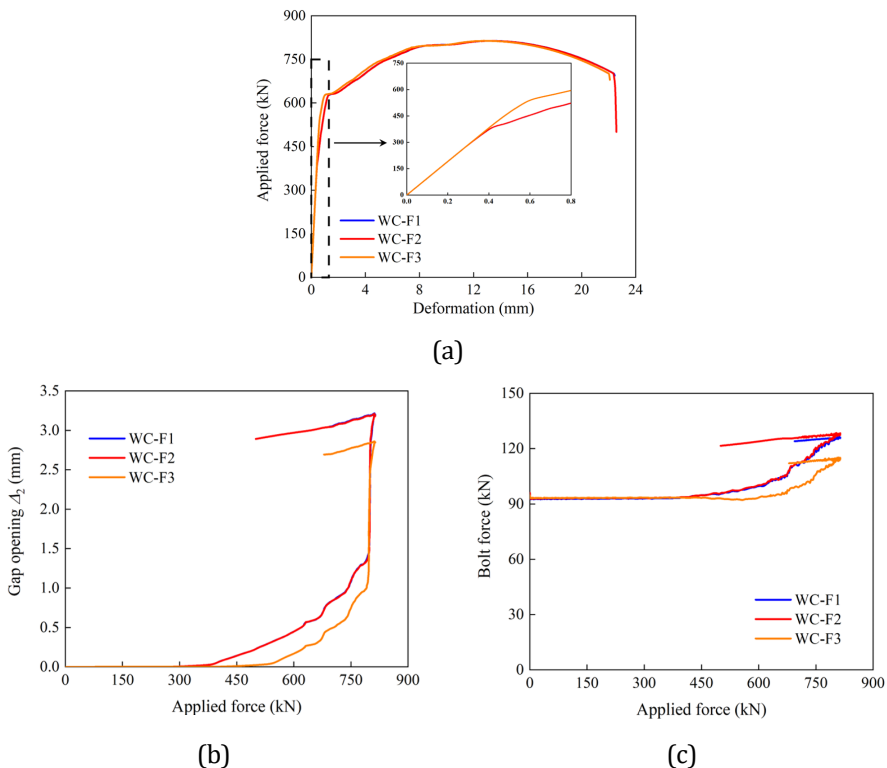


Fig. 2-32. Results of parametric analysis of bolt grade and friction coefficient. (a) load-deformation curve; (b) gap opening behaviour; (c) bolt force evolution

The comparison between WC-F1 and WC-F2 results shows that the influence of the steel grade of the bolt is negligible on the global and local deformation capacity. However, the lower friction coefficient μ introduces a higher contact pressure between segments according to Eq. 2-1. Consequently, the critical load of WC-F3 is higher than WC-F1, see a zoomed-in view in Fig. 2-32 (a) and (b). The gap opening Δ_2 and bolt force start to increase at 539 kN and 386 kN with the μ of 0.1 and 0.18, respectively. The value of the bolt stress range $\Delta\sigma_b$ of WC-F3 is lower than the one of WC-F1/F2 (see Table 2-3). The bolt is not involved in the FLS verification for WC-F3.

2.5.2 Influence of the preloading force

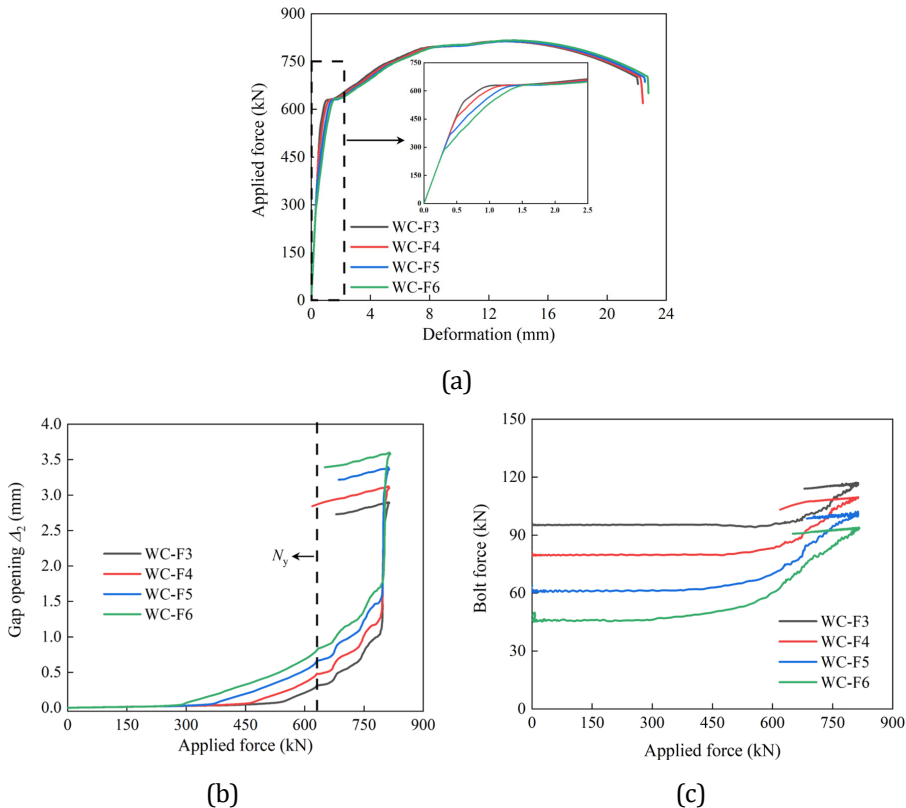


Fig. 2-33. Results of parametric analysis of P_c . (a) load-deformation curve; (b) gap opening behaviour; (c) bolt force evolution

Fig. 2-33 (a) indicates that P_c has negligible effects on the yield load and ultimate resistance of the specimen. A lower P_c leads to a smaller contact pressure between segments, resulting in a decreasing critical load $N_{c,F}$. The gap opening behaviour of the connection is strongly influenced by the preloading force P_c (Fig. 2-33 (b)). When P_c is reduced to 50 kN, Δ_2 at the yield load rises to 2.72 times the one with a P_c of 95 kN.

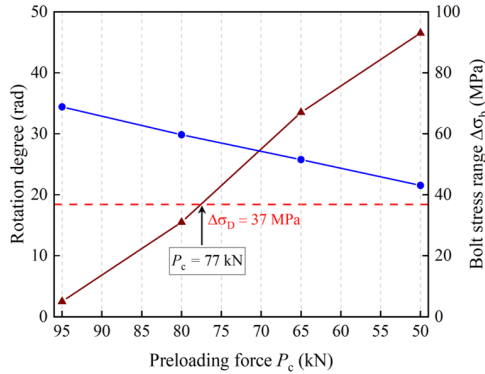


Fig. 2-34. Response of bolt stress range under different preloading force

As shown in Fig. 2-34, the bolt stress range needs to be considered for FLS verification when P_c is below 77 kN within the pre-lubricated connection. An accurate application of P_c is necessary in addition to reasonable design of P_c . Table 2-3 and Fig. 2-34 reveal that the relationship between P_c and bolt head rotation is linear. The bolt head rotation of 16° generates only 1 kN variation in P_c . Therefore the bolt preloading, with assumed friction coefficients, can be easily controlled by the bolt head rotation with high accuracy. Considering that $\Delta\sigma_b$ is ignorable within the critical load N_c , the only function of the bolt is to provide the contact pressure at the beginning under the design load lower than N_c .

2.6 CONCLUSION

The main characteristics of the 2nd generation of the C1 wedge connection used in large towers for offshore wind turbines are introduced in this chapter. An integrated study combining experimental and finite element analysis on its mechanical behaviour was conducted. The following conclusions are drawn:

- The bolted ring flange connection is loaded with a tension transfer force in the upper tower segment by eccentrically positioned bolts, while the C1 wedge connection shows a direct and concentric load transfer. A fairly small lateral bolt preload can be converted to a larger vertical preload in this connection. Under uniaxial and cyclic tensile loading, the failure mode of the C1 wedge connection is net section failure of the lower segment instead of the bolt.
- Experimental results under cyclic loading show that stiffness degradation and bolt force variation occur when the imposed load exceeds the critical load. Moreover, the results demonstrate that the ultimate tensile load resistance of the specimen is not influenced by the loss of the bolt pretension.
- The FE analysis matches well with the experimental results. This indicates the proposed FE models could predict the mechanical behaviour satisfactorily and provide evidence for evaluation and further development of the C1 wedge

- connection both for the ULS and FLS designs. The FE simulation provides practical guidance to design the connection without bolt failure.
- The bolt grade has a negligible influence on the global and local performance of the specimen. On the contrary, the friction coefficient μ and preloading force of the bolt P_c significantly influence the evolution of the gap opening and bolt force. Although the bolt is not critical for the tensile failure mode of the specimen, P_c is also decisive to guarantee the bolt is not involved in the fatigue design. It is suggested to design the connection to make sure the design load is lower than the critical load to avoid any bolt damage.

This chapter addresses research question Q1) by analyzing the experimental and numerical results of down-scaled specimens of the C1 wedge connection. The validated FE model of the C1 wedge connection will be used in Chapter 3. Furthermore, chapter 2 shows the deformation of the segments is influenced by the free boundary condition of the segment in the experiments. The effect of the tower continuity on the wedge connection behaviour will be further discussed in Chapter 3.

REFERENCES

- [1] The C1 wedge connections, (n.d.). <https://c1connections.com/> (accessed March 9, 2022).
- [2] K.E.Y. Creusen, G. Misios, J.S. Winkes, M. Veljkovic, Introducing the C1 Wedge Connection, *Steel Constr.* 15 (2022) 13–25. <https://doi.org/10.1002/STCO.202100039>.
- [3] C1 connections obtains DNV certification for the C1 wedge connection™, (n.d.). <https://c1connections.com/news/c1-connections-obtains-dnv-certification-for-the-c1-wedge-connection/> (accessed November 1, 2022).
- [4] J. Liu, H. Ouyang, J. Peng, C. Zhang, P. Zhou, L. Ma, M. Zhu, Experimental and numerical studies of bolted joints subjected to axial excitation, *Wear.* 346–347 (2016) 66–77. <https://doi.org/10.1016/j.WEAR.2015.10.012>.
- [5] VDI 2230 Part I: Systematic calculation of highly stressed bolted joints Joints with one cylindrical bolt, 2003.
- [6] EN-10083-3: Steels for quenching and tempering, Berlin: Beuth, 2016.
- [7] P.N.E. Naveen, M. Chaitanya Mayee, P. Gayathri, B. Kiran Goriparthi, K. Raghu Ram Mohan Reddy, Design and optimization of nylon 66 reinforced composite gears using genetic algorithm, *Mater. Today Proc.* 46 (2021) 514–519. <https://doi.org/10.1016/J.MATPR.2020.10.694>.
- [8] M. Pavlović, Z. Marković, M. Veljković, D. Bucrossed D Signevac, Bolted shear connectors vs. headed studs behaviour in push-out tests, *J. Constr. Steel Res.* (2013). <https://doi.org/10.1016/j.jcsr.2013.05.003>.
- [9] M. Yahyai, V. Kodur, A. Rezaeian, Residual mechanical properties of high-strength steel bolts after exposure to elevated temperature, *J. Mater. Civ. Eng.* 30 (2018) 04018240. [https://doi.org/10.1061/\(ASCE\)MT.1943-5533.0002416](https://doi.org/10.1061/(ASCE)MT.1943-5533.0002416).
- [10] Y. Cho, C. Lee, J.-J. Yee, D.-K. Kim, Modeling of ductile fracture for SS275 structural steel sheets, *Appl. Sci.* 11 (2021) 5392. <https://doi.org/10.3390/APP11125392>.
- [11] Y. Ling, Uniaxial true stress-strain after necking, *AMP J. Technol.* 5 (1996) 37–48.
- [12] F. Yang, M. Veljkovic, Y. Liu, Ductile damage model calibration for high-strength structural steels, *Constr. Build. Mater.* 263 (2020) 120632. <https://doi.org/10.1016/J.CONBUILDMAT.2020.120632>.
- [13] F. Yang, M. Veljkovic, L. Cheng, Fracture simulation of fully and partially threaded bolts under tension, *Ce/Papers.* 4 (2021) 156–161. <https://doi.org/10.1002/CEPA.1275>.
- [14] A.M. Kanvinde, A.M. Asce, G.G. Deierlein, F. Asce, Void growth model and stress modified critical strain model to predict ductile fracture in structural steels, *J. Struct. Eng.* 132 (2006) 1907–1918. <https://doi.org/10.1061/ASCE0733-94452006132:121907>.
- [15] A.M. Kanvinde, A.M. Asce, G.G. Deierlein, F. Asce, Finite-element simulation of ductile fracture in reduced section pull-plates using micromechanics-based fracture models, *J. Struct. Eng.* 133 (2007) 656–664. <https://doi.org/10.1061/ASCE0733-94452007133:5656>.
- [16] Simulia, Abaqus/CAE User’s Manual, Version 6.14, 2016.
- [17] L.J. Jia, H. Kuwamura, Ductile fracture simulation of structural steels under monotonic tension, *J. Struct. Eng.* (United States). 140 (2014). [https://doi.org/10.1061/\(ASCE\)ST.1943-541X.0000944](https://doi.org/10.1061/(ASCE)ST.1943-541X.0000944).
- [18] E. Dragoni, Effect of Thread Pitch and Frictional Coefficient on the Stress Concentration in Metric Nut-Bolt Connections, *J. Offshore Mech. Arct. Eng.* 116 (1994) 21–27. <https://doi.org/10.1115/1.2920123>.

- [19] K.I. Tserpes, P. Papanikos, T. Kermanidis, A three-dimensional progressive damage model for bolted joints in composite laminates subjected to tensile loading, *Fatigue Fract. Eng. Mater. Struct.* 24 (2001) 663–675. <https://doi.org/10.1046/j.1460-2695.2001.00424.x>.
- [20] A.M.P. De Jesus, A.L.L. Da Silva, J.A.F.O. Correia, Fatigue of riveted and bolted joints made of puddle iron—A numerical approach, *J. Constr. Steel Res.* 102 (2014) 164–177. <https://doi.org/10.1016/j.jcsr.2014.06.012>.
- [21] J. Braithwaite, I.G. Goenaga, B. Tafazzolimoghaddam, A. Mehmanparast, Sensitivity analysis of friction and creep deformation effects on preload relaxation in offshore wind turbine bolted connections, *Appl. Ocean Res.* 101 (2020) 102225. <https://doi.org/10.1016/j.apor.2020.102225>.
- [22] EN 1993-1-9: Eurocode 3: Design of steel structures – Part 1-9: Fatigue., 2005.

3. COMPARATIVE STUDY ON MECHANICAL BEHAVIOUR OF CONNECTIONS

The chapter compares the tensile behaviour and fatigue performance of three connections by validated finite element (FE) simulation and analysis. The following three types of connections: a conventional bolted ring flange (RF) connection, a ring flange connection with defined contact surfaces (RFD), and a C1 wedge connection (C1-WC) are considered. A series of parametric FE analyses are carried out to examine the impact of the applied boundary conditions, bolt pretension level, and steel grade on the behaviour of connections.

This chapter addresses the second research question Q2) and is organized as follows: Sections 3.1 and 3.2 introduce the characteristics of the three connections. Section 3.3 describes the experimental work. Section 3.4 shows the details of FE modelling and demonstrates the accuracy of the simulation method. Parametric studies about tensile behaviour and fatigue performance are performed in Sections 3.5 and 3.6, respectively. Section 3.7 presents the results of the comparison between connections. Finally, the conclusions are drawn in Section 3.8.

3.1 INTRODUCTION

The behaviour of RF and RFD connections is dominantly dependent on bolt resistance. The bolt assembly is under combined tension and bending loads due to the eccentricity between the tower segment and the bolts in the RF/RFD connections. On the contrary, the load from the upper to lower tower segment is transferred centrally between the segments in the C1-WC. The required bolt size for such centric connection is much smaller than in RF/RFD connections. The variation of bolt force is almost negligible under service loads, and the bolt is still in an elastic state at the ultimate limit state. This connection has been successfully certified by DNV in 2021 [1], and it is anticipated to be continually optimized and developed over the next few years.

An appropriate selection of the MP-TP connection plays a significant role in the overall competitiveness of the OWFs and is essential for ensuring structural integrity. Although investigations into individual connections has been carried out in different aspects, there is virtually no research associated with a quantitative comparison between the above-introduced connections. Meanwhile, laboratory tests via the segment approach are generally adopted to investigate the mechanical behaviour of connection [2,3]. The constraints in hoop direction provided by the tower are not considered in the segment model. Therefore, the segment approach may not accurately reflect the continuity of the tower's connection. In pursuit of a reliable connection design, it is crucial to conduct a comparative study on the effect of the segmentation of the tower connection in deriving connection properties for design.

Considering that large-scale laboratory tests are expensive and difficult to perform, numerical simulation using advanced FE models can be taken as an affordable and effective method. This numerical tool is capable of providing a deeper understanding of connections than physical tests. In this chapter, the FE method is adopted to simulate the mechanical behaviour of three types of connections without considering imperfections (gaps) between segments by ABAQUS. Both material inelastic and geometric nonlinearities are included in FE analysis. The developed FE models are first validated against the experimental results. Subsequently, the effect of the used boundary conditions, bolt pretension force, and steel grade on tensile behaviour and fatigue performance of connections are investigated. Finally, conclusions are drawn to provide in-depth information for the practical application and further optimisation of such connections.

3.2 INVESTIGATED CONNECTIONS

This section gives a short overview of the mechanical performance of the investigated connections under tensile loading in the segment model. Fig. 3-1 (a) illustrates the configuration of the RF connection. Two ring flange pieces are joined by a high-strength bolt that is evenly spaced for the RF connection. Before loading, a bolt pretension F_p is applied to create a compression zone between two steel flanges. The load transfer

behaviour of a typical RF connection is characterised by several stages with the imposed tensile load [4,5] (see Fig. 3-1 (b)).

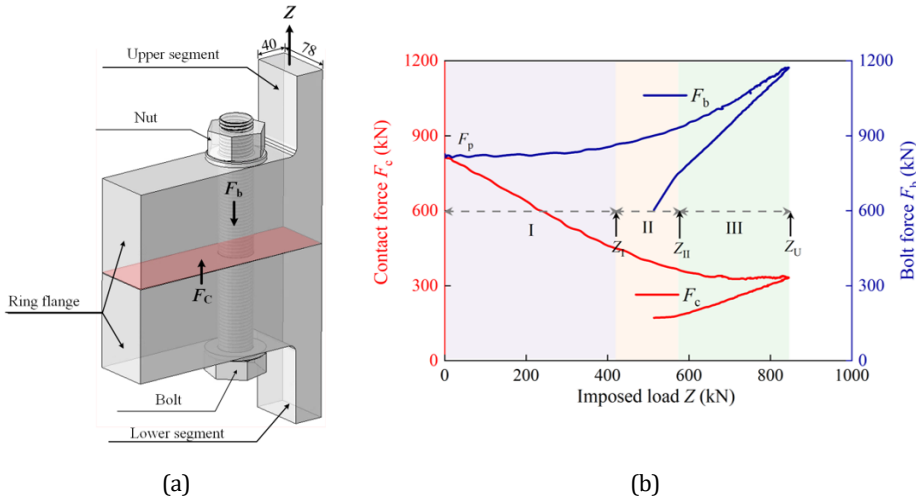


Fig. 3-1 Illustration of bolted ring-flange connections (RF) (a) RF connection (unit: mm); (b) Evolution of bolt and contact forces

Stage I - The increase of imposed load causes bending of the flanges, resulting in nonlinear decrease of the contact force F_c . The imposed load Z is mainly resisted via the redistribution of the contact force F_c . A slight increase of the bolt force F_b appears.

Stage II - After reaching the critical value of the imposed load Z_I , a large tensile load produces the successive opening of the contacts and expeditious increment of the bolt force F_b .

Stage III - Plastic deformation, at the “macro” level, of the flange and bolt occurs in this stage after reaching Z_{II} . The bolt force F_b increase linearly and only the area closed to the internal edge of the flanges is in contact resulting in a roughly constant contact force F_c .

Finally, the connection achieves the ultimate tensile strength Z_U and fails in two modes: rupture of the bolts and/or rupture of the bolt combined with plastic deformation of the flanges/segments.

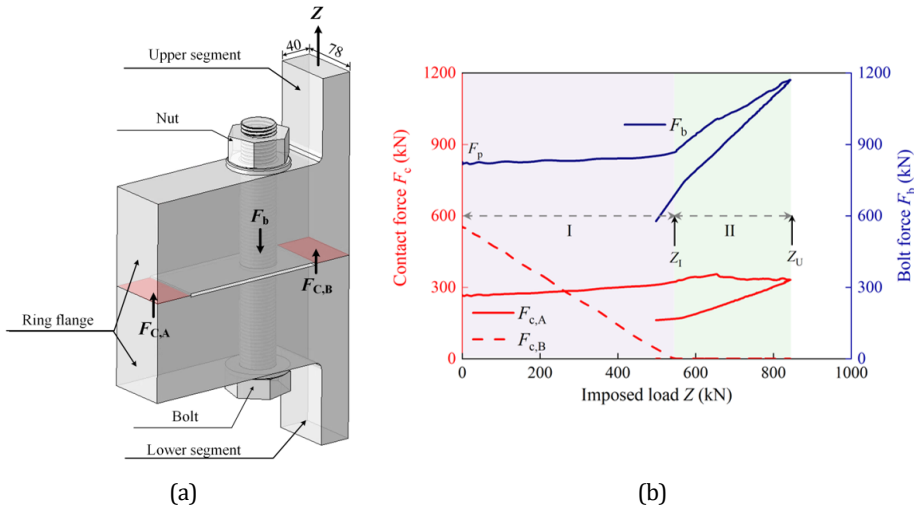


Fig. 3-2 Illustration of bolted ring-flange connections with defined contacts (RFD) (a) RFD connections (unit: mm) (b) Evolution of bolt and contact forces

Different from the continuous contact surface in RF connections, in RFD connections, the pretension bolt action F_p is transmitted via two clearly defined contact surfaces. There are two deformation stages for RFD connections in tension (as shown in Fig. 3-2):

Stage I – The imposed load is resisted through $F_{c,B}$ (the contact area directly beneath the segment plate). The bolt force F_b and contact force $F_{c,A}$ remain unchanged until $F_{c,B}$ is fully unloaded.

Stage II – The critical load Z_l is achieved when $F_{c,B} = 0$. After that, the bolt force increases steadily until the final fracture. The ultimate capacity of the RFD connection is nearly identical to the RF connection with similar geometrical features.

Only the bolt behaviour is profoundly influenced by the distinct surfaces. Consequently, the fatigue performance of an RFD connection differs from that of an RF connection. These observations are valid for the segment model or the full ring flange without the presence of imperfections, particularly parallel gaps [6–8]. The bolt force curve increases with a steeper slope if parallel gaps are present.

Bolt pretension is horizontally applied to the C1 wedge connection. Three generations of the C1 wedge connection been developed so far [9]. The behaviour of the second-generation design with a pin connection is investigated in chapter 2 (see Fig. 3-3). Two wedges immediately move towards each other with the pretension of the horizontal bolt, generating the increase in contact force F_c between the upper and lower segments. The applied tensile load is resisted by F_c at the beginning while the bolt force F_b is fairly constant throughout the loading process. The hand-calculation model was proposed by the company for designing the joint under ULS and FLS [10]. From Fig. 3-3

(b), the mechanical behaviour of a C1-WC is divided into three stages with the applied tensile load.

Stage I – The connection is in the elastic stage with the linearly decreased F_c . The critical load Z_I is defined at the end of the elastic stage.

Stage II – After exceeding Z_I , the connection behaves nonlinearly with increasing local plastic deformation until achieving the yield strength of the lower segment (Z_{II}).

Stage III – The lower segment undergoes considerable plastic deformation successively until an apparent necking failure occurs.

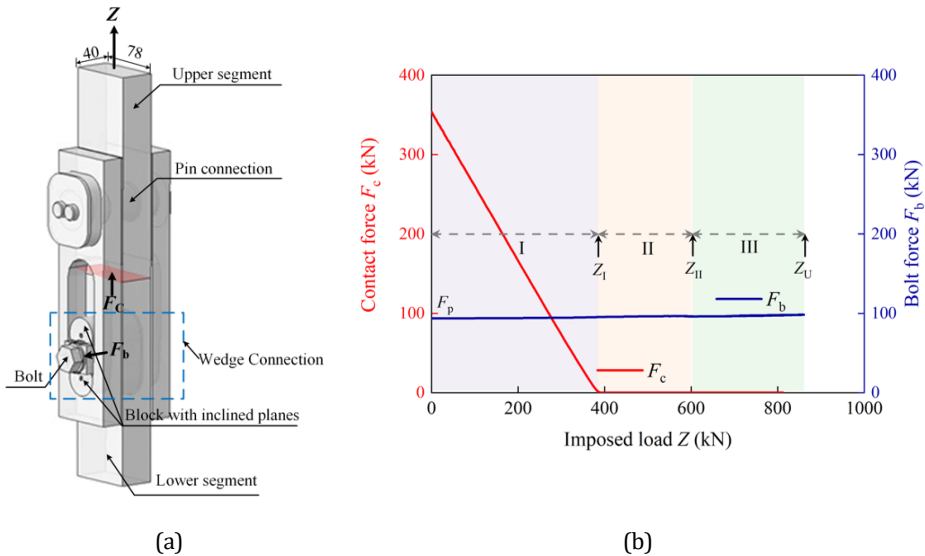


Fig. 3-3 Illustration of C1 wedge connections (C1-WCs) (a) C1-WC (unit: mm) (b) Evolution of bolt and contact forces

3.3 EXPERIMENTAL WORK

The experimental program that was used to validate the FE simulation method is briefly described in this section. All the tests were performed in the Stevin II lab at TU Delft. An extensive experimental program aiming at analysing the structural performance of ring-flange connections with M56 bolts was carried out subjected to static and cyclic loading [11]. Fig. 3-4 shows the test set-up for the RF connection under static loads. Both the top and bottom ends of the segment were supported by two hinges. After bolt preloading, the specimen was loaded to failure under displacement control. The external load, bolt forces and deformation capacity were measured. Six linear variable differential transformers (LVDTs) were installed on the sides of the flange to track the movement of the flange contact surface during loading. The bolt was instrumented with strain gauges to measure the pretension force and the following evolution of bolt force. Although various variables were analysed in this series of experiments, the

experimental results of the RF connection with ISO bolt/nut assembly are used for further validation of the FE simulation method. The influence of bolt-related variables was not the focus of this study. Stripping failure of the bolt threads at the lower side of the flange was obtained from the test.

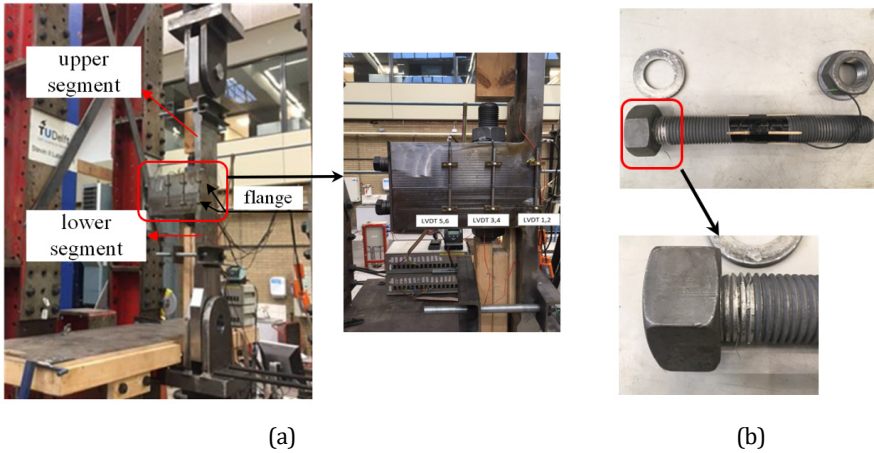


Fig. 3-4 Test set-up and failure mode for RF connections under static loads (a) Test set-up (b) Failure mode

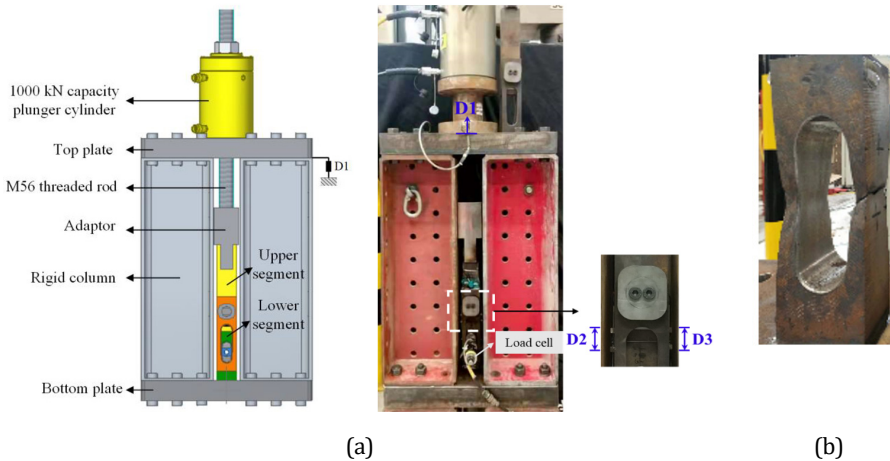


Fig. 3-5 Test set-up and failure mode for C1-WCs under static loads (a) Test set-up; (b) Failure mode

Pertaining to the C1-WC, static tests were conducted through a dedicated test set-up, as shown in Fig. 3-5. Different from the hinges used in the test of RF connections, the upper and lower segments were welded to rigid plates where the axial load was applied at the top plate by a hollow plunger cylinder. The applied load, bolt force and displacements in the connection were monitored during the tests. Three LVDTs (D1-D3) were

mounted to measure the axial deformation of the specimens and the gap opening between the contact segments. A load cell was installed on the M18 bolt to monitor the tensile force in the bolt. M18 was employed in down-scaled experiments. The failure was governed by the net cross-section ductile failure of the lower segment. The experimental response and failure mechanism are explained in great detail in chapter 2.

3.4 FE MODELLING OF CONNECTIONS

This section employs ABAQUS [12] to investigate the structural behaviour of the connections. All components affecting their performance are properly modelled to obtain accurate results from the FE analysis. The numerical simulation introduces the ductile damage material model for critical components. The associated material property parameters are chosen in accordance with the experiments. Finally, the effectiveness of the established FE models is demonstrated.

3.4.1 Geometry dimensions

To make a valid comparison between different connections, the geometry of connections and associated segments should be designed to have identical ultimate tensile strength. The experimental results of the C1-WC are adopted as the reference to design the RF/RFD connection. This is mainly because the design procedure for RF/RFD connection is more straightforward than that for the C1-WC. Hence, the developed FE model for RF/RFD connection in the comparative analysis is different from the geometrical features in the performed tests. However, the simulation method is similar so that the effectiveness of the developed FE models also can be validated using the previous test results.

It has been found that the ultimate tensile resistance of the C1-WC (Z_u) is independent of the preload force applied to the bolt [9]. The segments in C1-WCs have the following characteristics: the thickness and width of the segment are 40 mm and 78 mm, respectively (see Fig. 3-3). The ultimate capacity was calculated as $Z_u = A_{s,WC} \cdot f_u = 812$ kN, where $A_{s,WC}$ is the smallest net cross-section area of the lower segment and f_u is the measured ultimate tensile strength of S460 material [9] used in the segment of C1-WCs. Fig. 3-6 (c) presents the schematic geometry of the C1-WC. The M18 bolt is modelled with actual dimensions [9] measured by a digital caliper. The major diameters for the bolt and outer wedge threads are 18.18 mm and 17.90 mm, respectively. Minor diameters for the bolt and outer wedge threads are 15.20 mm and 15.48 mm, respectively. The measured pitch is 2.5 mm which is the recommended dimension for M18 bolt according to ISO 4014 [13].

The analytical models proposed by Petersen and Seidel [4,14] were used to design the geometry of the RF/RFD connection. Five approximated failure modes were considered, and the corresponding results are shown in Table 3-1. The tensile resistance for failure mode A is linked to bolt failure. Failure mode B represents the failure of the bolt

combined with the plastic deformation of the flange/segment. The failure of the shell and flange due to yielding is defined as failure mode C/D/E, where failure modes D/E should be used as they are more accurate and less conservative compared to using failure mode C. Table 3-1 shows that failure mode B controls the ULS of RF/RFD connections according to the analytical evaluation. The detailed geometry of RF and RFD connections is shown in Fig. 3-6 (a) and (b). An M42 bolt is utilized in these two connections. The M42 bolt was modelled in accordance with with Refs. [15] and [16]. The nominal height of the bolt head and nut is 25 mm and 34 mm, respectively. The nominal bolt length is 335.5 mm. The tolerance class of threads are defined as 6g (after coating) and 6H by ISO 965-1 [17].

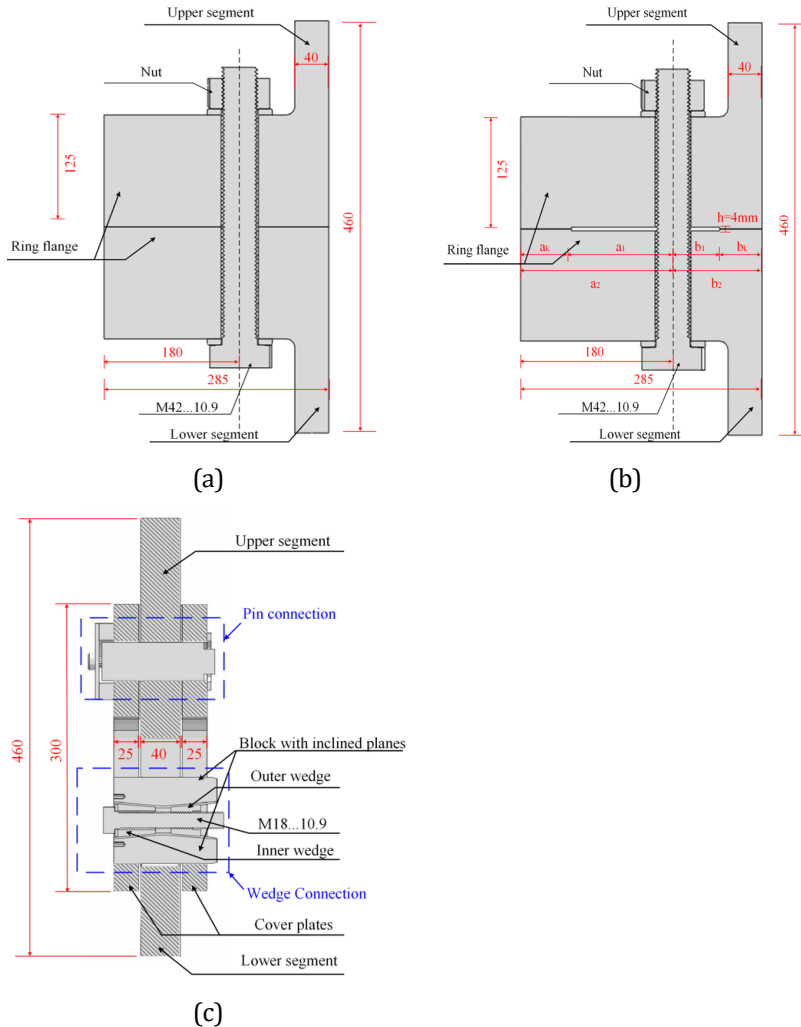


Fig. 3-6 Cut view of segment specimens with various connections (a) RF connection; (b) RFD connection; (c) C1-WC

Table 3-1 Evaluation of ultimate tensile resistance of RF/RFD connections

Failure mode	Analytical equations	Ultimate capacity
Mode A	$f_b A_s$	1179 kN
Mode B	$F_{U,B} = \frac{F_{t,Rd} a' + M_{pl,3}}{a' + b} = \min \left\{ \frac{F_{t,Rd} a' + \left[1 - \left(\frac{N_{ult,2}}{N_{pl,Rd,sh}} \right)^2 \right] M_{pl,Rd,sh}}{a' + b}, \frac{F_{t,Rd} a' + \left[\sqrt{1 - \left(\frac{N_{ult,2}}{V_{pl,Rd,fl}} \right)^2} \right] M_{pl,Rd,fl}}{a' + b} \right\}$	812 kN (governing failure mode)
	Note: $a' = \lambda a$ for $1.25 < a/b \leq 2.25$	[18]
Mode C	$F_{U,C} = \frac{M_{pl,3} + M_{pl,Rd,fl,net}}{b} = \min \left\{ \frac{\left[1 - \left(\frac{N_{ult,3}}{N_{pl,Rd,sh}} \right)^2 \right] M_{pl,Rd,sh} + M_{pl,Rd,fl,net}}{b}, \frac{\left[1 - \left(\frac{N_{ult,3}}{V_{pl,Rd,fl}} \right)^2 \right] M_{pl,Rd,fl} + M_{pl,Rd,fl,net}}{b} \right\}$	868 kN
Mode D	$F_{U,D} = \frac{M'_{pl,2} + \Delta M_{pl,2} + M_{pl,3}}{b'_D}$	1051 kN
Mode E	$F_{U,E} = \frac{M_{pl,2} + M_{pl,3}}{b'_E}$	2344 kN

Note: (a) The coefficient 0.9 and the partial safety factors for the ultimate tensile resistance of bolts are neglected in this chapter. (b) a detailed explanation can be found in [19,20] and Appendix.

The parameters of the contact surface in the RFD connection were determined by the recommendations provided by Krutshinna [21]. It summarized that the gap depth has less influence on the carrying behaviour. For the sake of manufacturing reasons, the smallest possible recess height $h/2 = 2$ mm was selected. The optimized value of b_k can be approximated as $b_2/2$. The parameters shown in Fig. 3-6 (b) are specified as: $a_k = b_k = 50$ mm, $a_1 = 130$ mm, $b_1 = 55$ mm, $a_2 = 180$ mm, $b_2 = 105$ mm.

3.4.2 Boundary conditions and mesh

The mechanical boundary conditions specified for these connections are shown in Fig. 3-7. The reference points RP1 and RP2 in the centre of the associated surfaces are kinetically coupled to the surfaces at the end, respectively. Fixed support boundary conditions are applied on RP2. The segment is uniformly arranged along a shell cylinder in a full-scale tower. The constraints caused by neighbouring shells were ignored in the conventional segment approach in laboratory conditions. To investigate the effectiveness of the conventional segment approach, various constraints were set for the free side surfaces, namely with or without tangential symmetric boundary conditions (BCs). The segment continuity corresponds to the lateral boundary condition with tangentially symmetric BC. It should be noted that the influence of tube diameter is not included here. The ideal fully constrained boundary condition is assumed in this research. While the influence of tube diameter could be considered by modelling the segment with springs in hoop direction.

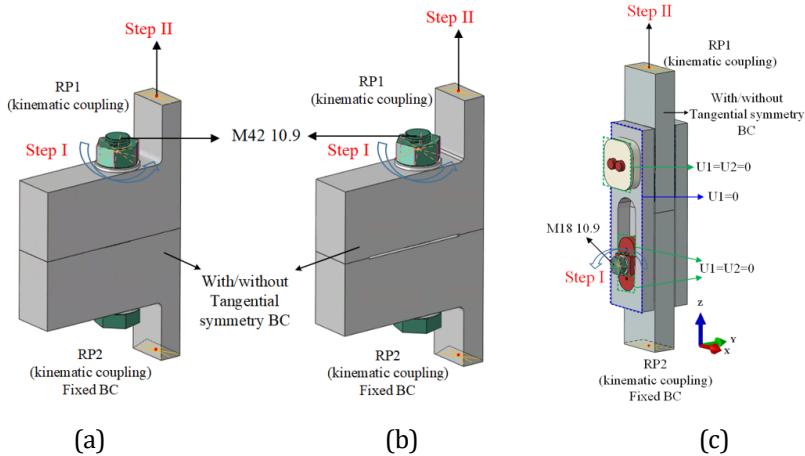


Fig. 3-7 Mechanical boundary conditions for various connections, (a) RF connection; (b) RFD connection; (c) C1-WC

Solid elements were used to model all components. The plate components were meshed using eight-node hexahedron linear solid elements with reduced integration (C3D8R). The machined components, namely the bolt, nut, threaded outer wedge, blocks and pin-bar with more complex geometry, were meshed with ten-node modified quadratic tetrahedron elements (C3D10M) to realize the free mesh. The detailed mesh for the C1-WC can be obtained from [9]. For the RF/RFD connections, the global size of

the solid elements in the bolt and nut is 8 mm, while in the threaded zone the element size is reduced to 3 mm. A global element size of 6 mm was used for the segments and flanges. The general contact method in ABAQUS/explicit was applied to all contact interactions [12]. The "hard" contact was defined in the normal direction to prevent penetration and tensile stress transfer across the interfaces. The tangential behaviour was modelled by a "penalty" frictional formulation which allows a relatively tiny movement between contact surfaces. The friction coefficient of 0.1 was used for all contacts in the FE models.

3.4.3 Computational procedure and loading

For each connection, two computation steps are carried out (see Fig. 3-7): bolt preloading (step I) and axial tensile loading along the Z direction (step II). The turn-of-nut method is used to apply the pretension bolt force [8]. As shown in Fig. 3-7, the hexagon edges of the nuts in the RF/RFD connections and the bolt head in the C1-WCs are kinematically connected to the reference point in their centre lines. Rotations of the reference points were applied along the axis of the bolt. The preloading forces in the bolt were obtained by measuring the contact pressure force at the inner washer surface. EN 1990-2 [22] states that the design bolt pretension force $F_{p,C}$ should be calculated using $F_{p,C} = \rho f_{ub} A_s$ ($\rho=0.70$), where f_{ub} is the ultimate tensile strength of the bolts and A_s is the tensile section area of the bolt. The partial safety factor was not considered in this chapter. Four different values of the preload coefficient ρ ranging from 0.25 to 0.70 were selected to investigate the effects of levels of F_p . Hence, various rotation angles were adopted to achieve different F_p , as shown in Table 3-2, Table 3-3, and Table 3-4. After preloading, axial tensile displacement along Z direction was implemented to RP1 at the top of the segment.

Table 3-2 Configuration details of FE models for RF connections

Specimen	ρ	$F_p = \rho f_{ub} A_s$ (kN)	Rotation (rad)	Boundary condition	Steel grade	Z _I (kN)	Z _U (kN)
RF-BC1-S460	0.70	825	2.10	BC1	S460	428	845
	0.55	649	1.64				
	0.40	472	1.19				
	0.25	295	0.75				
RF-BC2-S460	0.70	825	2.08	BC2	S460	428	853
	0.55	649	1.63				
	0.40	472	1.18				
	0.25	295	0.74				
RF-BC2-S355	0.70	825	2.12	BC2	S355	428	835
RF-BC2-S690	0.70	825	2.08		S690	428	883

Note: BC1-Without tangentially symmetric boundary condition; BC2- With tangentially symmetric boundary condition

Table 3-3 Configuration details of FE models for RFD connections

Specimen	ρ	$F_p = \rho f_{ub} A_s$ (kN)	Rotation (rad)	Boundary condition	Steel grade	Z_I (kN)	Z_U (kN)
RFD-BC1-S460	0.70	825	2.35	BC1	S460	543	843
	0.55	649	1.83				
	0.40	472	1.33				
	0.25	295	0.84				
RFD-BC2-S460	0.70	825	2.29	BC2	S460	543	853
	0.55	649	1.79				
	0.40	472	1.30				
	0.25	295	0.82				
RFD-BC2-S355	0.55	649	1.79	BC2	S355	427	835
RFD-BC2-S690	0.55	649	1.80		S690	427	882

Note: BC1-Without tangentially symmetric boundary condition; BC2- With tangentially symmetric boundary condition

Table 3-4 Configuration details of FE models for C1-WCs

Specimen	ρ	$F_p = \rho f_{ub} A_s$ (kN)	Rotation (rad)	Boundary condition	Steel grade	Z_I (kN)	Z_U (kN)
WC-BC1-S460	0.70	141	51.60	BC1	S460	762	817
	0.55	111	38.95				
	0.40	80	29.88				
	0.25	50	21.58				
WC-BC2-S460	0.70	141	49.59	BC2	S460	752	826
	0.55	111	38.05				
	0.40	80	29.19				
	0.25	50	21.27				
WC-BC2-S355	0.40	80	29.19	BC2	S355	221	682
WC-BC2-S690	0.40	80	29.19		S690	450	1032

Note: BC1-Without tangentially symmetric boundary condition; BC2- With tangentially symmetric boundary condition

An explicit solver was used to overcome the problem of convergence difficulties and enhance computational efficiency. After trial computations, a semi-automatic mass scaling option was used to shorten the computation time and guarantee the quasi-static analysis. The difference in the applied rotation between RF/RFD connections and C1-WCs is obvious. In contrast to applying pretension force in the bolt to clamp the flanges in RF/RFD connections, the horizontal bolt in the C1-WCs causes the movement of two wedges. Under applying the same rotation, the resulting bolt extension in RF/RFD connections is much larger than that in the C1-WCs. It is reported that the bolt head rotation of 2.8 rad only generates a 10 kN increment in F_p in C1-WCs from chapter 2. Consequently, the target time increment and period are different during the simulation for these connections. The target time increment for RF/RFD connections was set to be 0.5×10^{-6} s. The associated periods adopted for preloading and loading to failure steps are 0.1 s and 0.05 s, respectively. For the C1-WC, the time increment is set as 1.0×10^{-6} s. The periods for preloading and tensile loading are 2.5 s and 0.25 s, respectively.

3.4.4 Material models

Table 3-5 provides a list of the mechanical characteristics of the materials utilized in the FE model. Four kinds of material were introduced for major components in FE models, and they are displayed by different colours in Fig. 3-7. Three steel grades (S355/S460/S690) are specified for plate component to quantify the effect of steel strength on the mechanical performance of connections. The washer and pin connection parts were modelled as an elastic material, while elastic-plastic material was used to model other components. As insignificant plastic deformation occurs in machined parts in C1-WCs, the material behaviour of fastener assembly is represented by an idealized trilinear elastic-plastic hardening model, as shown in Fig. 3-8. Nominal material properties were adopted according to EN 10025-6 [23]. Engineering stress-strain curves were transformed into true stress-strain curves as input data in the ABAQUS plasticity model [24].

Table 3-5 Material properties adopted in FE models [23–25]

Components	Color	Material	E_0 (MPa)	f_y (MPa)	f_u (MPa)	ϵ_u	A	W	α	β
Washer/pin connection	White	Elastic	2.10e5	-	-	-	-	-	-	-
Fastener assembly	Red	34CrNiMo6	2.10e5	620	800	-	0.15	-	-	-
Bolt/nut	Green	10.9	2.10e5	957	1062	0.050	0.10	0	2	1.5
Plate	Grey	S355	2.10e5	375	517	0.175	0.32	0.1	1.8	
		S460	2.10e5	485	620	0.125	0.23	0	1.4	1.5
		S690	2.05e5	746	785	0.061	0.15	-0.4	1.3	

Note: E_0 – Young’s modulus; f_y and f_u is yield strength and ultimate strength, respectively; ϵ_u - the strain corresponding to ultimate strength; A - the ultimate elongation; W – weighting factor in full-range true stress-strain constitutive material model; α and β are two material-dependent parameters in Rice-Tracy fracture criterion.

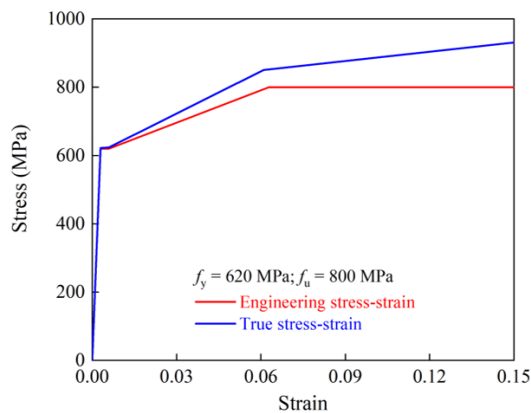


Fig. 3-8 Stress-strain curves for 34CrNiMo6 material [25]

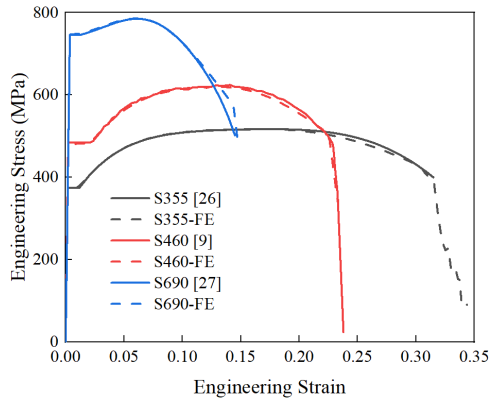


Fig. 3-9 Comparison between experimental and numerical engineering stress-strain curves [9,26,27]

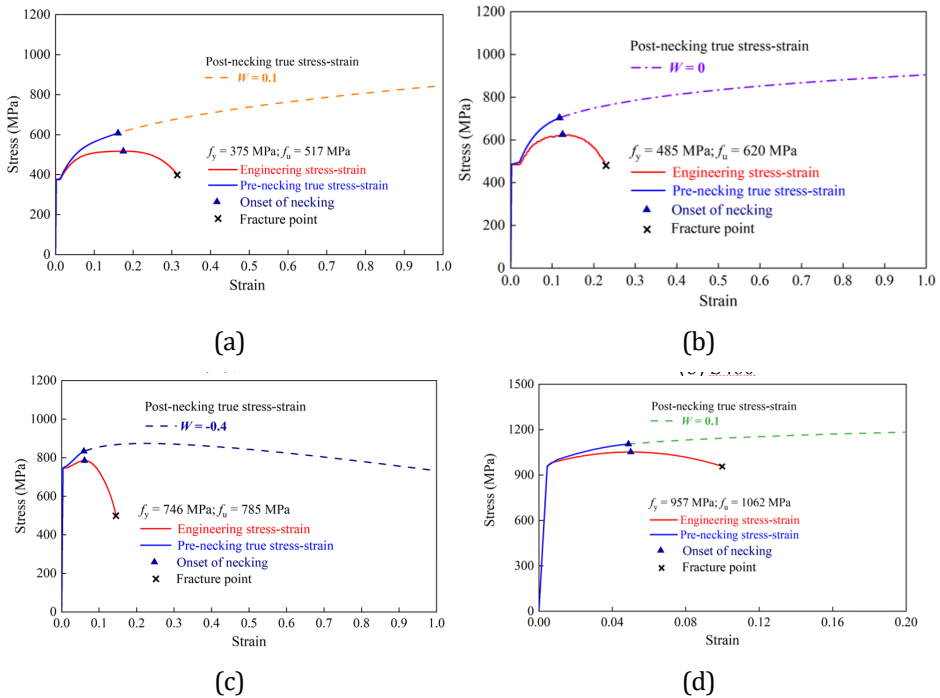


Fig. 3-10 Stress-strain curves of the critical parts in FE models; (a) S355; (b) S460; (c) S690; (d) Bolt Grade 10.9

The full-range stress-strain constitutive model and ductile damage model were used for plate components and bolts. The post-necking behaviour of the metal material can be successfully described by a combined linear and power law stress-strain law [24,28,29]. The only unknown variable, namely the weighting factor W , was calibrated using the measured material property. To accurately simulate the failure mode of connections, a

ductile damage model based on Rice-Tracey (RT) function was employed in this chapter [30,31]. Two material-dependent parameters α and β were calibrated by matching the engineering stress-strain curves obtained from test results [9,26,27,32], see Fig. 3-9. It should be noted that the material property of the bolt is obtained based on the assumption of a parabolic shape of the engineering stress-strain curve [8]. The curves can be drawn with measured yield strength and ultimate strength and the ultimate elongation $A = 10\%$ according to ISO 898-1 [33]. Fig. 3-10 shows the calibrated full-range stress-strain curves for the materials specified for plate components and bolts.

3.4.5 Validation of FE method

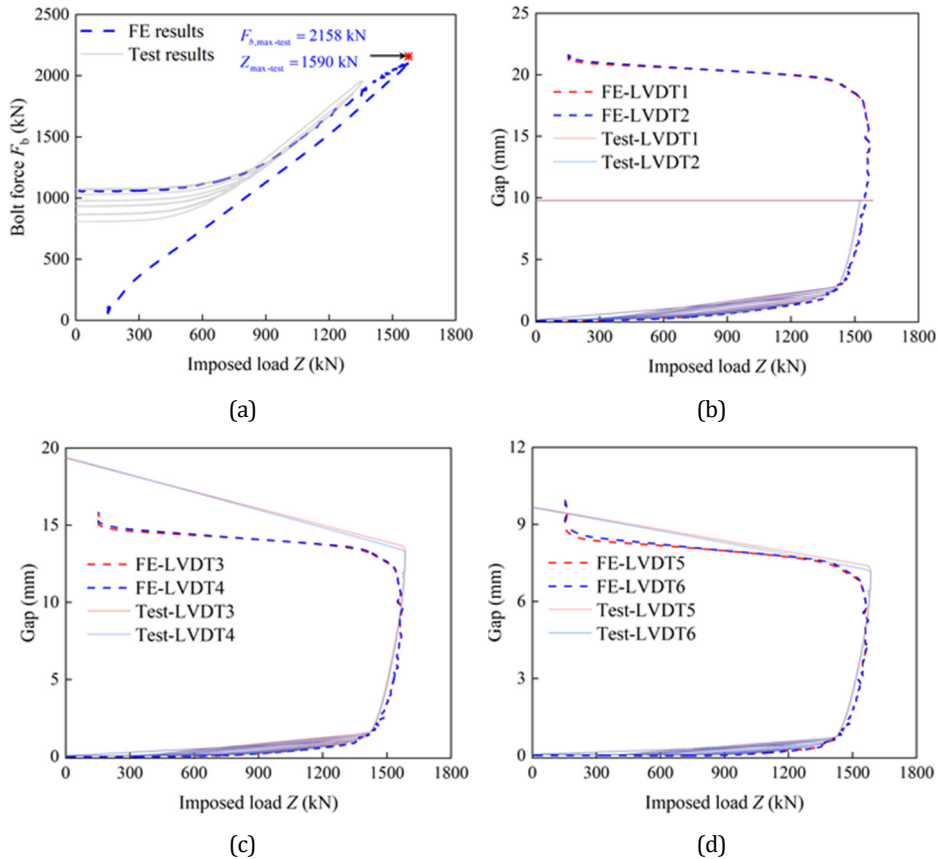


Fig. 3-11 Comparison between FE and test results of RF connections; (a) Bolt force F_b ; (b) Gap at LVDT1/2; (c) Gap at LVDT3/4; (d) Gap at LVDT5/6

The developed FE method for C1-WCs has been demonstrated in chapter 2. As mentioned before, the FE simulation method for RF/RFD connection was validated by the test results described in Section 3.3. In the test, after applying 5 cyclic loads via force control, the specimen was loaded to final failure via displacement control. An FE model

with identical geometry and boundary conditions to the test was established. Uniaxial tensile load applied in the cross-section of the upper segment was used in FE simulation for simplification. Comparisons were made between the numerical and experimental ultimate load capacity, bolt force evolution, and local deformation, as illustrated in Fig. 3-11. After the bolt exceeds its yield strength ($F_b > 1942$ kN), the actual experimental bolt force was not available from the used strain gauges. This is because the strain is not proportional to the bolt force outside the elastic region. The maximum bolt force $F_{b,max-test}$ was calculated according to the established simple analytical model: $F_{b,max-test} \times a = Z_{max-test} \times (a+e)$. a is the distance from the bolt axis to the flange edge, and e is the distance from the bolt axis to the shell mid plane at final fracture. The ultimate capacity of the specimen ($Z_{max-test}$) and the bolt ($F_{b,max-test}$) are also shown in Fig. 3-11 (a). It is found that the FE model can accurately predict the strength of the specimen and the bolt. As plotted in Fig. 3-11 (b)-(d), the simulated gap curves provide relatively good agreements with the envelope of the test results. The difference shown in Fig. 3-11 (b) is because LVDT1 and LVDT2 went out of range (10 mm) before the ultimate tensile strength during the test. Both experimental and numerical results show the bolt failure mode. Therefore, it is concluded that the FE simulation method for the RF connection realistically predicts the mechanical behaviour of this connection.

3.5 PARAMETRIC STUDIES ON TENSILE BEHAVIOUR

In this section, the influence of important parameters on the behaviour of connections under static loading was assessed based on the validated FE method. The parameters include the lateral boundary condition on the sides of the segment/flange in hoop direction (BC1/BC2), preload coefficient ρ (0.70, 0.55, 0.40, and 0.25), and the steel strength (S355, S460, and S690).

3.5.1 Effect of BC1/BC2

The FE models with the preload coefficient $\rho = 0.7$ were taken as the benchmark to analyse the effects of lateral boundary conditions. The detailed results are summarized in Table 3-2 and Fig. 3-12 represents the effect of BC1/BC2 on the behaviour of RF and RFD connections, namely specimens RF-BC1/BC2-S460 and RFD-BC1/BC2-S460. An insignificant variation was found between RF-BC1-S460 and RF-BC2-S460 in terms of load-displacement curves, evolution curves of bolt force, and gap between segments in the back view (see Fig. 3-12 (a), (c), and (e)). A similar observation is found for RFD-BC1-S460 and RFD-BC2-S460. These imply that the lateral boundary conditions have little influence on the tensile performance of RF and RFD connections. The circumferential stress generated under BC2 has negligible influence on the static tensile behaviour of RF/RFD connections. It is reasonable to use the segment approach to represent their static performance without considering imperfections. The bolt force evolution calculated using the proposed analytical models is included in Fig. 3-12 (c) and (d) to strengthen the reliability of the FE models. It is found that the Schmidt/Neuper estimation is conservative as reported in [2], which is accepted to

contain the detrimental influence of imperfections. The development of F_b obtained from analytical models for RFD connections agrees well with the FE results.

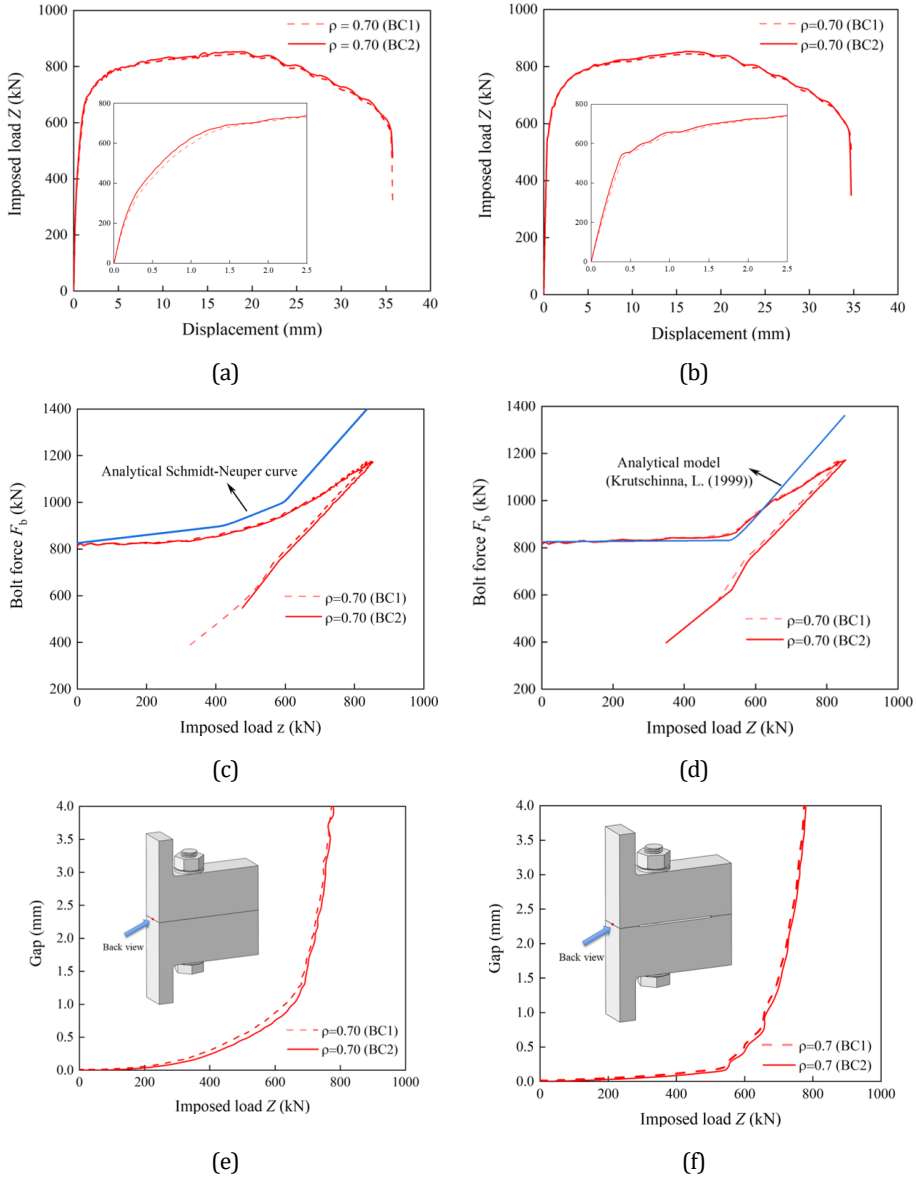


Fig. 3-12 Comparison of RF and RFD connections: (a) and (b) load-displacement curves; (c) and (d) bolt force evolution curves; (e) and (f) gap; ((a), (c), (e): RF-BC1/BC2-S460; (b), (d), (f): RFD-BC1/BC2-S460)

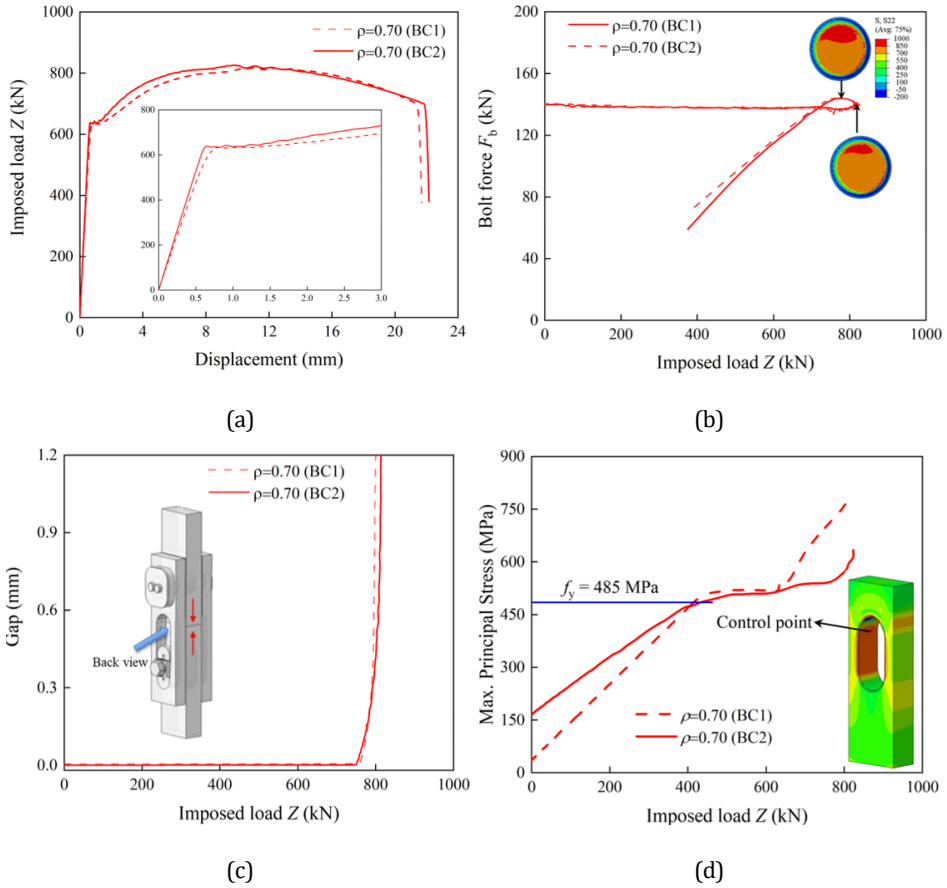


Fig. 3-13 Comparison between WC-BC1/BC2-S460; (a) Load-displacement curves; (b) Evolution curves of bolt force; (c) Gap; (d) Maximum principal stress

Fig. 3-13 illustrates the comparison between WC-BC1-S460 and WC-BC2-S460. A noticeable contrast begins at the yield plateau in the load-displacement curves and continues until the approximate peak load (see Fig. 3-13 (a) and Table 3-4). The evolution curves of bolt force and gap between the segments in the back view exhibit almost identical behaviour with BC1 and BC2, see Fig. 3-13 (b) and (c). It is reported that the lower block in C1-WC is subjected to bending as it spans two cover plates and the lower segment [34]. After reaching the ultimate capacity, the obvious deformation in the lower segment results in increased bending in the lower block and the bolt. The axial force distribution in the middle cross-section of the bolt is displayed in Fig. 3-13 (b). With the significantly increased deformation in the lower segment, the contact between the lower wedge connection and the lower segment is lost followed by suddenly decreasing bolt force. A control point is located at the transition region in the lower segment instead of the bolt from FE results. The maximum principal stress $\sigma_{pri,max}$ at this point until the maximum strength was extracted as shown in Fig. 3-13 (d). It is

found that $\sigma_{pri,max}$ increases linearly until reaching the yield limit strength f_y . With increasing imposed load, $\sigma_{pri,max}$ of WC-BC1-S460 exhibits a faster increase rate with a smaller initial value compared to that of WC-BC2-S460.

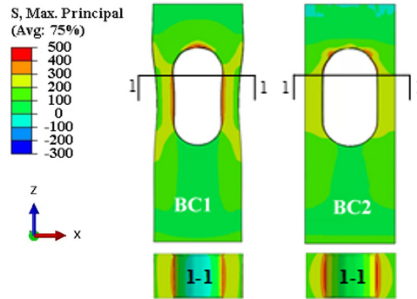


Fig. 3-14 Deformation and stress response of WC-BC1/BC2-S460 under $Z=240$ kN

To better reflect the effect of BC1/BC2, the deformation and stress response of the lower segment under the imposed load of 240 kN is shown in Fig. 3-14 as an example. The stress distribution at a certain cross-section of the hole is also displayed in Fig. 3-14. The deformation along X direction is magnified by a factor of 50. It is seen that the distribution of $\sigma_{pri,max}$ is heavily influenced by BC1 and BC2. Moreover, the distribution of $\sigma_{pri,max}$ along the centre line of the half oval hole is represented in Fig. 3-15. The negative maximum principal stress occurring between $0^\circ - 25^\circ$ is attributed to the compression force between the upper block and the lower segment at this region. The diagrams show that BC1 causes a more uniform distribution of stress response in the C1-WC. This could explain why the value of $\sigma_{pri,max}$ of WC-BC1-S460 at the control point (see Fig. 3-13 (d)) is smaller than the WC-BC2-S460 before reaching yield strength.

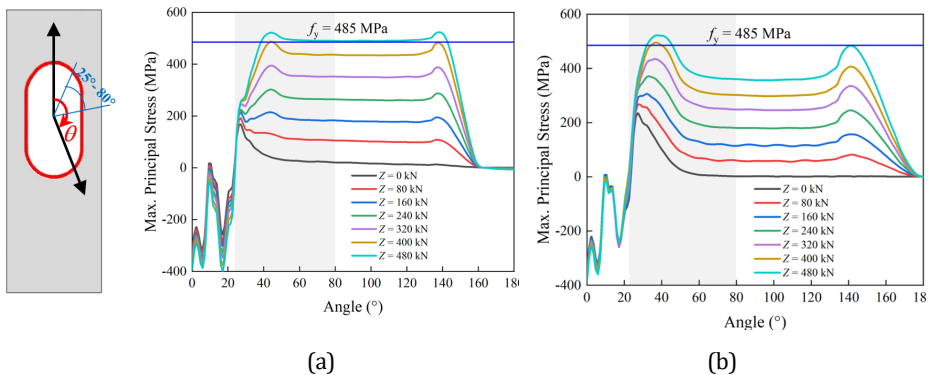


Fig. 3-15 Distribution of max principal stress of C1-WCs under BC1/BC2; (a) WC-BC1-S460; (b) WC-BC2-S460

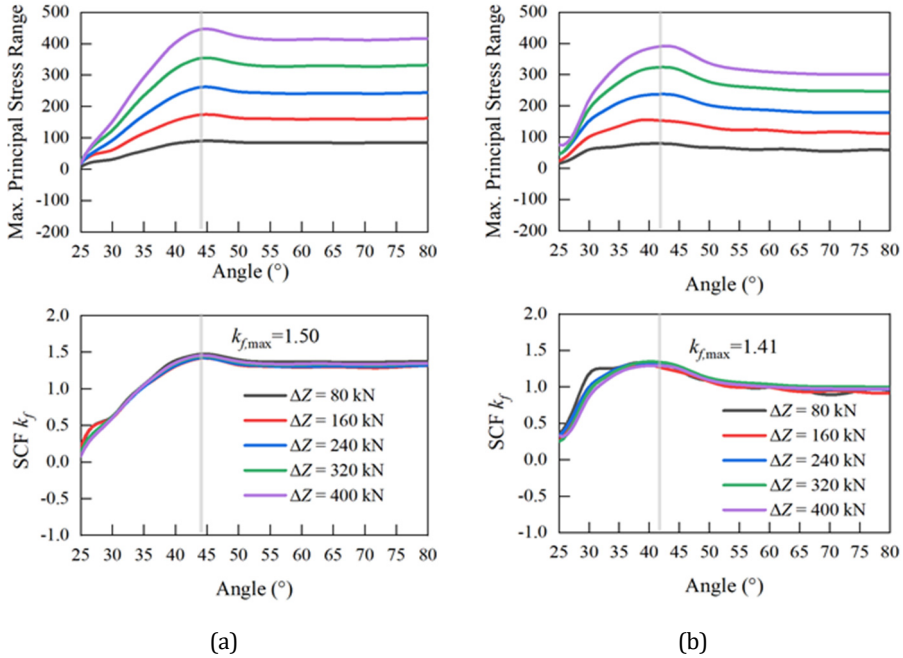


Fig. 3-16 Comparison of maximum principal stress range and SCF for WC-BC1/BC2-S460 (a) WC-BC1-S460 (b) WC-BC2-S460

Analysing the range of maximum principal stress $\Delta\sigma_{\text{pri,max}}$ and the stress concentration factor (SCF) k_f is crucial to identify the most vulnerable regions under fatigue in the lower segment in C1-WCs. To eliminate the influence of the initial stress introduced by various pretension levels (see Table 3-4), SCF is defined as the ratio of $\Delta\sigma_{\text{pri,max}}$ to the nominal stress for this connection. The grey shadow area marked in Fig. 3-15 is located between the angle 25° - 80° . Fig. 3-16 displays the response of $\Delta\sigma_{\text{pri,max}}$ and k_f in these localized regions, where $Z = 0$ kN is selected as the reference. As shown in Fig. 3-16, the position of the peak $\Delta\sigma_{\text{pri,max}}$ differs under BC1 and BC2. The $k_{f,\text{max}}$ corresponding to peak $\Delta\sigma_{\text{pri,max}}$ was obtained as 1.50 and 1.41 for WC-BC1-S460 and WC-BC2-S460, respectively. The $\Delta\sigma_{\text{pri,max}}$ and k_f under BC1 are higher than those under BC2. This is because the circumferential continuity (hoop stresses) causes increasing triaxiality followed by the larger SCF. This implies that the stress response in the lower segment of C1-WCs is greatly influenced by “circumferential” boundary conditions.

3.5.2 Effect of pretension level (coefficient ρ)

The effect of pretension level on the behaviour of RF, RFD, and C1-WC is shown in Fig. 3-17 and Fig. 3-18. The results of connections with BC2 are selected for comparison. The initial stiffness of these connections is degraded with reduced ρ (see Fig. 3-17 (a) and (b), Fig. 3-18 (a)). For RF and RFD connections with insufficient pretension force, the obvious rise of the bolt force F_b and gap appears earlier together with the lower critical value Z_i (see Table 3-2 and Table 3-3) As shown in Table 3-4 and Fig. 3-18 (b), Z_i

corresponding to the abruptly appearing gap between segments in C1-WCs also decreases with reduced ρ . It should be noted that the ultimate capacity Z_U for all types of connections is not related to the pretension level.

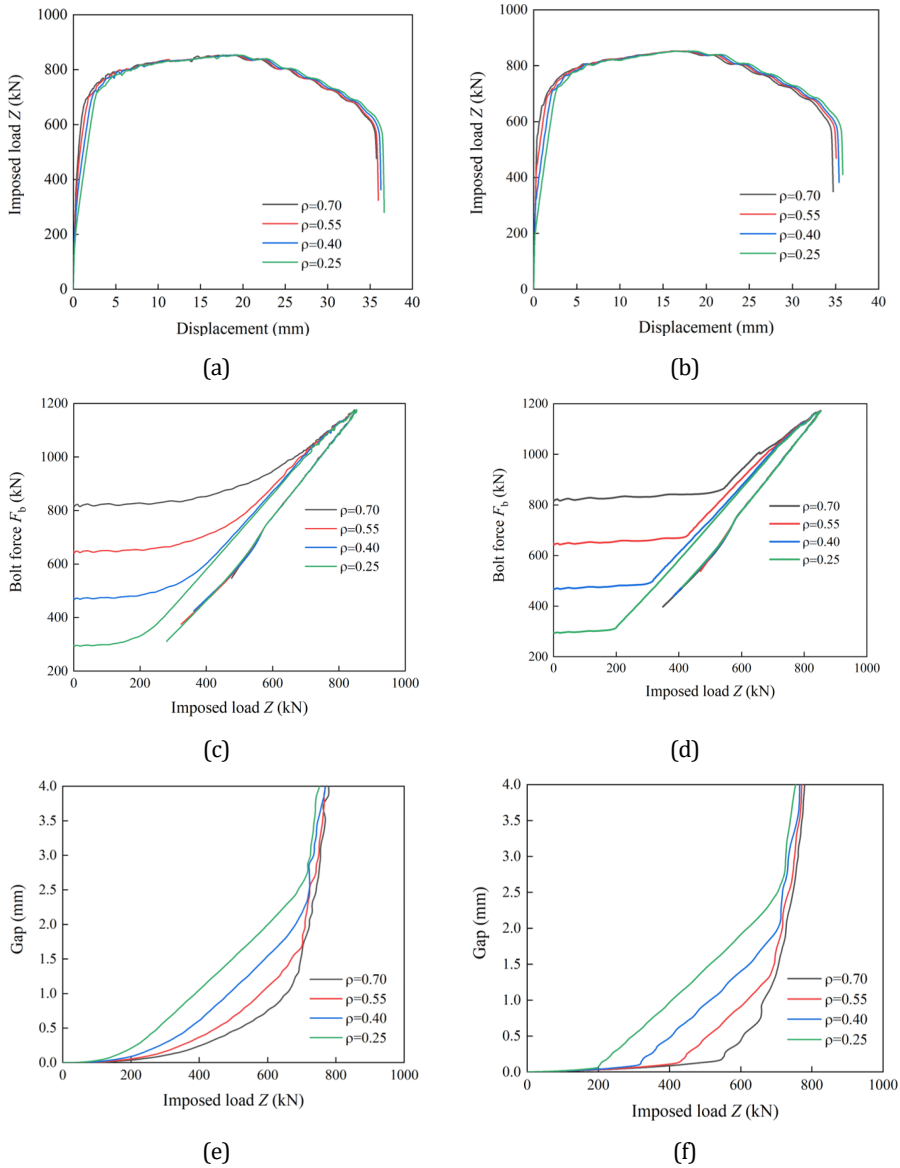


Fig. 3-17 Comparison of RF/RFD connections under various preload coefficient: (a) and (b) load-displacement curves, (c) and (d) bolt force evolution curves, and (e) and (f) gap; (a), (c), (e): RF-BC2-S460; (b), (d), (f) RFD-BC2-S460)

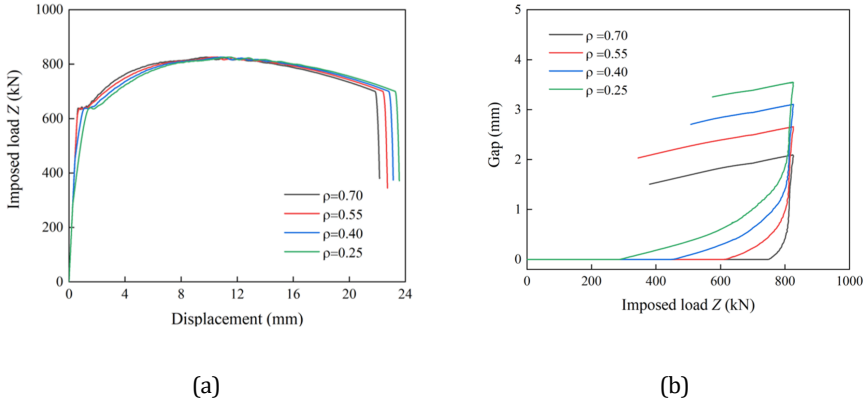


Fig. 3-18 Comparison of WC-BC2-S460 under various preload coefficient; (a) Load-displacement curves; (b) Gap

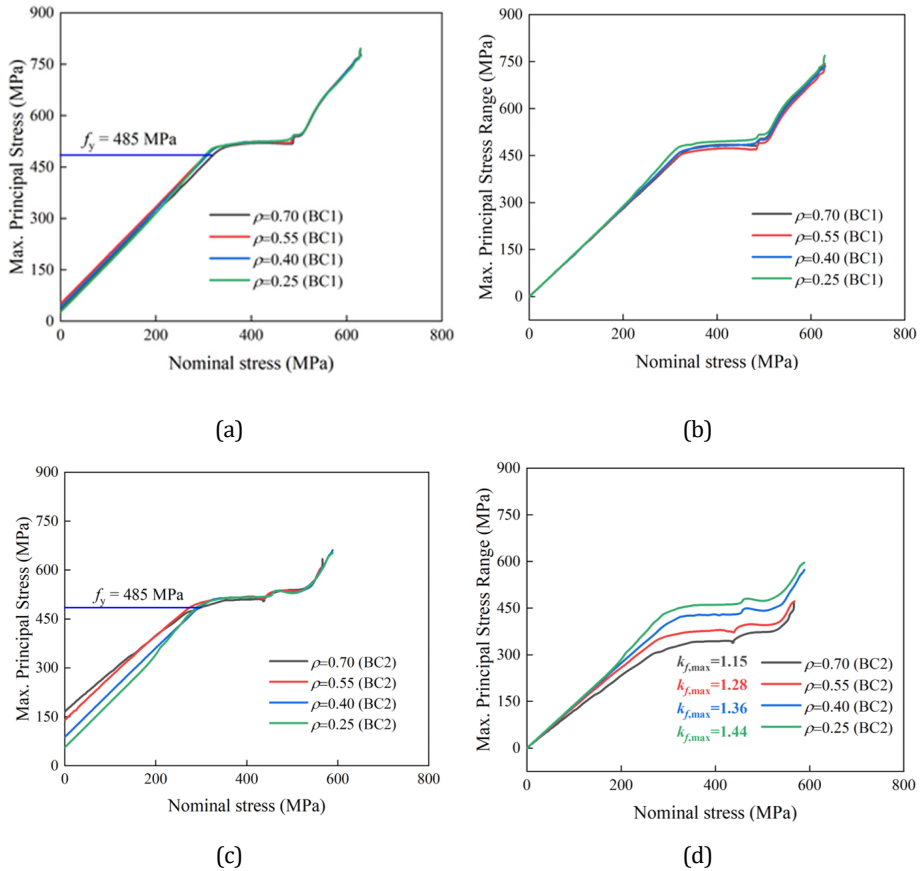
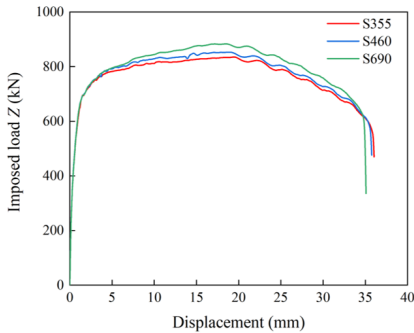


Fig. 3-19 Response of maximum principal stress of C1-WCs under various BC and ρ : (a) $\sigma_{pri,max}$ of WC-BC1-S460; (b) $\Delta\sigma_{pri,max}$ of WC-BC1-S460; (c) $\sigma_{pri,max}$ of WC-BC2-S460; (d) $\Delta\sigma_{pri,max}$ of WC-BC2-S460

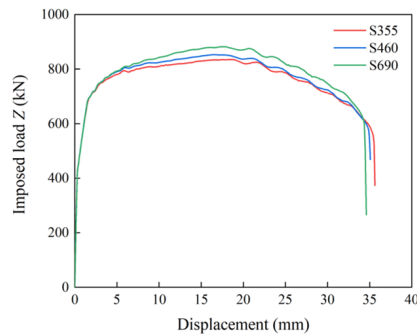
Fig. 3-19 compares the response of maximum principal stress at the control point of C1-WCs under various boundary conditions and preload coefficient ρ . It is interesting to find that the stress response of WC-BC1-S460 is approximately consistent under various ρ , see Fig. 3-19 (a) and (b). However, a larger ρ in WC-BC2-S460 generates a higher initial value of $\sigma_{pri,max}$ after preloading and a lower SCF $k_{f,max}$ before yielding strength. The lowest $\Delta\sigma_{pri,max}$ and $k_{f,max}$ of WC-BC2-S460 with $\rho = 0.70$ demonstrate the benefits of sufficient pretension level in C1-WCs. These results also necessitate the importance of investigating the lateral boundary conditions.

3.5.3 Effect of steel strength

To quantify the influence of various steel grades, the mechanical behaviour of RF and RFD connections with identical Z_l and boundary conditions are compared in this section. According to the analytical models, Z_l of RF connections with $\rho = 0.7$ is calculated as 428 kN which is equal to that of RFD connections with $\rho = 0.55$. Fig. 3-20 displays the comparison analysis between RF and RFD connections made of various steel grades. The governing failure mechanism is the plastic hinge in the shell/flange and the failure of the bolt. The ultimate resistance is increased by using higher steel grade for shell and flanges (Fig. 3-20 (a) and (b)). As presented in Fig. 3-20, the curves separate after reaching the imposed load of 720 kN both for RF and RFD connections. It is found that the nominal bolt stress exceeds the yield strength of bolts of 957 MPa. This implies that the imposed load is resisted by the introduced contact force between flanges after bolt pretension, bolts, and the segments/flanges sequentially. Before bolts yield, the major function of the shell and flange is to transfer the external load. The steel strength has no influence on the initial stage of the bolt force development and gap behaviour for the RF/RFD connection. This is verified by the FE results displayed in Fig. 3-20 (c)-(f).



(a)



(b)

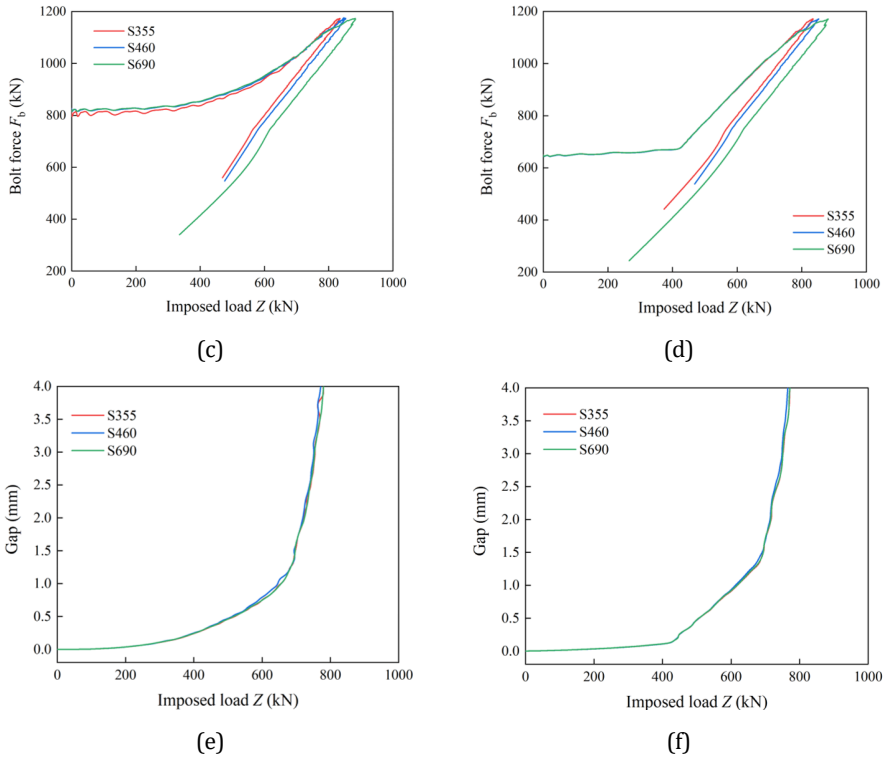


Fig. 3-20 Comparison of RF/RFD connections made of various steel grades: (a) and (b) load-displacement curves, (c) and (d) bolt force evolution curves, and (e) and (f) gap; ((a), (c), (e): RF-BC2-S355/460/690; (b), (d), (f): RFD-BC2-S355/460/690)

Fig. 3-21 shows a comparison between WC-BC2-S355, WC-BC2-S460, and WC-BC2-S690. The design value of the critical load Z_i is 450 kN. The segments in C1-WCs are the dominant part to resist the imposed load, instead of the bolt in the RF and RFD connections. Therefore, these three specimens behave differently in terms of the load-displacement curves, gap opening, and stress response. It is seen that the gap of WC-BC2-S355 develops much earlier than the other two specimens (Fig. 3-21 (b)). Under the designed critical load Z_i , the maximum principal stress of WC-BC2-S355 is around 400 MPa representing the appearance of developed plastic deformation, as shown in Fig. 3-21 (c). It is required that the connections are in the elastic stage, e.g. below the critical load Z_i load. The steel grade lower than S355 is not enough to satisfy the requirement. Therefore, it is suggested that the yield strength of steel grade in C1-WCs should be larger than $Z_i/A_{s,wc}$ for design, where $A_{s,wc}$ is the smallest net cross-section area of the lower segment.

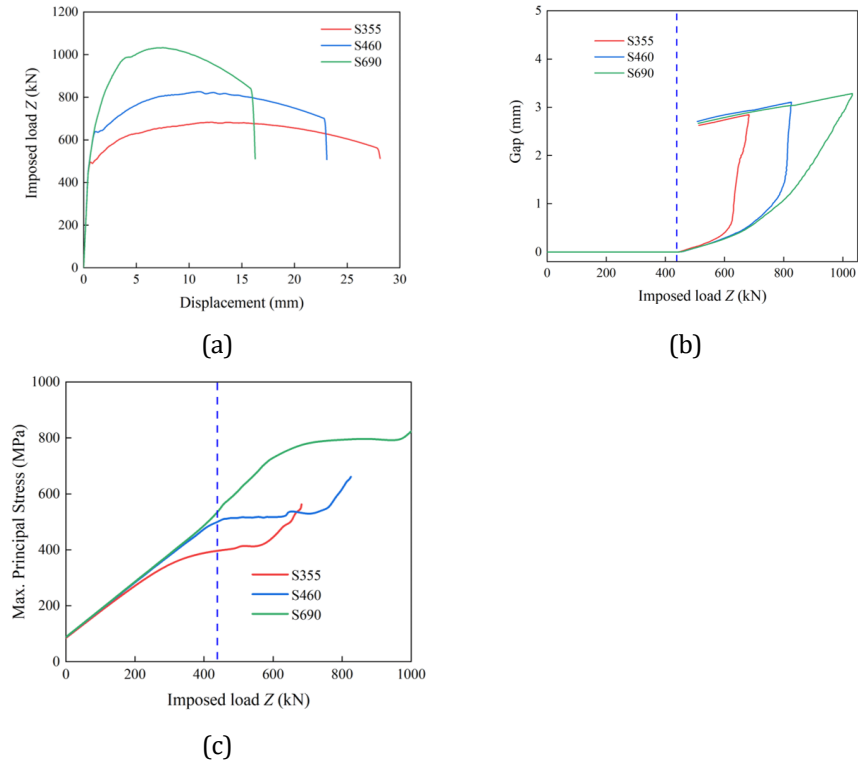


Fig. 3-21 Comparison of C1-WCs made of various steel grades; (a) Load-displacement curves; (b) Gap; (c) Maximum principal stress

3.6 PARAMETRIC STUDIES ON FATIGUE PERFORMANCE

The fatigue life of the RF and RFD connections is dependent on the fatigue resistance of the bolt corresponding to the fatigue detail category (FAT) of 50 (including the bending stresses) [35,36]. For bolts with a diameter of more than 30 mm, a reduction factor should be introduced when determining their fatigue resistance. FAT 46 is obtained for the RF/RFD connections with M42 bolts. Charlton [37] summarized that 65% of fatigue failure of bolts occurs in the root of the first loaded thread, 15% at the bolt head to shank radius, and 20% at the thread run-out. According to recent practical application, almost all fatigue failure of the bolt assembly occurs in the first engaged thread. Fig. 3-22 displays the distribution of the stress response along the bolt length of RF-BC2-S460. The location of the critical point and the trend of the bending moment are consistent with the previous chapter. The bending moment range of the bolt (ΔM) at this critical position is extracted from FE results. The stress range of RF and RFD connections is calculated as $\Delta\sigma = \Delta F_b / A_{s,bolt} + 2 \cdot \Delta M \cdot d_{bolt} / I_{bolt}$, where $A_{s,bolt}$ is the tensile stress area of the bolt, d_{bolt} is the effective diameter of the bolt, and I_{bolt} is the moment of inertia of the bolt. The axial force F_b and bending moment M were extracted using a free body cut with 100

slicing along the bolt length. A smooth curve is then produced using a cubic smoothing spline to mitigate the effect of scattering.

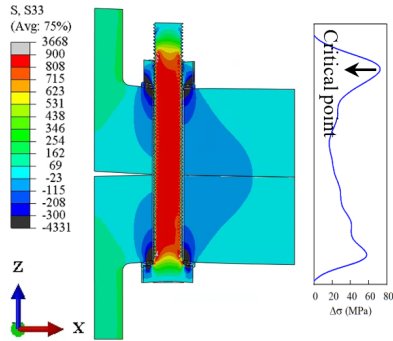


Fig. 3-22 Critical position in RF-BC2-S460 with $\rho=0.70$ under $Z=400$ kN

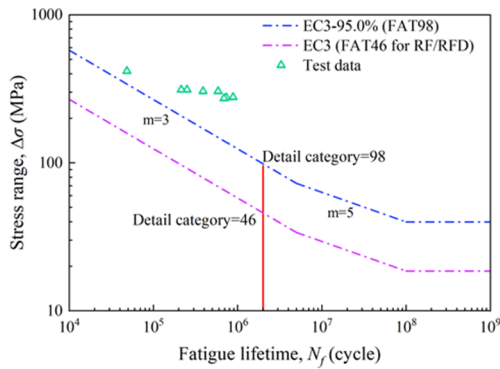


Fig. 3-23 S-N curves for C1-WCs

Referring to C1-WC, a log-log relation between stress range and fatigue life is obtained as $\log_{10}(N) = 12.282 - 3 \times \log_{10}(\Delta\sigma)$ with 75% confidence level and 95% probability of survival based on the scaled segment fatigue tests. The fatigue life S-N curves employed to evaluate the fatigue performance of the connections are shown in Fig. 3-23. The detail category $\Delta\sigma_c$ is predicted as 98 according to the definition in [35]. It should be noted a more comprehensive FLS assessment is required to confirm the detail category for C1-WC. The analyses in Section 3.5.1 show that the stress response of C1-WCs is significantly influenced by BC1/BC2, pretension force level, and steel strength. Therefore, an evaluation of the fatigue life of C1-WCs is presented. The range of maximum principal stress $\Delta\sigma_{pri,max}$ was used for calculating the fatigue resistance. In that case, the detail category incorporated with the stress concentration factor k_f should be used. k_f varies with different pretension levels under BC2. For simplification, $k_f = 1.5$ was used and the detail category FAT 98 was substituted by FAT 147 when using $\Delta\sigma_{pri,max}$ as the stress range. The results of the stress range in three connections under five nominal stress ranges ($\Delta\sigma_{seg} = 25, 51, 76, 102, 127$ (MPa)) applied to the top of the

upper segment are shown in Table 3-6, Table 3-7, and Table 3-8. The calculated stress ranges are then used to compute the related fatigue life. Results including the ratio between the fatigue life under BC1 and BC2 (N_{BC1}/N_{BC2}) are displayed in Table 3-9, Table 3-10 and Table 3-11. The infinite fatigue life in tables is replaced as definite fatigue life as 10^8 .

Table 3-6 Determined stress range $\Delta\sigma$ (MPa) of RF connections for different nominal stress ranges

ρ	Boundary condition	Nominal stress range $\Delta\sigma_{seg}$ (MPa)				
		25	51	76	102	127
0.70	BC1	6.0	8.0	27.1	39.3	73.0
	BC2	1.2	14.8	27.1	39.5	74.0
0.55	BC1	2.9	17.9	36.2	74.0	103.0
	BC2	3.4	18.1	36.1	69.6	102.8
0.40	BC1	6.7	24.4	61.3	109.3	185.5
	BC2	5.8	23.9	60.6	99.9	176.8
0.25	BC1	16.0	49.6	109.0	234.6	369.7
	BC2	14.9	46.8	103.4	223.3	358.8

Table 3-7 Determined stress range $\Delta\sigma$ (MPa) of RFD connections for different nominal stress ranges

ρ	Boundary condition	Nominal stress range $\Delta\sigma_{seg}$ (MPa)				
		25	51	76	102	127
0.70	BC1	15.9	17.4	35.5	36.2	36.4
	BC2	11.1	16.4	35.6	36.1	37.6
0.55	BC1	16.6	17.9	33.4	37.0	46.4
	BC2	9.7	17.3	34.4	39.0	49.2
0.40	BC1	13.9	23.5	35.3	69.9	172.9
	BC2	11.7	23.4	37.2	70.2	175.3
0.25	BC1	13.7	26.7	107.9	229.5	339.5
	BC2	11.4	26.9	105.8	232.4	355.5

Table 3-8 Determined stress range $\Delta\sigma_{pri,max}$ (MPa) of C1 WCs for different nominal stress ranges

ρ	Boundary condition	Nominal stress range $\Delta\sigma_{seg}$ (MPa)				
		25	51	76	102	127
0.70	BC1	95.4	181.8	274.7	375.1	470.2
	BC2	80.5	155.5	242.7	332.8	403.9
0.55	BC1	93.7	180.1	273.9	373.5	470.4
	BC2	81.5	160.8	245.8	321.7	409.5
0.40	BC1	92.5	178.9	272.5	371.8	462.3
	BC2	81.4	160.9	247.0	323.8	412.9
0.25	BC1	93.0	179.7	270.6	372.5	476.4
	BC2	82.0	161.3	274.8	335.1	424.0

Table 3-9 Fatigue life N of RF connections in number of cycles

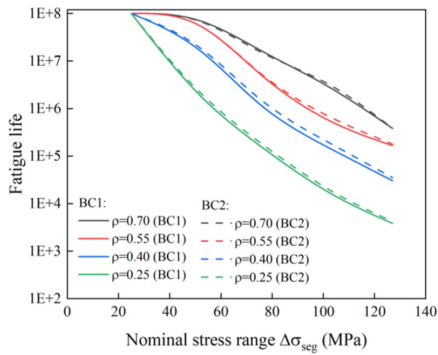
ρ	Boundary condition	Nominal stress range $\Delta\sigma_{seg}$ (MPa)				
		25	51	76	102	127
0.70	BC1	$>10^8$	$>10^8$	1.52×10^7	3.20×10^6	4.99×10^5
	BC2	$>10^8$	$>10^8$	1.54×10^7	3.16×10^6	4.79×10^5
	N_{BC1}/N_{BC2}	-	-	0.99	1.01	1.04
0.55	BC1	$>10^8$	$>10^8$	4.09×10^6	4.79×10^5	1.78×10^5
	BC2	$>10^8$	$>10^8$	4.12×10^6	5.76×10^5	1.79×10^5
	N_{BC1}/N_{BC2}	-	-	0.99	0.83	0.99
0.40	BC1	$>10^8$	2.57×10^7	8.43×10^5	1.49×10^5	3.04×10^4
	BC2	$>10^8$	2.89×10^7	8.73×10^5	1.95×10^5	3.52×10^4
	N_{BC1}/N_{BC2}	-	0.89	0.97	0.76	0.87
0.25	BC1	$>10^8$	1.59×10^6	1.50×10^5	1.50×10^4	3.84×10^3
	BC2	$>10^8$	1.89×10^6	1.76×10^5	1.74×10^4	4.20×10^3
	N_{BC1}/N_{BC2}	-	0.84	0.85	0.86	0.91

Table 3-10 Fatigue life N of RFD connections in number of cycles

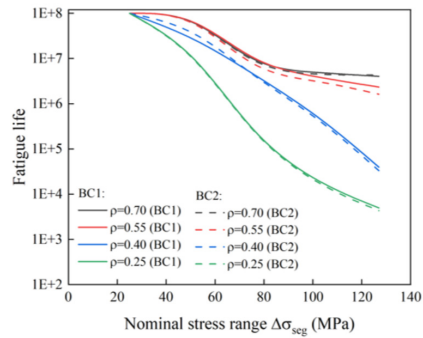
ρ	Boundary condition	Nominal stress range $\Delta\sigma_{seg}$ (MPa)				
		25	51	76	102	127
0.70	BC1	$>10^8$	$>10^8$	4.36×10^6	4.10×10^6	4.04×10^6
	BC2	$>10^8$	$>10^8$	4.30×10^6	4.13×10^6	3.65×10^6
	N_{BC1}/N_{BC2}	-	-	1.01	0.99	1.10
0.55	BC1	$>10^8$	$>10^8$	5.38×10^6	3.83×10^6	1.94×10^6
	BC2	$>10^8$	$>10^8$	4.76×10^6	3.28×10^6	1.63×10^6
	N_{BC1}/N_{BC2}	-	-	1.13	1.17	1.19
0.40	BC1	$>10^8$	3.09×10^7	4.42×10^6	5.69×10^5	3.76×10^4
	BC2	$>10^8$	3.21×10^7	3.78×10^6	5.62×10^5	3.61×10^4
	N_{BC1}/N_{BC2}	-	0.96	1.17	1.01	1.04
0.25	BC1	$>10^8$	1.65×10^7	1.54×10^5	1.61×10^4	4.96×10^3
	BC2	$>10^8$	1.58×10^7	1.64×10^5	1.55×10^4	4.32×10^3
	N_{BC1}/N_{BC2}	-	1.05	0.94	1.04	1.15

Table 3-11 Fatigue life N of C1-WCs in number of cycles

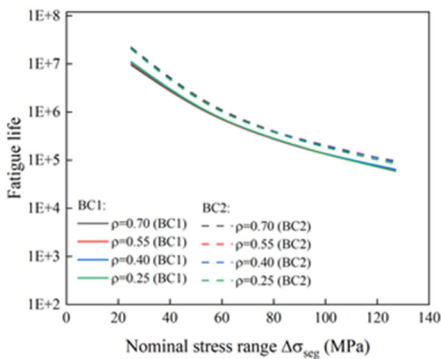
ρ	Boundary condition	Nominal stress range $\Delta\sigma_{seg}$ (MPa)				
		25	51	76	102	127
0.70	BC1	9.47×10^6	1.06×10^6	3.07×10^5	1.20×10^5	6.11×10^4
	BC2	2.21×10^7	1.69×10^6	4.45×10^5	1.72×10^5	9.64×10^4
	N_{BC1}/N_{BC2}	0.43	0.63	0.69	0.70	0.63
0.55	BC1	1.03×10^7	1.09×10^6	3.09×10^5	1.22×10^5	6.10×10^4
	BC2	2.08×10^7	1.53×10^6	4.28×10^5	1.91×10^5	9.25×10^4
	N_{BC1}/N_{BC2}	0.50	0.71	0.72	0.64	0.66
0.40	BC1	1.10×10^7	1.11×10^6	3.14×10^5	1.24×10^5	6.43×10^4
	BC2	2.09×10^7	1.53×10^6	4.22×10^5	1.87×10^5	9.02×10^4
	N_{BC1}/N_{BC2}	0.53	0.73	0.75	0.66	0.71
0.25	BC1	1.07×10^7	1.09×10^6	3.21×10^5	1.23×10^5	5.88×10^4
	BC2	2.02×10^7	1.51×10^6	4.18×10^5	1.69×10^5	8.34×10^4
	N_{BC1}/N_{BC2}	0.53	0.72	0.77	0.73	0.71



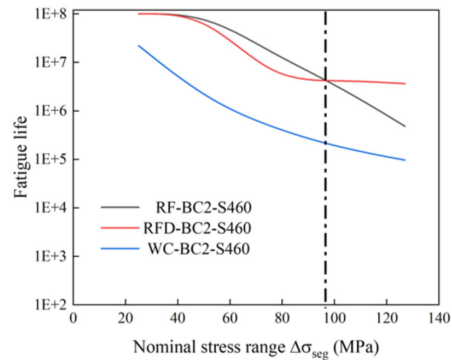
(a)



(b)



(c)



(d)

Fig. 3-24 Comparison of fatigue life in number of cycles of three connections with various BC and ρ ; (a) RF connections; (B) RFD connections; (c) C1-WCs (d) Results with $\rho=0.7$

The results of the fatigue life evaluation are more vividly presented in Fig. 3-24. It is observed that the deviation of the fatigue life of C1-WCs caused by various lateral boundary conditions is more dramatic compared to that of RF and RFD connections. The average value of N_{BC1}/N_{BC2} of RF, RFD, and C1-WC is 0.92, 1.07, and 0.66, respectively. In comparison to “complete tower” conditions (BC2), the laboratory segment fatigue tests properly represent the fatigue performance for RF/RFD connections. The prediction resistance is in a range of appr. $\pm 8\%$ as obtained in this case study. The segment test is rather conservative for C1-WCs by predicting resistance of -34% compared to the expected resistance in a complete tower. The fatigue performance of connections at the same and ideal pretension level ($\rho = 0.70$) is compared in Fig. 3-24 (d). The fatigue resistance of WC-BC2-S460 exhibits the least resistance under perfect conditions, i.e. when the contact surfaces of the connection are perfectly aligned and pretension force is maintained at its maximum level in the bolt throughout the connection's lifetime. Moreover, RFD-BC2-S460 offers excellent fatigue resistance specifically after $\Delta\sigma_{seg}$ exceeds 98 MPa, see Fig. 3-24 (d). The influence of steel strength on their fatigue performance is shown in Fig. 3-25. Its effect can be neglected as long as a suitable material is selected for the connections.

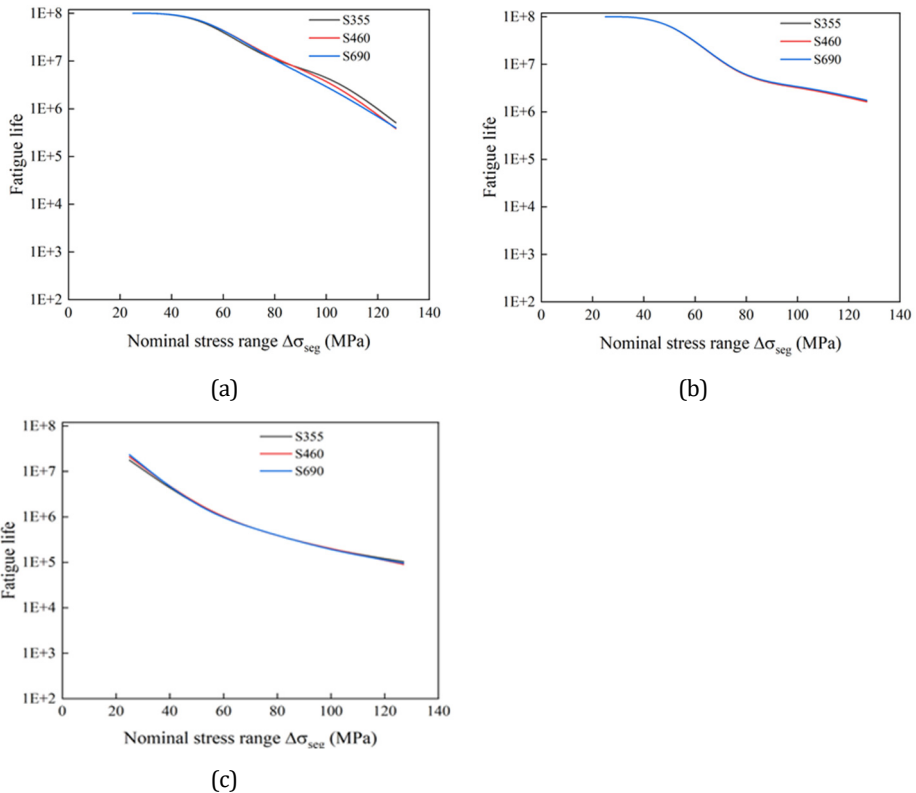


Fig. 3-25 Comparison of fatigue life in number of cycles of three connections with different steel strength; (a) RF-BC2 ($\rho=0.7$); (b) RFD-BC2 ($\rho=0.55$); (c) WC-BC2 ($\rho=0.4$)

Connections with bolts face a number of difficulties, which may appear during the assembly process or in service [38]. These difficulties include the accuracy of applied bolt force, self-loosening of bolts, and short-term and long-term relaxation of bolts. It is well known that the fatigue performance of RF and RFD connection is very sensitive to pretension force level in bolts. The most optimistic results about bolt force response under the identical nominal stress range can be extracted from the FE simulation. These bolt forces can be used to calculate the fatigue life of RF/RFD connections without imperfections.

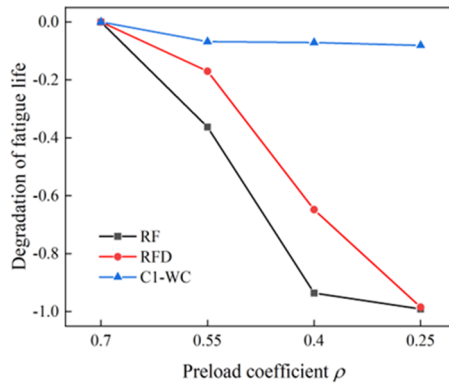


Fig. 3-26 Degradation of fatigue life

Fig. 3-26 shows the average discrepancy of fatigue life of connections with four preload coefficients ρ . It is clearly found that the fatigue performance of RF connections is the most negatively influenced by ρ . On the contrary, C1-WCs show robust fatigue performance even with varied ρ . The degradation of fatigue life of C1-WCs is 0.08 from $\rho=0.70$ to $\rho=0.25$. In other words, the fatigue performance of C1-WCs is insensitive to the variation of bolt preload force which could be generated by the issues mentioned above. However, these issues will lead to a huge degradation of the fatigue resistance of RF and RFD connections.

3.7 COMPARISON BETWEEN CONNECTIONS

To compare the performance of connections designed with similar Z_U and Z_I , specimens RF-BC2-S460, RFD-BC2-S460, and WC-BC2-S460 with three different preload coefficients ρ are selected. Table 3-12 and Fig. 3-27 illustrate the configuration details and results of the selected specimens. The initial stiffness is obtained by tangential approximation of the load-displacement curve within the critical load Z_I . RFD connections display slightly higher initial elastic stiffness than RF and C1-WCs. Fig. 3-27 (b) shows RFD-BC2-S460 achieves approximately similar fatigue performance to RF-BC2-S460 with lower bolt preload force (649 kN). The maximum bolt stress in C1-WC is within the elastic range of the bolt (see Fig. 3-27 (b)). The gap opening at the ultimate state of RF/RFD connections (20 mm) is around six times the one of C1 connections (3

mm), as seen in Fig. 3-27 (c). Compared to RF/RFD connections, the C1-WC shows the lowest gap before reaching Z_I . This implies that the bolts in the RF/RFD connections could be more prone to corrosion than C1-WC, which may accelerate the fatigue crack initiation and propagation [39]. The fatigue performance of the connections is compared in Fig. 3-27 (d). Although WC-BC2-S460 shows the lowest fatigue resistance for ideal conditions, the benefits of this connection become clear when more realistic conditions are considered, i.e. realistic level of execution tolerances between two tower segments which are causing lower levels of pretension forces in bolts.

Table 3-12 Configuration details of connections with similar Z_U and Z_I

Specimen	Bolt preload (kN)	Bolt rotation (rad)	Bolt	Initial stiffness (kN/mm)	Z_I (kN)	Z_U (kN)
RF-BC2-S460	825 (0.70Asfu)	2.08	M42-10.9	1564	428	853
RFD-BC2-S460	649 (0.55Asfu)	1.79	M42-10.9	1743	427	853
WC-BC2-S460	80 (0.40Asfu)	29.19	M18-10.9	1183	450	826

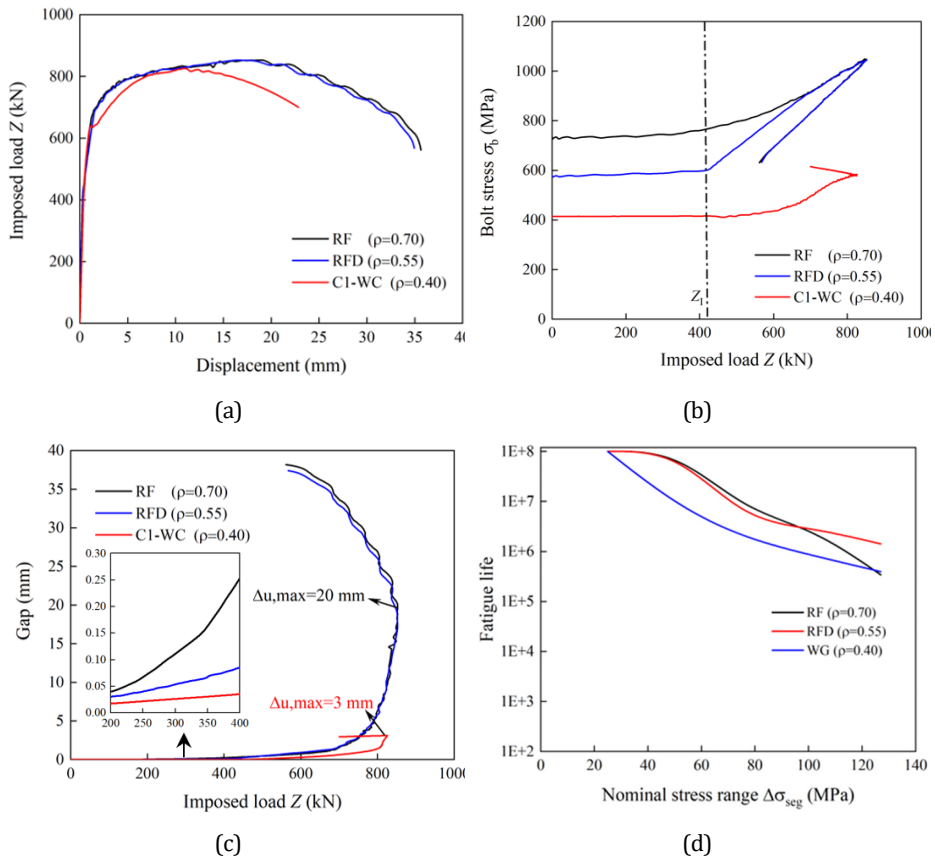


Fig. 3-27 Comparison between connections with similar Z_U and Z_I ; (a) Load-displacement curves; (b) Bolt stress development; (c) Gap; (d) Fatigue life in number of cycles

3.8 CONCLUSION

This chapter provides a comprehensive comparative analysis between three connections for possible use in towers supporting wind turbines, namely bolted ring-flange connection (RF), bolted ring-flange connection with a defined area (RFD), and the C1 wedge connection (C1-WC). Advanced FE models were established and validated against the performed test results. Afterwards, parametric studies on tensile behaviour and fatigue performance were performed to assess the effect of the lateral boundary conditions on the sides of the segment specimen, preload coefficient ρ , and steel strength. The following conclusions are drawn:

- The influence of “continuity” conditions, circumferential (hoop) stress, on the tensile static behaviour of RF and RFD connection, is negligible. However, the stress response of crucial components in C1-WCs is significantly influenced by the effect of circumferential stress. It is indicated that the BC1 causes a more uniform distribution of stress response in the C1 WC and a smaller stress concentration factor k_f . Furthermore, the ranges of maximum principal stress $\Delta\sigma_{\text{pri,max}}$ and stress concentration factors k_f of C1-WCs with BC2 are lower than that with BC1.
- The reduced pretension level in bolts, given by coefficient ρ leads to a noticeable reduction of initial stiffness and the critical load Z_I for L-flange connections, while their ultimate capacity Z_U remains constant. The stress response of C1-WCs, for different ρ , depends on the continuity boundary conditions. The stress response of C1-WCs with BC1 is rather consistent under various preload forces (ρ). However, by increasing ρ under BC2, a higher maximum principal stress $\sigma_{\text{pri,max}}$ is generated but with smaller $\Delta\sigma_{\text{pri,max}}$ and k_f . The benefits of a sufficient pretension level under ideal contact alignment are demonstrated for all three types of connections.
- Before the bolt yields, the effect of steel strength on the tensile behaviour of RF and RFD connections is limited. On the contrary, the strength of steel plays a significant role in the ultimate limit state of C1-WCs. This indicates the potential of using higher-strength steel in this connection. The recommended yield strength of the steel in the C1-WC should be greater than $Z_I/A_{s,WC}$.
- The effectiveness of the laboratory segment tests for three types of connections is thoroughly evaluated. The ratio between the fatigue life under BC1 and BC2 ($N_{\text{BC1}}/N_{\text{BC2}}$) for RF, RFD, and WG connections is 0.92, 1.07, and 0.66, respectively. The laboratory segment fatigue tests properly estimate the fatigue performance for RF/RFD connections (without imperfection) while leading to a rather conservative assessment for WG connections.
- Under a similar ULS/fatigue load, RFD exhibits higher initial stiffness compared to other connections. C1-WCs have the best corrosion protection capabilities. Between $\rho = 0.70$ and 0.25, the degradation of the fatigue resistance of RF/RFD connections is twelve times higher than C1-WCs (the

lifetime degradation of 0.08). This indicates that the C1 wedge connection is a very robust connection for offshore applications.

This chapter addresses research question Q2) by providing a quantitative comparison between three MP-TP connections. After investigating the mechanical behaviour of the C1 wedge connection in chapters 2 and 3, the following chapters will concentrate on assessing the healthy status of this connection by AE techniques.

REFERENCES

- [1] C1 connections obtains DNV certification for the C1 wedge connection™, (n.d.). <https://c1connections.com/news/c1-connections-obtains-dnv-certification-for-the-c1-wedge-connection/> (accessed November 1, 2022).
- [2] W. Weijtjens, A. Stang, C. Devriendt, P. Schaumann, Bolted ring flanges in offshore-wind support structures - in-situ validation of load-transfer behaviour, *J. Constr. Steel Res.* 176 (2021) 106361. <https://doi.org/10.1016/j.jcsr.2020.106361>.
- [3] C. Petersen, *Stahlbau (Steel Construction)*, Ed. Vieweg-Verlag, Braunschweig, (1997).
- [4] M. Seidel, Zur Bemessung geschraubter Ringflanschverbindungen von Windenergieanlagen [For dimensioning bolted annular flange connections of wind turbines], Leibniz Universität Hannover, 2001. <https://doi.org/10.13140/RG.2.2.14685.36328>.
- [5] L. Cheng, H. Xin, M. Veljkovic, Numerical analysis of ring flange connection with defined surface area, *Ce/Papers.* 4 (2021) 182–188. <https://doi.org/10.1002/CEPA.1279>.
- [6] M. Seidel, Tolerance requirements for flange connections in wind turbine support structures, *Stahlbau.* 87 (2018) 880–887. <https://doi.org/10.1002/stab.201810050>.
- [7] F. Wegener, M. Seidel, R. Glienke, F. Marten, M. Schwarz, Numerische Simulation von Vorspannkraftverlusten in Ringflanschverbindungen [Numerical simulation of loss of prestressing force in ring flange connections], *Stahlbau.* 89 (2020) 1003–1015. <https://doi.org/10.1002/STAB.202000055>.
- [8] M. Pavlović, C. Heistermann, M. Veljković, D. Pak, M. Feldmann, C. Rebelo, L.S. Da Silva, Connections in towers for wind converters, part I: Evaluation of down-scaled experiments, *J. Constr. Steel Res.* 115 (2015) 445–457. <https://doi.org/10.1016/j.jcsr.2015.09.002>.
- [9] L. Cheng, F. Yang, J.S. Winkes, M. Veljkovic, The C1 wedge connection in towers for wind turbine structures, tensile behaviour of a segment test, *Eng. Struct.* 282 (2023) 115799. <https://doi.org/10.1016/j.ENGSTRUCT.2023.115799>.
- [10] C1 Connections, Analytical design report-mock-up geometry windpark fryslan loads, 023-003, 2020.
- [11] P. de Vries, L-flange sub-component tests (internal report), 2021.
- [12] Simulia, Abaqus/CAE User's Manual, Version 6.14, 2016.
- [13] International Organization for Standardization (ISO), ISO 4014, Hexagon Head Bolts – Product Grades A and B, 2011.
- [14] C. Petersen, *Stahlbau: Grundlagen der Berechnung und baulichen Ausbildung von Stahlbauten [Steel construction: Basics of calculation and structural design of steel structures]*, Vieweg, 1993.
- [15] Deutscher Ausschuss für Stahlbau DASt, DASt-Guideline 021: Schraubenverbindungen aus feuerverzinkten Garnituren M39 bis 72, Stahlbau Verlags- und Service GmbH, Düsseldorf, 2013.
- [16] ISO, International Organization for Standardization (ISO), ISO 4017, Hexagon head screws product grades A and B, Switzerland, 2014.
- [17] ISO, International Organization for Standardization (ISO), ISO 965–1, ISO General purpose metric screw threads - tolerances, Switzerland, 2013.
- [18] I. Tobinaga, | Takeshi Ishihara, A study of action point correction factor for L-type flanges of wind turbine towers, *Wind Energy.* 21 (2018) 801–806. <https://doi.org/10.1002/we.2193>.

- [19] M. Veljkovic, M. Feldmann, J. Naumes, D. Pak, L. Simões da Silva, C. Rebelo, Wind turbine tower design, erection and maintenance, in: *Wind Energy Syst. Optimising Des. Constr. Safe Reliab. Oper.*, Woodhead P, 2010: pp. 274–300. <https://doi.org/10.1533/9780857090638.2.274>.
- [20] DNVGL-ST-0126, Support structures for wind turbines, 2018.
- [21] Lutz Kruttschinn, Untersuchungen zum Tragverhalten von Ringflanschsegmenten mit definierten Kontaktflächen [Investigations on the load-bearing behaviour of annular flange segments with defined contact surfaces], Universität Hannover, 1999.
- [22] EN 1090-2:2008+A1:2011, Execution of steel structures and aluminium structures - Part 2: technical requirements for steel structures, n.d.
- [23] EN 10025-6, Hot rolled products of structural steels – Part 6: Technical delivery conditions for flat products of high yield strength structural steels in the quenched and tempered condition, European Committee for Standardization, 2019.
- [24] F. Yang, M. Veljkovic, Y. Liu, Ductile damage model calibration for high-strength structural steels, *Constr. Build. Mater.* 263 (2020) 120632. <https://doi.org/10.1016/J.CONBUILDMAT.2020.120632>.
- [25] EN-10083-3: Steels for quenching and tempering, Berlin: Beuth, 2016.
- [26] L.J. Jia, H. Kuwamura, Ductile fracture simulation of structural steels under monotonic tension, *J. Struct. Eng. (United States)*. 140 (2014). [https://doi.org/10.1061/\(ASCE\)ST.1943-541X.0000944](https://doi.org/10.1061/(ASCE)ST.1943-541X.0000944).
- [27] P. Može, F. Yang, M. Veljkovic, Validation and application of bearing and block tearing resistance; background to prEN1993-1-8:2021, *J. Constr. Steel Res.* 187 (2021) 106985. <https://doi.org/10.1016/J.JCSR.2021.106985>.
- [28] Y. Ling, Uniaxial true stress-strain after necking, *AMP J. Technol.* 5 (1996) 37–48.
- [29] F. Yang, M. Veljkovic, L. Cheng, Fracture simulation of fully and partially threaded bolts under tension, *Ce/Papers.* 4 (2021) 156–161. <https://doi.org/10.1002/CEPA.1275>.
- [30] A.M. Kanvinde, A.M. Asce, G.G. Deierlein, F. Asce, Void growth model and stress modified critical strain model to predict ductile fracture in structural steels, *J. Struct. Eng.* 132 (2006) 1907–1918. <https://doi.org/10.1061/ASCE0733-94452006132:121907>.
- [31] A.M. Kanvinde, A.M. Asce, G.G. Deierlein, F. Asce, Finite-element simulation of ductile fracture in reduced section pull-plates using micromechanics-based fracture models, *J. Struct. Eng.* 133 (2007) 656–664. <https://doi.org/10.1061/ASCE0733-94452007133:5656>.
- [32] H.C. Ho, K.F. Chung, X. Liu, M. Xiao, D.A. Nethercot, Modelling tensile tests on high strength S690 steel materials undergoing large deformations, *Eng. Struct.* 192 (2019) 305–322. <https://doi.org/10.1016/J.ENGSTRUCT.2019.04.057>.
- [33] ISO 898-1, Mechanical properties of fasteners made of carbon steel and alloy steel-Part 1: Bolts, screws and studs with specified property classes-Coarse thread and fine pitch thread (ISO 898-1:2013), Brussels, Belgium, 2013.
- [34] K.E.Y. Creusen, G. Misios, J.S. Winkes, M. Veljkovic, Introducing the C1 Wedge Connection, *Steel Constr.* 15 (2022) 13–25. <https://doi.org/10.1002/STCO.202100039>.
- [35] EN 1993-1-9: Eurocode 3: Design of steel structures – Part 1-9: Fatigue, 2005.
- [36] DIN 14399-10, High-strength structural bolting assemblies for preloading, British Standard, 2009.

[37] R.S. Charlton, P. Eng, Threaded Fasteners: Part 1 - Failure Modes And Design Criteria of Connections, (2011). <http://onepetro.org/NACECORR/proceedings-pdf/CORR11/All-CORR11/NACE-11164/1684021/nace-11164.pdf> (accessed November 2, 2022).

[38] A. Mehmanparast, S. Lotfian, S.P. Vipin, A review of challenges and opportunities associated with bolted flange connections in the offshore wind industry, *Metals* (Basel). 10 (2020) 732. <https://doi.org/10.3390/MET10060732>.

[39] A. Mehmanparast, S. Lotfian, S.P. Vipin, A review of challenges and opportunities associated with bolted flange connections in the offshore wind industry, *Metals* (Basel). 10 (2020) 732. <https://doi.org/10.3390/met10060732>.

4. IDENTIFYING DEFORMATION STAGE BY ACOUSTIC EMISSION

Acoustic emission (AE) is widely used for identifying source mechanisms and the deformation stage of steel material. The effectiveness of this non-destructive monitoring technique heavily depends on the quality of the measured AE signals. However, the AE signals from deformation are easily contaminated by signals from noise in a noisy environment. This chapter presents a hybrid model for deformation stage identification, which combines a self-adaptive denoising technique and an Artificial neural network (ANN). In pursuit of model generality, AE signals were collected from tensile coupon tests with various steel materials and loading speeds.

This chapter addresses the third research question Q3) and is organized as follows: Section 4.1 introduces the application of AE monitoring for deformation stages identification. Section 4.2 presents the proposed SSA-VMD model. Section 4.3 demonstrates the performance of the proposed denoising method using a simulated AE signal. The experimental program and results are described in Section 4.4 Finally, Section 4.5 describes the employed ANN for signal identification with hyperparameter tuning. The conclusion is given in Section 4.6.

Part of this chapter has been prepared as a journal article: Cheng L, et al., Application of Acoustic emission for deformation stage identification combining SSA-VMD and ANN. Credit is also given to the master thesis: 'Qinkun Sun, Identification of deformation stages for specimens under tensile test based on Acoustic Emission Technique'.

4.1 INTRODUCTION

Dunegan et al. [1] first correlated the characteristics of collected AE signals to the fracture mechanisms of precipitated alloys, such as beryllium and aluminium. This research showed the potential of the AE technique for fracture analysis of metal materials. After that, systematic studies of AE signals generated during the tensile deformation of metal materials were conducted [2–6]. With the development of microstructural examination [7–9], the AE sources during the deformation process were explained using the underlying mechanism in metals and alloys. It was concluded that AE signals are dominantly produced by dislocation activity in the micro- and macro-yielding zones of metals, as well as at the final fracture.

The trend of AE features, such as amplitude, energy, counts, hits, and root-mean-square (RMS) have been successfully confirmed to interpret the rupture process of materials [6,10–16]. Other novel indicators were proposed with improvements in the AE monitoring systems and data processing techniques [17–20]. Although the regular pattern of AE activities for metal material deformation has been obtained, the related quantitative description is not transferable between studies. This is mainly because the AE characteristics are influenced by several factors, such as types of material, plasticity level, presence of any inclusions, and the employed AE acquisition system [21,22]. In addition, it has also been found that the signals generated during plastic deformation have overlapped distribution of AE features to final fracture [23]. If monitoring is not initiated at the beginning of the loading, it is challenging to distinguish the signals from plastic deformation and fracture based just on certain or synthetic analyses of AE features. Hence, it is necessary to propose a more generalized method to correlate the collected AE signals to deformation stages.

Artificial neural network (ANN) has been used to detect the deformation stage for certain steel materials exposed to static tensile loading [24,25]. The performance of the ANN method is highly dependent on the quality of AE signals. Whereas, the collected AE signals are always accompanied by complex noise in practical cases (e.g. friction noise between components and equipment, background noise from the environment). AE signals resulting from metal deformation are typically nonlinear and non-stationary [26]. Signal decomposition methods have been presented to decompose the nonstationary signals into several regular clear sub-signals, which can be effectively used to remove the noises of nonstationary signals. Representative methods include wavelet transform (WT) [27], empirical mode decomposition (EMD) [28], ensemble empirical mode decomposition (EEMD) [29], and variable mode decomposition (VMD) [30]. VMD outperforms the EMD and WT in terms of theoretical foundation, anti-noise performance and alleviating the mode mixing problem [31]. Whereas, the user-defined decomposition mode numbers severely affect its reliability. Furthermore, Zhou and Zhu [32] found that VMD cannot effectively isolate low-frequency random noise. To solve the abovementioned drawbacks, some studies proposed an improved VMD method combing with singular spectral analysis (SSA) [33], called the VMD-SSA method

[32,34,35]. The VMD algorithm first de-noises the data, and then the singular spectrum analysis (SSA) algorithm is used to further filter out the low-frequency noise. Although the VMD-SSA shows high de-noising precision and anti-noise robustness, it is time-consuming to select the proper number of rows of the Hankel matrix for specific signals in SSA.

This chapter represents one of the first attempts to employ SSA as the primary decomposition technique for AE signals. After verifying the performance of the proposed denoising method, measured AE signals were obtained via a series of coupon steel tensile tests. Moreover, to improve the generalization of the ANN model, the tests were conducted with various steel grades, geometry of coupons, and loading rates. The improved ANN was evaluated for signal identification during tensile deformation.

4.2 PROPOSED DENOISING METHODOLOGY

The SSA-VMD denoising approach is proposed to overcome issues with selecting the proper parameters for SSA and VMD (number of rows of the Hankel matrix of SSA and decomposition level of VMD). Two basic assumptions are: (1) signals are composed of several narrow-bandwidth signals; (2) the frequency of noise is overlapping with that of the real AE signals but the corresponding frequency peak is different. These two assumptions are theoretically accurate considering the nature of signals [36]. The idea behind this approach is that SSA can efficiently eliminate strong broadband noise, and VMD can accurately remove the narrowband noise. The full procedure is as follows:

Step 1: SSA

SSA is a principal component analysis for time series and is widely used to extract qualitative dynamics from noise-contaminated signals [33].

Step 1.1- Embedding: A one-dimensional AE signal $X = (x_1, \dots, x_N)$ is converted to a 2D matrix Y , namely the Hankel matrix.

$$Y = \begin{pmatrix} x_1 & x_2 & \dots & \dots & x_k \\ x_2 & x_3 & \dots & \dots & x_{k+1} \\ \cdot & \cdot & \dots & \dots & \cdot \\ \cdot & \cdot & \dots & \dots & \cdot \\ x_L & x_{L+1} & \dots & \dots & x_N \end{pmatrix} \quad \text{Eq. 4-1}$$

where L is the number of rows ($1 < L < N$) and K is defined as $N-L+1$. Xu et al. [37] concluded that L should be close to or higher than the number of samples in one period of the lowest frequency component.

Step 1.2 – Singular value decomposition (SVD): The matrix Y is decomposed into the product of three matrices: an orthogonal matrix U , a diagonal matrix S and the transpose of an orthogonal matrix V :

$$Y = USV^T \quad (S = [\text{diag}(\sigma_1, \sigma_2, \dots, \sigma_p), 0]) \quad \text{Eq. 4-2}$$

where S is an $L \times K$ diagonal matrix. σ_p are the nonnegative values in decreasing order of magnitude and $p = \min\{L, K\}$. The diagonal entries of S are called the singular values of X .

Step 1.3 – Regroup the signals: The singular values are grouped by calculating the energy differential spectrum D_i with a certain threshold η_σ :

$$D_i = \frac{\sigma_i^2 - \sigma_{i+1}^2}{(\sigma_i - \sigma_{i+1})^2}, \quad i=1, 2, \dots, (p-1) \quad \text{Eq. 4-3}$$

$$\eta_\sigma = D_1/300 \quad \text{Eq. 4-4}$$

where σ is the singular value, D_i is the sequence of energy differential spectrum, and p is the number of singular values. Singular value components m with D_i higher than η_σ are marked as signal-related components. The remaining singular values ($p-m$) are grouped as noise.

Step 1.4 – Reconstruction: The grouped sub-signals are reconstructed from a 2D matrix to a time series using the anti-diagonal averaging method [38]:

$$y_{rc,k} = \begin{cases} \frac{1}{k} \sum_{m=1}^k y_{m,k-m+1}^* & 1 \leq k < L^* \\ \frac{1}{L^*} \sum_{m=1}^{L^*} y_{m,k-m+1}^* & L^* \leq k \leq K^* \\ \frac{1}{N-k+1} \sum_{m=k-K^*+1}^{N-K^*+1} y_{m,k-m+1}^* & K^* \leq k \leq K^* \end{cases} \quad \text{Eq. 4-5}$$

where $L^* = \min(L, K)$, $K^* = \max(L, K)$, and when $L < K$, $y_{ij}^* = y_{ij}$ otherwise $y_{ij}^* = y_{ji}$, and $y_{ij}^* = y_{ij}$ is the element in Y . After SSA, the strong broadband noise signals are filtered efficiently.

Step 2: VMD

VMD decomposes signal X into an ensemble of band-limited intrinsic mode functions (IMFs) $u_k(t)$ [30], where k is the number of modes.

Step 2.1 – The construction variational problems: After applying the Hilbert transform, frequency mixing, and the heterodyne demodulation, this problem is described as:

$$\begin{cases} \min_{\{u_k\}, \{\omega_k\}} \left\{ \sum_{k=1}^K \left\| \partial_t \left[\left(\delta(t) + \frac{j}{\pi t} \right) u_k(t) \right] e^{-j\omega_k t} \right\|_2^2 \right\} \\ \text{subject to } \sum_{k=1}^K u_k = X \end{cases} \quad \text{Eq. 4-6}$$

The definition of each parameter can be found in [39]. The solution is obtained by employing the quadratic penalty term α and Lagrangian multipliers $\lambda(t)$. The constrained variational problem is converted to an unconstrained variational problem.

Step 2.2 – Solving the variational problem: The Alternate Direction Method of Multipliers (ADMM) is introduced to solve the unconstrained variational problem [40]. All the

modes in the frequency domain \hat{u}_k^{n+1} and corresponding centre frequency w_k^{n+1} are expressed as:

$$\hat{u}_k^{n+1}(w) = \frac{\hat{f}(w) - \sum_{i \neq k} \hat{u}_i(w) + \hat{\lambda}(w)/2}{1 + 2\alpha(w - \omega_k)^2} \quad \text{Eq. 4-7}$$

$$w_k^{n+1}(w) = \frac{\int_0^\infty \omega |\hat{u}_k(w)|^2 d\omega}{\int_0^\infty |\hat{u}_k(w)|^2 d\omega} \quad \text{Eq. 4-8}$$

Sud [41] discussed the possibility to determine the number of modes K a priori. The results show $K=6$ to 10 is suitable for wideband interferers. Considering the AE signals are distributed in a wide-band frequency range, $K=8$ is selected in this case, which means 8 IMFs are obtained after this step.

Step 2.3 – Minimize the fake modes: The correlation coefficients between the decomposed IMFs and the original signal is calculated, and a threshold is then defined as:

$$\eta_r = \rho \cdot R_{\max} \quad \text{Eq. 4-9}$$

where R_{\max} is the calculated maximum correlation coefficient. ρ is the ratio between the threshold and R_{\max} . ρ is equal to 0.025 in the following analysis after trials in certain cases. The modes with a correlation coefficient lower than η_r will be regarded as fake modes and removed. This step is significant because fake modes are common in real applications.

Step 2.4 – Use marginal spectrum to filter IMFs: Marginal spectrum (MS) based on the Hilbert-Huang spectrum (HHT) is an innovative technology for analyzing non-stationary and nonlinear signals [28]. The peak frequency and magnitude of the decomposed IMFs (via VMD) of the noise database can be identified using MS. After recognizing the dominant frequency characteristics of the noise database, the IMFs of AE signals after step 2.3 with the same frequency features as those of the noise database can be filtered. Then, the denoised AE signals can be reconstructed using the remaining IMFs.

4.3 EVALUATION OF SSA-VMD METHOD

4.3.1 Framework of SSA-VMD for denoising

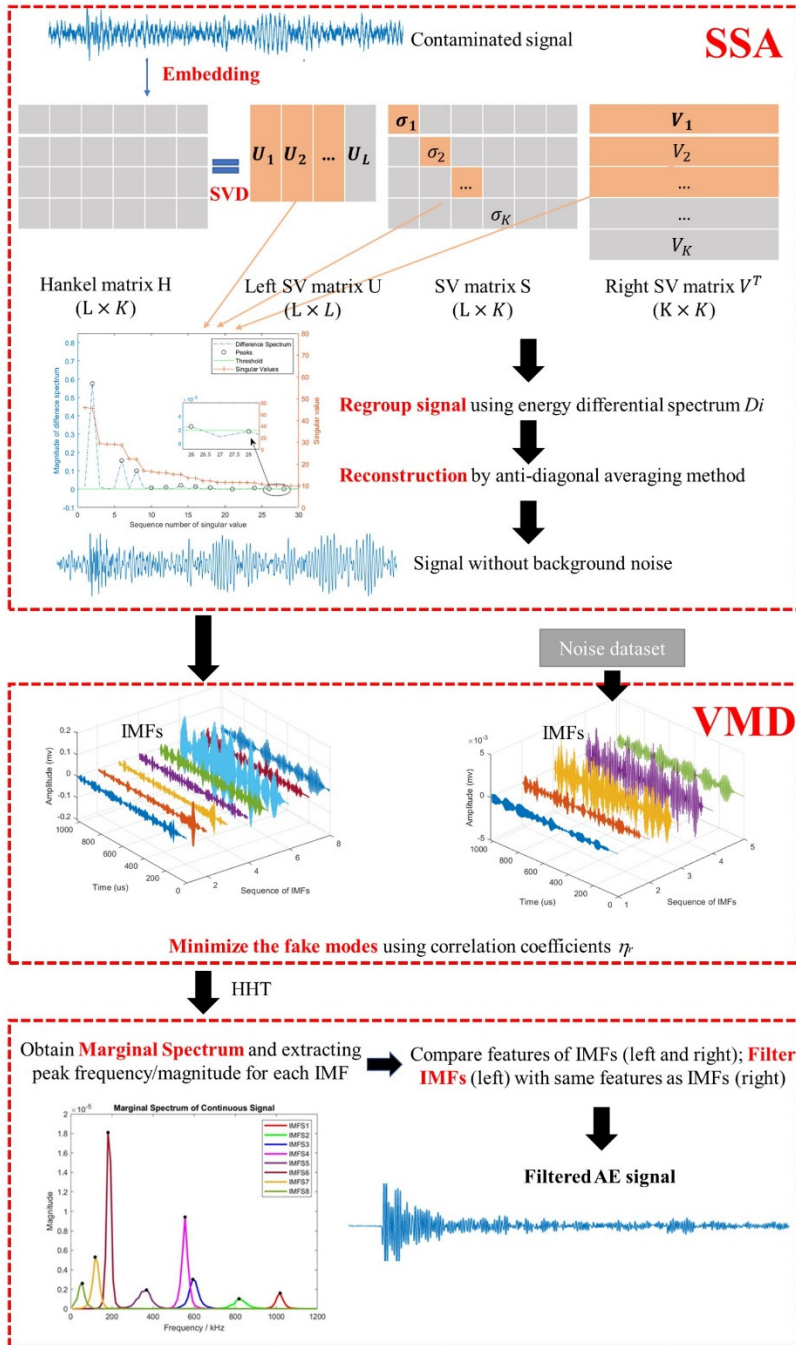


Fig. 4-1 Framework of SSA-VMD

A framework of SSA-VMD to denoise the AE signals is shown in Fig. 4-1. A numerical simulation is performed to test the performance of the proposed denoising method. Two types of noise exist in the laboratory environment of steel tensile deformation tests: wideband background noise, and narrowband mechanical noise (including friction noise and engine noise). Consequently, as shown in Fig. 4-2, background noise (X_B) and mechanical noise (X_M) are mixed with the original AE signal ($X_{AE,C}$) to obtain a contaminated signal (X_C).

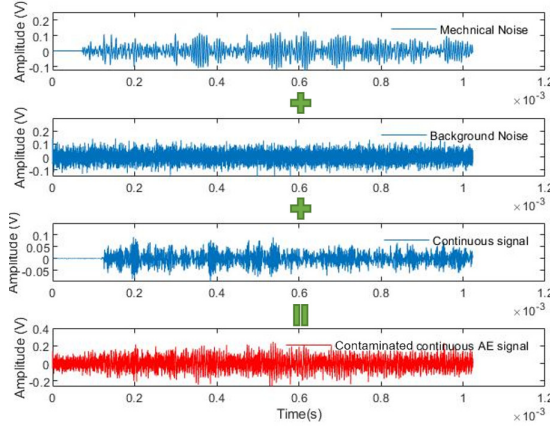


Fig. 4-2 Illustration of a contaminated continuous signal with SNR = -5 dB

AE signals can be generally classified into two basic types: (1) A burst AE signal with a clear pick and the following ringdown; and (2) a continuous AE signal which is a convolution of small burst signals. Continuous signals are more likely to be obscured by noise than burst-shape AE signals. Besides, continuous signals are compatible with the dislocation movement or plastic deformation of material generated during steel deformation [23,42]. Hence, in this simulation, a continuous signal was selected as the original signal. The original AE signal $X_{AE,C}$ is a continuous signal from the pencil lead break test on a steel specimen. X_B is a white noise simulated by Matlab with wideband frequency, and X_M is a detected AE signal at the beginning of a steel tensile test under a low load level. This signal can be regarded as the detected mechanical noise without any damage or dislocation movement in the material. The AE acquisition system and sensor used to record $X_{AE,C}$ and X_M are identical. Fig. 4-3 shows the frequency spectrum of the original AE signal and noise. Signal to noise ratio (SNR) is introduced to quantify the influence of the noise as:

$$SNR = 10 \times \log_{10} \left(\frac{\sum_{i=1}^N x(i)^2}{\sum_{i=1}^N y(i)^2} \right) \quad \text{Eq. 4-10}$$

where $x(i)$ is the original signal and $y(i)$ is the noise signal; N is the length of the signal. The SNR of the contaminated signal in this simulation is calculated as -5 dB. The negative SNR represents the practical cases with strong noise conditions ($SNR < 0$), which means the original signal is submerged into the noise signals.

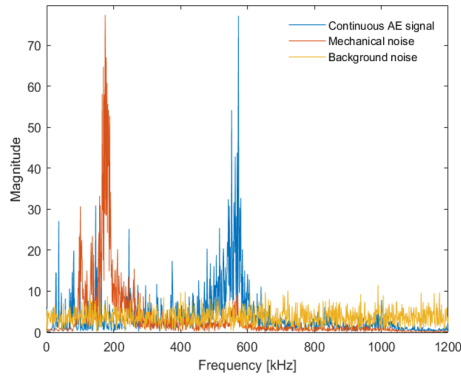


Fig. 4-3 Frequency spectrum of AE signals and noise signals

4.3.2 Denoising results by proposed SSA-VMD

Fig. 4-4 shows an overview of the denoise process for the contaminated continuous AE signal (X_C). The anticipated results after each step are correspondingly illustrated on the right side of the dashed line. In this simulation, X_M is the noise dataset to provide the features of narrow-band noise. The number of rows L of the Hankel matrix in step 1.1 is determined as follows. AE signals are measured by the AE acquisition system within the operating frequency range of 100 kHz - 1000 kHz. The sampling frequency F_s is 10 MHz with a time resolution Δ_t of 1×10^{-7} s. The corresponding maximum number of samples in the period is calculated as:

$$n_{\max} = T_{\max} / \Delta_t = (1 / 100 \text{ kHz}) / (1 \times 10^{-7}) = 100 \quad \text{Eq. 4-11}$$

Hence, SSA can obtain good performance with $L > 100$. To achieve a trade-off between the accuracy and calculation speed, L is defined as $N/64 = 160$, where N is the total number of samples in one signal. The comparison of $X_{AE,C}$ vs X_C^2 and X_M vs X_M^2 in the time domain and frequency domain is shown in Fig. 4-5. It implies that the original signal $X_{AE,C}$ and mechanical noise can be regrouped effectively.

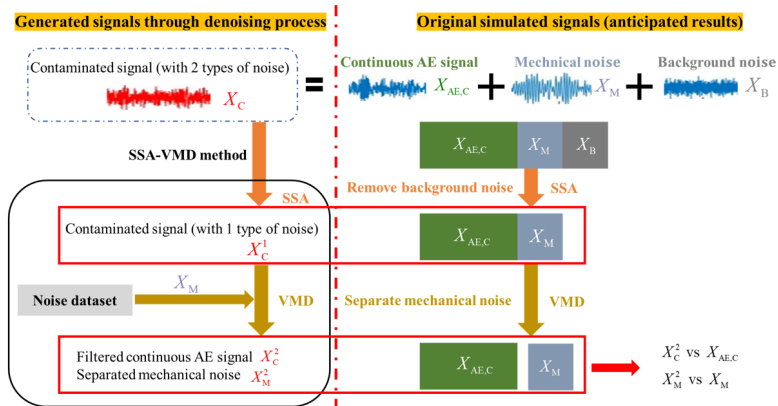
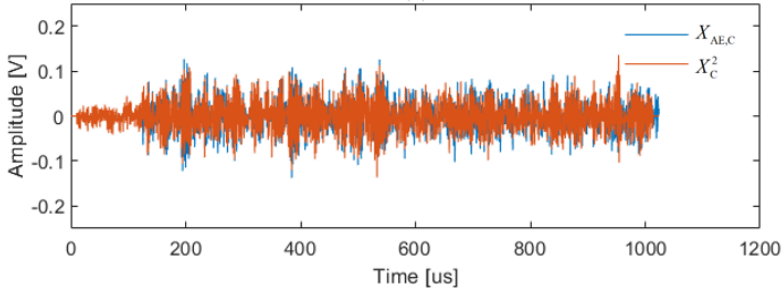
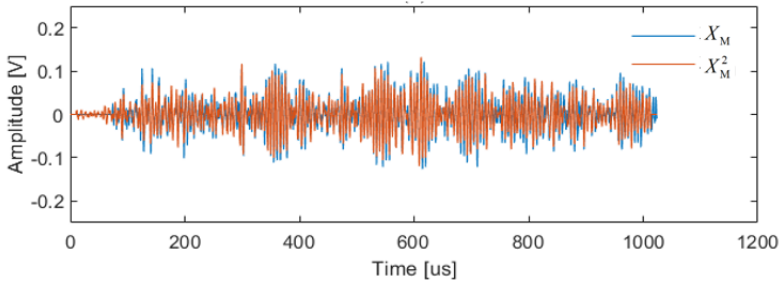


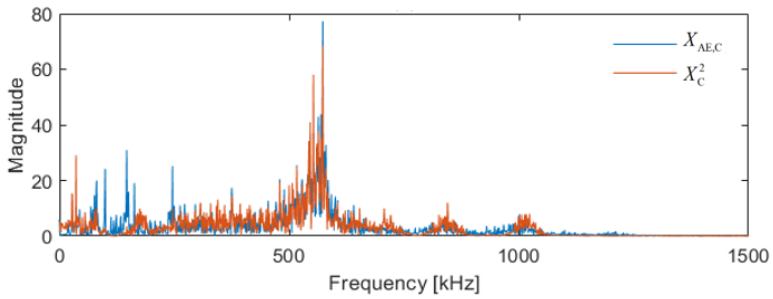
Fig. 4-4 Overview of the evaluation of the SSA-VMD method



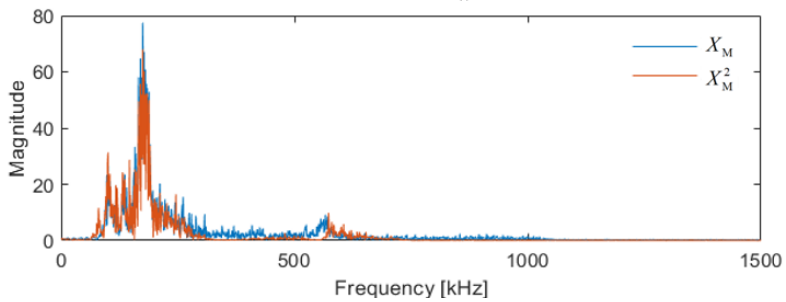
(a)



(b)



(c)



(d)

Fig. 4-5 Comparison between: (a) and (b) $X_{AE,C}$ vs X_C^2 , (c) and (d) X_M vs X_M^2

4.3.3 Comparison with other methods

Two signal-denoising methods, namely WT and SSA, were introduced for comparison. For WT denoising, the decomposition level L_{WT} was selected as 5 by considering the characteristic frequency of interest and sampling frequency. It is recommended to select wavelet functions with the properties of compact support (time-domain) and quick decay (frequency-domain) [43]. Therefore, the Symlets wavelet was employed as the wavelet function for analysis. SSA is not suitable for denoising the narrow-band mechanical noise. The optimal number of Hankel matrix rows L is determined by numerical analysis to improve the denoising quality. L is equal to 500 after checking the distribution of the DR index [37] with the various number of rows.

To evaluate the denoising effectiveness, Root-mean-square (RMS) values between the filtered signals X_c^2 and the original signal $X_{AE,C}$ were calculated as the indicator:

$$RMS = \sqrt{\frac{1}{N} \sum_{i=1}^N [X_c^2(i) - (X_{AE,C})]^2} \quad \text{Eq. 4-12}$$

where N is the signal length. Table 4-1 shows the denoising results using three methods.

Table 4-1 Comparison between WT, SSA, and proposed SSA-VMD

Denoising method	Adaptivity	Calculation time (s)	RMS
WT	No	0.21	0.0385
SSA	No	102.3	0.0228
SSA-VMD	Yes	9.22	0.0191

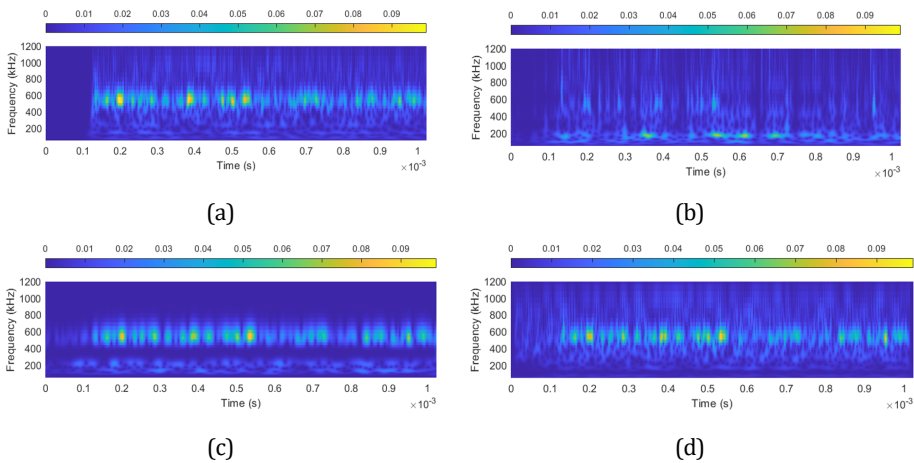


Fig. 4-6 Time-frequency plot of (a) original signal and filtered signals by (b) WT, (c) SSA, and (d) SSA-VMD

Moreover, Fig. 4-6 shows the time-frequency plot of the original signal and filtered signal using the different methods. It is found that: (1) WT and SSA are non-adaptive methods which need simulations to find appropriate setting parameters. (2) SSA-VMD

outperforms WT and SSA in terms of denoising accuracy with the lowest RMS; while the WT method failed to filter the noise around 100 kHz and part of the primary component was lost. (3) As for the computation time, WT is the fastest method. However, the time for prior selection of wavelet function and decomposition level is not included. These above observations demonstrate that SSA-VMD can eliminate the background noise and mechanical noise effectively while generally preserving the characteristics of the original signal.

4.4 EXPERIMENTAL STUDIES

4.4.1 Experimental set-up

The proposed denoising method was applied to the AE measurement of steel tensile deformation. Tensile coupon tests were performed to collect the AE signals during tensile steel deformation. As shown in Table 4-2, ten coupons were cut from cold-formed square steel tubes with three steel grades (S355, S500, and S700) with an identical cross-section area (80 mm²). Fig. 4-7 describes the profiles of the coupon specimens.

Table 4-2 Properties of coupon specimens

Sample	Geometry features		Unloading	Loading rate
	Nominal thickness t (mm)	Width b_0 (mm)		
S355-1	10	8	No	Varying
S355-2	10	8		Varying
S355-3	6	13.3		Varying
S355-4	6	13.3		Constant
S500-1	8	10	Yes	Constant
S500-2	10	8		Varying
S500-3	10	8		Constant
S700-1	10	8	Yes	Constant
S700-2	8	10		Varying
S700-3	8	10		Constant

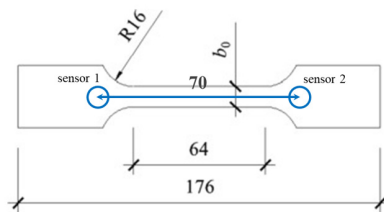


Fig. 4-7 Profiles of the coupon tensile specimens in mm [44]

An overview of the experimental set-up is shown in Fig. 4-8. Tensile tests were performed in an Instron testing machine with a maximum loading of 100 kN with displacement control. The deformation was measured by a 50 mm extensometer. The

AE acquisition system used for the tensile tests consisted of a physical AEwin system software with two piezoelectric sensors VS600-Z2 and pre-amplifiers with a uniform gain of 40 dB. The sensors were attached to the specimen symmetrically using a hot-melt adhesive. Before each test, pencil lead breaking tests were carried out to calibrate the response of the AE sensors. As shown in Fig. 4-8 (b), the frequency range of VS600-Z2 is 200 kHz-1000 kHz with a resonant frequency of around 600 kHz. It is reported that the recommended AE frequency range for metallic structures is 100 kHz-900 kHz [45]. Although this sensor is less sensitive in the range from 50 kHz to 200 kHz, it does also measure in this range. This sensor is chosen due to the limited space for the sensor. The operational frequency range in the AE acquisition system was set as 100 kHz – 1000 kHz. It has been demonstrated that the amplitude of AE signals from plastic deformation ranges from 30 to 60 dB [46]. The threshold was set to 30 dB to capture signals generated during deformation.

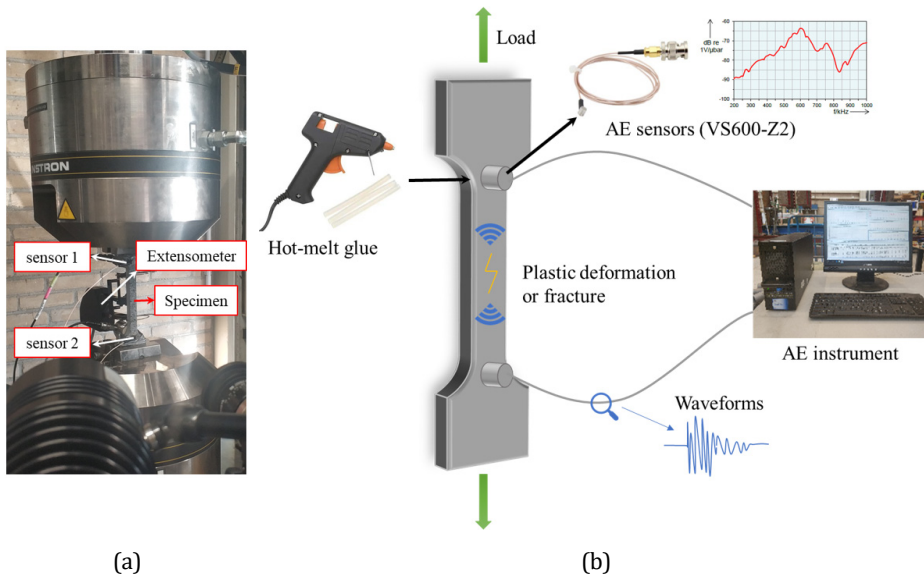


Fig. 4-8 Diagram of (a) Experimental set-up and (b) AE schematic

Considering constant load is not applicable in practical cases, varying loading rates were applied for the tensile tests (see Fig. 4-9). The selected loading rates meet the requirements of the Eurocode (0.01 m/s to 0.10 m/s). A loading rate of 0 mm/s means the holding stage and -0.01 mm/s represents the unloading stage. Fig. 4-9 shows the amplitude distribution of detected signals along the tensile process. It is found that numerous signals appeared at the beginning and unloading-reloading stages. The following factors contribute to this phenomenon: (1) friction noise is generated due to the contact between the grip and specimen at the beginning and during the unloading-reloading stage; (2) engine noise is from the vibration of the fluid pump in the loading frame. Hence, these signals can be classified in the noise database. The amplitude of

these signals is up to 50 dB which can cover the useful signals from plastic deformation. This implies the importance of applying the appropriate denoising method.

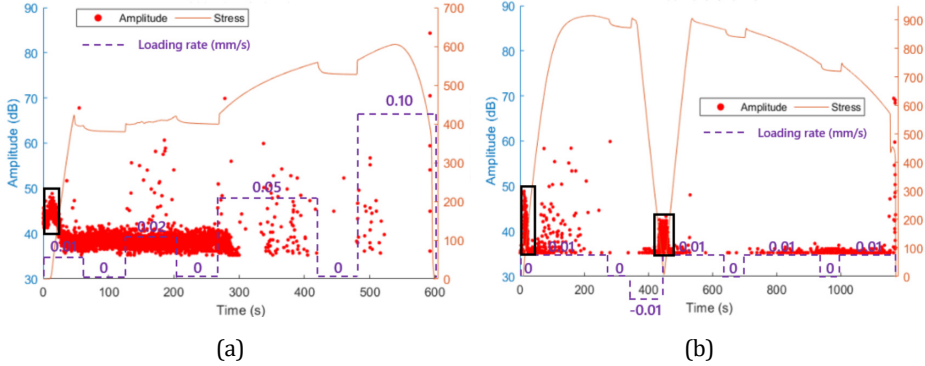


Fig. 4-9 Amplitude distribution of detected signals for (a) S355-1 and (b) S700-1

4.4.2 Experimental validation

The effectiveness of the proposed SSA-VMD in denoising measured AE signals is illustrated in this section. Denoising of the recorded AE signals from specimen S700-1 is taken as an example. In the previous simulation evaluation, only one mechanical noise signal constituted the noise database. The noise dataset during the tensile test consists of a large number of signals. The marginal spectrum of decomposed IMFs of detected AE signals in step 2.4 was calculated and is shown in Fig. 4-10. The X-axis is the sequence of IMFs. The y-axis and Z-axis are the extracted peak frequency and magnitude of each IMF. It is observed that four specific frequency ranges (red dash boxes) exist along all deformation procedures. There is a possibility that the IMFs located in these frequency ranges could be related to noise. To improve the accuracy and to avoid the error modes generated by spectral leakage, the density-magnitude index (DMI) is proposed to find the noise-related IMFs with the greatest possibility:

$$DMI(f_i) = \text{num}(f_i) / N_{\text{noise}} + \rho_M \times \text{normalization}(\overline{M}(f_i)) \quad \text{Eq. 4-13}$$

where $DMI(f_i)$ is the value of DMI under peak frequency f_i ; $\text{num}(f_i)$ is the number of IMFs with peak frequency f_i in the noise dataset; N_{noise} is the total number of IMFs in the noise dataset; ρ_M is determined as 0.3 as the weight factor; $\overline{M}(f_i)$ is mean magnitude for IMFs with frequency f_i . The first term describes the density of IMFs in the noise dataset with a specific peak frequency f_i . The second term is the magnitude determining which noise principal components are of dominant energy. The likelihood of noise-related IMFs increases with a higher density and magnitude. In this chapter, f_i with a DMI larger than 0.03 is regarded as the main frequency feature of noise-related IMFs. Finally, 18 peak frequencies were extracted as the main frequency components of noise-related IMFs with $DMI > 0.03$. The IMFs of the detected AE signals were filtered if they have the same frequency features as the extracted 18 peak frequencies from the noise dataset.

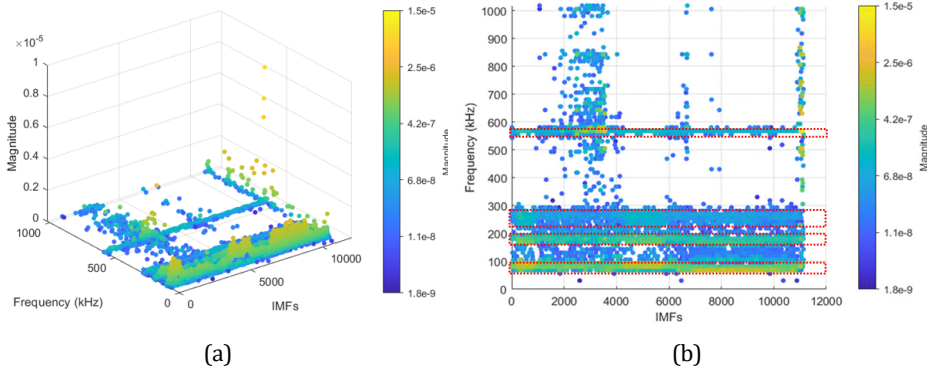


Fig. 4-10 Features of decomposed IMFs of detected AE signals of S700-1: (a) 3D plot and (b) top view

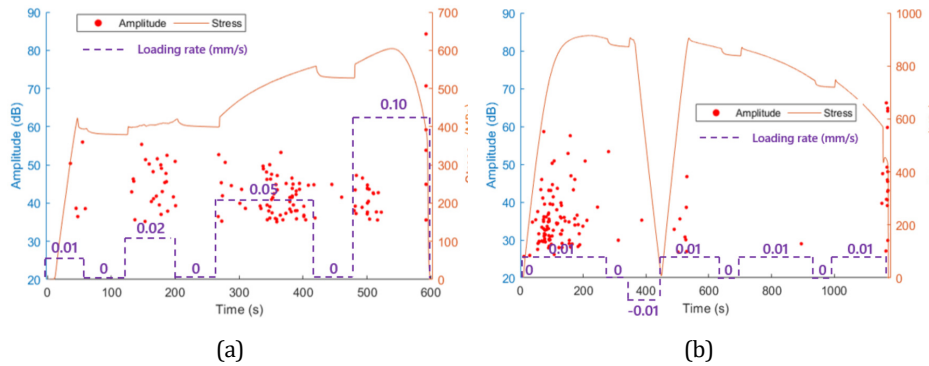


Fig. 4-11 Amplitude distribution of filtered signals for (a) S355-1, and (b) S700-1

The amplitude distribution of the filtered signals of S355-1 and S700-1 is shown in Fig. 4-11. Compared to Fig. 4-9, AE signals recorded at the beginning and during loading-unloading stages under low load levels disappear. It is noted that the amplitude of remaining AE signals is decreased which is attributed to that part of the power of the initially detected AE signals is generated by noise.

4.5 APPLICATION OF ANN FOR CLASSIFICATION

4.5.1 Introduction to the methodology

To identify the deformation stages of steel material, ANN was employed to establish the relationship between AE parameters and deformation stages. The algorithm of a fully connected neural network (FCNN), one typical type of ANN, is commonly used in material and structural damage identification [47]. Typically, a FCNN consists of an input layer, hidden layers, and an output layer, as shown in Fig. 4-12. Neurons in hidden layers combine values from the input layers transformed by communication links. A similar denoising procedure as described in section 4.2 is applied to all specimens. After that, the AE parameters, including amplitude, duration, signal strength, peak frequency,

energy and fuzzy cross-entropy, are extracted from the filtered AE signals as the input. Except for these conventional AE features, fuzzy cross-entropy has been proposed to interpret time-series signals recently [48,49]. This feature is useful to describe the complexity of AE signals with high sensitivity.

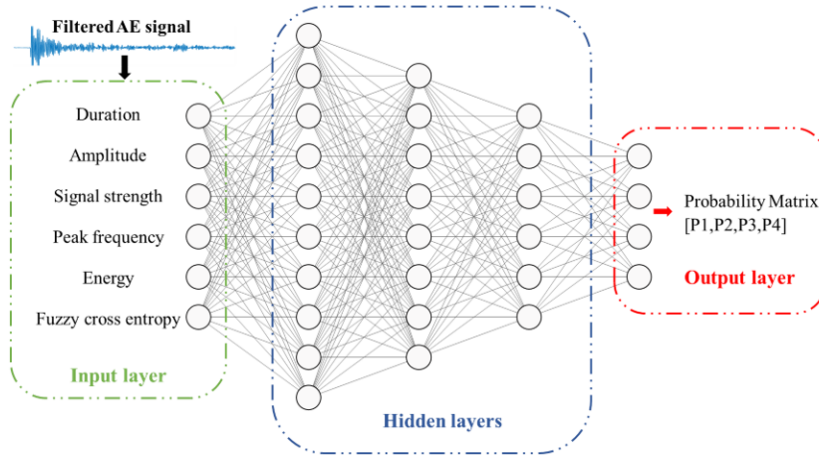


Fig. 4-12 Schematic of the applied ANN

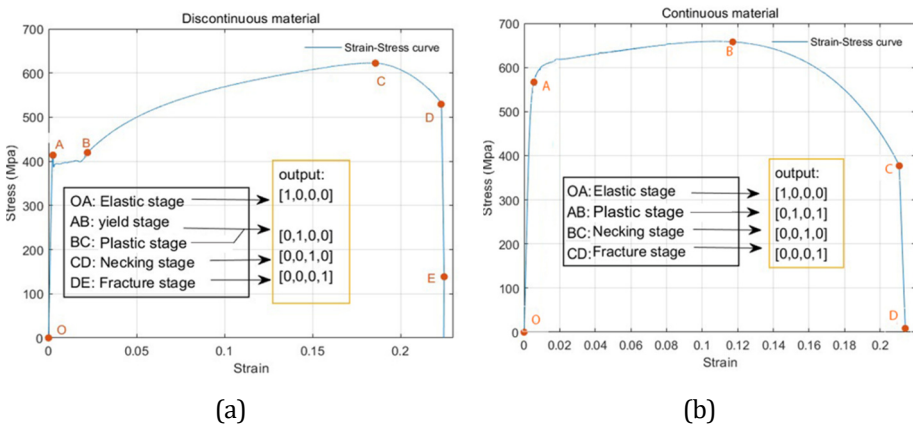


Fig. 4-13 Strain-stress curve for steel material: (a) discontinuous yielding material, and (b) continuous material

Generally, according to the appearance of a distinct plateau, the steel material can be classified as discontinuous yielding and continuous yielding materials (see Fig. 4-13). Various deformation stages are included in these two materials. It is well recognized that the AE signals depend on the AE source mechanisms. During the yielding and plastic stage, the AE source mechanism is the dislocation multiplication inside the material. When the specimen enters the necking stage, the specimen exhibits significant deformation. The freedom for further dislocation shrinks significantly with considerable dislocation congestion. Meanwhile, the formation of micro-cracks also

reduces the transmission of AE activity. Finally, the abrupt decrease in stress is followed by a sudden increase in the AE activity and amplitude of AE signals. The specimen starts to develop microscopic cracks and these cracks keep growing until the final fracture. Hence, stage AB and BC in discontinuous yielding material is summed into one stage. In total, no matter for discontinuous or continuous yielding material, four deformation stages are identified. Correspondingly, the output layer is a 4×1 vector [P1, P2, P3, P4] to represent the different deformation stages (see Fig. 4-13): [1, 0, 0, 0] represents the elastic stage; [0, 1, 0, 0] represents the plastic stage; [0, 0, 1, 0] represents the necking stage; and [0, 0, 0, 1] represents the final fracture stage. For S500 and S700 steel, an offset yield of 0.2% ($R_{p0.2}$) was used to determine the yield point A for these materials.

4.5.2 Architecture of the network

Table 4-3 summarizes the number of collected signals during the tensile tests. The samples are in unbalanced distribution for different stages which will decrease the prediction accuracy or generalization of the network. Focal loss is selected as the loss function to address the class imbalance problem. A modulating factor $(1-p_i)^\gamma$ and a weight factor α_t can adjust the weight of samples from each class for the multi-classification problem. The focal loss is designed as:

$$FL(p_i) = -\alpha_t (1-p_i)^\gamma \log(p_i) \quad \text{Eq. 4-14}$$

In this chapter, weight factors α_t are set as 1.5, 0.25, 2, and 1 for identifying yielding, plastic, necking, and fracture stages, respectively.

Table 4-3 Collected signals for machine learning-based analysis

Name	Number of data				Total
	Elastic stage	Plastic stage	Necking stage	Fracture stage	
S355-1	7	12	4	4	27
S355-2	2	155	1	101	259
S355-3	13	532	1	11	557
S355-4	15	386	1	52	454
S500-1	1	5	7	3	16
S500-2	18	5	3	7	33
S5003	35	41	43	7	126
S700-1	173	62	42	147	424
S700-2	75	1112	0	99	1286
S700-3	96	88	10	27	221
Total	435	2398	112	458	3403

A widely accepted approach, the K-fold cross-validation technique (K=5) [50], was utilized to train the network for classification with robustness to the overfitting problem. As illustrated in Fig. 4-14, the data set was randomly split into a test set (20%) and a training data set (80%) with a training fold (64%) and 5 disjoint validation folds (16%). Hyperparameters tuning was conducted to find the optimal solution. Hyperparameters include the learning rate η and the number of hidden layers was fine-tuned

using grid search. A Quantitative evaluation is provided by 5 indexes: Accuracy (ACC) and four areas under the receiver operating characteristics (ROC) curves ($AUC_i, i=1:4$). Accuracy (ACC) is defined as the correct number of predictions divided by the number of total data. This represents the total effectiveness of the classification. AUC_i measures the performance for each deformation stage classification. The average of these 5 indexes was employed as the indicator for the prediction accuracy. Based on the results of the hyper-parameters tuning, the optimal architecture is illustrated in Fig. 4-12 and the main hyper-parameters are summarized in Table 4-4. In the input layer, 6 input neurons represent duration, amplitude, signal strength, peak frequency, energy and fuzzy cross-entropy respectively. 3 hidden layers are set with 12, 8 and 6 artificial neuron units, respectively. The neuron units have 2 functions: a linear combination of input with regulated weightage and nonlinear complex functional mapping by ReLU activation functions. The output layer contains 4 neuron units which represent the possibility of 4 different deformation stages. The activation function is Softmax, which is appropriate for the multi-classification problem.

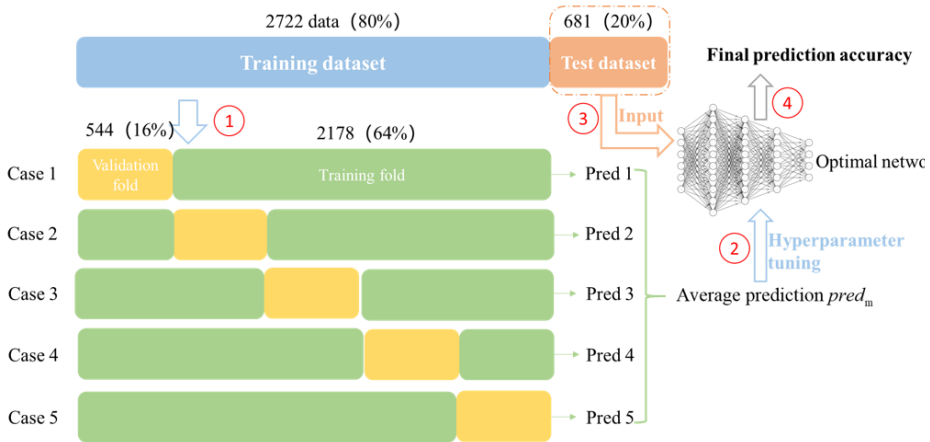


Fig. 4-14 Process of k-fold cross validation

Table 4-4 The main hyper-parameters of the proposed ANN

Learning rate	Number of hidden layers	Epoch	Batch size	Optimizer	Loss function
0.04	3	200	1000	Nadam	focal loss

4.5.3 Training results and discussion

To increase the converging speed, the training set is normalized before it is input into the networks. Fig. 4-15 illustrates the training history of loss and learning curves for the training and test dataset. The loss and accuracy values are shown at every 1 epoch and the maximum number of epochs employed in this chapter is 200. The loss begins with 0.45 and then a dramatic decreased tendency is observed until 100 iterations. Then the curve is flat indicating convergence. As indicated in Fig. 4-15 (b), the training curve starts with an accuracy of 0.6 which can be contributed to the good initial parameter setting. From 1 to 20 epochs, the accuracy rises rapidly and reaches 0.9 after 20 epochs for training and test dataset. Finally, the accuracy curve converges to an expected value of 0.93. The visualization of part classification results is shown in Fig. 4-16 and the corresponding accuracy index is summarized in Table 4-5. Without adopting the unloading-reloading phase, discontinuous material specimens provide higher-quality data thus deriving higher accuracy compared to continuous material.

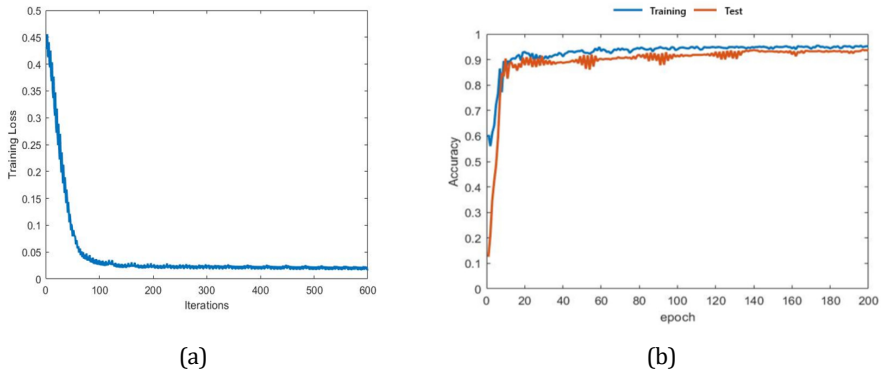
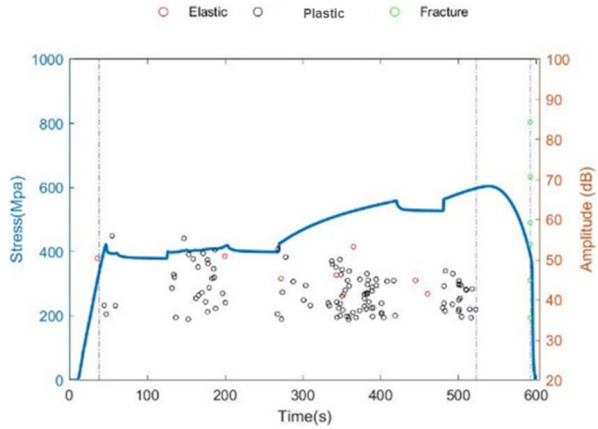


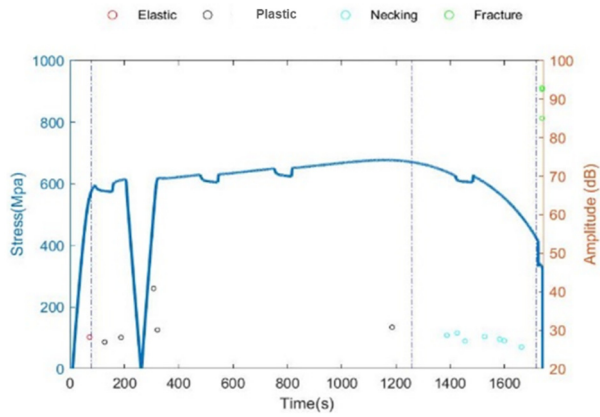
Fig. 4-15 (a) Loss and (b) learning curves of the optimized FCNN

Table 4-5 Classification accuracy for each specimen

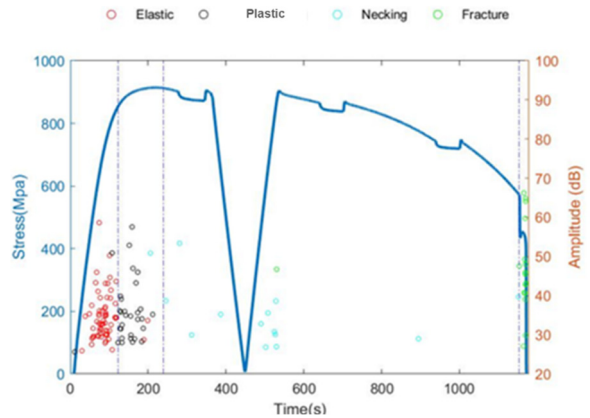
Material	Name	Accuracy
Discontinuous material	S355-1	0.963
	S355-2	0.950
	S355-3	0.922
	S355-4	0.958
Continuous material	S500-1	1.000
	S500-2	0.848
	S500-3	0.941
	S700-1	0.939
	S700-2	0.906
	S700-3	0.824



(a)



(b)



(c)

Fig. 4-16 Classification results visualization (a) S355-1, (b) S500-1, and (c) S700-1

Network generalization describes how well a trained network performs with new data [51]. Unseen data is collected from a continuous material specimen S700-4, with 8 mm thickness and constant loading rate. The specimen was tested under the same test setup and AE acquisition system. The collected AE signals were denoised by SSA-VMD with identical parameters as previously described. Fig. 4-17 shows the classification results for S700-4. The prediction accuracy is 0.87 which is smaller than 0.93 for the test dataset. Despite the decrease in accuracy, the results still demonstrate the efficiency of the trained ANN. It implies the potential of applying ANN-based deformation stage identification for various steel materials.

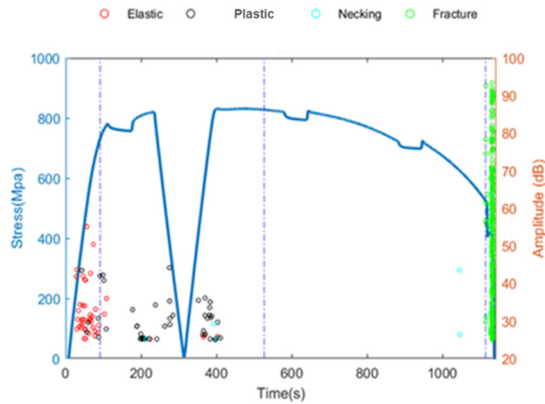


Fig. 4-17 Classification results of S700-4

4.6 CONCLUSION

The deformation of the steel member is vitally important to the safety of infrastructure. Identification of the deformation stage is possible to be achieved using Artificial neural network (ANN) combined with Acoustic emission (AE) monitoring. However, the efficiency of ANN-based deformation stage identification is hindered by the existence of noise in practical applications. The main objective of this chapter is to improve the application of ANN-based deformation stage identification with a proposed SSA-VMD denoising method. The key finding can be concluded as follows:

- The proposed SSA-VMD method is an adaptive algorithm for filtering both wide-band ground noise and narrow-band mechanical noise effectively. This method provides the solution to select the proper parameters without the time-consuming numerical simulation.
- Compared to conventional methods, i.e., WT and SSA, SSA-VMD can reduce noise while keeping relevant elements of the original signals under strong noise conditions ($\text{SNR} < 0$). The denoising performance of the proposed method was validated and demonstrated by using the simulation signals and real signals during tensile tests.

- The combination of SSA-VMD with ANN achieves the deformation stage identification successfully under a seriously noisy environment. Taking the features of filtered AE signals as the input, the designed ANN achieves a prediction accuracy of 0.93 for the test dataset and 0.87 for the unseen dataset. AE signals were collected from steel coupon tensile tests with various steel grades and loading conditions. The outcomes show the potential of ANN-based deformation stage identification in a broader application.

This chapter addresses research question Q3) by utilizing a combination of artificial neural network (ANN) and the singular spectrum analysis-vibration mode decomposition (SSA-VMD) denoising method. The results obtained from this chapter provide evidence for the efficacy of employing artificial intelligence techniques to process acoustic emission (AE) signals. Subsequent chapters will focus on investigating the use of thin-film lead zirconate titanate (PZT) for AE monitoring.

REFERENCES

- [1] H.L. Dunegan, D.O. Harris, C.A. Tatro, Fracture analysis by use of acoustic emission, *Eng. Fract. Mech.* 1 (1968) 105–122. [https://doi.org/10.1016/0013-7944\(68\)90018-0](https://doi.org/10.1016/0013-7944(68)90018-0).
- [2] H.N.G. Wadley, C.B. Scruby, Cooling rate effects on acoustic emission-microstructure relationships in ferritic steels, *J. Mater. Sci.* 1991 2621. 26 (1991) 5777–5792. <https://doi.org/10.1007/BF01130115>.
- [3] H.N.G. Wadley, C.B. Scruby, Spheroidal inclusion effects on acoustic emission-microstructural relations in ferritic steels, *J. Mater. Sci.* 1993 289. 28 (1993) 2517–2530. <https://doi.org/10.1007/BF01151687>.
- [4] C.B. Scruby, H.N.G. Wadley, Tempering effects on acoustic emission-microstructural relationships in ferritic steels, *J. Mater. Sci.* 1993 289. 28 (1993) 2501–2516. <https://doi.org/10.1007/BF01151686>.
- [5] C.K. Mukhopadhyay, K.K. Ray, T. Jayakumar, B. Raj, Acoustic emission from tensile deformation of unnotched and notched specimens of AISI type 304 stainless steels, *Mater. Sci. Eng. A.* 255 (1998) 98–106. [https://doi.org/10.1016/S0921-5093\(98\)00771-0](https://doi.org/10.1016/S0921-5093(98)00771-0).
- [6] S. Hao, S. Ramalingam, B.E. Klamecki, Acoustic emission monitoring of sheet metal forming: Characterization of the transducer, the work material and the process, *J. Mater. Process. Technol.* 101 (2000) 124–136. [https://doi.org/10.1016/S0924-0136\(00\)00441-6](https://doi.org/10.1016/S0924-0136(00)00441-6).
- [7] J. Ahmed, T. Zhang, D. Ozevin, M. Daly, A multiscale indentation-based technique to correlate acoustic emission with deformation mechanisms in complex alloys, *Mater. Charact.* 182 (2021) 111575. <https://doi.org/10.1016/J.MATCHAR.2021.111575>.
- [8] W. Zhou, Y.G. Du, S.D. Wang, Y.P. Liu, L.H. Ma, J. Liu, Effects of welding defects on the damage evolution of Q245R steel using acoustic emission and infrared thermography, *Nondestruct. Test. Eval.* (2022). <https://doi.org/10.1080/10589759.2022.2094377>.
- [9] J. Yang, C. Zhang, H. Li, Y. Xia, Z. Yang, B. Pang, H. Wang, G. Sun, The development of deformation mechanism during tension at different strain rates for GH4169 superalloys quantified by in-situ acoustic emission, *Mater. Today Commun.* 33 (2022) 104239. <https://doi.org/10.1016/J.MTCOMM.2022.104239>.
- [10] K. Barat, H.N. Bar, D. Mandal, H. Roy, S. Sivaprasad, S. Tarafder, Low temperature tensile deformation and acoustic emission signal characteristics of AISI 304LN stainless steel, *Mater. Sci. Eng. A.* 597 (2014) 37–45. <https://doi.org/10.1016/j.msea.2013.12.067>.
- [11] C. Sun, W. Zhang, Y. Ai, H. Que, Study of the tensile damage of high-strength aluminum alloy by acoustic emission, *Metals (Basel)*. 5 (2015) 2186–2199. <https://doi.org/10.3390/met5042186>.
- [12] T. Haneef, B. Baran Lahiri, S. Bagavathiappan, C. Kumar Mukhopadhyay, J. Philip, B. Purna Chandra Rao, T. Jayakumar, Study of the tensile behavior of AISI type 316 stainless steel using acoustic emission and infrared thermography techniques, *Integr. Med. Res.* 4 (2015) 241–253. <https://doi.org/10.1016/j.jmrt.2014.12.008>.
- [13] H. Sayar, M. Azadi, M. Alizadeh, Detection of Crack Initiation and Propagation in Aluminum Alloy Under Tensile Loading, Comparing Signals Acquired by Acoustic Emission and Vibration Sensors, *J. Nondestruct. Eval.* 38 (2019) 100. <https://doi.org/10.1007/s10921-019-0639-9>.
- [14] I. Lyasota, B. Kozub, J. Gawlik, Identification of the tensile damage of degraded carbon steel and ferritic alloy-steel by acoustic emission with in situ microscopic investigations, *Arch. Civ. Mech. Eng.* 19 (2019) 274–285. <https://doi.org/10.1016/j.acme.2018.09.011>.

- [15] J. Xu, T. Sun, Y. Xu, Q. Han, Fracture toughness research of G20Mn5QT cast steel based on the acoustic emission technique, *Constr. Build. Mater.* 230 (2020) 116904. <https://doi.org/10.1016/j.conbuildmat.2019.116904>.
- [16] A. Marchenkov, D. Chernov, D. Zhgut, A. Pankina, E. Rudenko, A. Poroykov, E. Kulikova, T. Kovaleva, Investigation of the Scale Factor Impact on the Results of Acoustic Emission Monitoring of the Steel Specimens Tension Process, *Appl. Sci.* 12 (2022) 8280. <https://doi.org/10.3390/APP12168280>.
- [17] J. Huang, Z. Zhang, C. Han, G. Yang, Identification of Deformation Stage and Crack Initiation in TC11 Alloys Using Acoustic Emission, *Appl. Sci.* 10 (2020) 3674. <https://doi.org/10.3390/app10113674>.
- [18] J. Vetrone, J.E. Obregon, E.J. Indacochea, D. Ozevin, The characterization of deformation stage of metals using acoustic emission combined with nonlinear ultrasonics, *Measurement*. 178 (2021) 109407. <https://doi.org/10.1016/j.measurement.2021.109407>.
- [19] S. Zou, F. Yan, G. Yang, W. Sun, The identification of the deformation stage of a metal specimen based on acoustic emission data analysis, *Sensors (Switzerland)*. 17 (2017). <https://doi.org/10.3390/s17040789>.
- [20] L. Zhang, S. Oskoe, H. Li, D. Ozevin, Combined Damage Index to Detect Plastic Deformation in Metals Using Acoustic Emission and Nonlinear Ultrasonics, *Materials (Basel)*. 11 (2018) 2151. <https://doi.org/10.3390/ma11112151>.
- [21] C.U. Grosse, M. Ohtsu, *Acoustic emission testing*, Springer Science & Business Media, 2008. <https://doi.org/10.1016/B978-0-12-804176-5.00028-1>.
- [22] K. Ono, *Acoustic Emission*, in: *Springer Handb. Acoust.*, Springer New York, New York, NY, 2014: pp. 1209–1229. https://doi.org/10.1007/978-1-4939-0755-7_30.
- [23] L. Cheng, H. Xin, R.M. Groves, M. Veljkovic, Plasticity and damage characteristic of acoustic emission signals for S460 steel exposed to tensile load, in: *Virtual Conf. Mech. Fatigue*, University of Porto, Portugal, 2020. https://www.researchgate.net/publication/344235805_Plasticity_and_damage_characteristic_of_acoustic_emission_signals_for_S460_steel_exposed_to_tensile_load.
- [24] H. Wang, H. Luo, Z. Han, Q. Zhong, Investigation of damage identification of 16Mn steel based on artificial neural networks and data fusion techniques in tensile test, *Lect. Notes Comput. Sci. (Including Subser. Lect. Notes Artif. Intell. Lect. Notes Bioinformatics)*. 5678 LNAI (2009) 696–703. https://doi.org/10.1007/978-3-642-03348-3_73/COVER.
- [25] J. Krajewska-Śpiewak, I. Lasota, B. Kozub, Application of classification neural networks for identification of damage stages of degraded low alloy steel based on acoustic emission data analysis, *Arch. Civ. Mech. Eng.* 20 (2020) 1–10. <https://doi.org/10.1007/S43452-020-00112-3/TABLES/4>.
- [26] X. Li, A brief review: acoustic emission method for tool wear monitoring during turning, *Int. J. Mach. Tools Manuf.* 42 (2002) 157–165. [https://doi.org/10.1016/S0890-6955\(01\)00108-0](https://doi.org/10.1016/S0890-6955(01)00108-0).
- [27] D. Bianchi, E. Mayrhofer, M. Gröschl, G. Betz, A. Vernes, Wavelet packet transform for detection of single events in acoustic emission signals, *Mech. Syst. Signal Process.* 64–65 (2015) 441–451. <https://doi.org/10.1016/j.ymssp.2015.04.014>.
- [28] N.E. Huang, Z. Shen, S.R. Long, M.C. Wu, H.H. Shih, Q. Zheng, N.-C. Yen, C.C. Tung, H.H. Liu, The empirical mode decomposition and the Hilbert spectrum for nonlinear and non-stationary time series analysis, *Proc. R. Soc. London. Ser. A Math. Phys. Eng. Sci.* 454 (1998) 903–995.
- [29] Z. Wu, N.E. Huang, Ensemble empirical mode decomposition: a noise-assisted data analysis method, *Adv. Adapt. Data Anal.* 1 (2011) 1–41. <https://doi.org/10.1142/S1793536909000047>.

- [30] K. Dragomiretskiy, D. Zosso, Variational mode decomposition, *IEEE Trans. Signal Process.* 62 (2014) 531–544. <https://doi.org/10.1109/TSP.2013.2288675>.
- [31] X. Zhao, P. Wu, X. Yin, A quadratic penalty item optimal variational mode decomposition method based on single-objective salp swarm algorithm, *Mech. Syst. Signal Process.* 138 (2020) 106567. <https://doi.org/10.1016/J.YMSSP.2019.106567>.
- [32] Y. Zhou, Z. Zhu, A hybrid method for noise suppression using variational mode decomposition and singular spectrum analysis, *J. Appl. Geophys.* 161 (2019) 105–115. <https://doi.org/10.1016/J.JAPPGEO.2018.10.025>.
- [33] D.S. Broomhead, G.P. King, On the qualitative analysis of experimental dynamic systems, *Phys. D Nonlinear Phenom.* 20 (1986) 217–236.
- [34] Y. Zhou, G. Wu, Unsupervised machine learning for waveform extraction in microseismic denoising, *J. Appl. Geophys.* 173 (2020) 103879. <https://doi.org/10.1016/J.JAPPGEO.2019.103879>.
- [35] S. Sud, Combined variational mode decomposition and singular spectral analysis for blind source separation in low signal-to-noise ratio environments, *Conf. Proc. - IEEE SOUTHEASTCON. 2021-March* (2021). <https://doi.org/10.1109/SOUTHEASTCON45413.2021.9401937>.
- [36] Z. May, M.K. Alam, N.A.A. Rahman, M.S. Mahmud, N.A. Nayan, Denoising of Hydrogen Evolution Acoustic Emission Signal Based on Non-Decimated Stationary Wavelet Transform, *Process.* 2020, Vol. 8, Page 1460. 8 (2020) 1460. <https://doi.org/10.3390/PR8111460>.
- [37] L. Xu, S. Chatterton, P. Pennacchi, Rolling element bearing diagnosis based on singular value decomposition and composite squared envelope spectrum, *Mech. Syst. Signal Process.* 148 (2021) 107174. <https://doi.org/10.1016/J.YMSSP.2020.107174>.
- [38] N. Golyandina, V. Nekrutkin, A.A. Zhigljavsky, Analysis of time series structure: SSA and related techniques, in: CRC Press, 2001.
- [39] Y.J. Natarajan, D. Subramaniam Nachimuthu, New SVM kernel soft computing models for wind speed prediction in renewable energy applications, *Soft Comput.* 24 (2020) 11441–11458. <https://doi.org/10.1007/S00500-019-04608-W/TABLES/5>.
- [40] B.W. Wah, T. Wang, Y. Shang, Z. Wu, Improving the performance of weighted Lagrange-multiplier methods for nonlinear constrained optimization, *Inf. Sci. (Ny)*. 124 (2000) 241–272. [https://doi.org/10.1016/S0020-0255\(99\)00081-X](https://doi.org/10.1016/S0020-0255(99)00081-X).
- [41] S. Sud, Blind, Non-stationary Source Separation Using Variational Mode Decomp..., *Signal Process. An Int. J.* 13 (2020) 11–20. <https://www.slideshare.net/CSCJournals/blind-nonstationary-source-separation-using-variational-mode-decomposition-with-mode-culling> (accessed November 15, 2022).
- [42] K. Horváth, D. Drozdenko, K. Máthis, J. Bohlen, P. Dobroň, Deformation behavior and acoustic emission response on uniaxial compression of extruded rectangular profile of MgZnZr alloy, *J. Alloys Compd.* 680 (2016) 623–632. <https://doi.org/10.1016/J.JALLCOM.2016.03.310>.
- [43] Z. Jin, D. Wang, W. Jin, B. Wen, The wavelet transform in the acoustic emission signal feature extraction of the rubbing fault, *Proc. - 2009 1st Int. Work. Database Technol. Appl. DBTA 2009.* (2009) 283–286. <https://doi.org/10.1109/DBTA.2009.164>.
- [44] R. Yan, H. Xin, F. Yang, H. El Bamby, M. Veljkovic, K. Mela, A method for determining the constitutive model of the heat-affected zone using digital image correlation, *Constr. Build. Mater.* 342 (2022) 127981. <https://doi.org/10.1016/J.CONBUILDMAT.2022.127981>.
- [45] D. Ozevin, MEMS acoustic emission sensors, *Appl. Sci.* 10 (2020) 8966. <https://doi.org/10.3390/app10248966>.

- [46] L. Toubal, H. Chaabouni, P. Bocher, C. Jianqiang, Monitoring fracture of high-strength steel under tensile and constant loading using acoustic emission analysis, *Eng. Fail. Anal.* 108 (2020) 104260. <https://doi.org/10.1016/j.engfailanal.2019.104260>.
- [47] L. Cheng, H. Xin, R.M. Groves, M. Veljkovic, Acoustic emission source location using Lamb wave propagation simulation and artificial neural network for I-shaped steel girder, *Constr. Build. Mater.* 273 (2021) 121706. <https://doi.org/10.1016/j.CONBUILDMAT.2020.121706>.
- [48] A. Deng, L. Zhao, Y. Bao, Acoustic emission recognition using fuzzy entropy, *Proc. - 2009 IEEE Int. Conf. Intell. Comput. Intell. Syst. ICIS 2009.* 4 (2009) 75–79. <https://doi.org/10.1109/ICICISYS.2009.5357744>.
- [49] Y. Wei, Y. Yang, M. Xu, W. Huang, Intelligent fault diagnosis of planetary gearbox based on refined composite hierarchical fuzzy entropy and random forest, *ISA Trans.* 109 (2021) 340–351. <https://doi.org/10.1016/J.ISATRA.2020.10.028>.
- [50] B. Muruganatham, M.A. Sanjith, B. Krishnakumar, S.A.V. Satya Murty, Roller element bearing fault diagnosis using singular spectrum analysis, *Mech. Syst. Signal Process.* 35 (2013) 150–166. <https://doi.org/10.1016/J.YMSSP.2012.08.019>.
- [51] Z. Chang, Z. Wan, Y. Xu, E. Schlangen, B. Šavija, Convolutional neural network for predicting crack pattern and stress-crack width curve of air-void structure in 3D printed concrete, *Eng. Fract. Mech.* 271 (2022) 108624. <https://doi.org/10.1016/J.ENGFRACTMECH.2022.108624>.

5. DATA LEVEL FUSION OF ACOUSTIC EMISSION SENSORS

Compared to conventional commercially available sensors for AE monitoring, thin PZT sensors are miniature, lightweight and affordable, which makes them viable options for AE monitoring in restricted-access areas such as in the C1 wedge connection investigated in this chapter. The low signal-to-noise ratio (SNR) of thin PZT sensors and their limited effectiveness in monitoring thick structures result in decreased reliability of a single classical thin PZT sensor for damage detection. This research aims to enhance the functionality of thin PZT sensors in AE applications by employing multiple thin PZT sensors and performing a data-level fusion of their outputs.

This chapter addresses the fourth research question Q4) and is organized as follows: Section 5.1 describes the background of the application of thin PZT sensors for acoustic emission monitoring. Section 5.2 illustrates the knowledge about Acoustic emission signals, the proposed criteria for the thin PZT sensors selection, and the Convolutional Neural Network (CNN). The experimental set-up and results discussion are shown in Sections 5.3 and 5.4. After that, Section 5.5 details the proposed methodology for data fusion of multiple thin PZT sensors and evaluates its performance. The conclusions are drawn in Section 5.6.

Part of this chapter has been published as a conference paper: Cheng L, Nokhbatolfoghahai A, Groves RM, Veljkovic M. Acoustic Emission-Based Detection in Restricted-Access Areas Using Multiple PZT Disc Sensors. In European Workshop on Structural Health Monitoring. The experiments were performed under the instruction of Dr. Ali Nokhbatolfoghahai in the NDT Lab of the Faculty of Aerospace Engineering, TU Delft.

5.1 INTRODUCTION

An in-situ monitoring system should be able to undertake a proper assessment of residual life and evaluate the degradation of structural components[1]. AE technology relies on the radiation of acoustic (elastic) waves in a medium. The elastic waves are produced by the energy released due to sudden internal deformation in a material [2,3], such as plastic deformation, crack formation/expansion, fiber breakage, delamination in composites, impact etc. An AE system is normally made up of sensors, preamplifiers, and data acquisition devices. The AE sensors are normally mounted on the surface of the material, as shown in Fig. 5-1 [4]. Surface motions $f(t)$ produced by the elastic waves are transformed to electronic signals $a(t)$ by the sensor transfer functions, which can be mathematically represented as

$$a(t) = f(t) * w(t) * w_f(t) * w_a(t) \quad \text{Eq. 5-1}$$

Where $w(t)$, $w_f(t)$, and $w_a(t)$ are the time transfer functions of the AE sensors, filters, and preamplifiers. These collected signals can yield useful information for SHM at different levels, including signal identification, damage localization, and life prediction. The frequency responses of the filters ($w_f(t)$) and amplifiers ($w_a(t)$) are commonly characterized by flat or constant responses [5]. This implies that the recorded AE signal $a(t)$ is highly susceptible by various $w(t)$ corresponding to different AE sensors. Thus, the sensitivity of the AE sensors is critical for AE monitoring.

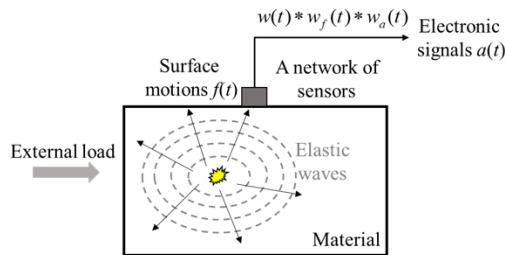


Fig. 5-1 Acoustic emission (AE) principle [4] where $w(t)$ is the transfer function of the AE sensor, $w_f(t)$ is the transfer function of the filter and $w_a(t)$ is the transfer function of the amplifier

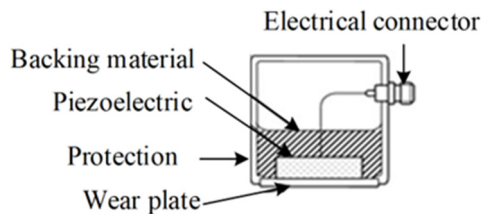


Fig. 5-2 Structures of conventional PZT bulky AE sensors [6]

AE-emitted signals are often recorded using high-sensitive piezoelectric sensors with the main frequency response within the 20 kHz to 1 MHz range. In conventional AE sensors, a PZT (Lead Zirconate Titanate) element is often enclosed in a stainless steel

housing to enhance sensitivity response. (see Fig. 5-2) [5,7]. They also have a detection face with wear plate to improve the electrical isolation from the tested object. Conventional bulky AE PZT sensors are designed technically as resonant or broadband types, such as the narrow band sensor R15 α [8] and wideband sensor WS α [9]. These conventional sensors have been successfully used in a variety of structures [10–15]. However, detecting AE signals with conventional sensors has inherent disadvantages, such as their bulky size and high cost. It is infeasible to apply large quantities of conventional AE sensors to the structure due to the high costs of the monitoring. Meanwhile, the non-negligible mass/volume of the sensors hinders their practical applications, especially for in-situ SHM [16]. Bulky AE sensors can be intrusive and potentially disturb the normal operation and functionality of the monitored structure.

A real-world example of the potential of AE for restricted access areas is shown in Fig. 5-3. This is an innovative C1 wedge connection used in offshore wind turbine (OWT) structures as introduced in chapters 2 and 3 [17]. To ensure the reliability of this connection, it is of paramount importance to have an effective method for early fatigue crack detection in this connection. But, the limited available space, with a height of less than 1 cm, makes it impractical to install conventional bulky AE sensors in the desired areas.

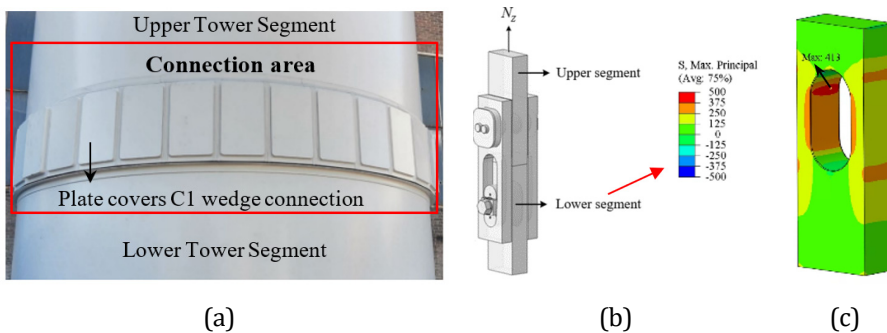


Fig. 5-3 The C1 wedge connection: (a) covered by corrosion protection plates in the OWT structure[17], (b) Lay-out of the connection (c) Principal stress distribution of the lower segment (the critical component)

Thin PZT sensors are miniature, low-cost, and lightweight, with several millimeters in height and a broadband response frequency. A thin PZT sensor works well for both exciting and detecting ultrasonic guided waves in SHM [18,19]. The installation process of thin PZTs can be complex and time-consuming, requiring expert knowledge and skills for proper placement and wiring. Over the past decade, numerous studies have demonstrated the feasibility of monitoring acoustic emissions with PWAS [20–23]. Compared to commercial sensors, thin PZTs can deliver equivalent detection findings regarding fatigue cracks in thin plate-like materials. However, they are less effective for monitoring the thick steel plate which only captured 5% AE events of recorded by R15I sensors [24]. Additionally, the analysis and comparison between conventional and PWAS are typically performed without any prior selection study for PWAS in passive

sensing applications [20,25]. Due to a lower signal-to-noise ratio (SNR), noise significantly impacts the efficiency of thin PZTs, hindering its performance. Furthermore, relying solely on measurements recorded by a single type of small PZT sensor may result in incomplete information regarding the underlying damage mechanism [26–28]. Using a single type of PWAS for AE monitoring has limited effectiveness, but it remains a viable alternative for monitoring critical areas with restricted access. To achieve accurate results in passive AE monitoring with PWAS, an optimized configuration of multiple PWAS and advanced signal processing methods are necessary.

Data fusion can extract information from the combination of different datasets instead of analyzing each dataset separately [29]. Generally, data fusion can be achieved on three levels: data level, feature level, and decision level [30,31]. At the data level, the original raw data are combined directly for further processing. In feature-level fusion, the feature extraction and selection from the original data are performed before further analysis. At the decision level, the decisions made from the different data sources are integrated to make the final assessment via particular combination rules. Previous works demonstrate the efficiency of combining data from multiple sensors to increase the accuracy and dependability of collected information. It is recommended to implement feature-based data fusion if the original data contain clearly distinguishable and adequate detectable features. In the case of an AE application with thin PZT sensors, data-level fusion is preferable since the original raw data from one thin PZT sensor type cannot represent all the essential characteristics of the damage mechanisms.

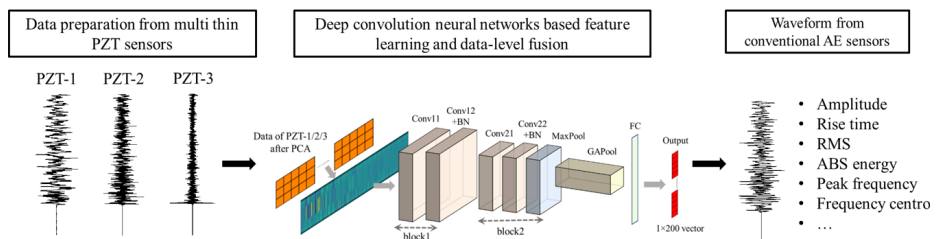


Fig. 5-4 A flowchart illustrating the proposed data-level fusion approach

However, the majority of research about multi-sensor data fusion has been performed at the feature level [32–36]. Considering the higher SNR ratio of conventional bulky AE PZT sensors, this chapter proposes a data-level fusion approach to reconstruct the signals from traditional AE sensors via the signals from thin PZT sensors (see Fig. 5-4). Compared to other available approaches, deep-learning-based approaches have been applied in a range of academic domains for image processing. Although 1D-CNNs can apply to time-series data, Wu et al. [37] have reported that 2D-CNNs perform better than the 1D-CNNs method and achieve higher accuracy and robustness. To enhance the efficiency of data-level fusion using CNN, PCA is used to minimize the dimensionality of the obtained waveforms without losing critical signal information. The output of the PCA is then adopted as the input to the CNN for data fusion.

This chapter explores the implementation of thin PZT sensors of different sizes for AE monitoring. To enhance the information completeness, criteria for choosing thin PZT sensors for a certain application are suggested. A detailed experimental analysis using Pencil break lead (PBL) tests on a compact-tension (CT) specimen was conducted to test the interchangeability between different types of sensors for AE monitoring. After that, I utilized a combination of multivariate analysis based on principal component analysis (PCA) and convolutional neural network (CNN) to fuse the signals from different thin PZT sensors. Finally, the performance of the established CNN was evaluated with the extracted features.

5.2 OVERVIEW OF THEORETICAL BACKGROUND

To explain the concept of the proposed methodology in more detail, Section 5.2 is divided into four parts. The most commonly employed acoustic emission signal features are briefly explained in Section 5.2.1. This is followed by the theory behind the thin PZT sensors and the proposed criteria for sensor selection in Section 5.2.2. Then, an introduction to the CNN architecture is given in Section 5.2.3. Principle Component Analysis (PCA) is utilized for dimensionality reduction of the input of the established CNN, which is presented in Section 5.2.4.

5.2.1 Acoustic emission signal features

SHM with the AE technique is properly explained by AE signal parameters. Fig. 5-5 shows the most widely used AE features in the time domain including amplitude, counts, duration, rise time, and count-to-peak. Absolute energy and signal strength are two features related to the area under the rectified signal envelope. Frequency-domain features also play a significant role in interpreting AE signals after fast Fourier transform (FFT). Representative parameters are the peak frequency (PF) and the frequency centroid (CF). PF is the frequency of the peak magnitude of the spectrum while CF is the centroid of the spectrum. Besides, AE signals can be described more precisely by the partial power (PP) features which measure the ratio of power in a user-specified frequency range (f_1 - f_2) to the complete power of a signal:

$$PP_{(f_1:f_2)} = \frac{\int_{f_1}^{f_2} U(f) df}{\int_0^{F/2} U^2(f) df} \quad \text{Eq. 5-2}$$

Where a power spectral density formula $U(f)$ is obtained using FFT from each signal, and F is the sampling frequency of the signals. $\int_0^{F/2} U^2(f) df$ computes the total power across the entire frequency range. Some further AE features are measured over a period of time, such as RMS (root mean square), AE hits, and rates.

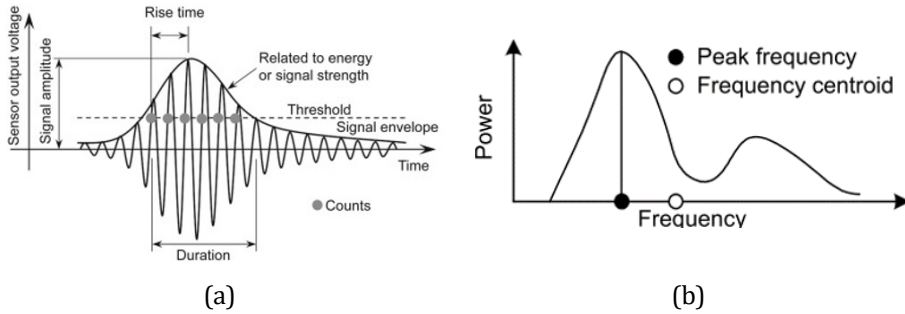


Fig. 5-5 Conventional AE features in (a) time domain [38], (b) frequency domain [5]

5.2.2 Thin PZT sensors selection criteria

Customized versions of thin PZT sensors are readily available. Shape, material, and geometry are key parameters for selecting thin PZT sensors. The following is a description of the basic theory underlying thin PZT sensors.

5.2.2.1 Shape determination

One of the most important factors for thin PZT sensors-based AE monitoring is the shape of the PZT element. In the monitoring of one-dimensional structural beams, rectangular thin PZT sensors are often used due to their strong directivity in signal receiving [39,40]. Whereas, a circular thin PZT sensor captures signals evenly from all directions. Therefore, thin PZT disc sensors are advantageous in two- or three-dimensional cases.

5.2.2.2 PZT Material

Two material parameters are significant when selecting suitable PZT materials [18], namely the piezoelectric charge coefficient d_{31} and the piezoelectric voltage coefficient g_{31} . The value of d_{31} is the mechanical strain in the in-plane direction (direction 1) experienced by a PZT material per unit of the electric field applied in the out-of-plane (direction 3). On the contrary, the value of g_{31} quantifies the out-of-plane electric field generated by a piezoelectric material per unit of mechanical stress applied in the in-plane direction. Therefore, d_{31} is an important indicator of the suitability of PZT material for actuator application, whereas, a higher g_{31} is favoured for sensing applications. PZT materials with the highest $d_{31} \times g_{31}$ are preferred for dual actuating and sensing applications. Table 5-1 presents the different types of materials from the selected PZT supplier (Physik Instrumente (PI)).

Table 5-1 Parameters for available piezoelectric materials

Parameter	PIC151	PIC255	PIC155	PIC153	PIC181	PIC141
$d_{31} \times 10^{-12} (\text{C/V})$	-210	-180	-165	-295	-120	-140
$g_{31} \times 10^{-3} (\text{Vm/V})$	-11.5	-11.3	-12.9	-8.1	-11.2	-13.1
$d_{31} \times g_{31} \times 10^{-15} (\text{m}^2/\text{V})$	2415	2034	2128.5	2389.5	1344	1834

5.2.2.3 Size of thin PZT sensors

Manufacturer-established graphs of the frequency response functions are available for conventional bulky AE sensors but not for thin PZT sensors. Based on previous research [41–43], a formulation incorporating sensor radius r_a and frequency was proposed by Ochôa et al.[44] for the sensor output voltage V_0 :

$$|V_0| \propto r_a \left[\sum_{\xi^S} \xi^S J_1(\xi^S r_a) + \sum_{\xi^A} \xi^A J_1(\xi^A r_a) \right] = f(\xi^S, \xi^A, r_a) \quad \text{Eq. 5-3}$$

where wavenumbers ξ^S and ξ^A represent the symmetric and antisymmetric Lamb wave modes, respectively. The wavenumbers are dependent on frequency, also known as a dispersion relationship. J_1 is the Bessel function of the first kind for Order 1. Eq. 5-3 enables the assessment of the sensitivity response of thin PZT sensors as receivers at various radiuses.

5.2.2.4 Thickness of thin PZT sensors

Owing to the electro-mechanical (E/M) behavior, an interaction occurs between the mechanical properties of the structure and the electrical impedance of the PZT sensors when they are attached to a structure [45]. It is possible to generate a risky transient area from states of resonance and anti-resonance of piezo ceramic. Using PZT sensors in this regime is detrimental to their steady and reliable performance. The following equations were proposed by Giurgutiu [19] for determining the electrical properties of a circular PZT sensor, including the influence of various PZT sensor thicknesses (TH):

$$Y(w) = iw\bar{C} \left\{ 1 - k_p^2 \left[1 - \frac{(1 + \nu_a) J_1(\bar{\phi})}{\bar{\phi} J_0(\bar{\phi}) - [(1 - \nu_a) - \bar{\chi}(w)(1 + \nu_a)] J_1(\bar{\phi})} \right] \right\} \quad \text{Eq. 5-4}$$

$$Z(w) = Y^{-1}(w) = \frac{1}{iw\bar{C}} \left\{ 1 - k_p^2 \left[1 - \frac{(1 + \nu_a) J_1(\bar{\phi})}{\bar{\phi} J_0(\bar{\phi}) - [(1 - \nu_a) - \bar{\chi}(w)(1 + \nu_a)] J_1(\bar{\phi})} \right] \right\}^{-1} \quad \text{Eq. 5-5}$$

where $Y(w)$ and $Z(w)$ is the E/M admittance and impedance response, respectively. \bar{C} is the electrical capacitance of the thin PZT sensors, k_p is the complex planar electromechanical coupling coefficient of the PZT material, ν_a is the Poisson ratio of the PZT material, J_1 and J_0 are Bessel functions of Order 1 and Order 0, respectively. The complex phase angle in the PZT material is represented by $\bar{\phi} = r_a \cdot (w / \bar{c}_a)$, where \bar{c}_a is

the complex in-plane wave speed in the PZT material and w is the angular frequency. The frequency-dependent complex stiffness ratio $\bar{\chi}(w)$ is given by $\bar{\chi}(w) = \bar{k}_{\text{str}}(w)/k_{\text{PWAS}}$, where $\bar{k}_{\text{str}}(w)$ is the structural stiffness and k_{PWAS} is the stiffness of the PZT sensors [19]. It should be noted that structural vibrations are considered in this calculation method. The mechanical damping ratio η and the electrical damping ratio δ are usually smaller than 5% for various thin PZT sensors [19]. Zeros in the denominator of Eq. 5-4 represent the resonance points, while zeros inside the curly brackets of Eq. 5-4 are anti-resonance points.

5.2.2.5 Criteria

The design methodology of thin PZT sensors for actuators and receivers was addressed in depth by Ochôa [44]. As for the AE application, the criteria for employing thin PZT sensors only as receivers are proposed: (a) The PZT sensors must have a high piezoelectric voltage coefficient of g_{31} and sufficient sensitivity over the frequency range for the intended application; (b) The E/M resonance point of the thin PZT sensors should not overlap with or be near the local peak of Eq. 5-3; (c) PZT sensors of greater thickness are preferred since their output response amplitudes are directly proportional to the thickness [46].

5.2.3 Convolution neural network

The conventional neural network (CNN) is a powerful tool for feature extraction and image analyses. In contrast to traditional Artificial neural networks (ANNs), CNN takes advantage of local connections, shared weights and sub-sampling. These operations enable the CNN model to extract representations of the image automatically at a low computational cost. A CNN is designed to process data from different arrays, such as 1D data like signals and sequences, 2D data for pictures or spectrograms, and 3D image data like computerized tomography (CT) scans.

A typical CNN model can be found in Fig. 5-6. It consists of three main kinds of layers, i.e., a convolutional (Conv) layer, a pooling layer and a fully connected (FC) layer [47]. A convolutional layer contains multiple filter kernels to extract local features over the whole image by the sliding process. These obtained features are then triggered by a non-linear function such as Sigmoid, Tanh, and ReLU. ReLU is the most frequently used activation function due to its simple implementation and less susceptibility to vanishing gradients [48]. Local response normalization (LRN) layers execute a mathematical operation on the $n \times n$ area to constrain the unbounded nature of ReLU. To address the issues of internal covariate shift, batch normalization (BN) is often used to stabilize and speed up network training [49].

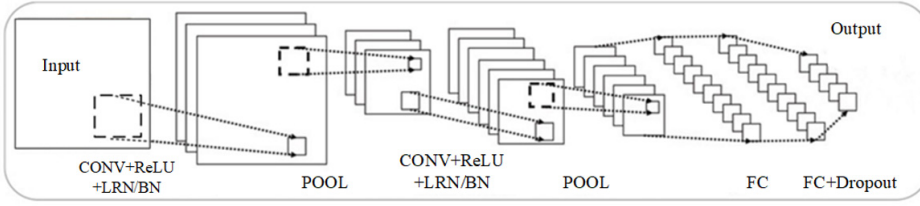


Fig. 5-6 Illustration of a typical conventional neural network

The generated feature maps usually have a considerable number of spatial dimensions after the convolutional operation. The pooling layer is added to reduce parameters, control over-fitting, and retain valid feature information. Convolution layers and pooling layers are repeated several times before being connected to the fully connected layers. In the fully connected layers, dropout layers randomly set input neurons as zero with a specific rate to avoid overfitting [50].

In this research, CNN is employed to fuse the signals from multiple thin PZT sensors to signals from the conventional AE sensors. The framework of the proposed CNN-based multi-sensor data fusion will be described in Section 5.5.

5.2.4 Principal component analysis

Considering computational inefficiency for data analysis, principal component analysis (PCA) is one of the most popular multivariate statistical analyses. This method can transform high-dimensional data into a low-dimensional subspace while retaining the most important features of the original data [51]. During the dimensional reduction process of PCA, new irrelevant variables defined as principal components (PC) are generated. The steps of PCA are described as follows for a matrix X with $M \times N$ dimensionality.

Firstly, matrix X with column-wise zero empirical mean is obtained by:

$$X' = \begin{bmatrix} x_{11} - \bar{x}_1 & x_{12} - \bar{x}_2 & \cdots & x_{1N} - \bar{x}_N \\ x_{21} - \bar{x}_1 & x_{22} - \bar{x}_2 & \cdots & x_{2N} - \bar{x}_N \\ \vdots & \vdots & \ddots & \vdots \\ x_{M1} - \bar{x}_1 & x_{M2} - \bar{x}_2 & \cdots & x_{MN} - \bar{x}_N \end{bmatrix} \quad \text{Eq. 5-6}$$

where \bar{x}_j ($j=1,2,\dots,N$) is the mean of each j -th column.

Then, the principal components transformation can be extracted with singular value decomposition (SVD) by:

$$X' = U \Sigma W^T \quad \text{Eq. 5-7}$$

where U is an M -by- M left singular matrix of X , Σ is an M -by- N rectangular diagonal matrix and W is an N -by- N right singular matrix of X . Finally, the reduced matrix X'' is derived from:

$$X'' = X'W(1:k,:)^T \quad \text{Eq. 5-8}$$

where k is the number of principal components. The cumulative contribution rate (CCR) is used to select the proper number of principle components which is expressed as

$$CCR = \sum_{i=1}^k D_i / \sum_{i=1}^N D_i \quad \text{Eq. 5-9}$$

where D_i is the singular values of matrix Σ in decreasing order, representing the directions of the variances. The goal is to select the value of k to be as small as possible but with a reasonably high CCR . In the context of SHM, PCA has been extensively applied with the extracted features from AE signals in the time domain [52]. To enhance the efficiency of data-level fusion using CNN, PCA is used to minimize the dimensionality of the obtained waveforms without losing critical signal information. The output of the PCA is then adopted as the input to the CNN for data fusion.

5.3 EXPERIMENTAL SET-UP

5.3.1 Sensors applied for measurements

After determining the shape and material of PZT sensors, the procedure for PZT geometry selection comprises the following four steps (see Fig. 5-7): (1) input various r_a into Eq. 5-3 and calculate corresponding sensor output functions; (2) choose a variety of PZT sensors with adequate sensitivity in the target frequency range; (3) input different thicknesses (TH) of thin PZT sensors (<1 mm) to Eq. 5-4 and calculate the E/M response; determining the optional thickness satisfying criteria (b) in section 5.2.2.5; (4) choose the larger thickness according to criteria (c) in section 5.2.2.5. Following this procedure, PZT-1 (r_a :10 mm \times TH: 0.79 mm), PZT-2 (r_a :5 mm \times TH: 0.8 mm), and PZT-3 (r_a :3 mm \times TH: 0.5 mm) were selected for monitoring CT specimens.

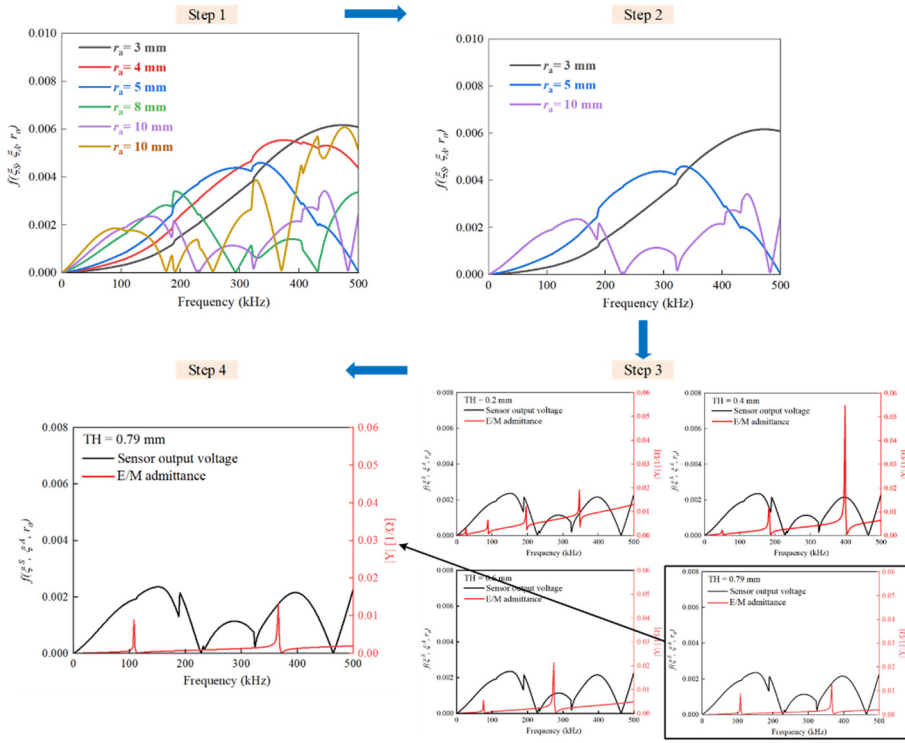


Fig. 5-7 Four steps for PZT geometry selection

Table 5-2 Characteristics of sensors [8,9,53]

Parameters	R15 α	WS α	PZT-1	PZT-2	PZT-3
Weight (g)	34	32	1.90	0.49	0.18
r_a (mm)	9.5	9.5	10	5	3
TH (mm)	22.40	21.40	0.79	0.80	0.50
Material	PZT-5A[54]	PZT-5A	PIC155	PIC155	PIC255
$g_{31} \times 10^{-3}$ (Vm/N)	-12.4	-12.4	-12.9	-12.9	-11.3

Note: r_a and TH are the radius and thickness of the selected sensors, respectively.

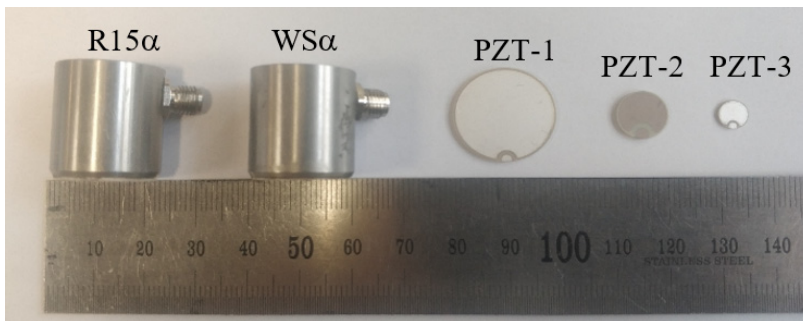


Fig. 5-8 Illustration of the sensors used in the measurement

The properties of the selected three types of thin PZT sensors are illustrated in Table 5-2 and Fig. 5-8. In thin PZTs, the resonance and anti-resonance points are always close to each other [19]. Hence, it is sufficient to find resonance points with infinite admittance. Fig. 5-9 displays the sensor output $f(\xi^S, \xi^A, r_a)$ and E/M admittance response $|Y|$ of PZT-1/2/3, which satisfy criteria (c) in section 5.2.2.5.

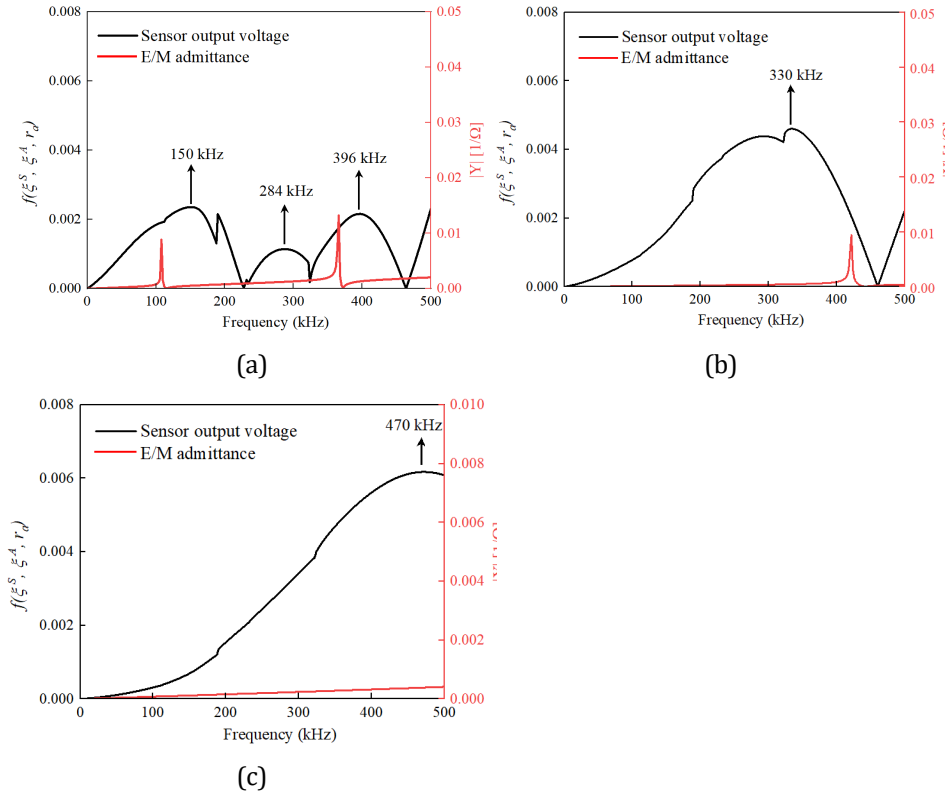


Fig. 5-9 Sensor output $f(\xi^S, \xi^A, r_a)$ and E/M admittance response of PZT-: (a) 1, (b) 2, and (c) 3

For the $R15\alpha$ sensor and $WS\alpha$ sensor, their frequency sensitivity spectra are obtained from MISTRAS Group [8,9] (Fig. 5-10). The sensor output for PZT-1/2/3 is calculated using Eq. 5-3, see Fig. 5-11. Frequencies beyond 500 kHz are removed because they are useless for the majority of applications [7]. Considering that the sensitivity response of conventional AE sensors is in decibels (dB), the sensor output voltage $y=f(\xi^S, \xi^A, r_a)\times TH$ is converted to decibels in Fig. 5-11 (b) using $dB = 20 \cdot \log_{10}(y)$. Fig. 5-11 shows that these three thin PZT sensors together span a frequency range of 0-500 kHz efficiently, which is inaccessible to individual thin PZT sensors.

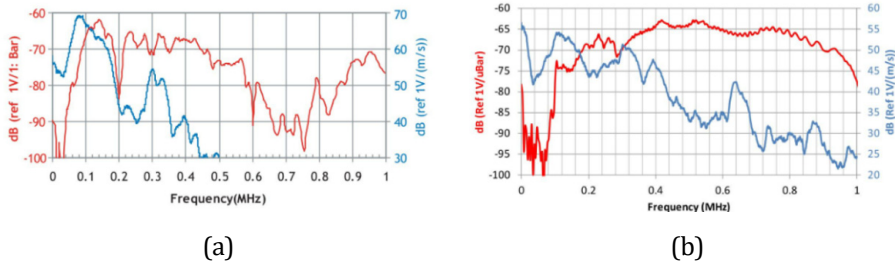


Fig. 5-10 Frequency sensitivity spectrum of (a) R15 α [8], (b) WS α [9] sensor

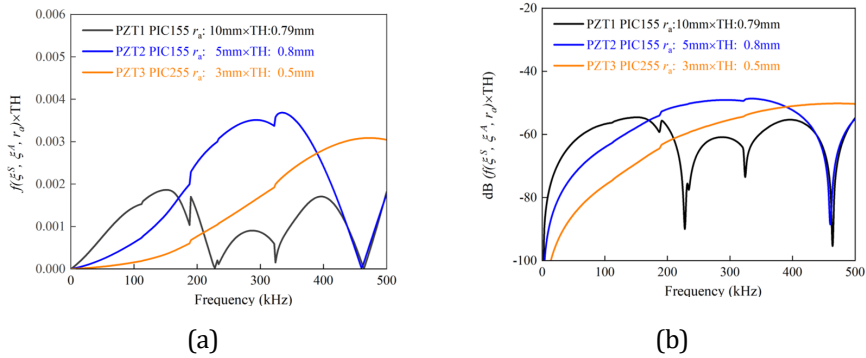


Fig. 5-11 Sensor output of PZT-1/2/3: (a) Frequency vs $f(\xi^S, \xi^A, r_a) \times TH$, (b) Frequency vs $\log(f(\xi^S, \xi^A, r_a) \times TH)$ (TH is the thickness of PZT sensors)

5.3.2 Measurement setup

To assess the feasibility of thin PZT sensors of different sizes and to compare the results with those recorded using the conventional bulky AE sensors, compact tension (CT) specimens (85 mm length, 85 mm width and 15 mm thickness), steel grade S355 were tested. The plate dimensions were selected such that the geometrical complexity and thick plate are included in the measurements. Two sensor combinations were used in the tests (see Fig. 5-12 (a)): (1) R15 α and PZT-1/2/3; and (2) WS α and PZT-1/2/3. To simulate the crack initiation, pencil lead breaking tests were performed at the notch tip (see Fig. 5-12 (b)). A total number of 120 pencil lead break tests were performed for each sensor layout while the parameters and settings remained the same for each test. To obtain enough data with randomness and uncertainty [55], the pencil leads were broken with various free lengths of 2-4 mm and contact angles of 20°-60°. The R15 α sensor and WS α sensors were mounted on the specimen surface using a thin layer of silicone grease as an ultrasonic couplant. The thin PZT sensors were bonded to the specimen surface using cyanoacrylate glue.

An eight-channel MISTRAS AE system with a 40dB pre-amplifier was used. A threshold value of 50 dB was set to filter noise. Each measurement was recorded at a sampling rate of 5 MSPS (one sample per 0.2 μ s) and 800 μ s long to capture the entire waveform. A pre-trigger of 256 μ s was defined to capture the signal sources. The peak defined time

(PDT), hit definite time (HDT), hit lookout time (HLT) and max duration was set as 400 μs , 800 μs , 800 μs and 99 ms, respectively. These timing parameters were determined by PBL trial tests. These four timing parameters play significant roles in data acquisition, including hits recording and signal feature extraction.

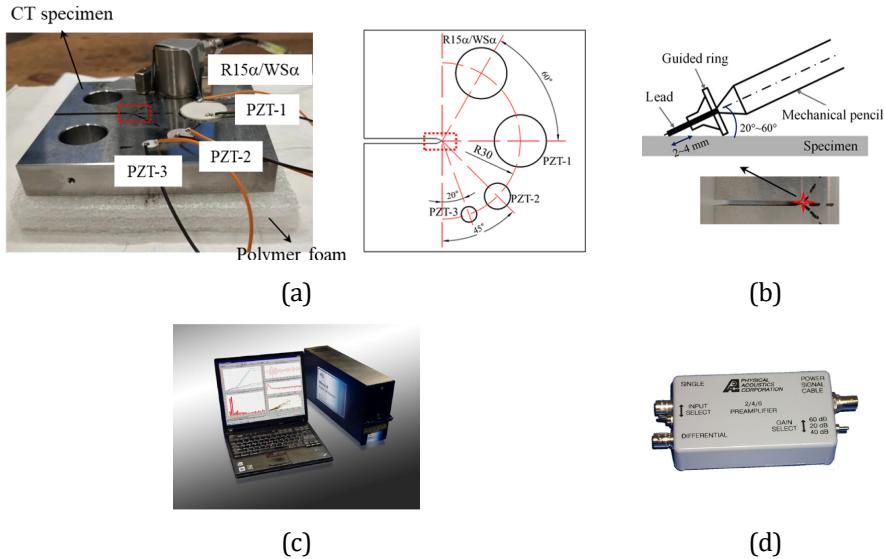


Fig. 5-12 Experimental set-up: (a) Layout of sensors; (b) Illustration of PBL tests; (c) Mistras AE system Express-8; (d) 2/4/6 signal amplifier

5.4 EXPERIMENTAL RESULTS DISCUSSION

AE signals experience multiple reflections, refractions and mode conversion as a result of the geometrical complexity and dynamic environment [15,56]. During the PBL tests, background noise can be eliminated effectively by recording signals without loading. However, the AE hits caused by side-edge reflection and electronic noise cannot be completely avoided after breaking pencil leads. Hence, the recorded signals are separated into two categories: (a) the directly arrived hits as PBL signals; (b) other hits as noise signals. This section compares the PBL signals and noise signals recorded by the chosen sensors. PBL signals measured from multi-sensors (in each layout) are identified using data association [34]. An association is considered if the signals appear within a temporal window of less than 20 μs . This value is selected to account for the influence of sensor size on signal acquisition time.

5.4.1 Signal response from breaking pencil leads

The similarity of PBL signals recorded from five types of sensors was analyzed using a cross-correlation coefficient (CCC) [57]. The higher value of CCC corresponds to a higher similarity between the signals from different pairs of sensors. The CCC of $x(t)$ and $y(t)$ is calculated as:

$$r_{xy}(\tau) = \int_{-\infty}^{\infty} x(t)y(t + \tau)dt \tag{Eq. 5-10}$$

where τ means the time shift of one signal with respect to another. The average value of the maximum cross-correlation coefficient (MCCC) obtained during 120 PBL events is summarized in Table 5-3. A low similarity between PBL signals from conventional AE sensors and thin PZT sensors is observed in Table 5-3.

Table 5-3 Similarity of PBL signals

Pair of sensors	R15 α	WS α	PZT-1	PZT-2	PZT-3
R15 α	1	0.24	0.16	0.17	0.08
WS α	0.24	1	0.11	0.15	0.08
PZT-1	0.16	0.11	1	0.17	0.14
PZT-2	0.17	0.15	0.17	1	0.12
PZT-3	0.08	0.08	0.14	0.12	1

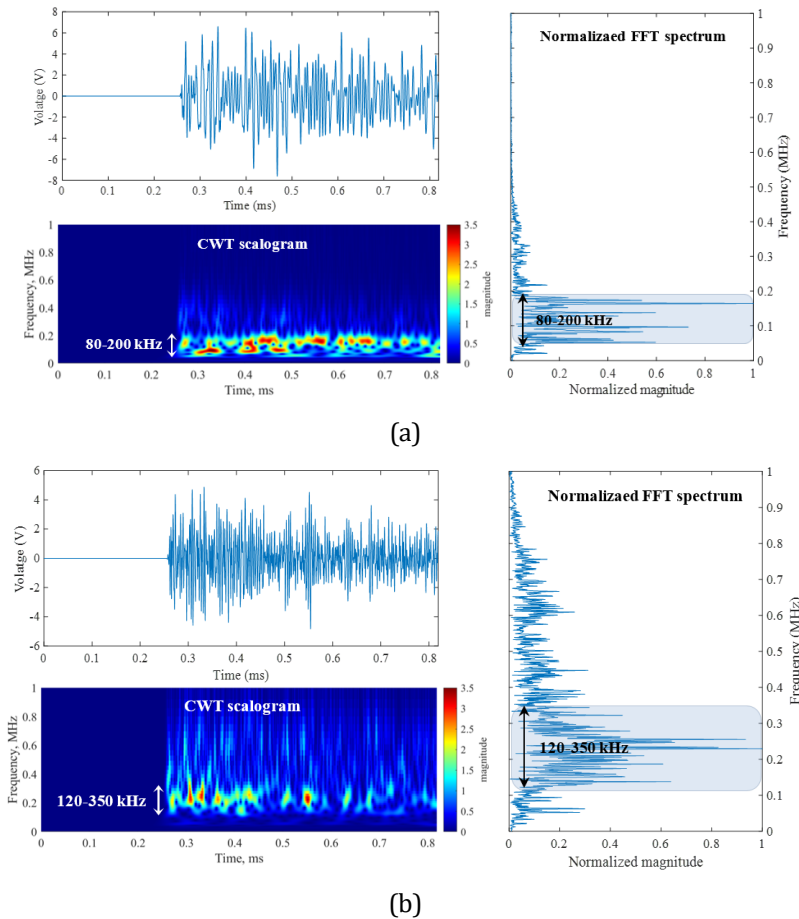
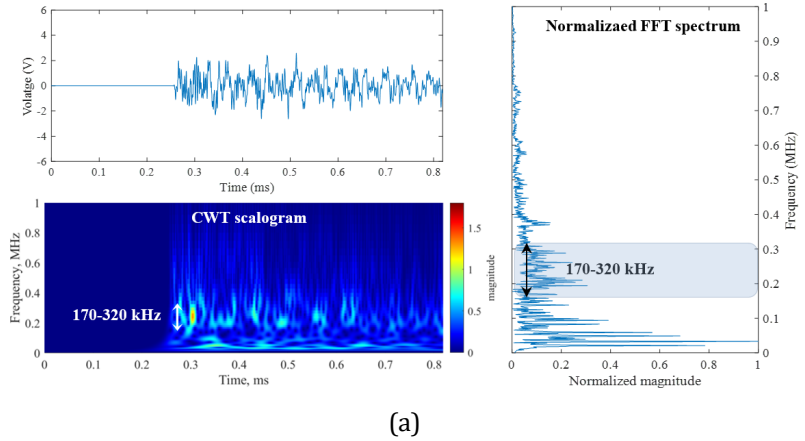
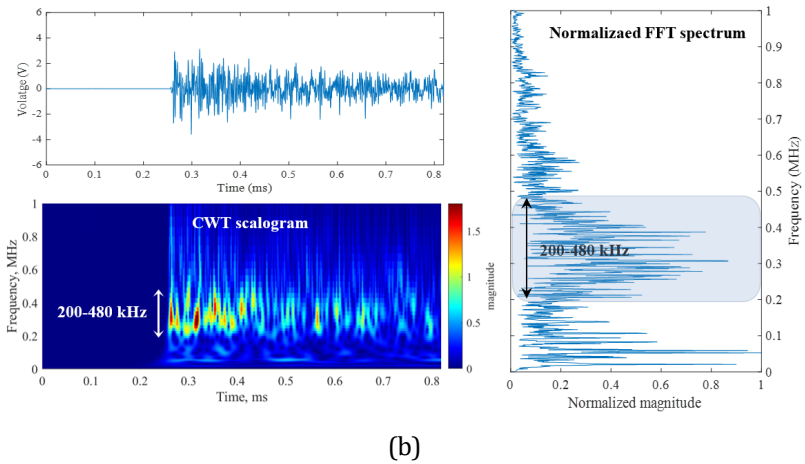


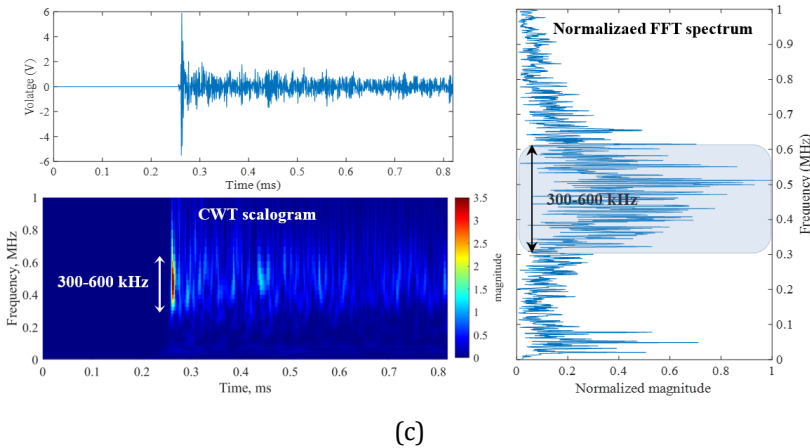
Fig. 5-13 Example of AE signals captured by: (a) R15 α sensor, (b) WS α sensor



(a)



(b)



(c)

Fig. 5-14 Example of AE signals captured by PZT-: (a) 1, (b) 2, and (c) 3

Examples of the waveform in the time domain, corresponding Continuous Wavelet Transform (CWT) scalogram, and FFT spectrum of PBL signals are shown in Fig. 5-13 and Fig. 5-14. The CWT scalograms are employed to accurately discriminate the distribution of signal energy in both the time and frequency domains. The waveforms show significant differences and only PZT-3 exhibits a burst-type response. Differences are also strong in the CWT scalograms based on the Gabor wavelet of the waveforms as well. The aperture effect significantly distorts signals received by sensors with larger sizes, resulting in the possibility of distortion caused by scattering or reflections [58]. The $WS\alpha$ sensor is characterized by a flat frequency response over a wideband frequency range of 100-1000 kHz. This sensor enables more accurate identification of the natural frequency characteristics of AE sources. An average value of $PP_{(80:500\text{kHz})}$ of 92% was calculated from the $WS\alpha$ sensor. Therefore, 80-500 kHz is selected as the primary frequency band of interest in the target objective.

Table 5-4 Time dependency of the frequency content of signals from different sensors

	R15 α	WS α	PZT1	PZT2	PZT3
Resonant frequency (kHz)	150	650	150/284/396	330	470
Frequency band with high sensitivity (kHz)	80-200	120-350	170-320	250-450	300-600
Overlap in amplitude distribution	No	No	Yes	Yes	Yes
Overlap in the frequency domain	Obviously	Partially	Obviously	Partially	Obviously

Table 5-4 describes the properties of the signals obtained from various sensors. Except for the nature of the frequency content of interest, the recorded signals are also influenced by the sensitivity response of the sensors. The first row in Table 5-4 presents the resonant frequency of each sensor. The resonant frequency of the R15 α and WS α sensors can be obtained from the manufacturers, and is shown in Fig. 5-10. Pertaining to PZT-1/2/3, the peaks of their sensor output functions (see Fig. 5-11) are extracted as the resonant frequency. In the frequency band of interest, PZT-1 has multiple resonant frequencies compared to other sensors. The frequency band with high sensitivity of sensors can be identified according to the typical boundary of the areas with high magnitude in the CWT scalograms from Fig. 5-13 and Fig. 5-14. The WS α sensors clarify that the primary frequency composition of detected signals is between 120 and 350 kHz, which is the original feature of the AE source. However, the R15 α sensor drastically changes its frequency content to 80-200 kHz. Similarly, the frequency sensitivity of thin PZT sensors also affects the nature of the AE-emitted source (see the second row in Table 5-4). This implies that thin PZT sensors cannot entirely be regarded as non-resonant devices [59–61]. The findings highlight the effect of sensor size as well as the drawbacks of employing a single type of thin PZT sensor.

5.4.2 Signal distinction

Compared to other features, the amplitude of signals is independent of the acquisition threshold [62]. The amplitude distribution of recorded signals during the PBL tests is shown in Fig. 5-15 to quantify the uncertainty of the recorded signals. As seen in Fig. 5-15, the R15 α sensor presents a much higher amplitude compared to the other sensors, representing a higher sensitivity. The median values of amplitude from the other sensors are approximately similar to each other. Noise signals can be distinguished effectively by considering the amplitude of the signals. The amplitude of PBL signals captured by R15 α and WS α usually exceeds 88 dB. Signal association techniques are employed to distinguish PBL signals from noise signals for PZT-1/2/3. However, the conventional bulky AE sensors show a more reliable performance than thin PZT sensors without overlap of amplitude distribution between PBL and noise signals. The fourth row in Table 5-4 presents the overlap in amplitude distribution of sensors.

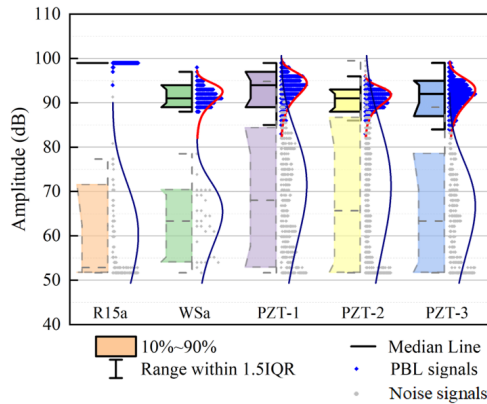


Fig. 5-15 Amplitude distribution of PBL signals and noise signals

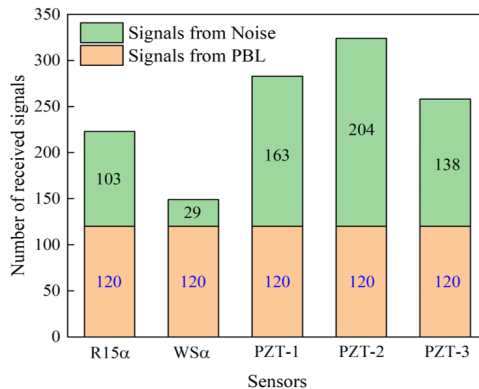


Fig. 5-16 Number of received signals during PBL tests

The distinction between signals from PBL and noise is necessary to guarantee the sensor performance for damage detection. As seen in Fig. 5-16, the $WS\alpha$ sensor captures the smallest number of noise signals compared to other sensors. In contrast, it can be observed that other sensors record a significant amount of noise signals that are not the first arrived signals. This indicates that $WS\alpha$ sensors offer superior data quality compared to the other sensors, highlighting their enhanced performance in capturing the desired signals. Fig. 5-17 shows the comparison between signals recorded by different types of sensors in the frequency domain. The PBL signals recorded by R15 α , PZT-1 and PZT-3 clearly overlap with the noise signals in the frequency domain. On the contrary, the noise signals from $WS\alpha$ and PZT-2 can be efficiently filtered by high-pass and low-pass filtering with a narrow overlap band, respectively. The situation of overlap in the frequency domain between recorded PBL and noise signals is summarized in Table 5-4. Considering that the R15 α sensor is more sensitive to noise than $WS\alpha$, $WS\alpha$ shows a performance benefit in AE detection, especially in a noisy environment.

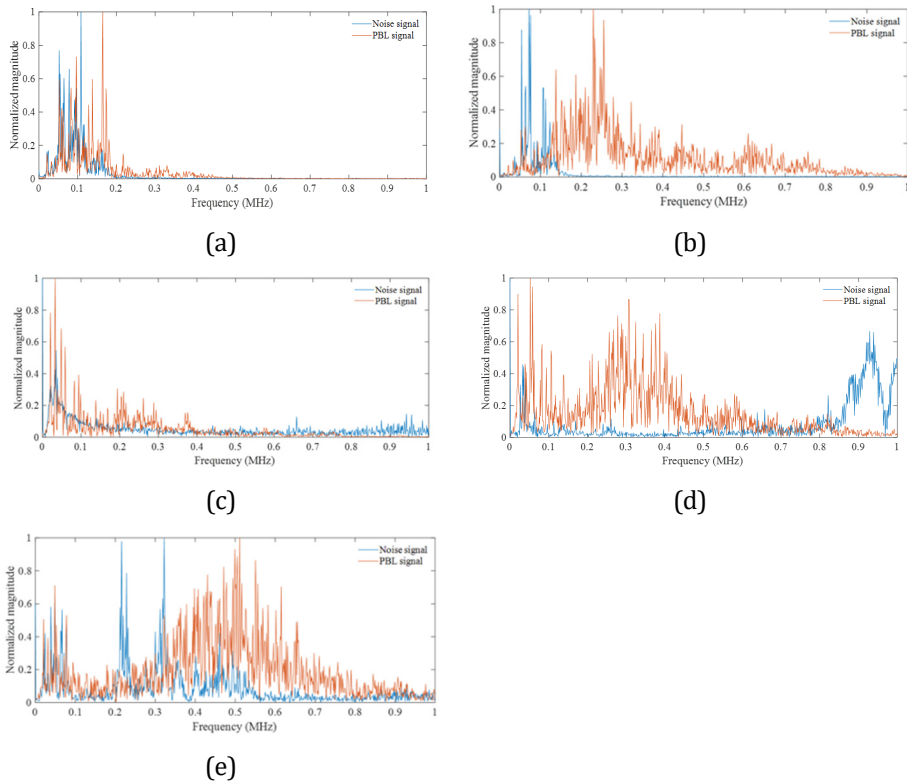


Fig. 5-17 Comparison of signals from: (a) R15 α , (b) $WS\alpha$, (c) PZT-1, (d) PZT-2, and (e) PZT-3

5.5 DATA FUSION OF MULTIPLE THIN PZT SENSORS

As described in Section 5.4, the $WS\alpha$ sensor is an attractive option for AE detection in a noisy situation. To extend the application of thin PZT sensors in fatigue monitoring of structures, this section proposes a methodology to fuse the data from multiple thin PZT sensors to $WS\alpha$ sensors.

5.5.1 Data preparation

The experimental set-up for the fatigue test is presented in Fig. 5-18. PBL tests were performed manually at the notch tip of the installed CT specimens with a similar measurement set-up as indicated in section 5.3.2. In this set-up, pencil leads were broken from both sides of the specimens to represent the actual crack initiation. In total, 5484 pairs of PBL signals were captured using data association. The signals captured by thin PZT sensors were prepared as the input data, while the output was the signals received by the $WS\alpha$ sensor.

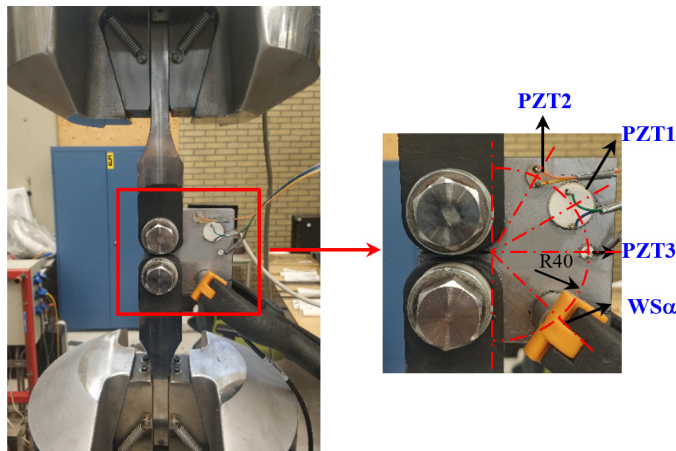


Fig. 5-18 Experimental set-up for data fusion

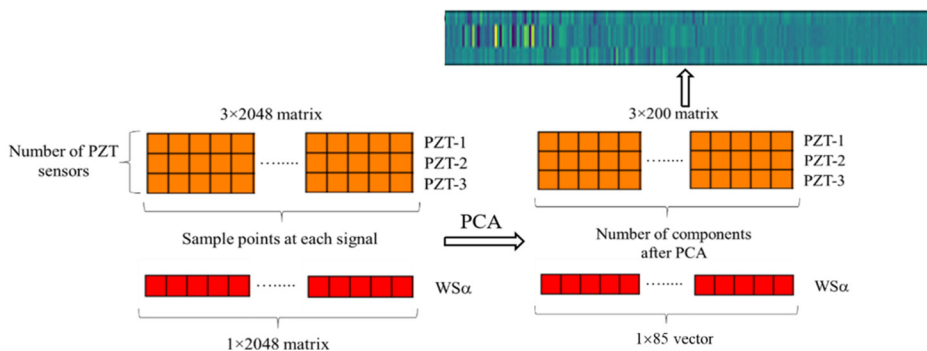


Fig. 5-19 Preparation of database by PCA

To increase the computational efficiency, the signals used for data fusion are pre-processed in the following steps: (1) remove pre-trigger of 256 μs ; (2) cut waveform to a certain wavelength of 200 μs to make sure a satisfactory frequency resolution of 5 kHz; (3) remove external noise from the reflection that contaminates the signals through the implementation of appropriate filters 80-500 kHz. (4) PCA is applied to reduce the number of features as seen in Fig. 5-19, which makes the machine learning model simpler and less data-hungry. It should be noted that PCA was employed for the signals both from the thin PZT sensors and the $\text{WS}\alpha$. PCA is conducted with the open-source Python package scikitlearn.

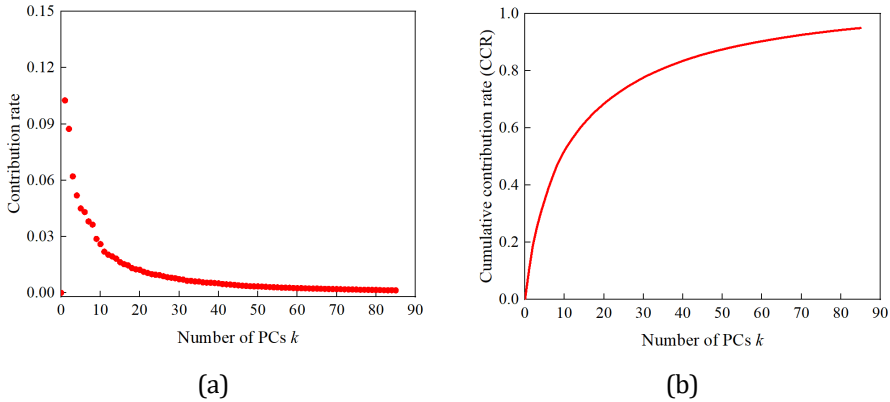


Fig. 5-20 (a) The relationship between the number of PCs and CCR (b) The contribution rate for the first 16 principal components

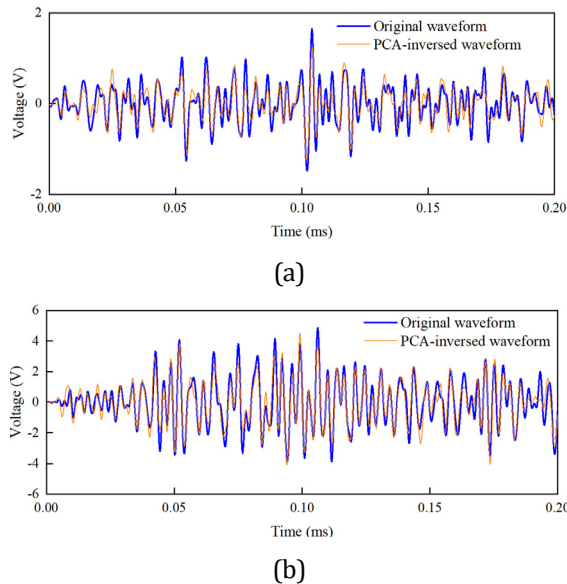


Fig. 5-21 Comparison between original and PCA inversed waveforms (a) example 1; (b) example 2;

The cumulative contribution rate (CCR) of the first 85 principle components (PCs) is described in Fig. 5-20 (a). CCR increases accordingly as the number of employed PCs increases and reaches around 95% with $k = 85$. This indicates that most information in the waveforms is represented by the first part of the PCs. A similar observation can also be made from Fig. 5-20 (b), which shows the contribution rate of the first 85 PCs. Hence, it is determined that PCA is efficient to compress the feature number from 2048 to 85 with only a 5% loss of the total information in the original waveforms. Fig. 5-21 shows two randomly picked examples to illustrate the comparison between original waveforms and PCA-inversed waveforms. Although 1D-CNNs can apply to time-series data, Wu et al. [37] have reported that 2D-CNNs perform better than the 1D-CNNs method and achieve higher accuracy and robustness. Consequently, the reduced 3×85 matrix of 5484 events was saved as images as shown in Fig. 5-19. These images were then passed as the input data for the CNN model in this research. The corresponding dimension of output data was also decreased from 2048 to a vector with 85 features.

5.5.2 Customized model evolution

The contribution rate of each principal component is represented by the PCA singular value D_i . To signify the uneven contribution of features in the CNN model, a weighted Mean Squared Error (MSE) is utilized [63] as the loss function. PCs with higher contribution rates are weighted more heavily than those with low contribution rates.

$$\text{Weighted MSE} = \sum_{i=1}^n \sum_{j=1}^r \frac{\lambda_i}{\sum_{k=1}^{85} \lambda_k} (y_{i,j} - y'_{i,j})^2 \quad \text{Eq. 5-11}$$

The i -th sample's actual and predicted values in the j -th feature are represented by y_{ij} and y'_{ij} , respectively. The CNN model is capable of being trained with information about the different importance of PCs using the adjusted MSE.

The cross-correlation function is commonly used to evaluate the similarity between time series [64]. Hence, the averaged MCCC between actual and predicted value after PCA-inverse is calculated as the assessment indicator.

$$\text{Accuracy} = \frac{1}{n} \sum_{i=1}^n \text{MCCC}(Y_i, Y'_i) \quad \text{Eq. 5-12}$$

The i -th sample's actual and predicted values after PCA-inverse transformation are represented by Y_i and Y'_i , respectively.

5.5.3 CNN model construction

The developed model is named $N_{\text{AE-PZT}}$, which means that it is a "Network trained to fuse the output from thin PZT sensors for AE monitoring". $N_{\text{AE-PZT}}$ adopts the waveform information from thin PZT sensors as input values. Similar to a typical CNN model, the input is transformed into a more and more abstract and composite representation layer by layer. Finally, the signal from the conventional bulky AE sensor is reconstructed.

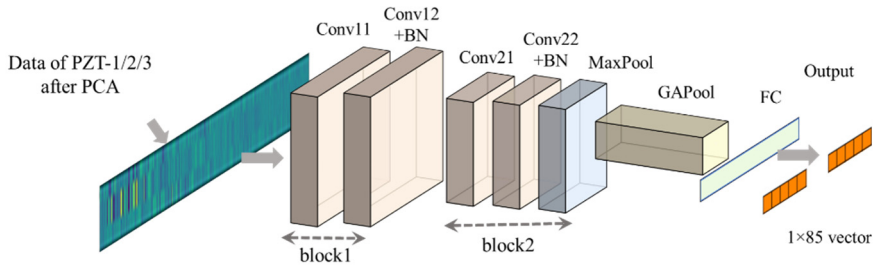


Fig. 5-22 Architecture of the proposed model N_{AE-PZT}

N_{AE-PZT} is a fully convolutional neural network as shown in Fig. 5-22. The first layer is the input layer of $3 \times 85 \times 3$ pixels resolutions. The input layer receives images representing the signals from three types of thin PZT sensors, and then these images are fed into 2 Conv blocks. Each Conv block contains two Conv layers with ReLU as an activation function and a Batch Normalization (BN) layer. In the second Conv block, a Maximum Pooling (MaxPool) layer is added to reduce the number of features. Ultimately, the feature maps are flattened into a single 1×85 vector via a Global Average Pooling (GAPool) layer and a Fully Connected (FC) layer.

Three kinds of CNNs with identical layers and different channels of feature maps are adopted which are named $N_{AE-PZT,1}$, $N_{AE-PZT,2}$ and $N_{AE-PZT,3}$ respectively. The detailed network settings are given in Table 5-5. During the convolution operation, the kernel size was selected as 3×3 by considering the real input size and processing time. Fig. 5-23 describes the process of max pooling and average pooling in CNN.

Table 5-5 The configuration of the CNN architecture

Layer	Type	Channels of the feature map			Kernel size	Stride	Padding	Activation
		$N_{AE-PZT,1}$	$N_{AE-PZT,2}$	$N_{AE-PZT,3}$				
1	Conv	32	64	128	3×3	1×1	1×1	ReLU
2	Conv	64	128	256	3×3	1×1	1×1	ReLU
3	BN	—	—	—	—	—	—	—
4	Conv	128	256	512	3×3	1×1	1×1	ReLU
5	Conv	256	512	1024	3×3	1×1	1×1	ReLU
6	BN	—	—	—	—	—	—	—
7	Max-Pool	—	—	—	2×2	2×2	0	—
8	GAPool	—	—	—	—	—	—	—
9	FC	—	—	—	—	—	—	—

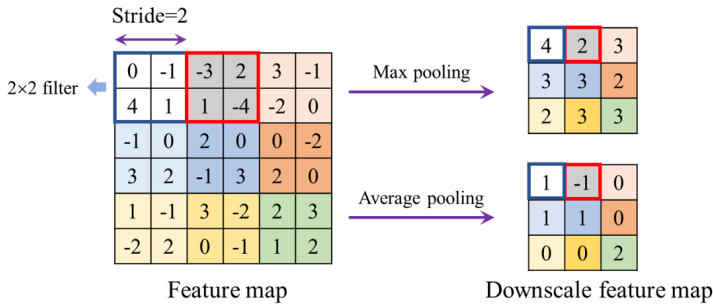


Fig. 5-23 Example for max and average pooling layers

5.5.4 CNN model training

Training is the learning process of the CNN to find the best configuration of parameters in the CNN model. The dataset as described in section 5.5.1 was imported into the constructed CNN architecture. A comparison study of three kinds of CNNs was performed to investigate the influence of the complexity of the network. The CNN model adopts a split dataset in a ratio of 4:1 because of the relatively small dataset. Thus, there are 4935 and 549 samples in the training and testing datasets, respectively. Testing data is not used for training the network. A batch size equal to 32 was adopted with a shuffling approach to redistribute the data for better performance. This CNN model was built and trained with a learning rate of 0.001 in PyTorch.

5.5.5 Evaluation of the trained CNN

Fig. 5-24 illustrates the training history of loss and learning curves of three models for the training and validation dataset. The loss and accuracy values are shown in every 1 epoch and the maximum number of epochs employed in this chapter is 500. The accuracy represents the difference between the actual and predicted waveforms from the associated $WS\alpha$ sensor. The increasing rate of training accuracy is very fast at the beginning of the training process. Afterwards, the value of loss and accuracy becomes steady. The final accuracy of three CNNs is above 95% for training data. The final testing accuracy of $N_{AE,PZT1}$, $N_{AE,PZT2}$ and $N_{AE,PZT3}$ reaches 76%, 79% and 82%, respectively. Under identical layers, $N_{AE,PZT3}$ delivers the best prediction performance which was selected for further analysis.

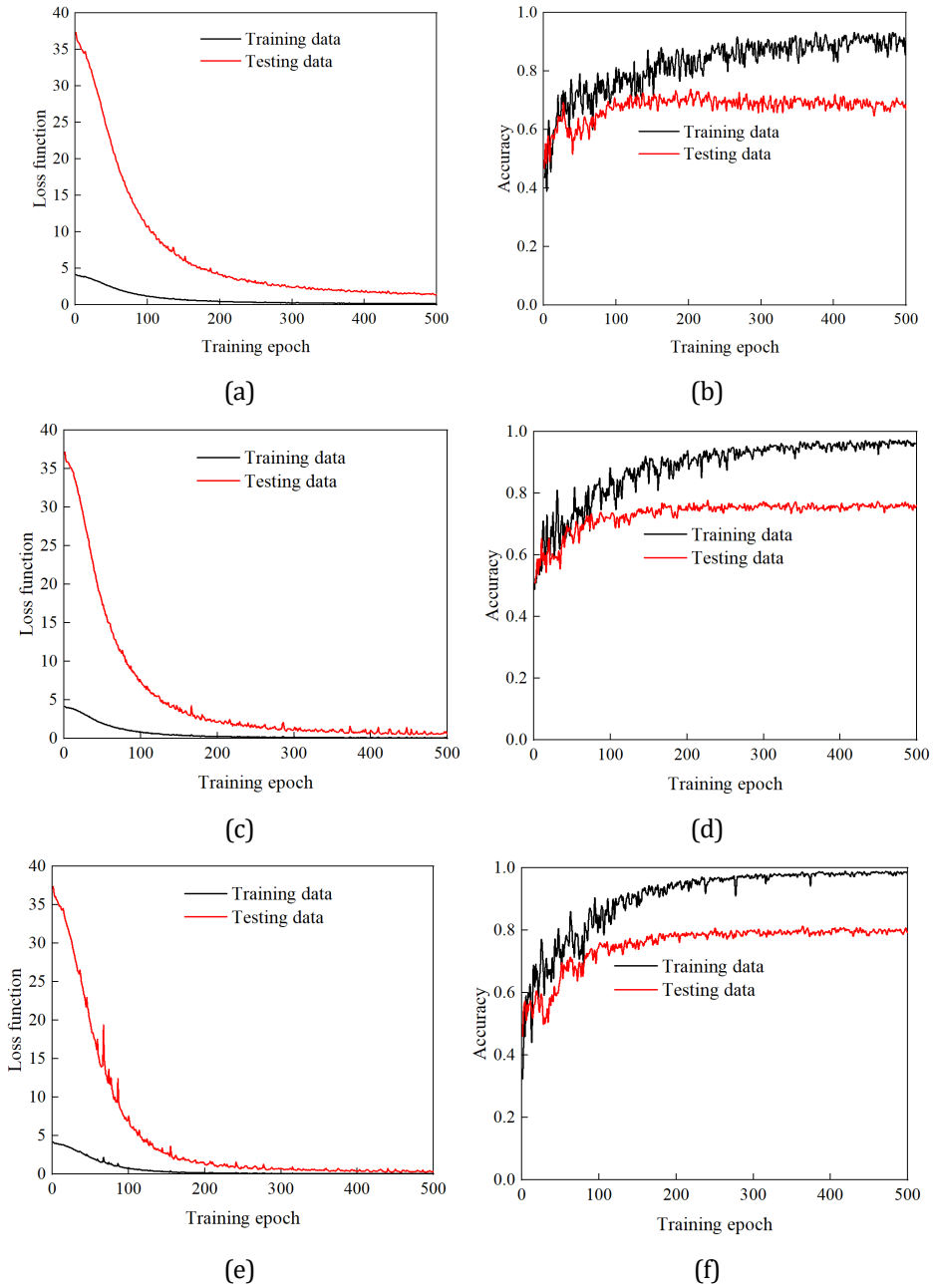


Fig. 5-24 (a) Loss and (b) learning curves of N_{AE_PZT1} ; (c) Loss and (d) learning curves of N_{AE_PZT2} ; (e) Loss and (f) learning curves of N_{AE_PZT3}

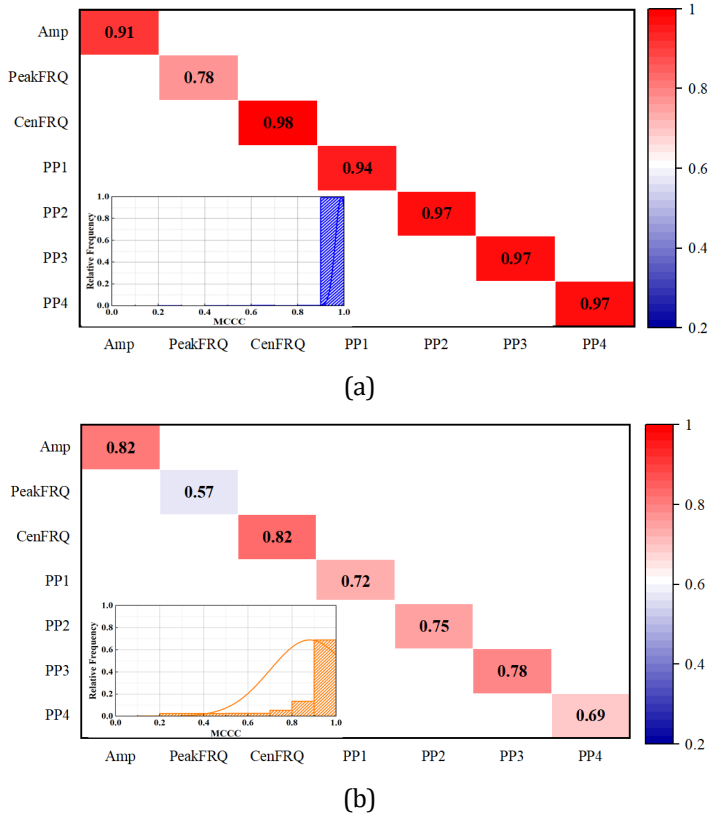
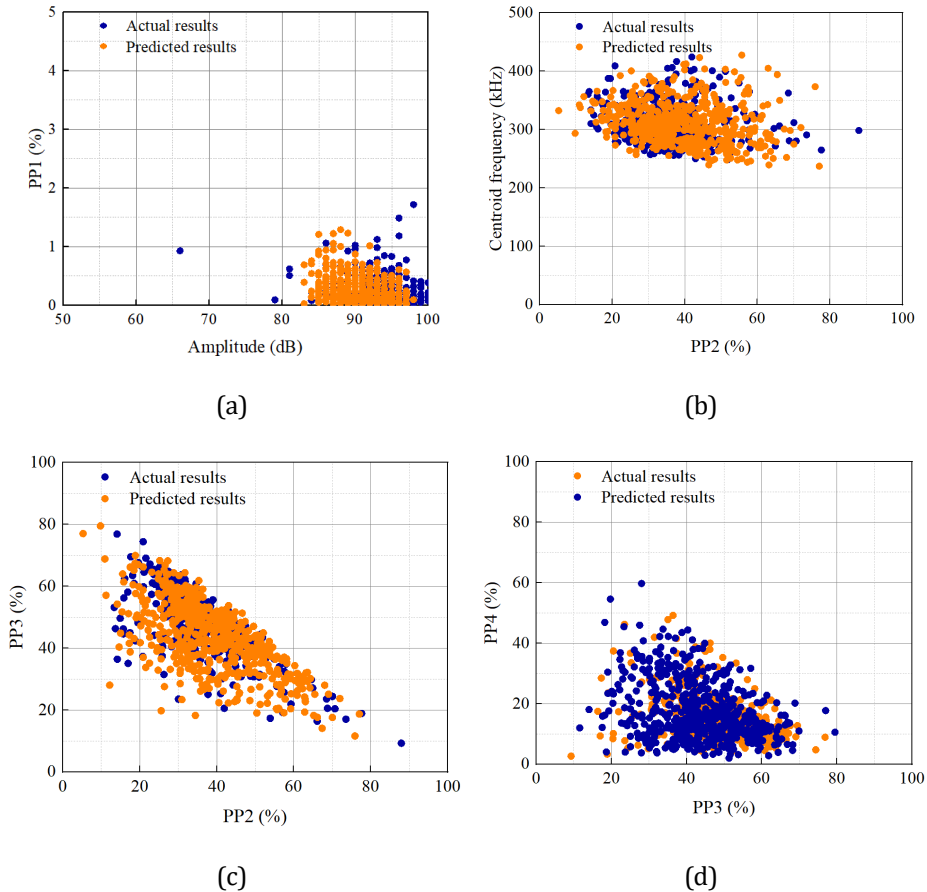


Fig. 5-25 Feature correlation matrix and MCCC between actual and predicted results of (a) training dataset, (b) testing dataset

The relative frequency of MCCC between the actual and predicted results was calculated to show the percentage of samples with high prediction accuracy. As shown in Fig. 5-25 (bottom-left corner), it was found that the mean MCCC value is 99% for the training dataset and 86% for the testing dataset. To further evaluate the reliability of the N_{AE_PZT1} , the AE features listed in Table 5-6 were extracted from the actual and predicted waveforms for comparison. These features have been extracted as they are slightly threshold-dependent [62] and have been applied effectively for damage identification [65–68]. Fig. 5-25 shows the correlation matrix of AE features from actual and predicted results. The average value of the correlation coefficients for the training data and validation data are 93% and 74%, respectively. It should be noted that the correlation value of the peak frequency is relatively lower than the other features. This can be attributed to the characteristics of the wide-band frequency response of the $WS\alpha$ sensor.

Table 5-6 Description of the selected AE features

Features	Symbol	Unit
Amplitude	Amp	dB
Peak frequency	PeakFRQ	kHz
Frequency central	CenFRQ	kHz
Partial power 1 [0-80 kHz]	PP1	%
Partial power 2 [80-200 kHz]	PP2	%
Partial power 3 [200-300 kHz]	PP3	%
Partial power 4 [300-500 kHz]	PP4	%

**Fig. 5-26 Distributions of AE parameters extracted from actual and predicted results**

Mean absolute deviation (MAD) quantifies the spread in the dataset. It is computed as the average of the absolute differences between each data point and the mean value. A smaller MAD represents a dataset that is more clustered. After calculating, it was found that the peak frequency of the actual waveforms from the $WS\alpha$ sensor has the highest MAD of 0.13, while the MAD values of the other features are less than 0.09. This

demonstrates that peak frequency is more widespread and less effective for identification and classification. Hence, Fig. 5-26 presents the distributions of the parameters with high feature correlation values except for the peak frequency. By comparison, the distribution of these parameters predicted by N_{AE_PZT3} closely coincides with the distribution of actual results in the test dataset. These results further justify that the proposed network model N_{AE_PZT3} can effectively reconstruct the waveforms from the reference sensor, even though 14% of the test dataset fails to be reconstructed with high accuracy using N_{AE_PZT3} .

5.6 CONCLUSION

To enhance the functionality of thin PZT sensors-based AE application, this chapter presents a methodology for performing a data-level fusion of outputs from various thin PZT sensors. The performance of selected thin PZT sensors was compared to bulky AE sensors, which are widely used for SHM in several fields. After identifying the advantages of the $WS\alpha$ sensor, the reconstruction of the signal measured via $WS\alpha$ was successfully achieved by fusing the signals from multiple thin PZT sensors using a developed CNN model N_{AE_PZT} . The key findings are summarized as follows:

- A criterion for defining the optimal thin PZT sensors has been proposed aiming at passive sensing application for AE monitoring. It is recommended to choose thin PZT sensors to achieve a high sensitivity response among the interested frequency band for the specific application. The feasibility of the selected thin PZT sensors is identified using PBL tests. The chosen three thin PZT sensors are found to be more effective in covering the frequency range than individual thin PZT sensors.
- According to the comparative analysis performed for sensors response captured from breaking pencil leads test on the CT specimens, the $R15\alpha$ sensor and thin PZT sensors alter the original features of the AE-emitted source dramatically. While $WS\alpha$ sensor represents the nature of the AE source with higher fidelity due to its flat and wideband frequency response function.
- Compared to other types of sensors, the $WS\alpha$ sensor captures the smallest number of noise signals during PBL tests. Besides, the signal response of $WS\alpha$ sensor shows a slight overlap in amplitude and frequency content distribution between PBL and noise signals. Thus, the $WS\alpha$ sensor is an attractive option concerning the clear distinction between signals from PBL and noise.
- 5484 PBL events were used to train and evaluate the performance of the three developed CNNs with different architectures. All the CNNs can deliver convincing prediction performance in reconstructing the waveforms from the reference sensor, with the accuracy all above 95% for training data. $N_{AE_PZT,3}$ reaches satisfying accuracy than the other two models.
- The feature correlation analysis and similarity analysis are carried out for all datasets. The distribution patterns of seven AE parameters with high feature

correlation values predicted by $N_{AE-PZT,3}$ are found to be consistent with that the actual results. As a result, the proposed method shows the promising application potential to enable damage detection using multi-thin PZT sensors combining with a waveform-based data-fusion method.

This chapter answers research question Q4) by employing a data-level fusion method to fuse the signals from multiple thin PZT sensors. By accurately reconstructing and identifying damage-related signal features of $WS\alpha$, damage detection can be performed after successful data fusion of multiple thin PZT sensors. This proposed methodology is validated using PBL tests, which are less challenging compared to practical situations. The following chapter will investigate the performance of thin PZT sensors on fatigue damage detection.

REFERENCES

- [1] A. Nair, C.S. Cai, Acoustic emission monitoring of bridges: Review and case studies, *Eng. Struct.* 32 (2010) 1704–1714. <https://doi.org/10.1016/j.engstruct.2010.02.020>.
- [2] ASTM E976-10. Standard guide for determining the reproducibility of acoustic emission sensor response, ASTM International, 2016.
- [3] ASTM E1316. Standard terminology for nondestructive examinations, ASTM International, 2014.
- [4] L. Cheng, A. Nokhbatolfighahai, R.M. Groves, M. Veljkovic, Acoustic emission-based detection in restricted-access areas using multiple PZT disc sensors, in: *Eur. Work. Struct. Heal. Monit.*, Springer, Cham, 2023: pp. 619–629. https://doi.org/10.1007/978-3-031-07254-3_62.
- [5] C.U. Grosse, M. Ohtsu, *Acoustic emission testing*, Springer Science & Business Media, 2008. <https://doi.org/10.1016/B978-0-12-804176-5.00028-1>.
- [6] H. Nakamura, *Practical acoustic emission testing*, The Japanese Society for Non-Destructive; Springer, Tokyo, Japan, 2016. <https://doi.org/10.1007/978-4-431-55072-3>.
- [7] D. Ozevin, MEMS acoustic emission sensors, *Appl. Sci.* 10 (2020) 8966. <https://doi.org/10.3390/app10248966>.
- [8] Model_R15a, (n.d.). https://www.physicalacoustics.com/content/literature/sensors/Model_R15a.pdf (accessed February 20, 2022).
- [9] Model_WSa, (n.d.). https://www.physicalacoustics.com/content/literature/sensors/Model_WSa.pdf (accessed February 20, 2022).
- [10] R. Liu, B. Yang, E. Zio, X. Chen, Artificial intelligence for fault diagnosis of rotating machinery: A review, *Mech. Syst. Signal Process.* 108 (2018) 33–47. <https://doi.org/10.1016/j.ymsp.2018.02.016>.
- [11] R. Joseph, H. Mei, A. Migot, V. Giurgiutiu, Crack-length estimation for structural health monitoring using the high-frequency resonances excited by the energy release during fatigue-crack growth, *Sensors*. 21 (2021) 4221. <https://doi.org/10.3390/s21124221>.
- [12] J. Yu, P. Ziehl, F. Matta, A. Pollock, Acoustic emission detection of fatigue damage in cruciform welded joints, *J. Constr. Steel Res.* 86 (2013) 85–91. <https://doi.org/10.1016/j.jcsr.2013.03.017>.
- [13] D. Wotzka, A. Cichoń, Study on the influence of measuring AE sensor type on the effectiveness of OLTC defect classification, *Sensors*. 20 (2020) 3095. <https://doi.org/10.3390/S20113095>.
- [14] S.X. Chen, L. Zhou, Y.Q. Ni, X.Z. Liu, An acoustic-homologous transfer learning approach for acoustic emission-based rail condition evaluation, *Struct. Heal. Monit.* 20 (2020) 2161–2181. <https://doi.org/10.1177/1475921720976941>.
- [15] L. Cheng, H. Xin, R.M. Groves, M. Veljkovic, Acoustic emission source location using Lamb wave propagation simulation and artificial neural network for I-shaped steel girder, *Constr. Build. Mater.* 273 (2021) 121706. <https://doi.org/10.1016/j.CONBUILDMAT.2020.121706>.
- [16] G. Theses, A. Enrique Avila Gomez, A. Gomez, A. Enrique, *Development MEMS Acoustic Emission Sensors*, 2017. <https://scholarcommons.usf.edu/etd> (accessed June 11, 2022).
- [17] K.E.Y. Creusen, G. Misios, J.S. Winkes, M. Veljkovic, Introducing the C1 Wedge Connection, *Steel Constr.* 15 (2022) 13–25. <https://doi.org/10.1002/STCO.202100039>.

- [18] V. Giurgiutiu, A.N. Zagrai, Characterization of piezoelectric wafer active sensors, *J. Intell. Mater. Syst. Struct.* 11 (2000) 959–976. <https://doi.org/10.1106/A1HU-23JD-M5AU-ENGW>.
- [19] V. Giurgiutiu, *Structural health monitoring with piezoelectric wafer active sensors*, Elsevier, 2007.
- [20] L. Yu, S. Momeni, V. Godinez, V. Giurgiutiu, P. Ziehl, J. Yu, Dual mode sensing with low-profile piezoelectric thin wafer sensors for steel bridge crack detection and diagnosis, *Adv. Civ. Eng.* 2012 (2012). <https://doi.org/10.1155/2012/402179>.
- [21] Y. Bhuiyan, B. Lin, V. Giurgiutiu, Acoustic emission sensor effect and waveform evolution during fatigue crack growth in thin metallic plate, *Orig. Artic. J. Intell. Mater. Syst. Struct.* 29 (2018) 1275–1284. <https://doi.org/10.1177/1045389X17730930>.
- [22] T. Jiang, Y. Zhang, L. Wang, L. Zhang, G. Song, Monitoring fatigue damage of modular bridge expansion joints using piezoceramic transducers, *Sensors*. 18 (2018) 3973. <https://doi.org/10.3390/s18113973>.
- [23] X. Zhang, L. Zhang, L. Liu, L. Huo, Tension monitoring of wedge connection using piezoceramic transducers and wavelet packet analysis method, *Sensors*. 20 (2020) 364. <https://doi.org/10.3390/s20020364>.
- [24] L. Yu, S. Momeni, V. Godinez, V. Giurgiutiu, Adaptation of PWAS Transducers to Acoustic Emission Sensors, (2011). <https://doi.org/10.1117/12.880157>.
- [25] B. Trujillo, A. Zagrai, D. Meisner, S. Momeni, Monitoring of Acoustic Emission Activity using Thin Wafer Piezoelectric Sensors, in: 21th Annu. Int. Symp. Smart Struct. Mater. + NDE Heal. Monit. Diagnostics, n.d.
- [26] N. Godin, P. Reynaud, G. Fantozzi, Challenges and limitations in the identification of acoustic emission signature of damage mechanisms in composites materials, *Appl. Sci.* 8 (2018) 1267. <https://doi.org/10.3390/app8081267>.
- [27] T. Le Gall, T. Monnier, C. Fusco, N. Godin, S.E. Hebaz, Towards quantitative acoustic emission by finite element modelling: Contribution of modal analysis and identification of pertinent descriptors, *Appl. Sci.* 8 (2018) 2557. <https://doi.org/10.3390/app8122557>.
- [28] Z. Hamam, N. Godin, C. Fusco, T. Monnier, Modelling of acoustic emission signals due to fiber break in a model composite carbon/epoxy: Experimental validation and parametric study, *Appl. Sci.* 9 (2019) 5124. <https://doi.org/10.3390/app9235124>.
- [29] R.T. Wu, M.R. Jahanshahi, Data fusion approaches for structural health monitoring and system identification: Past, present, and future, *Struct. Heal. Monit.* 19 (2018) 552–586. <https://doi.org/10.1177/1475921718798769>.
- [30] D.L. Hall, J. Llinas, An introduction to multisensor data fusion, in: *Proc. IEEE*, 1997: pp. 6–23. <https://doi.org/10.1109/5.554205>.
- [31] Klein LA, *Sensor and data fusion: a tool for information assessment and decision making*, SPIE Press, Bellingham, Washington, 2004.
- [32] H. Saboonchi, D. Ozevin, M. Kabir, MEMS sensor fusion: Acoustic emission and strain, *Sensors Actuators A Phys.* 247 (2016) 566–578. <https://doi.org/10.1016/j.SNA.2016.05.014>.
- [33] E. Dehghan Niri, A. Farhidzadeh, S. Salamone, Adaptive multisensor data fusion for acoustic emission (AE) source localization in noisy environment, *Struct. Heal. Monit.* 12 (2013) 59–77. <https://doi.org/10.1177/1475921712462937>.
- [34] N. Guel, Z. Hamam, N. Godin, P. Reynaud, O. Caty, F. Bouillon, A. Paillasa, Data merging of AE sensors with different frequency resolution for the detection and identification of damage in

- oxide-based ceramic matrix composites, *Materials* (Basel). 13 (2020) 4691. <https://doi.org/10.3390/ma13204691>.
- [35] M. Liu, X. Yao, J. Zhang, W. Chen, X. Jing, K. Wang, Multi-sensor data fusion for remaining useful life prediction of machining tools by iabc-bpnn in dry milling operations, *Sensors*. 20 (2020) 4657. <https://doi.org/10.3390/S20174657>.
- [36] A. Broer, G. Galanopoulos, R. Benedictus, T. Loutas, D. Zarouchas, Fusion-based damage diagnostics for stiffened composite panels, *Struct. Heal. Monit.* (2021) 147592172110071. <https://doi.org/10.1177/14759217211007127>.
- [37] Y. Wu, F. Yang, Y. Liu, X. Zha, S. Yuan, A comparison of 1-D and 2-D deep convolutional neural networks in ECG classification, *ArXiv Prepr. ArXiv1810.07088*. (2018). <https://doi.org/10.48550/arxiv.1810.07088>.
- [38] M. ElBatanouny, M. Abdelrahman, P. Ziehl, Review of acoustic emission corrosion monitoring of prestressed Concrete bridges, in: *PCI Conv. Natl. Bridg. Conf.*, Washington, DC, 2014.
- [39] S.S. Kessler, S.M. Spearing, C. Soutis, Damage detection in composite materials using Lamb wave methods, *Smart Mater. Struct.* 11 (2002) 269. <https://doi.org/10.1088/0964-1726/11/2/310>.
- [40] Z. Su, L. Ye, X. Bu, X. Wang, Y.W. Mai, Quantitative assessment of damage in a structural beam based on wave propagation by impact excitation, *Struct. Heal. Monit.* 2 (2016) 27–40. <https://doi.org/10.1177/145792103029779>.
- [41] H. Sohn, S.J. Lee, Lamb wave tuning curve calibration for surface-bonded piezoelectric transducers, *Smart Mater. Struct.* 19 (2010) 015007. <https://doi.org/10.1088/0964-1726/19/1/015007>.
- [42] A. Raghavan, C.E.S. Cesnik, Finite-dimensional piezoelectric transducer modeling for guided wave based structural health monitoring, *Smart Mater. Struct.* 14 (2005) 1448–1461. <https://doi.org/10.1088/0964-1726/14/6/037>.
- [43] Z. Su, L. Ye, Identification of damage using Lamb waves, Springer Science & Business Media, 2009.
- [44] P. Ochôa, R.M. Groves, R. Benedictus, Systematic multiparameter design methodology for an ultrasonic health monitoring system for full-scale composite aircraft primary structures, *Struct. Control Heal. Monit.* 26 (2019) e2340. <https://doi.org/10.1002/stc.2340>.
- [45] E. Silva De Freitas, F. Guimarães Baptista, Experimental analysis of the feasibility of low-cost piezoelectric diaphragms in impedance-based SHM applications, *Sensors Actuators A*. 238 (2016) 220–228. <https://doi.org/10.1016/j.sna.2015.11.031>.
- [46] D. Inman, C. Farrar, V. Junior, V. Junior, *Damage prognosis: for aerospace, civil and mechanical systems*, John Wiley & Sons, 2005. <https://books.google.com/books?hl=zh-CN&lr=&id=NgCM6S6rSzgC&oi=fnd&pg=PR13&dq=Damage+Prognosis:+for+Aero-+space,+Civil+and+Mechanical+Systems&ots=AQfjC1girV&sig=AtME3yCrHVCYwUai9fE9aOOUVTY> (accessed March 24, 2022).
- [47] H. Xin, L. Cheng, R. Diender, M. Veljkovic, Fracture acoustic emission signals identification of stay cables in bridge engineering application using deep transfer learning and wavelet analysis, *Adv. Bridg. Eng.* 1 (2020) 1–16. <https://doi.org/10.1186/s43251-020-00006-7>.
- [48] M.Z. Alom, T.M. Taha, C. Yakopcic, S. Westberg, P. Sidike, M.S. Nasrin, M. Hasan, B.C. Van Essen, A.A.S. Awwal, V.K. Asari, A state-of-the-art survey on deep learning theory and architectures, *Electronics*. 8 (2019). <https://doi.org/10.3390/electronics8030292>.

- [49] T. Koskinen, I. Virkkunen, O. Siljama, O. Jessen-Juhler, The Effect of Different Flaw Data to Machine Learning Powered Ultrasonic Inspection, *J. Nondestruct. Eval.* 40 (2021) 24. <https://doi.org/10.1007/s10921-021-00757-x>.
- [50] H. Wu, X. Gu, Towards dropout training for convolutional neural networks, *Neural Networks.* 71 (2015) 1–10. <https://doi.org/10.1016/J.NEUNET.2015.07.007>.
- [51] H. Abdi, L.J. Williams, *Principal Component Analysis*, Wiley Interdiscip. Rev. Comput. Stat. 2 (2010) 433–459. <https://doi.org/10.1007/B98835>.
- [52] D. Baccar, D. Söffker, Identification and classification of failure modes in laminated composites by using a multivariate statistical analysis of wavelet coefficients, *Mech. Syst. Signal Process.* 96 (2017) 77–87. <https://doi.org/10.1016/j.ymssp.2017.03.047>.
- [53] Piezoceramic Materials, (n.d.). <https://www.piceramic.com/en/expertise/piezotechnology/piezoelectric-materials> (accessed March 23, 2023).
- [54] H. Boukabache, C. Escriba, J.-Y. Fourniols, Toward smart aerospace structures: design of a piezoelectric sensor and its analog interface for flaw detection, *Sensors.* 14 (2014) 20543–20561. <https://doi.org/10.3390/s141120543i>.
- [55] M. Sause, Investigation of pencil-lead breaks as acoustic emission sources, *J. Acoust. Emiss.* 29 (2011) 184–196.
- [56] M.A. Haile, N.E. Bordick, J.C. Riddick, Distributed acoustic emission sensing for large complex air structures, *Struct. Heal. Monit.* 17 (2018) 624–634. <https://doi.org/10.1177/1475921717714614>.
- [57] A. Mukherjee, A. Banerjee, Analysis of acoustic emission signal for crack detection and distance measurement on steel structure, *Acoust. Aust.* 49 (2020) 133–149. <https://doi.org/10.1007/s40857-020-00208-z>.
- [58] E. Tsangouri, D.G. Aggelis, The influence of sensor size on acoustic emission waveforms—a numerical study, *Appl. Sci.* 8 (2018) 168. <https://doi.org/10.3390/APP8020168>.
- [59] V. Giurgiutiu, A. Zagrai, J. Jing Bao, Piezoelectric wafer embedded active sensors for aging aircraft structural health monitoring, *Struct. Heal. Monit.* 1 (2002) 41–61.
- [60] M. Gresil, V. Giurgiutiu, Prediction of attenuated guided waves propagation in carbon fiber composites using Rayleigh damping model, *J. Intell. Mater. Syst. Struct.* 26 (2015) 2151–2169. <https://doi.org/10.1177/1045389X14549870>.
- [61] L. Capineri, A. Bulletti, V.M.N. Passaro, Ultrasonic Guided-Waves Sensors and Integrated Structural Health Monitoring Systems for Impact Detection and Localization: A Review, *Sensors.* (2021). <https://doi.org/10.3390/s21092929>.
- [62] F.T. Santo, T.P. Sattar, G. Edwards, Validation of acoustic emission waveform entropy as a damage identification feature, *Appl. Sci.* 9 (2019) 4070. <https://doi.org/10.3390/app9194070>.
- [63] Z. Chang, Z. Wan, Y. Xu, E. Schlangen, B. Šavija, Convolutional neural network for predicting crack pattern and stress-crack width curve of air-void structure in 3D printed concrete, *Eng. Fract. Mech.* (2022) 108624. <https://doi.org/10.1016/J.ENGFRACMECH.2022.108624>.
- [64] C. Cassisi, P. Montalto, M. Aliotta, A. Cannata, A. Pulvirenti, Similarity Measures and Dimensionality Reduction Techniques for Time Series Data Mining, (2012).
- [65] M.G.R. Sause, A. Gribov, A.R. Unwin, S. Horn, Pattern recognition approach to identify natural clusters of acoustic emission signals, *Pattern Recognit. Lett.* 33 (2012) 17–23. <https://doi.org/10.1016/J.PATREC.2011.09.018>.
- [66] M. Kharrat, E. Ramasso, V. Placet, M.L. Boubakar, A signal processing approach for enhanced Acoustic Emission data analysis in high activity systems: Application to organic matrix composites,

Mech. Syst. Signal Process. 70–71 (2016) 1038–1055.
<https://doi.org/10.1016/j.ymssp.2015.08.028>.

[67] B. Wisner, K. Mazur, V. Perumal, K.P. Baxevanakis, L. An, G. Feng, A. Kontsos, Acoustic emission signal processing framework to identify fracture in aluminum alloys, *Eng. Fract. Mech.* 210 (2019) 367–380. <https://doi.org/10.1016/j.engfracmech.2018.04.027>.

[68] J. Vetrone, J.E. Obregon, E.J. Indacochea, D. Ozevin, The characterization of deformation stage of metals using acoustic emission combined with nonlinear ultrasonics, *Measurement*. 178 (2021) 109407. <https://doi.org/10.1016/j.measurement.2021.109407>.

6. EARLY FATIGUE DAMAGE DETECTION BY ACOUSTIC EMISSION

The space limitations of the lower segment holes in the C1-WC make it difficult to detect surface cracks with commercial sensors. Thin PZT sensors are small and lightweight which are suitable for use in restricted-access areas. However, their poor signal-to-noise ratio hinders their effectiveness in AE monitoring. In this study, a baseline-based approach is proposed to improve the detection efficiency of thin PZT sensors. A benchmark model correlating the damage state of specimens is created by breaking pencil leads. Multivariate feature vectors are extracted and then mapped to the Mahalanobis distance for identification. The proposed method is validated by testing compact specimens (CT) and C1-WC specimens. To supplement the detection results of AE, other monitoring techniques such as digital image correlation (DIC), crack propagation gauges, and distributed optical fiber sensors (DOFS) are also used. The experimental setup, signal acquisition, and detection efficiency of various techniques are briefly introduced.

This chapter addresses the fourth research question (Q4) from a second perspective and is organized as follows: Section 6.2 presents a brief introduction to the proposed baseline-based method. The details of the experimental tests about CT specimens and C1-WCs are described in Section 6.3. The corresponding discussion about the detection results is given in Section 6.4 and Section 6.5, respectively. Finally, Section 6.6 provides the conclusions of this paper.

6.1 INTRODUCTION

Over the past few decades, offshore wind turbines (OWTs) have grown significantly due to their ability to harness more powerful and consistent offshore winds to generate renewable energy [1,2]. Among the various types of foundations used for OWTs, the monopile foundation is the most common, accounting for around 80% of existing projects [3]. To ensure the structural integrity of OWTs, the connection between the monopile foundation and transition piece (TP) is critical [4]. Dynamic loads from winds and waves are the primary loads on OWTs and can cause iterative deterioration and crack initiation, eventually leading to fracture. Fatigue damage of the MP-TP connection could cause catastrophic failure of OWTs. Fatigue damage of the MP-TP connection could result in catastrophic failure of OWTs. Early detection of damage is therefore essential to provide warning signs and prevent complete collapse.

The acoustic emission (AE) technique is a non-destructive testing (NDT) method that has successfully been applied to identify fatigue damage in various structures [5]. Compared to other NDT methods, the primary advantage of AE techniques are their ability to monitor in real-time and long-term without interrupting the original process. The AE technique records electrical signals converted from elastic stress waves generated by the suddenly released energy from deformation within the material [6]. During the fatigue fracture process, the major AE sources are crack initiation, crack propagation, and crack opening and closure [7]. Numerous studies have linked AE features and crack growth behavior [8–12]. The most commonly used AE features include cumulative counts, absolute energy, and hits. However, these features depend on the selected threshold during monitoring, and threshold setting is user-defined [13]. Novel entropy-based AE features have been proposed to characterize damage in materials. Entropy-based features measure the unique probability distribution of samples in each AE waveform, such as Shannon's entropy, Renyi entropy, Tsallis entropy, and Power Spectral Entropy [14–17]. It has been revealed that the crack onset is well correlated with cumulative entropies [14].

Commercial AE sensors, such as $WS\alpha$ and $R15\alpha$ sensors, are typically used in combination with the above methods [15,18–20]. However, the bulky size of the commercial sensors hinders their application for monitoring damage in restricted-access areas. Recently, an innovative connection called C1-wedge connection (C1-WCs) has been developed and its advantages and novelty have been demonstrated in chapters 2 and 3 [4,21]. As a robust connection for offshore applications, C1-WCs have the advantage of reducing construction, installation, and maintenance costs [21]. It has been reported that fatigue damage occurs from the inside of the connections, where conventional bulky AE sensors cannot be used. In addition to the commercial sensors, thin and miniature PZT (Lead Zirconate Titanate) sensors with a thickness smaller than 1 mm work well for both excitation and detection of ultrasonic guided waves in structural health monitoring (SHM) [22,23]. Some researchers have compared the performance of commercial sensors and thin PZT sensors [24,25]. Compared to

commercial sensors, thin PZT sensors can deliver equivalent detection findings regarding fatigue cracks in thin plate-like materials. However, thin PZT sensors are less effective for monitoring the thick steel plate. For example, only capture 5% AE events of that recorded by R15I sensors [26]. They have low signal-to-noise (SNR) ratio during AE monitoring. Yu et al. found the cumulative AE features of thin PZT sensors can only detect the emergence of cracks when their size reaches 0.83 mm [27]. Hence, a new signal processing method is required to enable the use of thin PZT sensors for early fatigue damage warning, especially for structures with complex geometry and thick plates.

One signal processing method, the baseline-based method, for AE monitoring has been proposed for damage detection in SHM [28–32]. This approach involves establishing a benchmark model of noise or background signals, and then continuously monitoring abnormalities that deviate significantly from the baseline. Such abnormalities are typically caused by damage occurring with respect to the health condition of structures. To detect these anomalies, similarity or difference measures are calculated between signals from an inspection phase and those from a pristine state. Methods for anomaly detection include cross-correlation [31,33], magnitude squared coherence (MSC) [34], and distance-based anomaly detection [35,36]. Distance-based anomaly detection allows for the early detection of structural damage, providing valuable insights for maintenance and repair actions. It's worth noting that the selection of the appropriate distance metric, threshold, and reference dataset depends on the specific application and the characteristics of the monitored structure.

Experimental investigations have shown that accurate damage detection can be obtained using thin PZT sensors when coupled with the established baseline model [31,37]. However, the effectiveness of distance-based anomaly detection heavily relies on the quality and representativeness of the reference dataset. It is difficult to establish a benchmark model that represents all possible pristine states due to the uncertainty of the environmental and operational conditions in real-world applications. To address this limitation, a novel baseline-based method is proposed in this chapter for the early detection of fatigue cracks. Instead of using the health condition as the benchmark model, the signals from the “damage” state are collected as the reference. The primary objective of this paper is to provide early warning using AE technique for C1-WCs. Towards this end, signals generated by pencil-lead breaking (PBL) are collected as the dataset representing AE signals related to crack initiation. The effectiveness of the proposed methodology is validated at the sub-component level using thick compact tension (CT) specimens, and at the element level using segment specimens with C1-WCs. Both PBL tests and fatigue tests were conducted at each level.

6.2 THE PROPOSED DAMAGE DETECTION METHOD

The key premise of this method is to develop an appropriate benchmark model that represents the "damage" state. One classical approach for generating crack-like AE signals is to use the Hsu-Nielsen source (pencil leads breaking PBL) [38]. PBL generates a monopole source that is oriented at an angle with respect to the surface of the specimen, whereas crack formation and growth produce dipole sources that are parallel to the planar direction of the specimen. Hamstad et al., conducted a series of numerical and experimental investigations on the difference between PBL signals and crack-related signals in plates [39–41]. The results demonstrate that monopole PBLs on the edge of the plate created waves that most closely resembled those from dipole-type sources near the surface [39]. Considering that cracks typically nucleate at the surface of metals, it is reasonable to use the PBL signals as the reference dataset to identify the crack initiation but not for further crack growth.

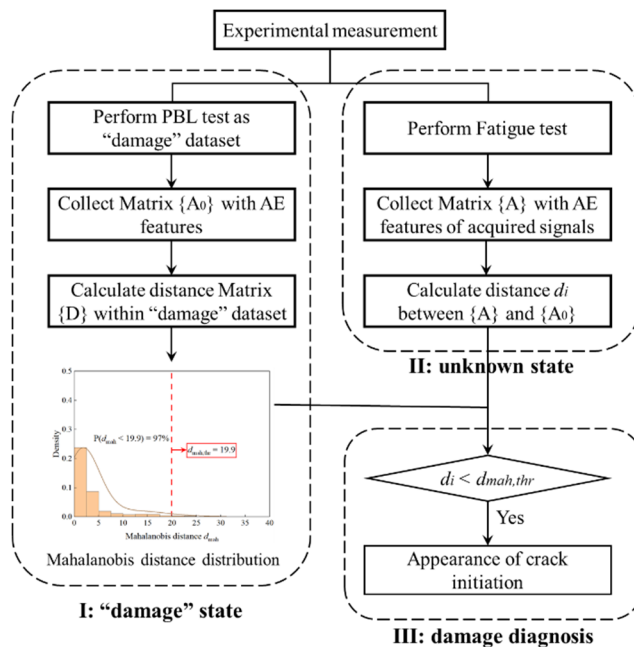


Fig. 6-1 Illustration of the proposed baseline-based damage detection method

As shown in Fig. 6-1, there are three steps in the proposed method:

Step I: create a benchmark model as the "damage" state

PBL should be collected at the same spot with the same angle and orientation to guarantee repeatable AE sources. The exact position of crack nucleation is unknown before the fatigue tests. To collect enough data with randomness and uncertainty [38], the pencil leads were broken with various free lengths of 2–4 mm and contact angles of 20°–60°. PBL signals are then recorded by AE measurement system.

To establish the feature matrix $\{A_0\}$ of the “damage” dataset, the AE features listed in Table 5-6 are extracted from the PBL signals. A bandpass filter with a frequency range of 80-500 kHz is applied to the collected PBL signals to eliminate external noise and signal reflection contamination. Previous research has demonstrated that AE features in the frequency domain are effective in correlating the appearance of damage and that these features outperform other candidates [42]. Partial power (PP) features are also employed, which measure the ratio of power in a user-specified frequency range (f_1 - f_2) to the complete power of a signal:

$$PP_{(f_1:f_2)} = \int_{f_1}^{f_2} U(f) df / \int_0^{F/2} U^2(f) df \quad \text{Eq. 6-1}$$

where a power spectral density formula $U(f)$ is obtained using FFT from each signal, and F is the sampling frequency of the signals. $\int_0^{F/2} U^2(f) df$ computes the total power across the entire frequency range. Ultimately, a feature matrix $\{A_0\}$ consisting of five vectors is generated.

Table 6-1 Description of the selected AE features

Features	Symbol	Unit
Peak frequency	PeakFRQ	kHz
Frequency central	CenFRQ	kHz
Partial power 2 [80-200 kHz]	PP2	%
Partial power 3 [200-300 kHz]	PP3	%
Partial power 4 [300-500 kHz]	PP4	%

To integrate the feature vectors in $\{A_0\}$, Mahalanobis distance (MD) is utilized to create a multidimensional measurement scale. MD is a multivariate distance metric for measuring the distance between a point or vector and a distribution. It has been shown to be an efficient technique for pairwise distance calculations, making it an extremely useful tool in multivariate anomaly detection. The Mahalanobis distance d_{mah} is calculated by measuring the distance between the features of the j -th PBL signal and the “damage” states, resulting in the creation of a distance matrix $\{D\}$. With certain probability confidence, a reliable threshold $d_{mah,thr}$ is determined using kernel distribution with a 97% survival probability.

Step II: acquire dataset from an unknown state

During the fatigue test, AE signals are acquired using the identical AE measurement to the PBL test. A feature matrix $\{A\}$ is obtained using the AE features listed in Table 6-1. After that, The Mahalanobis distance d_i between the features of i -th acquired signals in $\{A\}$ and $\{A_0\}$ of the “damage” dataset is taken as the damage indicator (DI).

Step III: perform damage diagnosis

If the damage indices d_i are above the selected threshold $d_{mah,thr}$, the outliers correlate to the safe state because the reference dataset is related to the "damage" condition. On the contrary, the damage is diagnosed in the acquired data if $d_i < d_{mah,thr}$.

6.3 EXPERIMENTAL SET-UP

6.3.1 Compact tension specimens

Fig. 6-2 (a) depicts the geometry of the CT specimens manufactured from S355 steel grade. The experimental measurement was conducted in two parts. In the first part, PBL tests were performed on the notch tip of the CT specimens to generate signals related to crack initiation (see Fig. 6-2 (b)). A MISTRAS AE system, supplied by the Physical Acoustic Corporation (PAC), was employed to record the "damage" dataset. The signals were recorded at a 5 MSPS sampling rate with a threshold of 50 dB and a 40dB pre-amplifier. Two CT specimens with different sensor layouts were used to study the effect of sensor type on the measurement, see Fig. 6-3. The employed sensors included one WSA wide-band AE sensor and two thin PZT (Lead Zirconate Titanate) sensors named PZT1 and PZT2, respectively. Their frequency sensitivities are shown in Fig. 6-4. The sensitivity response of the WSA sensor is available from the manufacturer [43]. An analytical function has been proposed to estimate the sensor output of PZT1 and PZT2 sensors [44,45]. PZT1 and PZT2 were selected in accordance with the selection criteria proposed in the previous chapter.

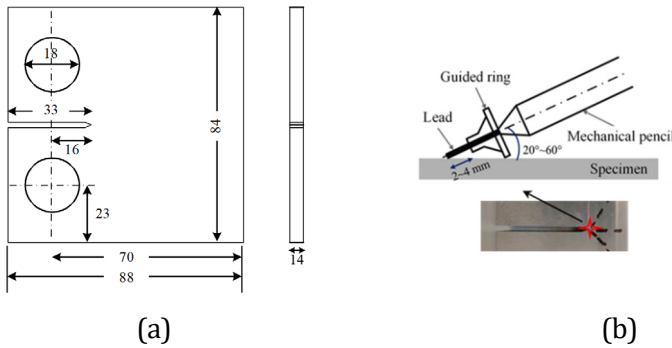


Fig. 6-2 Illustration of (a) CT specimens and (b) PBL signal collection (unit: mm)

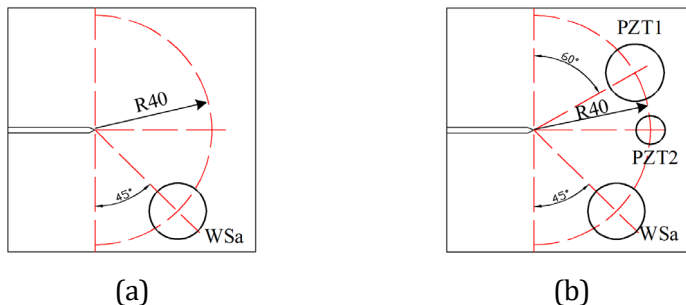
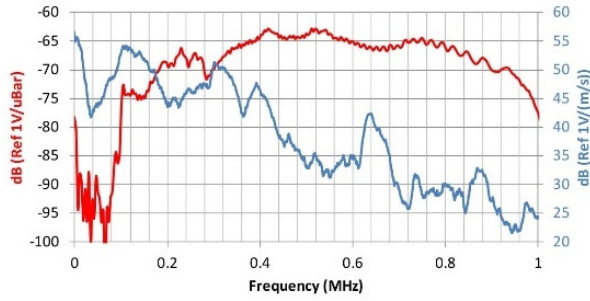
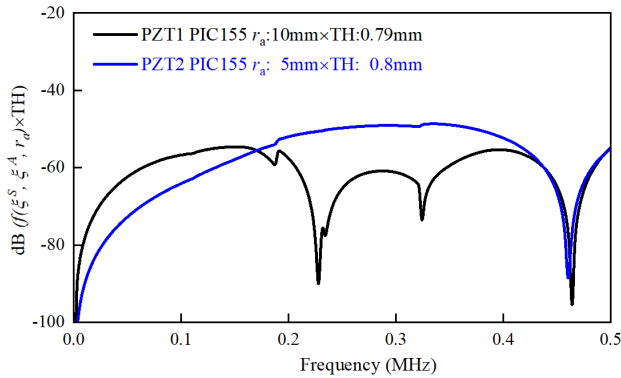


Fig. 6-3 Layout of sensors for CT specimens: (a) CT-1 and (b) CT-2



(a)



(b)

Fig. 6-4 Frequency sensitivity spectrum of (a) $WS\alpha$ [43], and (b) PZT1 and PZT2[45]

The second part of the experimental measurement involved conducting a standard fatigue test on the same specimen subjected to a constant-amplitude tensile loading. The fatigue tests were performed under load-controlled conditions using a hydraulic Instron testing machine (with a loading frequency of 10 Hz, $R_s = 0.25$, max load = 20 kN). Here, R_s is defined as the ratio between the maximum and minimum load levels. The test set-up is illustrated in Fig. 6-5. As experimentally supportive methods for AE interpretation, 2D digital image correlation (DIC) and a crack propagation gauge were utilized during the fatigue tests.

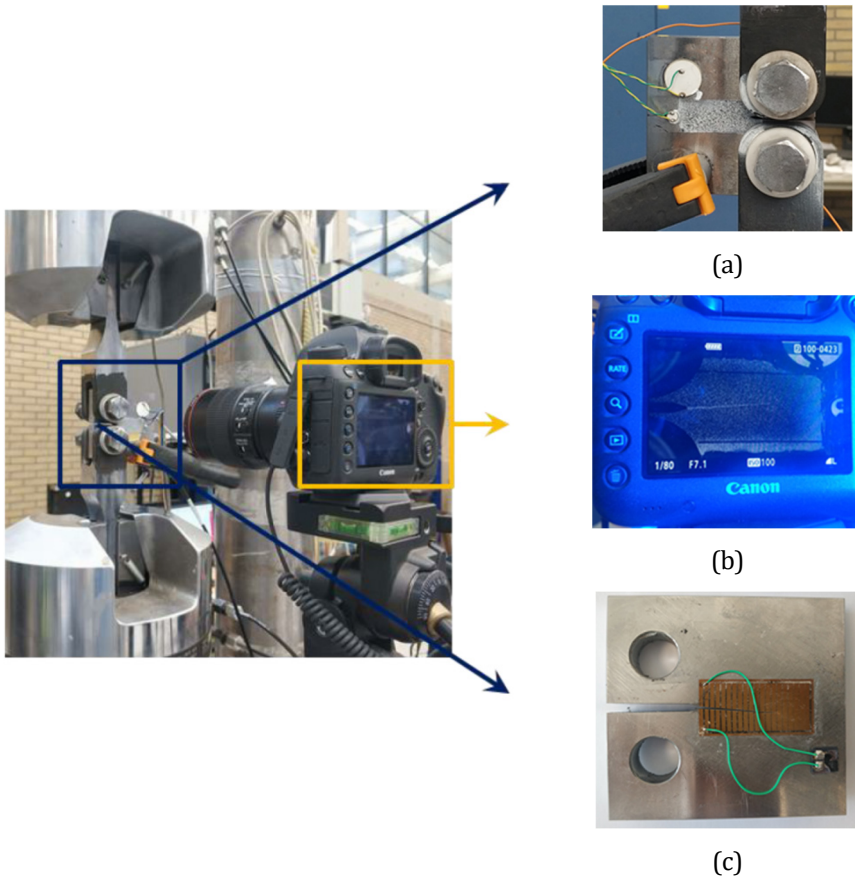


Fig. 6-5 Test set-up of CT specimens with (a) AE technique; (b) 2D DIC measurement, and (c) crack propagation gauge

The DIC method enables the capture of high-resolution strain fields on the surface of the object. Previous research has demonstrated the potential of combining AE and DIC for health monitoring [46,47]. The DIC system consists of a high-speed camera, a backlight source, and a speckle pattern sprayed on the specimen surface. The camera was positioned in front of the test specimen to capture the displacement of the speckles as pictures. These images were then post-processed using the GOM DIC software. DIC pictures were taken at the maximum tensile load F_{\max} with intervals of 1000 cycles (from B_0 to B_k where k is the number of images). The photograph is triggered by the Instron controller. The load history of the fatigue test is shown in Fig. 6-6. The accuracy of DIC measurement is dependent on the speckle pattern on the surface of the specimen [48]. In comparison to DIC, crack propagation gauges provide a more direct measurement of the crack lengths [49]. A crack propagation gauge (TK-09-CPC03-003/DP) was mounted on the polished surface at the back of the specimen, as shown in

Fig. 6-5 (c) and Fig. 6-7. The gauge comprises twenty vertical resistor stands with a centerline distance of 2.03 mm. The results obtained from the crack propagation gauge were utilized to verify the accuracy of the DIC measurements.

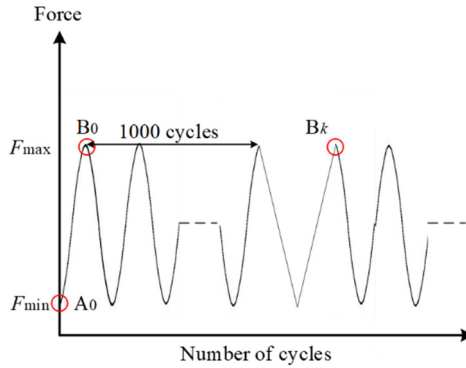


Fig. 6-6 DIC image capture during fatigue CT tests

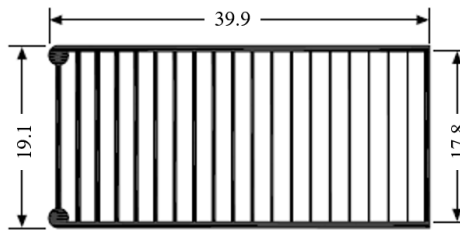


Fig. 6-7 Dimension of crack gauges of TK-09-CPC03-003/DP

6.3.2 Segment specimen with C1-WC

Similar to the experimental measurement of CT specimens, both PBL and fatigue tests were conducted on the C1-WC as shown in Fig. 6-8. Fig. 6-8 (b) displays the special sensor layout employed for collecting AE signals in the experiments. Four PZT sensors were installed on the internal flat surface of the lower segment for AE monitoring. To collect the “damage” dataset for the C1-WC, pencil leads were broken along the marked red line on the edge of the overall hole of the lower segment pre-assembly, as shown in Fig. 6-9. In order to accurately select PBL signals, the $WS\alpha$ sensor was used as the reference sensor [45]. The same AE measurement system as in the CT specimens was employed.

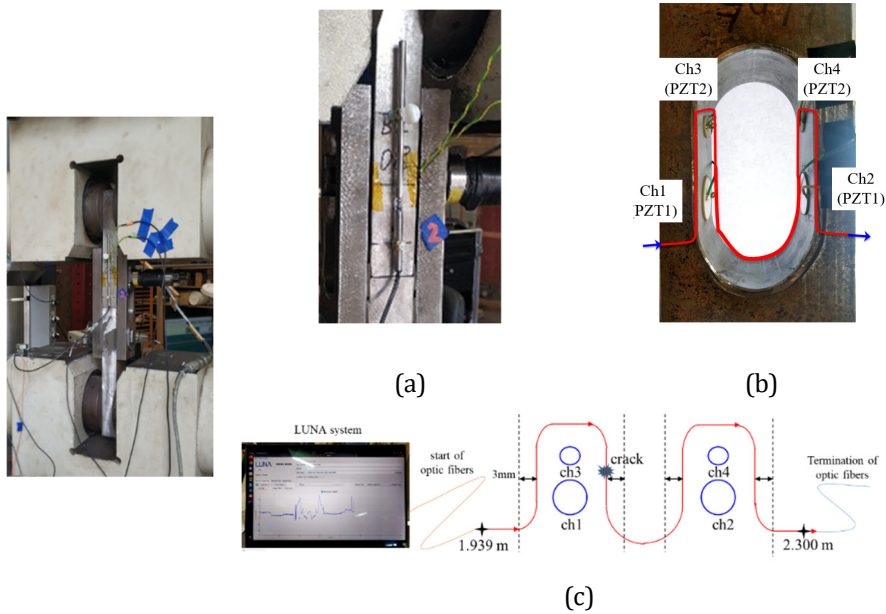


Fig. 6-8 Test set-up of C1-WC specimen, including (a) LVDT, (b) AE technique, and (c) schematic of the DOFS position measurement

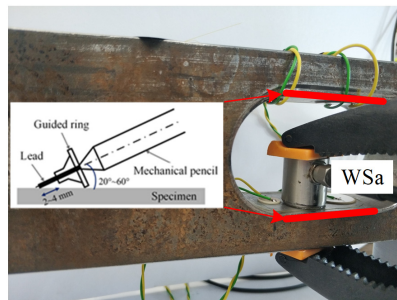


Fig. 6-9 PBL signal collection during C1-WCs

After assembling the segment specimen, a fatigue test was conducted. Due to space limitations, the conventional $WS\alpha$ sensor could not be mounted close to the critical area. The bolt was pretensioned during the assembly with a horizontal force of 80 kN. A critical tensile load of 470 kN was defined for the C1-WC due to their special design [21]. An axial tensile cyclic fatigue loading was applied with R_s of 0.1 and F_{max} of 450 kN. This load condition was selected as the design fatigue load should be approximately the same as the critical load.

Although DIC is sufficient to characterize surface damage, it is limited in providing information about internal microscopic behaviour efficiently [5]. Therefore, DIC was not employed for fatigue damage monitoring of C1-WCs. Instead, to complement the AE measurement, the linear variable displacement transducer (LVDT) and distributed

optical fiber sensors (DOFS) were used to measure the deformation (see Fig. 6-8 (a) and (c)). Two external LVDTs were attached to the middle part of the lower segment to measure the elongation from the outside.

DOFS technology enables the measurement of strain distribution with thousands of sensing points along a structure [50,51]. By detecting changes in the strain field, the occurrence of damage in structures can be identified using optical fibers. In this study, a single-mode pigtail (G652) optic fiber from SQS Fiber Optics was adhesively bonded to the surface of the internal lower segment, as shown in Fig. 6-8 (c). A coreless fiber was included at the end of the fibers to terminate the measurement and minimize noise caused by unwanted reflections. The distributed strain along the overall hole was recorded using a LUNA Optical Distributed Sensor Interrogator (ODiSI 6104). The DOFS measurement was taken at an acquisition rate of 31.25 Hz and a spatial resolution of 0.65 mm. The start and end points of the fibers are indicated in Fig. 6-8 (c).

6.4 DAMAGE MONITORING OF CT SPECIMENS

6.4.1 DIC approach

Fig. 6-10 shows the strain nephogram of CT-1 obtained through DIC measurement. Image (B_0) captured at the maximum load of the first cycle was chosen as the reference stage. The initial deformation induced by F_{max} was eliminated since the focus is on the deformation caused by the crack. The longitudinal strain along the y-direction was processed using the reference field. The high-strain region surrounding the crack tip is a typical indicator of crack initiation. However, there is currently no standard threshold for the strain value that identifies the crack tip.

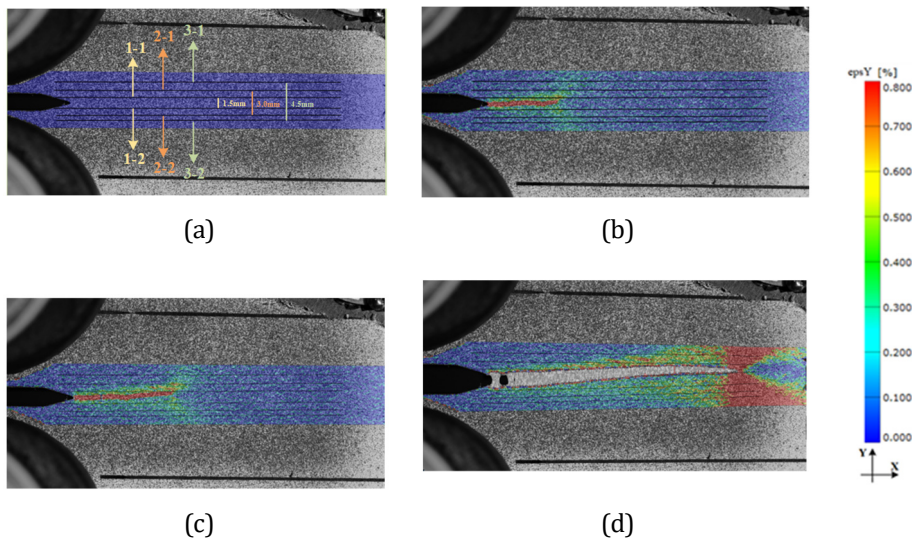


Fig. 6-10 DIC contour of CT-1: (a) at B_0 , (b) at 1.40×10^5 cycles, (c) at 1.63×10^5 cycles, and (d) at 2.10×10^5 cycles

To identify the crack tip, three pairs of horizontal lines are drawn as the distributed virtual extensometers. The distance between the data points along the m^{th} pair of lines at i^{th} image $d_m^i(x)$ can be extracted using the DIC algorithm, according to:

$$d_m^i(x) = \varepsilon_{y,m-1}^i(x) - \varepsilon_{y,m-2}^i(x) \quad (i \geq 0 \text{ and } m = 1, 2, 3) \quad \text{Eq. 6-2}$$

where x is the position of the data point along the X axis, as shown in Fig. 6-11. The notch tip is regarded as the original point with $x = 0$, and $i = 0$ represents the reference stage. The relative distance difference $\Delta d_m^i(x)$ can be calculated as:

$$\Delta d_m^i(x) = d_m^i(x) - d_m^0(x) \quad \text{Eq. 6-3}$$

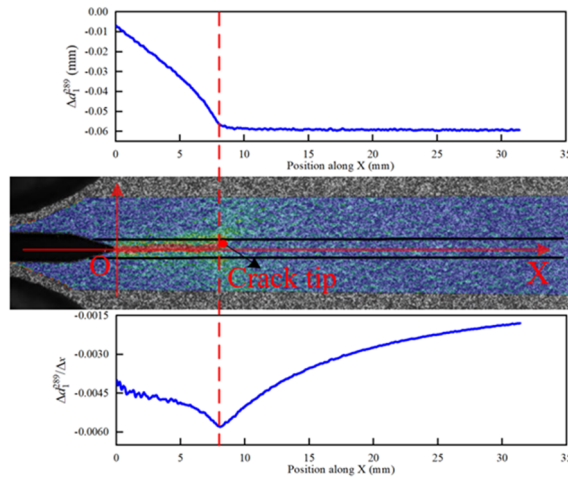


Fig. 6-11 Identification of crack tip at 1.40×10^5 cycles (289-th images) of CT-1

The resolution of the results improves with decreasing distance between the horizontal lines. However, once the crack tip surpasses the area between the current pair of lines, the next pair of horizontal lines should be used to identify the crack tip. For example, the crack tip surpasses the area between lines 1-1 and 1-2 reaching 1.40×10^5 cycles (Fig. 6-10 (b)). After that, the measurement results between lines 2-1 and 2-2 should be used for identifying the crack tip between 1.40×10^5 and 1.63×10^5 cycles (Fig. 6-10 (c)). Taking the image at 1.40×10^5 cycles (289th images) as an example, a sudden change in the slope of $\Delta \text{dim}(x)$ is observed at the end of the high strain field (Fig. 6-11). This is because a negligible distance difference indicates no change between the current and the reference images. Consequently, $\Delta \text{dim}(x) / \Delta(x)$ is obtained to identify the transit point of the slope of $\Delta \text{dim}(x)$, namely the position of the crack tip (bottom of Fig. 6-11).

6.4.2 Results of crack propagation gauges

As mentioned in Section 6.3.1, the DIC-based crack tip identification approach is supported using the results obtained from crack propagation gauges. The crack tip is

identified in the gauges by a sudden jump in resistance once the crack reaches the vertical strands (see Fig. 6-12). A comparison of the crack length obtained using DIC and crack propagation gauges is presented in Fig. 6-13. It is important to note that the crack length mentioned in this study refers to the projection of the actual crack along the X axis. As the first vertical line in the gauges is 1.8 mm away from the edge, the gauges cannot provide the signal of the onset of the crack. The consistency between the results obtained from DIC and gauges supports the use of DIC to identify the number of cycles corresponding to crack initiation.

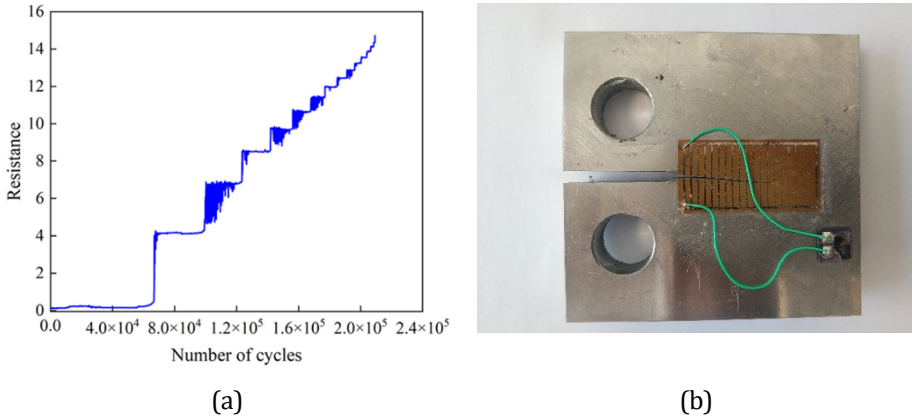


Fig. 6-12 (a) Response of crack propagation gauges and (b) failure modes of CT-1

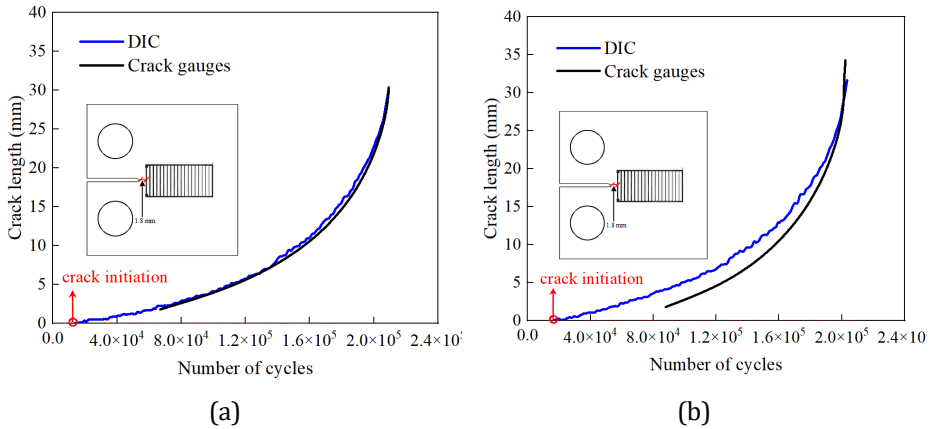


Fig. 6-13 Results of crack length from DIC and crack gauges (a) CT-1 (b) CT-2

6.4.3 AE monitoring

1500 PBL tests were conducted on CT-1 and CT-2 at every 5 seconds, respectively. As described in section 6.2, the feature matrix $\{A_0\}$ comprising PP2, PP3, PP4, peak frequency, and frequency centroid is obtained. A density plot is used to visualize the distribution of the feature matrix. Fig. 6-14 shows the density plot of PP2 and PP3 of PBL signals from all sensors, where the “hot” red regions represent high density, and

the “cold” blue regions denote low density with a gradient in between. There is a high probability that damage-related signals are located in the dense regions of the distribution of the feature matrix. The distance matrix $\{D\}$ is obtained by calculating the MD between the feature matrix of each observation to the reference dataset. Fig. 6-15 shows the distance matrix histogram of the reference dataset including the determined threshold $d_{mas,thr}$.

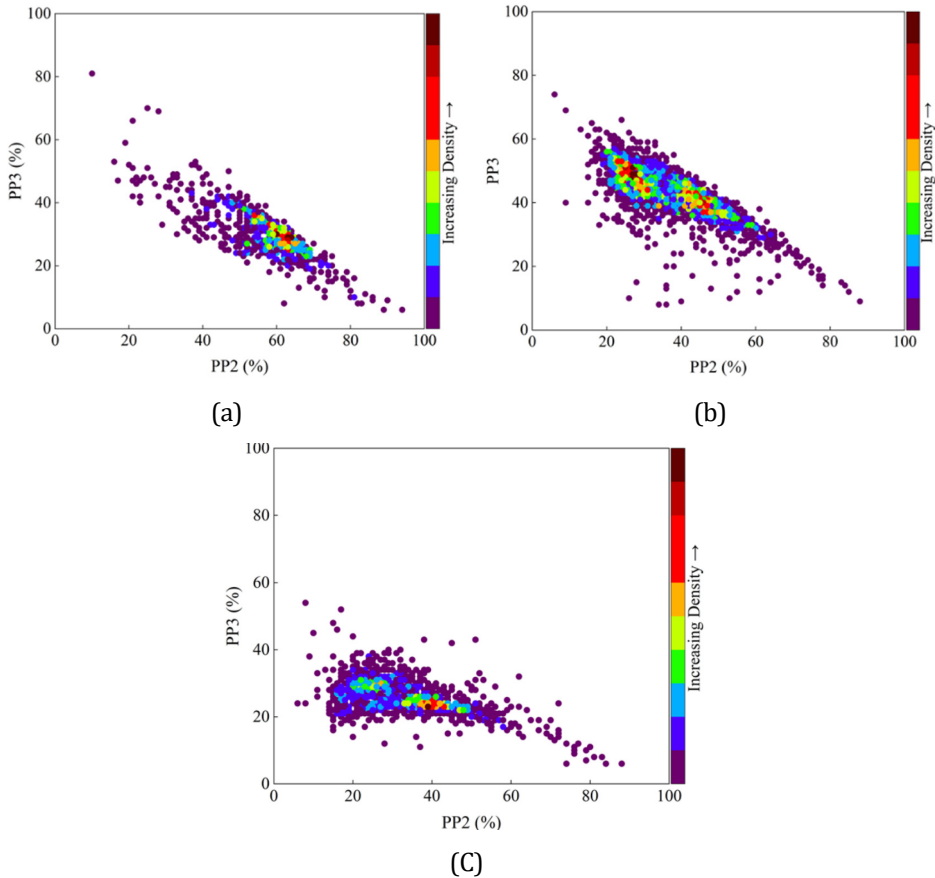


Fig. 6-14 Distribution of features of PBL signals from (a) WS α , (b) PZT1, and (c) PZT2

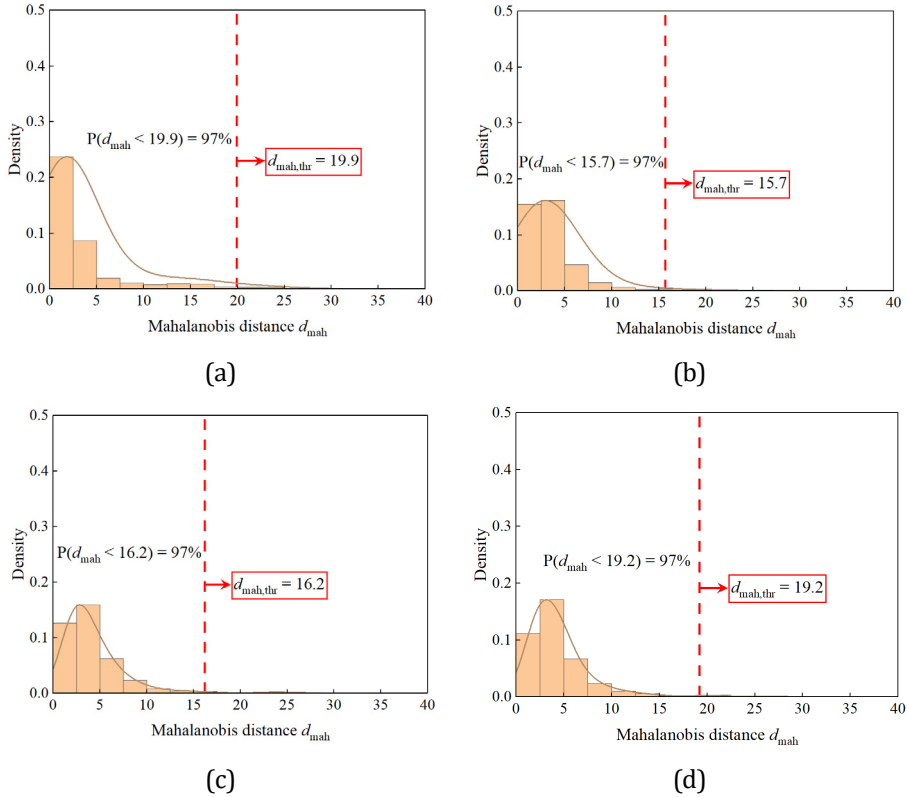


Fig. 6-15 Probability distribution of distance matrix $\{D\}$ of PBL signals from (a) CT-1-WS α , (b) CT-2-WS α , (c) CT-2-PZT1, and (d) CT-2-PZT2

As the main focus of the fatigue tests is crack initiation, AE signals acquired up to 3.0×10^4 cycles are analyzed. Fig. 6-16 shows the MD d_i calculated between the features of i -th acquired signals and $\{A_0\}$. Table 6-2 summarizes the detected number of cycles to crack initiation by DIC and AE for the CT specimens. The results show that the PZT sensors collect fewer AE events than the WS α sensor, which is consistent with previous findings reported in [27]. Nevertheless, thin PZT sensors in conjunction with the proposed approach can provide efficient detection results as the WS α sensor (see Table 6-2).

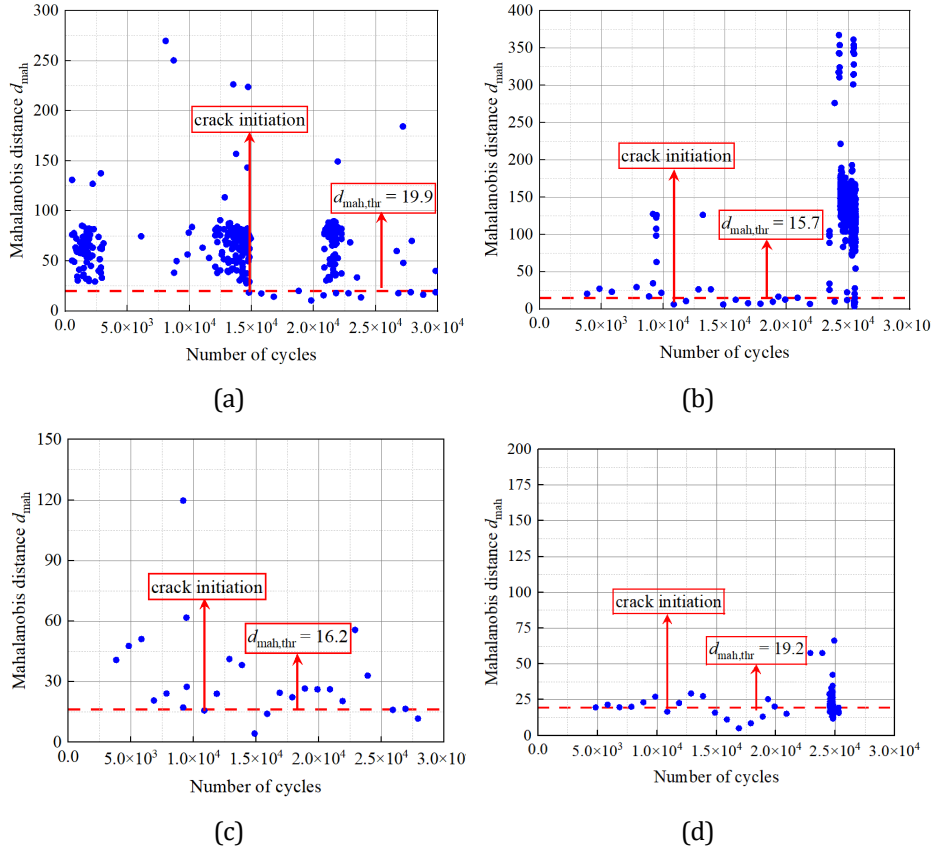


Fig. 6-16 Mahalanobis distance between acquired signals and reference state (a) CT-1-WS α , (b) CT-2-WS α , (c) CT-2-PZT1, and (d) CT-2-PZT2

Table 6-2 Number of cycles at the crack initiation

Specimens	Measurement techniques			
	Acoustic emission	DIC	FOS	LVDT
CT-1	1.47×10^4	1.63×10^4	-	-
CT-2	1.09×10^4	1.35×10^4	-	-
C1-WC	3.39×10^4	-	3.93×10^4	5.47×10^4

6.5 EARLY WARNING FOR C1-WC

6.5.1 Results of DOFS and LVDT measurement

The failure modes of the C1-WC specimen are illustrated in Fig. 6-17. The crack was initiated from the edge of the hole in the lower segment. As the crack continues to grow, it will enter a stable crack growth zone. When the crack reaches a critical size, it can no longer support the applied load leading to a sudden fracture of the C1-WC.

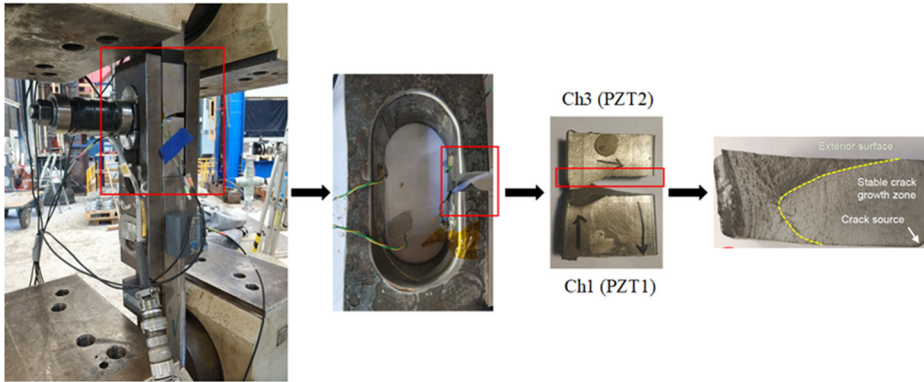


Fig. 6-17 Failure mode of C1-WCs

The approximate location of the crack source can be inferred from Fig. 6-17. The effective length of the optical fibers attached to the specimen was confirmed to be between $x = 2.0456$ to $x = 2.0482$ m, where x denotes the distance to the fiber termination. The space between the distributed data points collected along the fiber is 0.6 mm. The strain measured within this range during the fatigue test is depicted in Fig. 6-18. A gradual increase in the measured strain is observed from the selected data points, owing to the introduction of slight plastic deformation at the beginning of the fatigue test, which corresponds to cyclic hardening of the material. The rate of increase in the measured strain at the data point $x = 2.0482$ m changed significantly at around 3.93×10^4 cycles, which is interpreted as an indication of crack initiation. This sudden increase in strain can be attributed to the stress concentration near the crack tip.

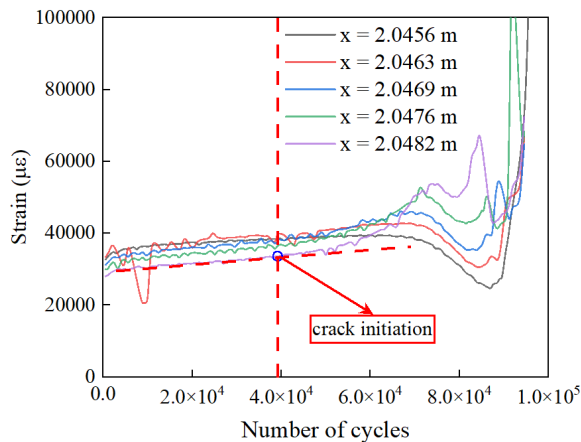


Fig. 6-18 Measured strain results of C1-WC

Fig. 6-19 displays the dynamic stiffness obtained from the LVDT measurements. The stiffness is determined as the maximum load divided by the maximum deformation recorded by the LVDT. A sudden drop in stiffness indicates the onset of crack initiation.

However, since the LVDT was affixed to the exterior surface of the specimen, its sensitivity to detect cracks originating from the interior is limited compared to DOFS measurements.

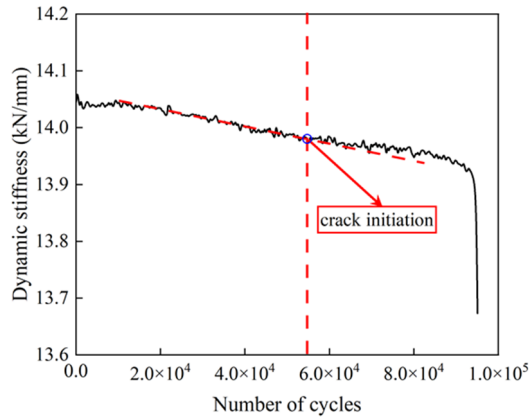


Fig. 6-19 Dynamic stiffness calculation

6.5.2 Results of AE measurement

In the context of AE monitoring of C1-WCs, 1200 PBL signals are recorded prior to the assembly of the specimen. Fig. 6-17 shows that Ch3 is located closest to the region of crack damage. The density plot of two frequency-domain features and the distribution of the distance matrix $\{D\}$ of Ch3 from PBL signals is shown in Fig. 6-20. The damage identification threshold is computed to be 21.6, and the number of cycles to the initiation of the crack is estimated to be 3.39×10^4 (see Fig. 6-21). Table 6-2 presents the detection results using various monitoring techniques for C1-WC specimen. Among the employed methods, AE technique offers significantly earlier warning signs of fatigue damage than LVDT measurement. Although DOFS demonstrates comparable detection performance, DOFS exhibit a limited strain measurement range, which may not capture the full range of strains encountered by the metal material during fatigue loading [52]. Additionally, DOFS are prone to mechanical damage, such as bending, crushing, or stretching, which can result in permanent signal loss or reduced accuracy [53]. Furthermore, the installation and maintenance of DOFS can be costly, particularly over long distances or in harsh environments, which may limit their practicality in certain applications.

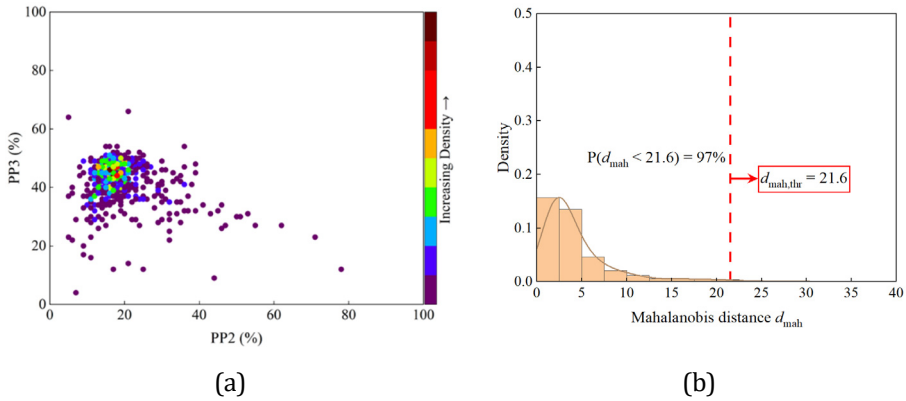


Fig. 6-20 Distribution of (a) features (b) MD of ch3 from PBL signals

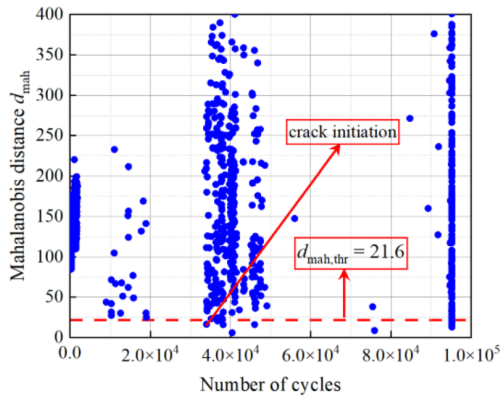


Fig. 6-21 distance results of C1-WCs fatigue test

6.6 CONCLUSION

The objective of this chapter is to investigate the use of acoustic emission (AE) monitoring by thin PZT sensors for early fatigue damage detection in restricted-access areas. A baseline-based method was proposed to achieve this goal. First, a benchmark model of the “damage” state was created by extracting the damage-sensitive features from pencil-breaking leads (PBL) generated signals. The multivariate feature vectors were then mapped to Mahalanobis distance (MD) for identification. A threshold was defined to distinguish the “damage” state and normal state at a 97% probability of the MD distribution in the benchmark model. Second, the MD between the feature vector from acquired AE signals and the benchmark model was calculated as the damage indicator (DI). Finally, the damage was diagnosed if the DI of an unknown state is lower than the defined threshold.

Using the proposed methodology, thin PZT sensors can successfully detect the time when premature cracks occur, providing early damage warning for C1-WC with

complex geometry and thick plates. Additionally, a digital image correlation (DIC)-based detection method was also discussed in this chapter. This approach is adaptive and objective in identifying the crack tip accurately, making it a powerful support measurement technique.

The proposed method only requires pre-knowledge of the critical area. In conjunction with numerical analysis, regions of possible damage locations can be identified and regarded as primary areas of concern. To collect the dataset for the proposed baseline-based method, PBL tests can be conducted once the critical area is identified. These tests do not need to be conducted on real structures, but can be done on a plate of the same thickness and material as the real structures.

This chapter addresses research question Q4) by proposing a baseline-based approach. The PBL-generated dataset is regarded as the “damage” benchmark model. This study demonstrates that the proposed approach is highly successful in detecting early damage in C1-WC using AE monitoring by thin PZT sensors.

REFERENCES

- [1] V. Igwemezie, A. Mehmanparast, A. Kolios, Current trend in offshore wind energy sector and material requirements for fatigue resistance improvement in large wind turbine support structures – A review, *Renew. Sustain. Energy Rev.* 101 (2019) 181–196. <https://doi.org/10.1016/J.RSER.2018.11.002>.
- [2] H. Díaz, C. Guedes Soares, Review of the current status, technology and future trends of offshore wind farms, *Ocean Eng.* 209 (2020) 107381. <https://doi.org/10.1016/J.OCEANENG.2020.107381>.
- [3] WindEurope, Offshore wind in Europe - key trends and statistics 2021, (2021). <https://windeurope.org/intelligence-platform/product/offshore-wind-in-europe-key-trends-and-statistics-2021/>.
- [4] H. Ryan, A. Annoni, J. Winkes, A. Mehmanparast, Optimising design parameters for offshore wind MP-TP wedge connection technology using analytical techniques, *Ocean Eng.* 268 (2023) 113562. <https://doi.org/10.1016/J.OCEANENG.2022.113562>.
- [5] B. Wisner, K. Mazur, A. Kontsos, The use of nondestructive evaluation methods in fatigue: A review, *Fatigue Fract. Eng. Mater. Struct.* 43 (2020) 859–878. <https://doi.org/10.1111/ffe.13208>.
- [6] C.U. Grosse, M. Ohtsu, *Acoustic emission testing*, Springer Science & Business Media, 2008. <https://doi.org/10.1016/B978-0-12-804176-5.00028-1>.
- [7] S. Beskhyroun, L.D. Wegner, B.F. Sparling, Crack detection and characterization techniques - An overview, *Struct. Control Heal. Monit.* (2011) n/a-n/a. <https://doi.org/10.1002/stc>.
- [8] A. Keshtgar, C.M. Sauerbrunn, M. Modarres, Structural reliability prediction using acoustic emission-based modeling of fatigue crack growth, *Appl. Sci.* 8 (2018). <https://doi.org/10.3390/app8081225>.
- [9] P.A. Vanniamparambil, I. Bartoli, K. Hazeli, J. Cuadra, E. Schwartz, R. Saralaya, A. Kontsos, An integrated structural health monitoring approach for crack growth monitoring, *J. Intell. Mater. Syst. Struct.* 23 (2012) 1563–1573. https://doi.org/10.1177/1045389X12447987/ASSET/IMAGES/LARGE/10.1177_1045389X12447987-FIG2.JPEG.
- [10] T. Shiraiwa, H. Takahashi, M. Enoki, Acoustic emission analysis during fatigue crack propagation by Bayesian statistical modeling, *Mater. Sci. Eng. A.* 778 (2020) 139087. <https://doi.org/10.1016/j.msea.2020.139087>.
- [11] M. Rabiei, M. Modarres, Quantitative methods for structural health management using in situ acoustic emission monitoring, *Int. J. Fatigue.* 49 (2013) 81–89. <https://doi.org/10.1016/j.ijfatigue.2012.12.001>.
- [12] A. Krampikowska, R. Pała, I. Dzioba, G. Świt, The use of the acoustic emission method to identify crack growth in 40CrMo steel, *Materials (Basel)*. 12 (2019) 1–14. <https://doi.org/10.3390/ma12132140>.
- [13] F.T. Santo, T.P. Sattar, G. Edwards, Validation of acoustic emission waveform entropy as a damage identification feature, *Appl. Sci.* 9 (2019) 4070. <https://doi.org/10.3390/app9194070>.
- [14] A. Kahirdeh, C. Sauerbrunn, H. Yun, M. Modarres, A parametric approach to acoustic entropy estimation for assessment of fatigue damage, *Int. J. Fatigue.* 100 (2017) 229–237. <https://doi.org/10.1016/j.ijfatigue.2017.03.019>.

- [15] M. Chai, Z. Zhang, Q. Duan, A new qualitative acoustic emission parameter based on Shannon's entropy for damage monitoring, *Mech. Syst. Signal Process.* 100 (2018) 617–629. <https://doi.org/10.1016/j.ymsp.2017.08.007>.
- [16] D. Li, K. Sze, C. Kuang, C.G. Koh, Rail crack monitoring based on Tsallis synchrosqueezed wavelet entropy of acoustic emission signals: A field study, *Struct. Heal. Monit.* 17 (2018) 1410–1424. <https://doi.org/10.1177/1475921717742339>.
- [17] A.K. Das, C.K.Y. Leung, Power spectral entropy of acoustic emission signal as a new damage indicator to identify the operating regime of strain hardening cementitious composites, *Cem. Concr. Compos.* 104 (2019) 103409. <https://doi.org/10.1016/j.cemconcomp.2019.103409>.
- [18] J. Kumar, S. Ahmad, C.K. Mukhopadhyay, T. Jayakumar, V. Kumar, Acoustic emission studies for characterization of fatigue crack growth behavior in HSLA steel, *Nondestruct. Test. Eval.* 31 (2016) 77–96. <https://doi.org/10.1080/10589759.2015.1070850>.
- [19] F.F. Barsoum, J. Suleman, A. Korcak, E.V.K. Hill, Acoustic Emission Monitoring and Fatigue Life Prediction in Axially Loaded Notched Steel Specimens, *J. Acoust. Emiss.* (2009) 27. <https://www.ndt.net/article/jae/papers/27-040.pdf>.
- [20] D. D'Angela, M. Ercolino, Acoustic emission entropy: An innovative approach for structural health monitoring of fracture-critical metallic components subjected to fatigue loading, *Fatigue Fract. Eng. Mater. Struct.* 44 (2021) 1041–1058. <https://doi.org/10.1111/ffe.13412>.
- [21] L. Cheng, F. Yang, J.S. Winkes, M. Veljkovic, The C1 wedge connection in towers for wind turbine structures, tensile behaviour of a segment test, *Eng. Struct.* 282 (2023) 115799. <https://doi.org/10.1016/j.ENGSTRUCT.2023.115799>.
- [22] V. Giurgiutiu, *Structural health monitoring with piezoelectric wafer active sensors*, Elsevier, 2007.
- [23] J.C. Garrett, H. Mei, V. Giurgiutiu, An Artificial Intelligence Approach to Fatigue Crack Length Estimation from Acoustic Emission Waves in Thin Metallic Plates, *Appl. Sci.* 2022, Vol. 12, Page 1372. 12 (2022) 1372. <https://doi.org/10.3390/APP12031372>.
- [24] Y. Bhuiyan, B. Lin, V. Giurgiutiu, Characterization of piezoelectric wafer active sensor for acoustic emission sensing, (2018). <https://doi.org/10.1016/j.ultras.2018.08.020>.
- [25] B. Trujillo, A. Zagari, D. Meisner, S. Momeni, Monitoring of Acoustic Emission Activity using Thin Wafer Piezoelectric Sensors, in: 21th Annu. Int. Symp. Smart Struct. Mater. + NDE Heal. Monit. Diagnostics, n.d.
- [26] L. Yu, S. Momeni, V. Godinez, V. Giurgiutiu, Adaptation of PWAS Transducers to Acoustic Emission Sensors, (2011). <https://doi.org/10.1117/12.880157>.
- [27] L. Yu, S. Momeni, V. Godinez, V. Giurgiutiu, P. Ziehl, J. Yu, Dual mode sensing with low-profile piezoelectric thin wafer sensors for steel bridge crack detection and diagnosis, *Adv. Civ. Eng.* 2012 (2012). <https://doi.org/10.1155/2012/402179>.
- [28] I.N. Giannakeas, Z. Sharif Khodaei, M.H. Aliabadi, Digital clone testing platform for the assessment of SHM systems under uncertainty, *Mech. Syst. Signal Process.* 163 (2022) 108150. <https://doi.org/10.1016/j.YMSSP.2021.108150>.
- [29] A. De Luca, D. Perfetto, A. De Fenza, G. Petrone, F. Caputo, Guided wave SHM system for damage detection in complex composite structure, *Theor. Appl. Fract. Mech.* 105 (2020) 102408. <https://doi.org/10.1016/j.tafmec.2019.102408>.
- [30] Z. Su, L. Ye, *Identification of damage using Lamb waves*, Springer Science & Business Media, 2009.

- [31] N. Yue, Z. SharifKhodaei, M. Aliabadi, Damage Detection in Large Composite Stiffened Panels based on a Novel SHM Building Block, *Smart Mater. Struct.* (2021). <https://doi.org/10.1088/1361-665X/abe4b4>.
- [32] M. Rautela, J. Senthilnath, E. Monaco, S. Gopalakrishnan, Delamination prediction in composite panels using unsupervised-feature learning methods with wavelet-enhanced guided wave representations, *Compos. Struct.* 291 (2022) 115579. <https://doi.org/10.1016/J.COMPSTRUCT.2022.115579>.
- [33] R. Joseph, M.Y. Bhuiyan, V. Giurgiutiu, Acoustic emission from vibration of cracked sheet-metal samples, *Eng. Fract. Mech.* (2019). <https://doi.org/10.1016/j.engfracmech.2019.106544>.
- [34] C.U. Grosse, F. Finck, J.H. Kurz, H.W. Reinhardt, Improvements of AE technique using wavelet algorithms, coherence functions and automatic data analysis, in: *Constr. Build. Mater.*, 2004. <https://doi.org/10.1016/j.conbuildmat.2003.10.010>.
- [35] M. Yeager, B. Gregory, C. Key, M. Todd, On using robust Mahalanobis distance estimations for feature discrimination in a damage detection scenario, *Struct. Heal. Monit.* 18 (2018) 245–253. <https://doi.org/10.1177/1475921717748878>.
- [36] H. Sarmadi, A. Karamodin, A novel anomaly detection method based on adaptive Mahalanobis-squared distance and one-class kNN rule for structural health monitoring under environmental effects, *Mech. Syst. Signal Process.* 140 (2020) 106495. <https://doi.org/10.1016/J.YMSSP.2019.106495>.
- [37] J.A.S. Paixão, S. da Silva, E. Figueiredo, Damage Quantification in Composite Structures Using Autoregressive Models, in: *Proc. 13th Int. Conf. Damage Assess. Struct., Pleiades journals*, 2020: pp. 804–815. https://doi.org/10.1007/978-981-13-8331-1_63/FIGURES/8.
- [38] M. Sause, Investigation of pencil-lead breaks as acoustic emission sources, *J. Acoust. Emiss.* 29 (2011) 184–196.
- [39] M.A. Hamstad, Acoustic emission signals generated by monopole (pencil-lead break) versus dipole sources: finite element modeling and experiments, 25 (2007) 92–106.
- [40] J. Gary, M.A. Hamstad, On the far-field structure of waves generated by a pencil-break on a thin plate, *J. Acoust. Emiss.* 12 (1994) 157–170.
- [41] A.M. Zelenyak, M.A. Hamstad, M.G.R. Sause, Modeling of acoustic emission signal propagation in waveguides, *Sensors (Switzerland)*. 15 (2015) 11805–11822. <https://doi.org/10.3390/s150511805>.
- [42] S.F. Karimian, M. Modarres, Acoustic emission signal clustering in CFRP laminates using a new feature set based on waveform analysis and information entropy analysis, *Compos. Struct.* 268 (2021) 113987. <https://doi.org/10.1016/J.COMPSTRUCT.2021.113987>.
- [43] Model_WSa, (n.d.). https://www.physicalacoustics.com/content/literature/sensors/Model_WSa.pdf (accessed February 20, 2022).
- [44] P. Ochoa, R.M. Groves, R. Benedictus, Systematic multiparameter design methodology for an ultrasonic health monitoring system for full-scale composite aircraft primary structures, *Struct. Control Heal. Monit.* 26 (2019) e2340. <https://doi.org/10.1002/stc.2340>.
- [45] L. Cheng, A. Nokhbatolfighahai, R.M. Groves, M. Veljkovic, Acoustic emission-based detection in restricted-access areas using multiple PZT disc sensors, in: *Eur. Work. Struct. Heal. Monit.*, Springer, Cham, 2023: pp. 619–629. https://doi.org/10.1007/978-3-031-07254-3_62.
- [46] B. Zhao, D. Lei, J. Fu, L. Yang, W. Xu, Experimental study on micro-damage identification in reinforced concrete beam with wavelet packet and DIC method, *Constr. Build. Mater.* 210 (2019) 338–346. <https://doi.org/10.1016/J.CONBUILDMAT.2019.03.175>.

- [47] S. Nag-Chowdhury, H. Bellégou, I. Pillin, M. Castro, P. Longrais, J.F. Feller, Crossed investigation of damage in composites with embedded quantum resistive strain sensors (sQRS), acoustic emission (AE) and digital image correlation (DIC), *Compos. Sci. Technol.* 160 (2018) 79–85. <https://doi.org/10.1016/J.COMPSCITECH.2018.03.023>.
- [48] R. Yan, H. El Bamby, M. Veljkovic, H. Xin, F. Yang, A method for identifying the boundary of regions in welded coupon specimens using digital image correlation, *Mater. Des.* 210 (2021) 110073. <https://doi.org/10.1016/J.MATDES.2021.110073>.
- [49] D. Vashishth, Rising crack-growth-resistance behavior in cortical bone:: implications for toughness measurements, *J. Biomech.* 37 (2004) 943–946. <https://doi.org/10.1016/J.JBIOMECH.2003.11.003>.
- [50] U.M.N. Jayawickrema, H.M.C.M. Herath, N.K. Hettiarachchi, H.P. Sooriyaarachchi, J.A. Epaarachchi, Fibre-optic sensor and deep learning-based structural health monitoring systems for civil structures: A review, *Measurement* 199 (2022) 111543. <https://doi.org/10.1016/J.MEASUREMENT.2022.111543>.
- [51] A. Broer, G. Galanopoulos, R. Benedictus, T. Loutas, D. Zarouchas, Fusion-based damage diagnostics for stiffened composite panels, *Struct. Heal. Monit.* (2021) 147592172110071. <https://doi.org/10.1177/14759217211007127>.
- [52] A. Barrias, J.R. Casas, S. Villalba, A Review of Distributed Optical Fiber Sensors for Civil Engineering Applications, *Sensors* 2016, Vol. 16, Page 748. 16 (2016) 748. <https://doi.org/10.3390/S16050748>.
- [53] H. Mohamad, A.M. Asce, K. Soga, M. Asce, ; Adam Pellew, P.J. Bennett, Performance Monitoring of a Secant-Piled Wall Using Distributed Fiber Optic Strain Sensing, *J. Geotech. Geoenvironmental Eng.* 137 (2011) 1236–1243. [https://doi.org/10.1061/\(ASCE\)GT.1943-5606.0000543](https://doi.org/10.1061/(ASCE)GT.1943-5606.0000543).

7. CONCLUSIONS AND RECOMMENDATIONS

In this chapter, a brief overview of this research work is given. The research questions are revisited, and the main conclusions are summarized for each question. Additionally, recommendations are provided for future research, with a focus on exploring the practical applications of the proposed methods for real-time monitoring purposes.

7.1 CONCLUSIONS

The main research questions and sub research questions were, reproduced from Section 1.3, as follows:

Main research questions: *How can the performance of the C1 wedge connection be effectively characterized and its material degradation detected by the AE technique?*

Q1: How can the mechanical performance of the C1 wedge connection be investigated under static and cyclic tensile loading conditions?

Q2: How can the performance between various types of MP-TP connections be compared?

Q3: How can the performance of the AE technique for identifying the deformation stage of metal be improved in a noisy environment?

Q4: How can the efficiency of AE monitoring by thin PZT sensors be improved to detect damage in structures with complex geometry and thick plates?

Referring to the established research questions, the final goal of this thesis is to develop efficient assessment tools to explore the implementation of the C1-WCs in a wind farm. Destructive testing and non-destructive testing method are used in this research work to get the mechanical property and evaluate the status of C1-WCs, respectively. The general conclusions are given below:

Characterise the tensile behaviour of 2nd generation of the C1-WC:

This relates to Q1. Stiffness degradation and bolt force variation of the C1-WC under cyclic loading were quantitatively evaluated. It was found that the effect of cyclic loading is negligible as long as the applied load does not exceed the critical load. An advanced finite element (FE) model was developed in chapter 2. The validated FE model provides a deeper understanding of the load transfer mechanism and the complex interaction between the parts. Through parametric analysis, it is suggested to apply sufficient preloading force to avoid any bolt failure. The FE results demonstrate that inaccurate bolt preloading can be effectively avoided during the installation, which enhances confidence in implementing this connection. The developed FE model allows the industry to conduct a more detailed analysis of C1-WCs for further development. By developing such a sophisticated model, design solutions can be validated with significantly less experimental testing.

Compare the performance between various connections:

This relates to Q2. The selection of connections is vital to the overall competitiveness of OWTs. In this research, the efficiency of the laboratory segment test was investigated. It was found that the laboratory segment fatigue tests lead to a rather conservative assessment for C1-WCs, emphasizing the need to consider this effect during connection design. Meanwhile, C1-WCs were shown to be a robust connection for offshore applications, exhibiting less sensitivity to preload force. A correlation between static

and fatigue connection behaviour and performance was discovered. The method used to extract the bolt stress provides an opportunity to evaluate the fatigue performance of the bolted flange connection. Instead of requiring expensive and time-consuming physical testing, FE-assisted investigation can accurately simulate the behaviour of different types of connections. The results also provide in-depth knowledge for the practical application of such connections and further optimization.

Propose a hybrid model for deformation stage identification:

This relates to Q3. The effectiveness of the AE monitoring technique heavily depends on the quality of the measured AE signals. The proposed SSA-VMD method is an adaptive algorithm for filtering both wide-band ground noise and narrow-band mechanical noise effectively. This method provided a solution to select the proper parameters for noise filtering without the time-consuming numerical simulation. It can reduce noise while preserving relevant elements of the original signals under strong noise conditions ($\text{SNR} < 0$). The combination of SSA-VMD with ANN achieved the deformation stage identification successfully under a seriously noisy environment. These findings provide the basis for the development of new methodologies for monitoring the structural health of in-service steel structures.

Propose a data-driven fusion based method for using multiple thin PZT sensors:

This relates to Q4. A criterion for selecting the optimal thin PZT sensors was proposed aiming at passive sensing applications for AE monitoring. It is recommended to choose thin PZT sensors that exhibit high-sensitivity responses within the frequency band of interest for the specific application. A data-driven fusion based method was proposed to reconstruct the signals from the conventional sensor by using multiple thin PZT sensors. This method is useful when the conventional sensor cannot be used for the restricted-access area. Converting the thin PZT signals to conventional AE sensors can make damage identification easier, as the features from conventional AE sensors are more representative. Specifically, the proposed method reconstructs AE features from the frequency domain with high accuracy, which plays a significant role in damage identification. These findings demonstrate the potential application of fusing multiple thin PZT sensors for damage indication. Such studies are expected to shed new light on possible improvements in the performance of thin PZT sensors in AE monitoring.

Propose a baseline-based method for early damage warning:

This pertains to Q4 from a second perspective. A baseline-driven method was proposed to improve the detection efficiency of thin PZT sensors. A benchmark model correlating to the early damage state is created by breaking pencil leads. Multivariate feature vectors are extracted and then mapped to the Mahalanobis distance for identification. Using the proposed methodology, thin PZT sensors can successfully detect the onset of premature cracks, providing early damage warning for structures with complex geometry and thick plates, such as C1-WC. Importantly, the proposed method only requires pre-knowledge of the critical area. In conjunction with numerical analysis, regions of possible damage locations can be identified and regarded as primary areas

of concern. Overall, this method can be extended and applied to detect damage in other structures with similar damage mechanisms, making it a valuable tool for structural health monitoring.

7.2 RECOMMENDATION FOR FUTURE WORK

In this work, the efficient assessment tools were developed to explore the implementation of the C1-WCs in a wind farm. Further research is recommended as follows.

1. To consider the spatial effects on the behaviour of the C1-WC, it is recommended to conduct numerical analyses using a full-scale model of C1-WC. Additionally, the steel material used in this research for numerical simulation was calibrated using static tensile testing. Uniaxial and multi-axial cyclic loading testing could be added to obtain the fatigue damage parameter, which is helpful to perform the fatigue assessment of the C1-WC. A more robust assessment of its fatigue performance can be obtained, which is essential for ensuring its durability and safety.
2. The comparison between C1-WC, RF connection, and RF connection with defined contacts was carried out using the segment model. However, previous research has demonstrated that the gap (imperfection) plays an essential role in evaluating the fatigue performance of RF connections. The full-scale model with RF connection containing the gaps could be examined to provide more trustworthy guidance for connection.
3. It is important to note that the collected AE signals are dependent on the measurement system used in the measurement process. The boundary reflections, sensor response and sensor sensitivity could affect the waveforms. These effects were omitted in the proposed methodology. Although the effectiveness of the SSA-VMD method has been confirmed by the denoising results of both simulation and measured signals, further investigation with more experimental results is necessary to confirm its universality.
4. Furthermore, to assess the performance of the Artificial Neural Network (ANN)-based deformation stage identification, it is recommended to provide supporting information from microstructural examinations. Such an approach would provide more comprehensive insights into the deformation mechanisms and help to validate the accuracy of the ANN-based deformation stage identification method.
5. The data-level fusion approach using multi-thin PZT sensors has been validated using PBL tests, which are less challenging than practical situations. In future work, it is recommended to consider the uncertainties caused by different sensor layouts, measuring cables, and soldering qualities to train the CNN and obtain more accurate results. Conducting comparative studies of deep learning methods and architectures would be beneficial to improve the accuracy of damage detection using thin PZT

sensors. Moreover, fatigue tests are imperative to the development and validation of the proposed approach.

6. The findings presented in this thesis should be further extended to investigate the effects of material types, sample geometries, and loading configurations on AE generation to establish the reliability of the AE technique. Additionally, finite element modelling approaches should be developed to enhance the understanding of the AE signal propagation and detection process, which can help to characterize the reliability of the AE technique for sensors placed at different locations. This information can be used to make informed decisions on the optimal choice of sensor placement for a particular installation.

Future work should focus on applying the techniques proposed in this study for real-life monitoring purposes. While laboratory tests were conducted to mimic real-life conditions, additional challenges can arise from environmental factors, structural complexity, and the presence of a wide range of AE sources.

SUMMARY

In the past two decades, offshore wind has emerged as a new source of renewable energy. This highlights the requirement for the utilisation of larger and more efficient offshore wind turbines (OWTs). The connections used in support structures of OWTs are critical to ensure the excellent structural performance of OWTs. An alternative option is the C1 wedge connection (C1-WC) to join virtually all the wind turbine generator (WTG) towers to their foundations. This connection shows promising potential in reducing construction, installation, and maintenance costs by eliminating the ring flange and using smaller diameter bolts.

Till now, C1-WC has undergone three generations of development. A more comprehensive research program is required to explore its implementation in a wind farm. The load transfer mechanism and critical component of C1 wedge connections are different to the conventional bolted ring flange (RF) connections. It is important to understand the mechanical behaviour of this connection. Meanwhile, support structures are exposed to the harsh environment during the service life of the OWTs. Material degradation and local cracks in the connection are inevitable to affect the serviceability of OWTs. A need for a reliable and rigorous structural health monitoring (SHM) system for the connection is evident. As one of the non-destructive techniques (NDT), Acoustic emission (AE) has been extensively used in early damage detection and real-time assessment of steel structures. Despite its successful applications, challenges still exist in using AE technique for monitoring applications, especially in analysing the recorded data. Therefore, the research aims to assist in understanding mechanical behaviour and evaluating the health status of the innovative connection.

An extensive experimental program was conducted to evaluate the static and cyclic behaviour of the C1-WCs. Additionally, a detailed 3D non-linear finite element (FE) model of the C1-WCs has been developed. The incorporation of material non-linearity and ductile damage allows the FE model to model the post-necking and final fracture of the connection. The FE model replicates with a good agreement the experimental tensile static and cyclic tests up to the final damage and reproduces the joint behaviour correctly. Parametric studies investigate the influence of bolt grade, the friction coefficient between contact surfaces, and the preloading force level on mechanical behaviour. Moreover, a quantitative comparison between C1-WC and two types of connections (RF connection and RF connection with defined contacts) is performed to provide practical insights into the selection and application of such connections and further optimization. FE-assisted analyses were performed to examine the effect of applied boundary conditions, bolt pretension level, and steel grade on the behaviour of the connections.

In addition to mechanical behaviour analysis, this research is also focused on developing data processing methods to address the challenges of AE monitoring for the C1-WCs. A hybrid model is proposed to identify the deformation stage of metal material.

This method combines a self-adaptive denoising technique and an Artificial neural network (ANN). To reduce noise in the AE signals, a decomposition-based denoising method is proposed based on singular spectral analysis (SSA) and variable mode decomposition (VMD), referred to as SSA-VMD. After denoising, an ANN is constructed to identify the deformation stage of steel materials using features extracted from the filtered AE signals as input.

Fatigue damage of the C1-WCs could result in catastrophic failure of OWTs. Due to space constraints, it can be challenging to detect surface cracks in the lower segment holes of the C1-WC using commercial sensors. Thin PZT sensors are lightweight and small, making them suitable for use in restricted-access areas. However, their poor signal-to-noise ratio can limit their effectiveness in AE monitoring. A criterion for selecting the optimal thin PZT sensors is proposed and a configuration is designed for multiple sensors. Two signal processing methods are then proposed in terms of this issue. Firstly, a data fusion-based method is proposed to enhance the functionality of thin PZT sensors in AE applications. Convolutional neural networks (CNNs) combined with principal component analysis (PCA) are employed for signal processing and data fusion. Secondly, a baseline-based method is proposed to provide early warning of the fatigue damage of C1-WCs using thin PZT sensors. A benchmark model correlating to the damage state is created by breaking pencil leads. Multi-variate feature vectors are extracted and then mapped to the Mahalanobis distance for identification.

Based on this research work, an efficient FE method has been developed to further improve the design of C1-WC. By providing an in-depth guideline for evaluating the mechanical performance of connections used in OWTs, this research has the potential to contribute to the development of more robust and reliable wind turbine structures. Moreover, the proposed signal processing methods for identifying the deformation stage and early fatigue damage can be further explored in structures with similar damage mechanisms. This can lead to the development of more accurate and effective methods for monitoring and assessing the health of offshore wind turbines, ultimately contributing to improved safety and reliability in the renewable energy industry.

SAMENVATTING

In de afgelopen twee decennia is offshore wind naar voren gekomen als een nieuwe bron van hernieuwbare energie. Dit benadrukt de behoefte aan het gebruik van grotere en efficiëntere offshore windturbines (OWTs). De verbindingen die worden gebruikt in ondersteunende structuren van OWTs zijn van cruciaal belang om de uitstekende structurele prestaties van OWTs te garanderen. Een alternatieve optie is de C1-wigverbinding (C1-WC) om vrijwel alle windturbinegenerator-torens (WTG) met hun funderingen te verbinden. Deze verbinding biedt veelbelovend potentieel voor het verlagen van de constructie-, installatie- en onderhoudskosten door de ringflens te elimineren en bouten met een kleinere diameter te gebruiken.

Tot nu toe heeft C1-WC drie generaties ontwikkeling doorgemaakt. Er is een uitgebreid onderzoeksprogramma nodig om de implementatie ervan in een windpark te verkennen. Het last overbrengings mechanisme en de kritieke component van C1-wigverbindingen zijn anders dan die van de conventionele geboude ringflensverbindingen (RF). Het is belangrijk om het mechanische gedrag van deze verbinding te begrijpen. Ondertussen worden ondersteuningsconstructies blootgesteld aan de barre omstandigheden tijdens de levensduur van de OWTs. Materiaaldegradatie en lokale scheuren in de verbinding zijn onvermijdelijk om de bruikbaarheid van OWTs aan te tasten. Er is duidelijk behoefte aan een betrouwbaar en rigoureuus systeem voor structurele gezondheidsmonitoring (SHM) voor de verbinding. Als een van de niet-destructieve technieken (NDT) is akoestische emissie (AE) op grote schaal gebruikt bij vroege schadedetectie en real-time beoordeling van staalconstructies. Ondanks de succesvolle toepassingen zijn er nog steeds uitdagingen bij het gebruik van AE-techniek voor monitoringtoepassingen, vooral bij het analyseren van de geregistreerde gegevens. Daarom is het onderzoek bedoeld om te helpen bij het begrijpen van mechanisch gedrag en het evalueren van de gezondheidsstatus van de innovatieve verbinding.

Er werd een uitgebreid experimenteel programma uitgevoerd om het statische en cyclische gedrag van de C1-WC's te evalueren. Daarnaast is een gedetailleerd 3D niet-lineair eindige elementen (FE) model van de C1-WC's ontwikkeld. Door de integratie van materiële niet-lineariteit en ductiele schade kan het FE-model de post-insnoering en uiteindelijke breuk van de verbinding modelleren. Het FE-model repliceert met een goede overeenkomst de experimentele statische en cyclische trekproeven tot aan de uiteindelijke schade en reproduceert het verbindingsgedrag correct. Parametrische studies onderzoeken de invloed van boutkwaliteit, de wrijvingscoëfficiënt tussen contactoppervlakken en het niveau van de voorspankracht op mechanisch gedrag. Bovendien wordt een kwantitatieve vergelijking tussen C1-WC en twee soorten verbindingen (RF-verbinding en RF-verbinding met gedefinieerde contacten) uitgevoerd om praktisch inzicht te geven in de selectie en toepassing van dergelijke

verbindingen en verdere optimalisatie. FE-geassisteerde analyses werden uitgevoerd om het effect van toegepaste randvoorwaarden, boutvoorspanningsniveau en staalkwaliteit op het gedrag van de verbindingen te onderzoeken.

Naast mechanische gedragsanalyse, dit onderzoek is ook gericht op het ontwikkelen van methoden voor gegevensverwerking om de uitdagingen van AE-monitoring voor de C1-WC's aan te pakken. Een hybride model wordt voorgesteld om het vervormingsstadium van metaalmateriaal te identificeren. Deze methode combineert een zelfaanpassende denoising-techniek en een kunstmatig neurale netwerk (ANN). Om ruis in de AE-signalen te verminderen, wordt een op decompositie gebaseerde denoising-methode voorgesteld op basis van singuliere spectrale analyse (SSA) en variabele modus-decompositie (VMD), waarnaar wordt verwezen als SSA-VMD. Na het verwijderen van ruis wordt een ANN geconstrueerd om het vervormingsstadium van staalmaterialen te identificeren met behulp van kenmerken die zijn geëxtraheerd uit de gefilterde AE-signalen als invoer.

Vermoeiingsschade van de C1-WCs kan leiden tot catastrofaal falen van OWTs. Vanwege ruimtebeperkingen kan het een uitdaging zijn om oppervlaktescheuren in de gaten in het onderste segment van de C1-WC te detecteren met behulp van commerciële sensoren. Dunne PZT-sensoren zijn lichtgewicht en klein, waardoor ze geschikt zijn voor gebruik in gebieden met beperkte toegang. Hun slechte signaal-ruisverhouding kan echter hun effectiviteit bij AE-bewaking beperken. Er wordt een criterium voorgesteld voor het selecteren van de optimale dunne PZT-sensoren en er wordt een configuratie ontworpen voor meerdere sensoren. Twee signaalverwerkingsmethoden worden vervolgens voorgesteld met betrekking tot dit probleem. Ten eerste wordt een op datafusie gebaseerde methode voorgesteld om de functionaliteit van dunne PZT-sensoren in AE-toepassingen te verbeteren convolutionele neurale netwerken (CNNs) gecombineerd met hoofdcomponentenanalyse (PCA) worden gebruikt voor signaalverwerking en datafusie. Ten tweede wordt een op basislijn gebaseerde methode voorgesteld om vroegtijdig te waarschuwen voor de vermoeidheidsschade van C1-WC's met behulp van dunne PZT-sensoren. Een benchmarkmodel dat correleert met de schadetoestand wordt gecreëerd door potloodstiften te breken. Multivariate kenmerkvectoren worden geëxtraheerd en vervolgens in kaart gebracht op de Mahalanobis-afstand voor identificatie.

Op basis van dit onderzoekswerk is een efficiënte FE-methode ontwikkeld om het ontwerp van C1-WC verder te verbeteren. Door een diepgaande richtlijn te bieden voor het evalueren van de mechanische prestaties van verbindingen die worden gebruikt in OWTs, heeft dit onderzoek het potentieel om bij te dragen aan de ontwikkeling van robuustere en betrouwbaardere windturbineconstructies. Bovendien kunnen de voorgestelde signaalverwerkingsmethoden voor het identificeren van de vervormingsfase en vroege vermoeiingsschade verder worden onderzocht in constructies met vergelijkbare schademechanismen. Dit kan leiden tot de ontwikkeling van nauwkeurigere en effectievere methoden voor het bewaken en beoordelen van de

gezondheid van offshore windturbines, wat uiteindelijk bijdraagt aan verbeterde veiligheid en betrouwbaarheid in de hernieuwbare energie-industrie.

ACKNOWLEDGMENTS

At the end of the thesis, I would like to express my grateful acknowledgement for all support from colleagues, friends, and family.

First and foremost, I would like to express my sincere gratitude to my promotor and supervisor, Prof. Dr. Milan Veljkovic. Thank you for offering me the position at TU Delft. During our meetings and discussions, you consistently encouraged me to engage in critical and independent thinking by presenting questions. You motivated me to share my research with audiences beyond our research group. Your expertise, invaluable insights, and continuous encouragement have played a pivotal role in shaping my academic growth and personal development. Additionally, I extend my sincere appreciation to my promotor, Dr. Roger Groves, who joined my supervision team after attending my GonoGo meeting. I am grateful for the valuable feedback and insightful discussions we have had regarding my research. You graciously introduced me to the NDT Lab and facilitated my integration into the team. In addition to your expertise in non-destructive testing, I also learned valuable communication skills from you.

I have amazing predecessors who guided me towards the acoustic emission world. Prof. Haohui Xin, thanks for your guidance and support as my daily supervisor in the early stages of my Ph.D. journey. You played a crucial role in introducing me to this fascinating research domain. Your patient and meticulous guidance empowered me to navigate through unfamiliar territories and equipped me with the necessary skills to perform experiments and conduct research effectively. I have always seen you as someone who is born to be a scientist. Dr. Ali Nokhbatolfoghahai, you started your post-doc in Roger's research group in 2020. Thanks for your guidance and support during the third and fourth years of my Ph.D. studies. Roger suggested I contact you to learn how to use the signal generator. Luckily, after that, we had quite frequent weekly meetings and I have already regarded you as my "daily supervisor". Your expertise in ultrasonic inspection has been truly helpful to my research. Our weekly discussions, often extending for hours in the lab, have significantly contributed to the advancement of my research. Your kind and approachable nature has made our interactions enjoyable and productive. Dr. Vincentius Ewald, several of your research works have served as a source of inspiration for me in the field of FE simulation for acoustic emission. During the initial months of my PhD, I proactively reached out to your office seeking consultation on FE simulation specifically related to waves. Given my limited familiarity with the subject and challenges with expressing myself in English, my questions may have been difficult to comprehend. However, you patiently answered my questions in detail and your willingness to share your FE model and offer guidance has been immensely helpful.

My research would not have been finished without having the opportunity to cooperate and communicate with so many excellent researchers. Dr. Fei Yang, it was your depth of knowledge and expertise in the field of bolts that has been instrumental in broadening my understanding and providing me with valuable insights. You always help me to find the value of my research and encourage me to transfer my research work to publications. Dr. Marc Seidel from Siemens, thank you for sharing valuable information about the L-flange project. Your strict dedication to research, as well as your expertise and ambition in exploring the development and application of L-flange connections, have been a tremendous source of inspiration for me. Jasper Winkes, Koen Creusen, and George Misios from C1 Connection B.V., I am grateful for your willingness to share all the details and information about the C1 wedge connection, without any hesitation. It was a pleasure working alongside you in the Stevin Lab during the experimental work, and I greatly benefited from the experience. I learned a great deal from your work efficiency and found inspiration in our discussions. Dr. Marko Pavlović, it was your research work about ring-flange connections that guided me to perform numerical simulation of connections. You generously shared insightful information about ring-flange connections for FE models. Dr. Yuguang Yang, thanks for providing constructive feedback during my GonoGo meeting. Your kindness in reminding me to consider the risks associated with my PhD has been immensely helpful.

I truly appreciate all the support for my experimental work. Peter De Vries, thanks for playing a vital role in my experimental work. Your guidance and thorough information regarding the uncertainties I needed to consider, such as booking the experimental setup, coordinating with technicians, and ensuring their availability, were irreplaceable. I would also like to extend my thanks to Fred Schilperoort for your kind assistance in answering my questions and providing the necessary devices when I needed them. Your support during the test was greatly appreciated. Giorgos Stamoulis, I am incredibly grateful for your assistance in conducting the tests, particularly in the realm of monitoring with DIC. I truly admire your passion and love for work and life. Kees van Beek, you have extensive knowledge about every test. Thanks for your patient guidance in assisting me with practical tasks, such as soldering and resolving sensor noise issues. Your kindness is truly appreciated. To Sam Reus and Jaap Elstgeest, I would like to express my thanks for your help in preparing the electrical equipment and related materials. Your support was crucial in ensuring a smooth workflow. John Hermsen, thanks for your help in polishing specimens.

I feel lucky to have known such fascinating office mates, groupmates, and faculty mates. Weijian Wu, you are an expert in welds and fatigue. Your guidance has been indispensable in enriching my understanding in this field. Rui Yan, we have dedicated a significant amount of time to performing coupon tests. Your feedback on my research work and academic career has been incredibly valuable. Your experience in connecting with factories and suppliers taught me valuable negotiation skills. Jincheng Yang and Mathieu Koetsier, I am grateful for the inspiration you provided in incorporating optic fibers into my tests. Your patience in guiding me through the procedure of installing

fibers and collecting data with the Luna system has been helpful. Marcio Moreira Arouche, thanks for teaching me about the micro-scope camera for scanning. I could not get useful images for simulating bolts without your instruction. Ding Liao, I was glad to cooperate with you. Your efficiency in research was impressive, and I appreciate your assistance in conducting the test when I was attending the conference. Anis Issam, your willingness to share your experience with me has been deeply appreciated. Your suggestion to prioritize thesis writing during the summer and not get overly consumed by ongoing work has made me reconsider my approach to completing my PhD thesis. I extend my thanks to David for collaborating on his project to perform AE monitoring. Qinkun Sun, the master's student under my supervision, I have truly enjoyed our communication and working together.

I would like to express my heartfelt gratitude to my (ex) officemates, Pei He and Zhanchong Shi. Our daily conversations and interactions have been a constant source of motivation and inspiration. A special thank you goes to Xiuli Wang for introducing me to X-sport, where I have discovered a profound sense of happiness through sports. We have also shared the experience of being library mates as we prepared to write our theses. Your qualities of self-discipline, enthusiasm for life, and dedication to sports are truly admirable. I would also like to extend my appreciation to the other members of our group: Xiaoling Liu, Weikang Feng, Da Xiang, Shuang Qiu, Tao Yang, Florentia Kavoura, Trayana Tankova, Hagar El Bamby, Michele Mirra, and Abhijith Kamath. Each of you has been an incredible colleague, always ready to lend a helping hand and provide insightful perspectives. Your friendship, encouragement, and collaborative spirit have made the Ph.D. experience immensely enjoyable and fulfilling.

I acknowledge the support and kindness from colleagues at the NDT Lab, Faculty of Aerospace. Nan Yue, I have a vivid memory of the day we first met at the NDT Lab in Aerospace. I had read your paper before meeting you, and it was truly gratifying to have the opportunity to meet you in person. Your energetic and outgoing personality, combined with your clear sense of purpose, left a lasting impression on me. Xiang Wang, I am grateful to you for introducing me to the Lab and inviting me to participate in the activities of the NDT group. Your inclusive nature has allowed me to become part of a vibrant and collaborative community.

I would also like to extend my heartfelt thanks to colleagues from 3ME, particularly Dr. Pooria Pahlavan, for generously lending me sensors and providing valuable feedback on my research during the EWSHM conference. Bert Scheeren, it was through Pooria's suggestion that I contacted you about sensors, and we coincidentally met again at EWSHM, even sharing the same flight. Your friendly and approachable demeanor made our interactions truly enjoyable. I have learned a great deal from you, especially in the field of Structural Health Monitoring.

I would like to express my sincere appreciation to Fanxiang Xu, Yuxuan Feng, Yi Xia, Mengmeng Gao, Lubin Huo, Fengqiao Zhang, Lichao Wu, Bo Li, Chi Jin, Xiaohui Liang, Xuhui Liang, Li Wang, Haoyu Li, Chenjie Yu, Quanxin Jiang, Langzi Chang, Yang Jin, Bowen Li, Dengxiao Lang, Jian Zhang, Chunyan He, Biyue Wang, Wenting Ma, Minfei

Liang, Zhi Wan, Jin Chen, Shan He, Zejia Zheng, Yu Chen, Shizhe Zhang, Kally Mao, Yading Xu, Hua Dong. The moments we shared, whether it was during lunches, dinners, parties, or trips, hold a special place in my heart. They are memories I will cherish forever. Thank you for being such amazing friends.

Zhiwei Qian, Jin Chang, Yun Wan, Xuan Li, Keji Pan, Yifan Fu, Shan Qu, Xinmin You, Qian Feng, Hao Yu, Zhao Chen, Chenlu Song, Yuan Wu. Knowing all of you has been an incredible stroke of luck. Thank you for providing me with countless constructive suggestions. Your guidance and support were crucial in helping me navigate the process. Without your help, my life in the Netherlands would have been much more challenging. I owe a tremendous amount of gratitude to my friends in China, especially Xing Cheng. Our friendship has spanned over 15 years, and I deeply appreciate your unwavering support during my emotional moments.

I am immensely grateful to my family for making my journey through my PhD filled with love. My heartfelt thanks go to my parents for bringing me up and instilling in me the courage to face challenges head-on. To my younger sisters and brother, thank you for sharing your happiness with me, bringing laughter into my life, and providing me with endless inspiration. A special expression of gratitude goes to my incredible mom, Yirong Wang. From you, I have learned the importance of strength and resilience. I am also deeply thankful to my grandparents, Yulan Zhang and Renning Wang, whose unwavering support has been a constant motivation for me.

I would like to give a special acknowledgement to my boyfriend, Ze Chang. In the last year of my PhD, you have partly worked as my daily supervisor, consistently pushing me to persevere and complete my PhD. I cannot imagine this journey without your unwavering companionship. I have learned the art of thinking ahead from you, and your academic inspiration has been truly impactful. Thank you for sharing in both my happiness and sadness throughout this journey.

Lu Cheng
Delft, July 2023

LIST OF PUBLICATIONS

JOURNAL PUBLICATIONS

1. **Cheng, L.**, Yang, F., Winkes, J. S. & Veljkovic, M. (2023). *The C1 wedge connection in towers for wind turbine structures, tensile behaviour of a segment test*. Engineering Structures, 282, 115799.
2. **Cheng, L.**, Yang, F., Seidel, M. & Veljkovic, M. (2023). *FE-assisted investigation for mechanical behaviour of connections in offshore wind turbine towers*. Engineering Structures, 285, 116039.
3. **Cheng, L.**, Nokhbatolfighahai, A., Groves, R. M., & Veljkovic, M. (2023). *Data level fusion of acoustic emission sensors using deep learning*. (Under review)
4. **Cheng, L.**, Sun, Q., Yan, R., Groves, R. M., & Veljkovic, M. (2023). *Application of Acoustic emission for deformation stage identification combining SSA-VMD and ANN*. (In preparation)
5. Liao, D., **Cheng, L.**, Veljkovic, M., Correial, J., Zhu, S., Winkes, J.S., Creusen, K. (2023) *Fatigue analysis on a thick steel plate with a central hole: a probabilistic perspective*. (In preparation)
6. Xin, H., Tarus, I., **Cheng, L.**, Veljkovic, M., Persem, N., & Lorich, L. (2021). *Experiments and numerical simulation of wire and arc additive manufactured steel materials*. Structures, 34 (1393-1402).
7. **Cheng, L.**, Xin, H., Groves, R. M., & Veljkovic, M. (2021). *Acoustic emission source location using Lamb wave propagation simulation and artificial neural network for I-shaped steel girder*. Construction and Building Materials, 273, 121706.
8. Xin, H., **Cheng, L.***, Diender, R., & Veljkovic, M. (2020). *Fracture acoustic emission signals identification of stay cables in bridge engineering application using deep transfer learning and wavelet analysis*. Advances in Bridge Engineering, 1(1), 1-16.

CONFERENCE PROCEEDINGS

1. **Cheng, L.**, Nokhbatolfighahai, A., Groves, R. M., & Veljkovic, M. (2023). *Acoustic Emission-Based Detection in Restricted-Access Areas Using Multiple PZT Disc Sensors*. In European Workshop on Structural Health Monitoring (pp. 619-629). Springer, Cham.
2. **Cheng, L.**, Xin, H., & Veljkovic, M. (2021). *Numerical analysis of ring flange connection with defined surface area*. ce/papers, 4(2-4), 182-188.

3. Yang, F., Veljkovic, M., & **Cheng, L.** (2021). *Fracture simulation of fully and partially threaded bolts under tension*. ce/papers, 4(2-4), 156-161.
4. **Cheng, L.**, Xin, H., Groves, R. M., & Veljkovic, M. (2020). *Plasticity and damage characteristic of acoustic emission signals for S460 steel exposed to tensile load*. In Virtual conference on mechanical fatigue.
5. **Cheng, L.**, Xin, H., & Veljkovic, M. (2019). *Acoustic emission source location in I girder based on experimental study and lamb wave propagation simulation*. ce/papers, 3(5-6), 3-12.

CURRICULUM VITAE

LU CHENG



27-11-1995 Born in ShanXi, China

EDUCATION

Sep. 2011 – July. 2015	B.SC student Civil Engineering Taiyuan University of Technology, China
Sep. 2015 – July. 2018	M.SC student Structural Engineering Dalian University of Technology, China
Oct. 2018 – Present	PhD. candidate Civil Engineering and Geoscience Delft University of Technology, The Netherlands